

AD-A153 204

PROCEEDINGS OF THE WORKSHOP ON NDE OF POLYMERS HELD AT  
VIMEIRO PORTUGAL ON 4-5 SEPTEMBER 1984(U) BRISTOL UNIV  
(ENGLAND) H H WILLS PHYSICS LAB 05 SEP 84

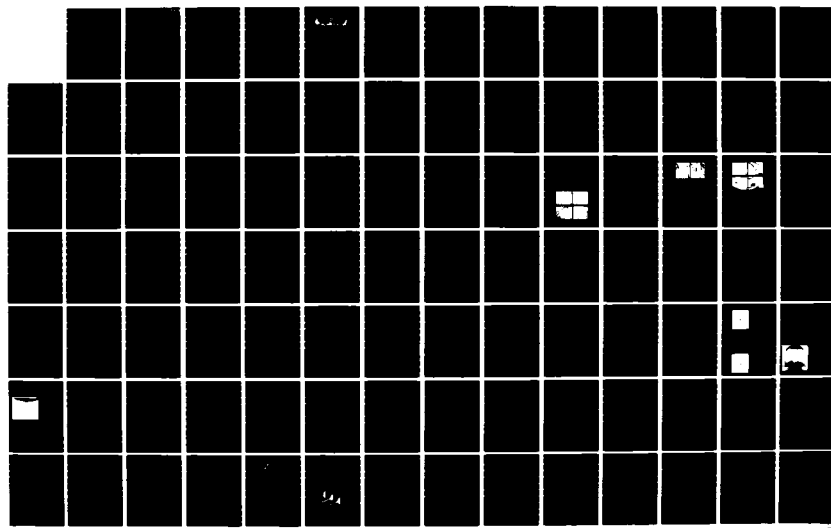
1/4

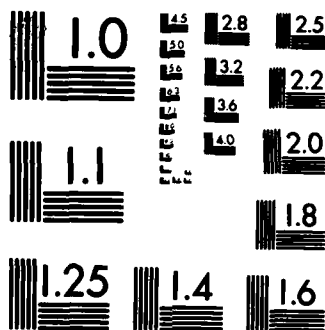
UNCLASSIFIED

DAJ45-84-M-0182

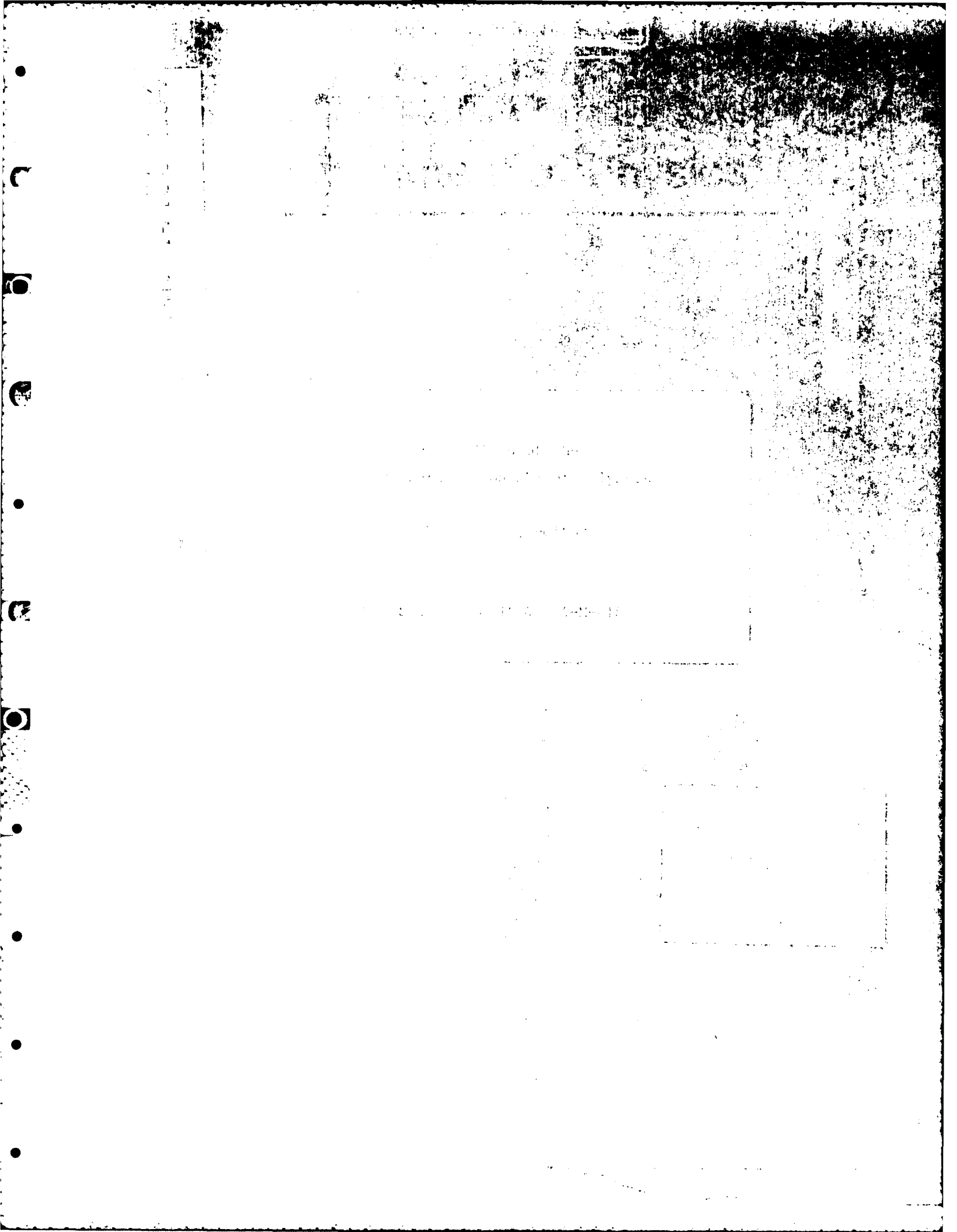
F/G 11/9

NL





MICROCOPY RESOLUTION TEST CHART  
NATIONAL BUREAU OF STANDARDS-1963-A



①

Proceedings of the  
Vimeiro Workshop on NDE of Polymers

K H G Ashbee, editor

Grant Number DAJA-45-84-M-0182

Handwritten notes and stamps in the bottom left corner, including a large 'A' and some illegible text.



**DTIC**  
**ELECTE**  
MAR 5 1985  
**A**

This document has been approved  
for public release and sale; its  
distribution is unlimited.



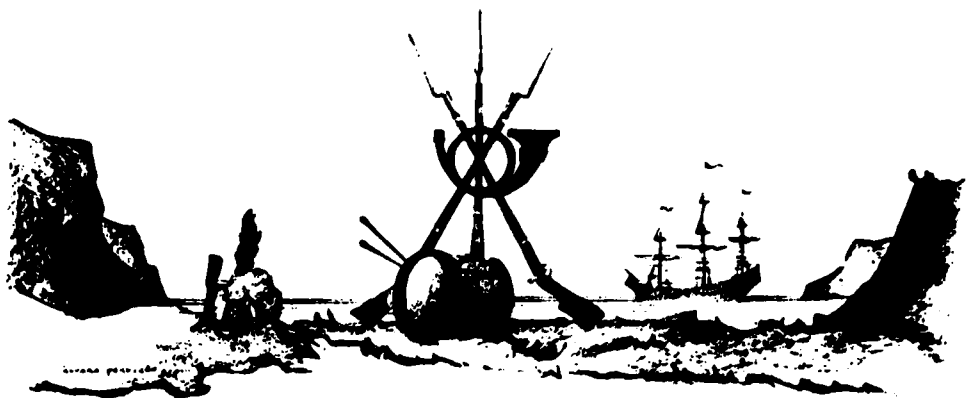
Proceedings of the Vimeiro Workshop on

POLYMER NDE

edited by K H G Ashbee

A two-day workshop held at the Hotel Golf Mar,  
Vimeiro, Portugal

September 4 and 5, 1984



GENERAL ARTHUR WELLESLEY,  
 LORD WELLINGTON, EMINENT CHIEF OF THE  
 ANGLO-PORTUGUESE FORCES DURING THE NAPOLEONIC  
 INVASIONS. GREAT FRIEND OF PORTUGAL AND ITS PEOPLE,  
 ADMIRER OF THEIR NEVER DENIED MILITARY PRIDE, CHOSE  
 THIS PLACE - PORTO NOVO BEACH - WHERE AN ENGLISH  
 FRIGATE AND ABOUT THIRTY TRANSPORT SHIPS ANCHORED  
 THE 20 TH AUGUST, 1808, FOR THE LANDING OF GENERAL  
 ANSTRUTHER'S BRIGADE, TOTALING 2400 MEN, AND ON THE  
 FOLLOWING DAY OF GENERAL CCKLAND'S BRIGADE  
 AMOUNTING TO 1750 MEN. THESE TROOPS HIGHLY  
 CONTRIBUTED FOR THE VICTORY OF THE DELIVERER ARMIES  
 AT THE VIMEIRO LANDS.

THE SOCIETY OF THE "GUAS DO VIMEIRO,  
 ASKED TO COLLECT THIS LEGEND IN ORDER TO REMIND  
 FUTURE GENERATIONS OF EXAMPLE OF THIS MEMORABLE  
 PASSAGE. WHEN ENGLAND, OUR OLD ALLY, HAD A VERY  
 PREPONDERANT ACTION, IN THE FIGHT FOR THE INTEGRITY OF  
 PORTUGAL.

PORTO NOVO, 21 ST. AUGUST 1966 THE 158 TH ANNIVERSARY OF THE VIMEIRO BATTLE

GOLF CLUB OF VIMEIRO THERMAL WATERS TORRES VEDRAS PORTUGAL 1966

## Introduction

Short presentations based on this collection of papers formed the basis of a workshop held at the Hotel Golf Mar, Vimeiro, Portugal on September 4 and 5, 1984. This workshop was initiated by Dr G Mayer of the US Army Research Office, Research Triangle Park, North Carolina 27709. Having identified an interest in the NDE of polymers, Dr Mayer convened a meeting at The Johns Hopkins University between himself, Professor R E Green Jr of the department of Materials Science and Engineering at Johns Hopkins, Dr R K Eby of the Polymers Division, National Bureau of Standards, and myself. We decided that the time was ripe for a workshop on the subject of real-time on-line methods for the nondestructive evaluation of components fabricated from polymeric materials.

In components fabricated from polymers, including polymers in the rubbery state and polymers reinforced with fibres, there exists the possibility of microstructural defects which have their origins in processing. These defects include inhomogeneous mixing, inclusion of foreign bodies, segregation, incomplete cure, inhomogeneous cure, molecular orientation, macroscopic anisotropy and residual stress. In addition to considering "states of the art" as practised in Europe, it was decided to address the feasibility of new exploitation of physical techniques to secure, for use as processing tools, the real-time detection of such defects.

This volume is a more complete statement of some of the European efforts towards achieving polymer NDE than was possible in a 2-day workshop. It does,

however, include transcriptions by the editor of comments made during the course of the workshop.

The workshop was supported by Grant No DAJA-45-84-M-0182 from the US Army Research, Development and Standardization Group - UK.

K H G Ashbee

Vimeiro, September 1984

### CONTRIBUTING AUTHORS

K H G Ashbee, University of Bristol, H H Wills Physics Laboratory, Tyndall Avenue, Bristol BS8 1TL, England

M F Ashby, University Engineering Department, Trumpington Street, Cambridge CB2 1PZ, England

W J Beranek, Netherlands Organization for Applied Scientific Research (TNO), Institute for Building Materials and Building Structures (IBBC), P O Box 49, 2600 AA Delft, The Netherlands

N Barracclough, CSIC, Residence de Investigadores, Pinar 21, Madrid 6, Spain

P W R Beaumont, University Engineering Department, Trumpington Street, Cambridge CB2 1PZ, England

A R Bunsell, Centre des Matériaux, Ecole National Supérieure des Mines de Paris, BP 87, 91003 - Evry Cedex, France

A D Carr, Marconi Research Centre, West Hanningfield Road, Great Baddow, Chelmsford, Essex, England

H Cherek, Institut für Kunststoffverarbeitung, Pontstr 49 - D5100, Aachen, West Germany

B Deloche, Laboratoire de Physique des Solides, Batiment 510, Université de Paris-Sud, 91405 Orsay, France

F C Frank, Orchard Cottage, Grove Road, Coombe Dingle, Bristol BS9 2RL, England

J-M Guenet, Centre de Recherches sur les Macromolécules (CRNS), 6 rue Boussingault, 67083 Strasbourg-Cedex, France

P D Hanstead, University of Bristol, H H Wills Physics Laboratory, Tyndall Avenue, Bristol BS8 1TL, England

J F Jansson, The Royal Institute of Technology, Department of Polymer Technology, S-100 44, Stockholm, Sweden

D Katz, Department of Materials Engineering, Technion, Israel Institute of Technology, Haifa, Israel

R Lyall, Bartol Limited, Pollard Moor Works, Padiham, Burnley, Lancashire BB12 7JR, England

G Marom, The Hebrew University of Jerusalem, Casali Institute of Applied Chemistry, 91904 Jerusalem, Israel

G Menges, Institut für Kunststoffverarbeitung, Pontstr 49 - D5100, Aachen, West Germany

M Moshfeghi, University of Bristol, H H Wills Physics Laboratory, Tyndall Avenue, Bristol BS8 1TL, England

B Ponsot, Centre des Matériaux, Ecole National Supérieure des Mines de Paris, BP 87, 91003 - Evry Cedex, France

A Poursartip, University Engineering Department, Trumpington Street, Cambridge CB2 1PZ, England

K L Reifsneider, Virginia Polytechnic Institute and State University, College of Engineering, Blacksburg, Virginia 24061-4899, USA

D M Sadler, Institut Laue-Langevin, 156X Centre de Tri-38042 Grenoble, Cedex, France

J P Sargent, University of Bristol, H H Wills Physics Laboratory, Tyndall Avenue, Bristol BS8 1TL, England

H Sundström, The Royal Institute of Technology, Department of Polymer Technology, S-100 44, Stockholm, Sweden

P S Theocaris, Department of Theoretical and Applied Mechanics, The National Technical University of Athens, Athens GR-157 73, Greece

D Turner, Avon Rubber Plc, Bath Road, Melksham, Wiltshire SN12 8AA, England

C E Upstill, University of Bristol, H H Wills Physics Laboratory, Tyndall Avenue, Bristol BS8 1TL, England

D Valentin, Centre des Matériaux, Ecole National Supérieure des Mines de Paris, BP 87, 91003 - Evry Cedex, France

F J Wright, Institut für Informationsverarbeitung, Universität Tübingen, Kötlinstraße 6, D-7400 Tübingen 1, West Germany

✓

→ Partial CONTENTS:

Chapter I: Microstructure at the molecular level;

F J Wright

Dislocations in wave trains, with special reference to the information they carry about microstructure

D Katz

Microphase separation in densely crosslinked polymers

P S Theocaris

Probing the mesophase layer in polymeric composites

Discussion

Chapter II: Molecular orientation;

J-M Guenet

The contribution of neutron scattering to the determination of chain trajectory in semi-crystalline isotactic polystyrene

D M Sadler

Molecular extension and orientation in a crystalline polymer

Discussion

Cont'd

Chapter III: NDE of laminates

D M Turner

Quality control and lifetime prediction of rubber fabric composites

K L Reifsneider

Feasibility of useful real time in-process evaluation of laminates

Discussion

Chapter IV: Acoustic emission

G Marom, A Mittelman and I Roman

"The value of in-process monitoring of acoustic emission during partial pressurisation of pressure vessels"

J-F Jansson and Henrik Sundström

The strain rate dependence of acoustic emission, including the detection and non-detection of defects known to be subjected to internal stress

D Valentin, B Ponsot and A R Bunsell

Qualitative and quantitative evaluation of damage in CFRP by acoustic emission during structural loading

Discussion



Chapter V: Control of fibre orientation in short fibre composites;

G Menges and H Cherek

"A non-destructive control of fibre content and orientation in SMC-articles"

F C Frank

"Orientation mapping"

Discussion

Chapter VI: Electromagnetic wave propagation in composite materials;

J P Sargent and C Upstill

"The propagation of light through fibre reinforced composites"

A D Carr

"Microwave propagation in carbon fibre reinforced composite material"

W J Beranek

"Potential of holographic interferometry for non-destructive testing of polymer composites"

Discussion

Chapter VII: Fracture mechanics as a method for quality control;

R Lyall

"uPVC - the state of the art"

A Poursartip, M F Ashby and P W R Beaumont

"Fatigue damage mechanics of fibrous laminates"

Discussion

Chapter VIII: Vibrations, elastic waves and ultrasonics;

N Barraclough

Variable frequency ultrasound detection of physical changes in gels and solids

M Moshfeghi and P D Hanstead

Ultrasound reflection tomography of cracks in polyester resin

Discussion

*Cont'd*  
Chapter LX: Rubber elasticity and anisotropy under stress.

B Deloche

"Chain orientation detected with deuterium NMR in uniaxially deformed polymeric networks"

K H G Ashbee and F C Frank

"Bi-dimensional compression testing"

Discussion

X

#### CONTRIBUTING AUTHORS

K H G Ashbee, University of Bristol, H H Wills Physics Laboratory, Tyndall Avenue, Bristol BS8 1TL, England

M F Ashby, University Engineering Department, Trumpington Street, Cambridge CB2 1PZ, England

W J Beranek, Netherlands Organization for Applied Scientific Research (TNO), Institute for Building Materials and Building Structures (IBBC), P O Box 49, 2600 AA Delft, The Netherlands

N Barraclough, CSIC, Residence de Investigadores, Pinar 21, Madrid 6, Spain

P W R Beaumont, University Engineering Department, Trumpington Street, Cambridge CB2 1PZ, England

R H Boyd, University of Utah, Department of Materials Science and Engineering, Utah, USA

A R Bunsell, Centre des Materiaux, Ecole National Supérieure des Mines de Paris, BP 87, 91003 - Evry Cedex, France

A D Carr, Marconi Research Centre, West Hanningfield Road, Great Baddow, Chelmsford, Essex, England

H Cherek, Institut für Kunststoffverarbeitung, Pontstr 49 - D5100, Aachen, FGR

B Deloche, Laboratoire de Physique des Solides, Batiment 510, Université de Paris-Sud, 91405 Orsay, France

F C Frank, Orchard Cottage, Grove Road, Coombe Dingle, Bristol BS9 2RL, England

J-M Guenet, Centre de Recherches sur les Macromolécules (CRNS), 6 rue Boussingault, 67083 Strasbourg-Cedex, France

P D Hanstead, University of Bristol, H H Wills Physics Laboratory, Tyndall Avenue, Bristol BS8 1TL, England

J F Jansson, The Royal Institute of Technology, Department of Polymer Technology, S-100 44, Stockholm, Sweden

D Katz, Department of Materials Engineering, Technion, Israel Institute of Technology, Haifa, Israel

R Lyall, Bartol Limited, Pollard Moor Works, Padiham, Burnley, Lancashire BB12 7JR, England

G Marom, The Hebrew University of Jerusalem, Casali Institute of Applied Chemistry, 91904 Jerusalem, Israel

G Menges, Institut für Kunststoffverarbeitung, Pontstr 49 - D5100, Aachen, FGR

M Moshfeghi, University of Bristol, H H Wills Physics Laboratory, Tyndall Avenue, Bristol BS8 1TL, England

B Ponsot, Centre des Matériaux, Ecole National Supérieure des Mines de Paris, BP 87, 91003 - Evry Cedex, France

A Poursartip, University Engineering Department, Trumpington Street, Cambridge CB2 1PZ, England

K L Reifsneider, Virginia Polytechnic Institute and State University, College of Engineering, Blacksburg, Virginia 24061-4899, USA

D M Sadler, Institut Laue-Langevin, 156X Centre de Tri-38042 Grenoble, Cedex, France

J P Sargent, University of Bristol, H H Wills Physics Laboratory, Tyndall Avenue, Bristol BS8 1TL, England

H Sundström, The Royal Institute of Technology, Department of Polymer Technology, S-100 44, Stockholm, Sweden

P S Theocaris, Department of Theoretical and Applied Mechanics, The National Technical University of Athens, Athens GR-157 73, Greece

D Turner, Avon Rubber Plc, Bath Road, Melksham, Wiltshire SN12 8AA, England

C E Upstill, University of Bristol, H H Wills Physics Laboratory, Tyndall Avenue, Bristol BS8 1TL, England

D Valentin, Centre des Matériaux, Ecole National Supérieure des Mines de Paris, BP 87, 91003 - Evry Cedex, France

F J Wright, Institut für Informationsverarbeitung, Universität Tübingen, Kostlinstrasse 6, D-7400 Tübingen 1, FGR

## CONTENTS

### Session I: Microstructure at the molecular level

F J Wright

"Dislocations in wave trains, with special reference to the information they carry about microstructure"

D Katz

"Microphase separation in densely crosslinked polymers"

P S Theocaris

"Probing the mesophase layer in polymeric materials"

### Session II: Molecular orientation

J-M Guenet

"The contribution of neutron scattering to the determination of chain trajectory in semi-crystalline isotactic polystyrene"

D M Sadler

"Molecular extensions and orientation in crystalline polymers"

R H Boyd

"Orientation of the amorphous fraction in semi-crystalline polymers from dielectric relaxation measurements"

Session III: NDE of laminates

D Turner

"Quality control and lifetime prediction of rubber fabric composites - state of the art"

K L Reifsneider

"Feasibility of real time in-process evaluation of laminates"

Session IV: Acoustic emission

G Marom

"The value of in-process monitoring of acoustic emission during partial pressurisation of pressure vessels"

J F Jansson and Henrik Sundström

"The strain rate dependence of acoustic emission, including the detection and non-detection of defects known to be subjected to internal stress"

D Valentin, B Ponsot and A R Bunsell

"Qualitative and quantitative evaluation of damage in carbon fibre composites by acoustic emission during structural loading"

Session V: Control of fibre orientation in short fibre composites

G Menges and H Cherek

"A non-destructive control of fibre content in SMC-articles"

F C Frank

"Orientation mapping"

Session VI: Electromagnetic wave propagation in composite materials

J P Sargent and C Upstill

"The propagation of light through fibre reinforced composites"

A D Carr

"Microwave propagation in unidirectional carbon fibre reinforced composite material"

W J Beranek

"Potential of holographic interferometry for NDE of polymer composites"

Session VII: Fracture mechanics as a method for quality control

R Lyall

"Assessment of PVC pressure pipe manufacture - state of the art"

A Poursartip, M F Ashby and P W R Beaumont

"Fatigue damage mechanics of fibrous laminates"



Session VIII: Vibrations, elastic waves and ultrasonics

N Barraclough

"Variable frequency ultrasound applied to detect physical changes in gels and solids"

M Moshfeghi and P D Hanstead

"Ultrasound reflection tomography of cracks in polyester resin"

Session IX: Rubber elasticity and anisotropy under stress

B Deloche

"Chain orientation detected with deuterium NMR in uniaxially deformed polymeric networks"

K H G Ashbee and F C Frank

"Bi-dimensional compression testing"

Session X: Closing remarks

Session I: Microstructure at the molecular level

DISLOCATIONS IN WAVE TRAINS, WITH SPECIAL  
REFERENCE TO THE INFORMATION THEY CARRY ABOUT  
MICROSTRUCTURE

F. J. Wright

Institut für Informationsverarbeitung, Universität Tübingen,  
Köstlinstraße 6, D-7400 Tübingen 1, West Germany

ABSTRACT

Wavefront dislocations are edges of wavefronts, which may be modeled by phase singularities, and hence zeros, of a complex wavefunction. In a pulsed field they typically move along trajectories closely related to the continuous-wave amplitude minima at the carrier frequency. In the presence of noise, dislocations may be localized to an accuracy proportional to the S/N ratio. Dislocation trajectories and motion, and their dependence on pulse shape, are investigated for 1- and 2-point-scatterer models of microstructural defects, both within and without an incident plane beam.

1. Introduction to wavefront dislocations

The concept of wavefront dislocations was introduced into wave theory ten years ago by Nye & Berry (1974), in order to explain their observations of ultrasonic pulses reflected from a rough surface in an experiment designed to model radio echo sounding. In a review that sets wavefront dislocations in the general context of wavefield singularities, Berry (1981) summarized the observations as follows. "The incident wave was a quasi-monochromatic pulse and the reflected wave, received at a point and displayed on an oscilloscope as sound pressure vs. time, was an extended train of disorderly oscillations. On moving the receiver to explore the wave at different places, it was quite common to observe two wavecrests move apart and an extra crest appear between them, or the time-reversed sequence of events." Figure 1 shows two examples: as  $\theta$  increases two new wavecrests appear at  $\tau=0$  -- one at  $\theta \sim 23^\circ$  and another at  $\theta \sim 45^\circ$ . The wavecrests appear antisymmetrically in figure 1(a) and symmetrically in figure 1(b) -- in general they will appear asymmetrically.

If a wavecrest/trough pair is equated to a wavefront, then the appearance of a new wavecrest corresponds to crossing the edge of a wavefront. Nye & Berry named these edges 'wavefront dislocations' by analogy with the

---

The preparation of this paper was supported by the  
Stiftung Volkswagenwerk, FRG.

Permanent address (from September 1984): School of  
Mathematical Sciences, Queen Mary College, University  
of London, Mile End Road, London E1 4NS, UK

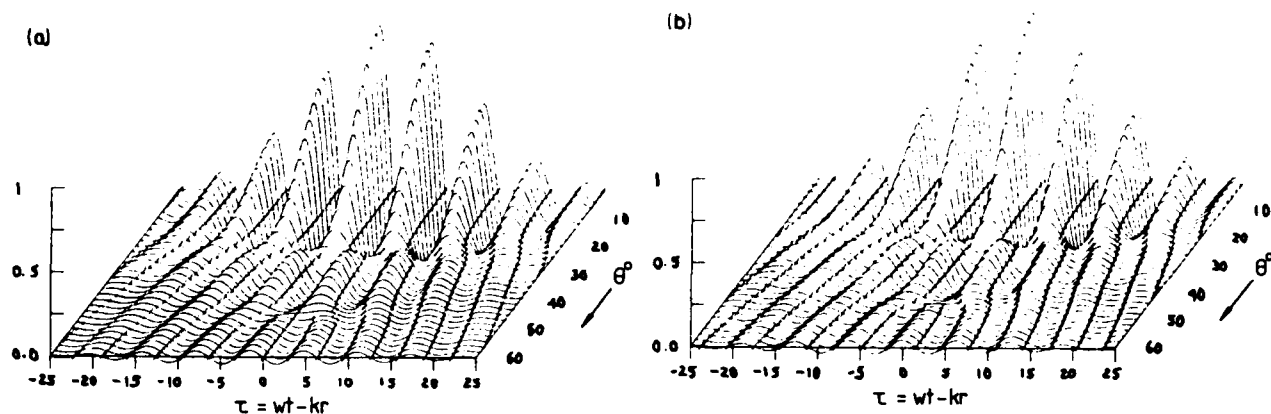


Figure 1. Farfield pulse wavefunction for a circular piston radiator: (a) real part; (b) imaginary part. From Wright & Berry (1984).

edges of atomic planes in imperfect crystals. They are most interesting in wavefields that are generated from a gentle modulation of a continuous wave (cw), i.e. are quasi-monochromatic, because then the dislocations typically move. It is possible to analyse wavefront dislocations directly in terms of crests and troughs of a real wavefunction (Wright 1979), but because wavefront dislocations are features of a quasi-monochromatic wavefield it is possible, and more convenient, to use a complex representation. I shall consider only scalar waves, which can be written in amplitude-phase form as

$$\psi(\underline{r}, t) = \rho(\underline{r}, t) e^{i\chi(\underline{r}, t)},$$

where  $\rho$  and  $\chi$  are real-scalar-valued functions that are uniquely determined (modulo  $2\pi$  for  $\chi$ ) by  $\psi$  unless  $\psi=0$ , in which case  $\chi$  is indeterminate. Wavefronts may be defined by the equation  $\chi(\underline{r}, t) = \text{constant modulo } 2\pi$ , and end, i.e. become undefined, where  $\chi$  is undefined. Hence wavefront dislocations are defined by  $\text{Re}\psi(\underline{r}, t) = \text{Im}\psi(\underline{r}, t) = 0$ : two equations which therefore typically define time-dependent lines in 3D or points in 2D.

The simplest way that  $\psi(\underline{r}, t)$  can pass through zero is linearly -- then very close to the zero the equiphase lines (lines of constant  $\chi$ ) look typically as in figure 2(a). This makes it clear how a wavefront which corresponds to one specific phase, say 0, can end in this model. It also illustrates the sense in which a wavefront dislocation is a topological singularity, characterized by a topological invariant called its dislocation strength. This is  $(1/2\pi)\oint_C d\chi$ , where  $C$  is any path encircling the dislocation once, analogous to the Burgers' circuit around a crystal dislocation; the strength of the dislocation shown in figure 2(a) is clearly +1 (if  $C$  is traversed in the conventional sense). The topological nature of dislocations gives them a useful robustness: they can only interact so as to conserve global dislocation strength, and they can only end on boundaries.

The main purpose of Nye & Berry (1974) was to demonstrate the closeness of the analogy between wavefront and crystal dislocations. By constructing simple local model solutions of the scalar wave equation, they showed that wavefront dislocations can have multiple strength, be of edge or screw type (in 3D), glide and climb. For example, Wright (1979) discussed the following local model of a straight strength- $n$  mixed screw-edge dislocation in an otherwise plane wave traveling along the  $z$  axis:

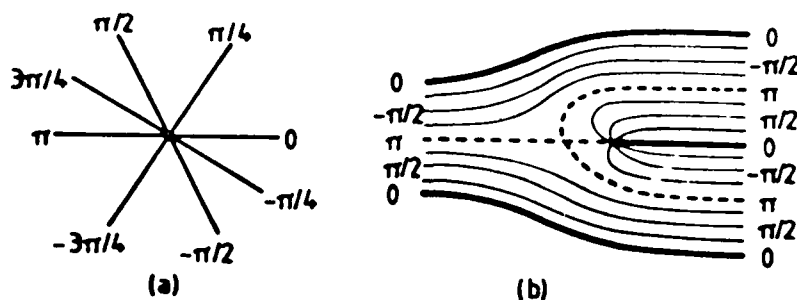


Figure 2. Local (a) and global (b) equiphase lines around a single-strength dislocation in two dimensions. After Nye & Berry (1974).

$$\psi(x, y, \zeta) = (x + \beta_s y + \beta_e \zeta)^n e^{ik\zeta}, \quad \text{where } \zeta = z - ct.$$

However, multiple-strength dislocations are unstable, and so will not typically be seen. Such a model shows that globally the equiphase lines in a section through a simple dislocation must look like figure 2(b). Lines at phase zero have been thickened to represent wavefronts; the phase saddle (here at phase  $\pi$ ) is essential to fit the structure of figure 2(a) into an asymptotically-plane wave.

Nye (1981a) has put the characterization of wavefront dislocations on a more rigorous basis and justified theoretical use of a complex wavefunction. Dislocation effects in electromagnetic waves have been investigated theoretically by Nye (1981b, 1983a,b), and dislocation statistics by Berry (1978); both topics are potentially relevant to NDE of microstructure.

Dislocations have been investigated theoretically in a two-beam model and around a cusped caustic by Wright & Nye (1982). The latter investigation was numerical, using a bandwidth-perturbation theory. The most realistic model in which dislocations have been studied is in the soundfield of a pulsed circular piston radiator, by Wright & Berry (1984). This study was again mostly numerical, and figure 3 shows two of the nearfield plots. The top line is the symmetry axis,  $R$  and  $Z$  are measured in units of the piston radius, which is represented by the double line at the top of the left side. Figure 3(a) is a typical phase plot; it shows an isolated dislocation that was born on the axis, and a pair of dislocations that were born just in front of the piston on a circle of approximately half the piston radius. They are all born in the tail of the pulse. As the pulse propagates, the dislocations glide roughly along the 'valleys', or dark fringes, of the continuous wavefield, as shown in figure 3(b). Initially they fall further into the tail of the pulse, then they rapidly catch up to appear at the centre of the pulse in the far field as shown in figure 1, at angles very close but not equal to the far field cw nulls. The general behaviour is typical of all the models studied, including those I will introduce below, and has been verified experimentally by Humphrey (1980).

## 2. Detection of wavefront dislocations

I have defined wavefront dislocations to be the time-dependent amplitude-zeros of a pulsed wavefield. Therefore, the most obvious way to detect them is to demodulate the received signal and look for zero crossings of the resulting envelope. However, this is likely to be unreliable, because fluctuations in the zero reference level will shift the

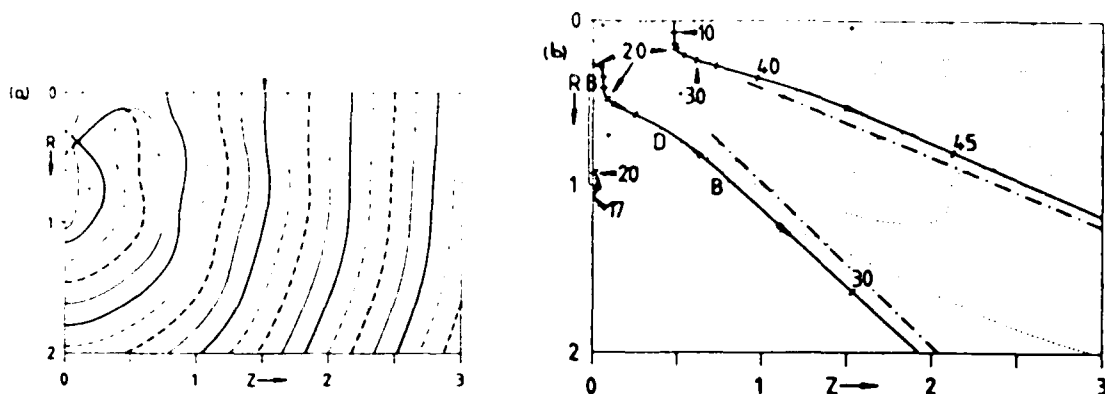


Figure 3. Nearfield of a pulsed circular piston radiator, from Wright & Berry (1984): (a) phase superimposed on amplitude ... ; (b) dislocation trajectories and times, and cw farfield null angles ----, superimposed on cw amplitude ... .

dislocations, and could apparently destroy or create them (in pairs). The failure of this method is because demodulating by definition destroys the phase information, and wavefront dislocations are essentially phase structures. Appreciating this, Walford et al. (1977) built an Argand-plane display for their phase-sensitive radio-echo sounder, in which the imaginary part of the received signal is reconstructed from the real part alone on the assumption of a restricted bandwidth (see also Nye 1981a) and plotted against it on an oscilloscope screen after removing the cw time dependence. At a fixed point in space the display traces out some kind of loop, parametrized by time. The rotation of this loop as the receiver is moved in space is a very sensitive indicator of phase changes of the modulation, and hence of dislocations.

Probably the biggest failure in the analogy between crystal and wavefront dislocations is that whereas crystal dislocations correspond to regions of high energy density, wavefront dislocations correspond to regions of low energy density. In such regions a signal is swamped by noise. The effect is to 'smear out' the dislocation so that it can only be localized to within some region, and not to a point. In the neighbourhood of a simple dislocation the wave amplitude varies linearly. Measuring all amplitudes in terms of the (nominal) peak signal amplitude  $S$  gives a graph like figure 4. Clearly, the linear size  $D$  of the region within which the dislocation might lie is proportional to  $(N/S)$ , but the details depend on the precise waveform. Performing a circuit at distance  $D$  from the true dislocation, where the signal can be reliably measured, will give  $\oint dx = \pm 2\pi$ , confirming that the circuit contains unit dislocation strength, but precisely what constitutes this is hidden in noise.

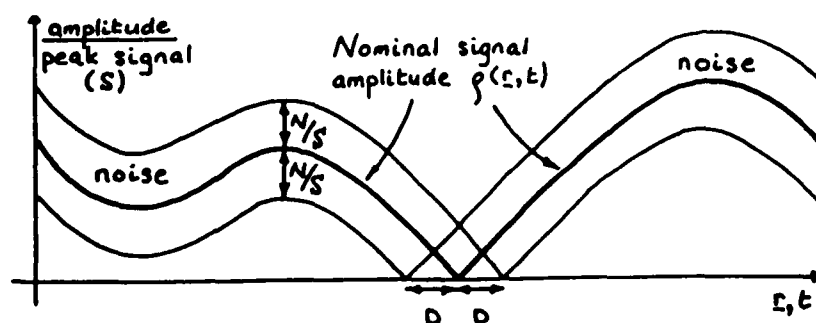


Figure 4. Signal and noise near a simple dislocation.

### 3. Wavefront dislocations created by point scatterers: 2 basic models

My aim in the rest of this paper is to give a general impression of the behaviour of wavefront dislocations created by scattering from microstructural defects (which might include crystal dislocations!) in an otherwise homogeneous medium. Consistent with the general analogy between waves and mechanics, in a region of a wavefield generated by 2 rays the dislocations can be easily studied analytically; for 3 rays they can be studied analytically in special cases, usually perturbatively; otherwise numerical solution by computer is necessary. I shall restrict my attention to the former two cases in two dimensions, which physically relates to line scatterers. All the models I shall consider are related to the two-beam model of Wright & Nye (1982), and I will build them up in order of increasing complexity.

Scattering from microstructure implies the far field, because the scatterer is assumed to be compact and buried inaccessibly inside a specimen. Hence I shall consider only a plane incident wave, given for cw by  $e^{i(kz - \omega t)}$ . When the cw driving signal  $e^{-i\omega t}$  is modulated by  $f(t)$ , the incident wave becomes  $f(t - z/c)e^{i(kz - \omega t)}$  by Fourier synthesis, and scattered waves will acquire a pulse envelope in the same way. There are two scenarios for detection of the scattered wave: the detected wave either includes or excludes the incident wave. The latter might apply if the incident wave is a narrow beam, if the detector has high directional sensitivity, or in modeling monostatic geometry. This distinction makes a big difference for dislocations, so I shall consider both cases.

At least for fairly high frequencies, one expects the received signal to be dominated by a small number of contributions from geometrical rays. Then any scatterer can be modelled by point scatterers situated at the feet of these dominant rays. Widely separated scattering points will primarily behave independently, especially in a pulsed field where time-delays are important. Therefore, I consider a single point scatterer, and two closely-spaced point scatterers, each represented by a scattering amplitude and phase as shown in figure 5, which I assume independent of frequency.

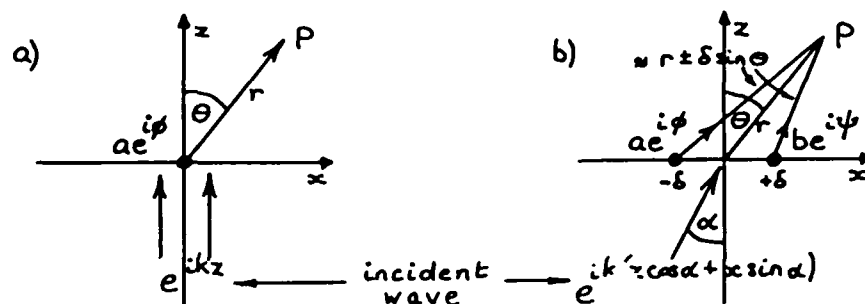


Figure 5. Scattering geometry for (a) one and (b) two point scatterers. P is the observation point.

Each model will be analysed first for an incident cw of angular frequency  $\omega$ , and then for that wave modulated with some real envelope function  $f(t) = F(\sigma t)$ . Here  $\sigma \propto$  bandwidth and  $1/\sigma \propto$  pulse-length. I shall assume  $f(\sigma t) > 0$  for all finite  $t$  to avoid intrinsic dislocations -- those present in the incident pulse. As a specific example, I will usually take  $f$  to be the Gaussian

$$f(t) = \exp(-\sigma^2 t^2 / 2). \quad (1)$$

This model facilitates calculations, but in practice it is probably hard to make a pulse that is (a) symmetrical and (b) decays asymptotically as fast as a Gaussian. Simple pulse-shaping circuits are likely to give a simple exponential decay, which is conveniently modeled by the hyperbolic secant

$$f(t) = \text{sech}(\sigma t) \equiv 2/(e^{\sigma t} + e^{-\sigma t}). \quad (2)$$

Pulse shape has considerable influence on dislocations.

#### 4. Wavefront dislocations outside the incident beam

Only the two-point model of figure 5(b) is interesting -- the cw far-field scattered wavefunction is

$$\begin{aligned} & \left( a r^{-1/2} e^{i(\phi - k\delta \sin \alpha)} e^{i(k[r + \delta \sin \theta] - \omega t)} + \right. \\ & \quad \left. b r^{-1/2} e^{i(\psi + k\delta \sin \alpha)} e^{i(k[r - \delta \sin \theta] - \omega t)} \right) (1 + O(\delta/r)) \\ & \sim r^{-1/2} e^{i((\phi + \psi)/2 + kr - \omega t)} ((a+b)\cos D + i(a-b)\sin D) \end{aligned} \quad (3)$$

where  $D \equiv (\phi - \psi)/2 + \omega \Delta$  and  $\Delta \equiv \delta(\sin \theta - \sin \alpha)/c$ .

The scattered intensity (amplitude squared) is proportional to  $(a-b)^2 + 4ab\cos^2 D$ . Since  $a, b > 0$  by definition, the cw field has far-field maxima/minima of intensity at angles  $\theta$  such that  $D = N\pi$ ,  $(N+1/2)\pi$  resp., but there are no cw nulls unless  $a=b$ , i.e. there are no cw dislocations.

The scattered pulse field is

$$r^{-1/2} e^{i((\phi + \psi)/2 + kr - \omega t)} \left[ a e^{iD} f(t - r/c - \Delta) + b e^{-iD} f(t - r/c + \Delta) \right]. \quad (4)$$

Wavefront dislocations are zeros of this wavefunction. The conditions for this are that the two terms in square brackets must be in phase opposition, so that  $D = -D + (2N+1)\pi$ , i.e.  $D = (N+1/2)\pi$ , and must have equal amplitudes, so that

$$af(t - r/c - \Delta) = bf(t - r/c + \Delta). \quad (5)$$

The phase condition shows that the dislocations will travel exactly along the cw valleys -- the lines of minimum cw intensity. This is hardly surprising, and in any '2-ray' system this must be so. Experience suggests that in general it is true approximately, but not exactly. The only general theory available, the bandwidth-perturbation theory of Wright & Nye (1982), gives the result that wavefront dislocations in long pulses travel approximately along the surfaces in space on which the cw intensity is locally minimal with respect to frequency at the pulse centre frequency. It is easy to show that for any field of the form  $a e^{i(\phi + \omega A(\underline{r}, t))} + b e^{i(\psi + \omega B(\underline{r}, t))}$  the latter are exactly the surfaces on which the phases of the two terms are opposed, i.e. the surfaces of minimum intensity, but for a general field this is not so.

From (4) it is reasonable to define the pulse centre to lie at  $\tau \equiv t - r/c = 0$ . If  $a=b$ , and  $f$  is symmetric, one solution of (5) is clearly  $\tau=0$ ; if  $f$  decreases monotonically away from its peak, as I shall always



assume, then this solution is unique. The dislocations occur at the pulse-centre also in the far field of the piston radiator (Wright & Berry 1984), but not exactly at the far-field cw null angle.

If  $a \neq b$ , or if  $f$  is asymmetric, the dislocation will be shifted from  $\tau=0$ , e.g. for the Gaussian envelope (1) the dislocation occurs at  $\tau = \tau_D \equiv (\ln(b/a))/2\sigma^2 \Delta$  as illustrated in figure 6. In this model,  $\tau_D$  can have either sign, depending on the relative strengths of the two scatterers.

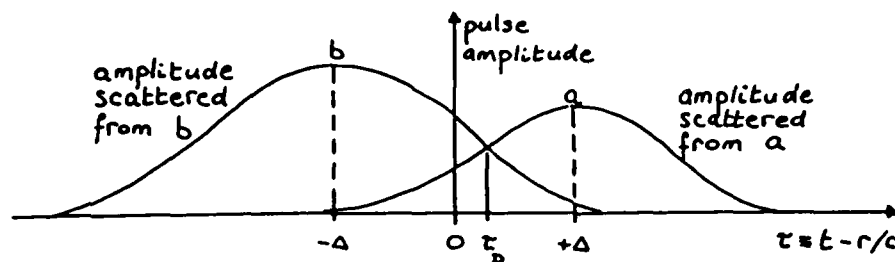


Figure 6. Dislocation time for a Gaussian pulse if  $a < b$ .

##### 5. Wavefront dislocations inside the incident beam: single point scatterer

The incident cw field, plus that scattered by the single point of figure 5(a), is

$$e^{-i\omega t} \left( e^{ikz} + a r^{-1/2} e^{i(\phi + kr)} \right).$$

The phase-opposition condition for cw minima is

$$\phi + kr = kz + (2n+1)\pi, \text{ or } r = z + \phi_n, \quad (6)$$

where  $\phi_n \equiv (2n+1)\pi - \phi$ . Since  $r \geq z$  because  $r^2 \equiv x^2 + z^2$ , there are solutions only for  $\phi_n \geq 0$ . They are the family of parabolae, labelled by  $n$ , with equation

$$z = (x^2/\phi_n - \phi_n)/2$$

shown in figure 7. For weak far-field scattering we can assume that observations are made only where  $a \ll r^{1/2}$ , so there are no (observable) cw nulls.

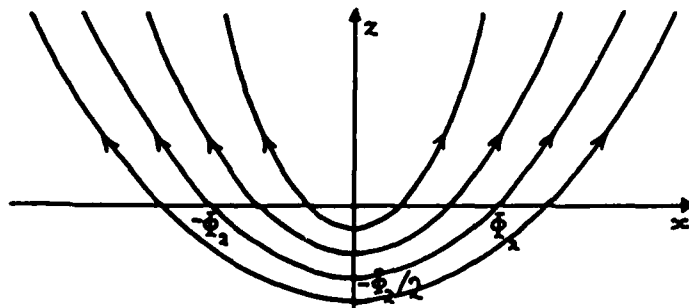


Figure 7. Parabolic dislocation trajectories.

The incident-plus-scattered pulse field is

$$e^{-i\omega t} \left( f(t-z/c) e^{ikz} + ar^{-1/2} f(t-r/c) e^{i(\phi+kr)} \right). \quad (7)$$

Once again the phase-opposition condition implies that any dislocation trajectories must be exactly contained within the cw minima -- this is another '2-ray' model.

Because  $ar^{-1/2} \ll 1$ , the first term in (7) will dominate the wave-field, so I shall now define the pulse centre to occur at  $\tau \equiv t-z/c = 0$ . Furthermore, the weak second term always arrives later than the first, because  $r \geq z$ , as shown in figure 8. Hence a dislocation can only occur at  $\tau \equiv \tau_D \geq 0$ , i.e. in the tail of the pulse, as observed in the piston radiator.

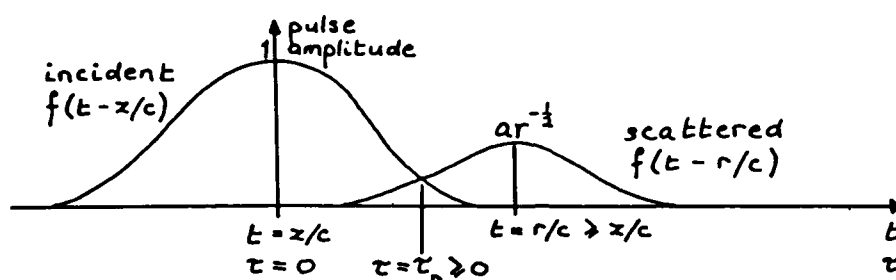


Figure 8. Incident and scattered pulse amplitudes.

The time at which a dislocation will pass a given point on the trajectory, if at all, is determined by the amplitude condition, which using (6) may now be written as

$$f(\tau_D) = ar^{-1/2} f(\tau_D - \phi_n/c), \quad (8)$$

where  $\phi_n$  is a constant on any trajectory. For the Gaussian envelope (1), the solution as a function of  $z$  is

$$t_D - \frac{z}{c} \equiv \tau_D = \frac{1}{2} \left( \frac{\phi_n}{c} + \frac{c}{\sigma^2 \phi_n} \ln \left( \frac{z + \phi_n}{a^2} \right) \right),$$

which is sketched in figure 9(a). Every potential trajectory point is traversed once by a dislocation. A pair is born (B) at the vertex (on the  $z$  axis) of each parabola (figure 7), already in the tail of the pulse, and moves roughly with the pulse along the trajectory, but dropping back logarithmically ever further into the tail as the scattered wave gets weaker.

Let us now consider the sech pulse (2), which is probably a more realistic model envelope. Using this in (8) gives

$$\cosh(\sigma\tau) = (r^{1/2}/a) \cosh(\sigma(\tau - \phi_n/c)).$$

The limiting form as  $\tau \rightarrow \pm\infty$  is

$$e^{\pm\sigma\tau} \sim (r^{1/2}/a) e^{\pm\sigma(\tau - \phi_n/c)} \quad \text{and hence} \quad r (= z + \phi_n) \sim a^2 e^{\pm 2\sigma\phi_n/c}.$$

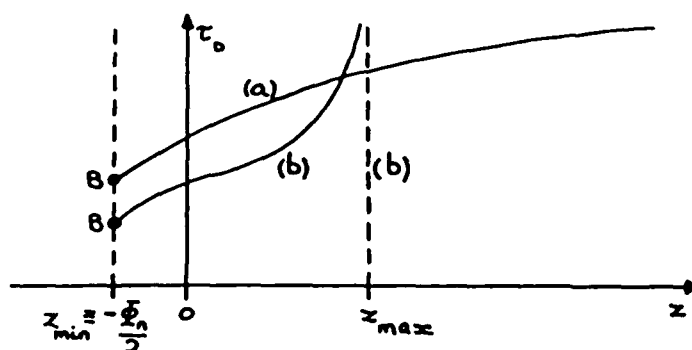


Figure 9. Dislocation delay for (a) a Gaussian envelope, (b) a sech envelope.

This imposes limits on the extent of the trajectory that a dislocation in this pulse can explore, namely

$$a^2 e^{-2\sigma\phi_n/c} - \phi_n \leq z \leq a^2 e^{2\sigma\phi_n/c} - \phi_n \equiv z_{\max}.$$

The lower limit is not important, and for sufficiently weak scattering imposes no constraint at all, since the trajectory satisfies  $-\phi_n/2 \leq z$  anyway. The upper limit means that the dislocations only travel a finite distance from the scatterer, i.e. they are confined. Only in the infinite bandwidth limit ( $\sigma \rightarrow \infty$ ) of an extremely short pulse is the whole parabola explored; in the cw limit ( $\sigma \rightarrow 0$ ) the trajectory shrinks to nothing (cf. Wright & Nye 1982). The dislocation delay is

$$\tau_D = \frac{1}{\sigma} \operatorname{artanh} \left( \coth \left( \frac{\sigma\phi_n}{c} \right) - \frac{a}{(z+\phi_n)^{1/2}} \operatorname{cosech} \left( \frac{\sigma\phi_n}{c} \right) \right),$$

which is sketched in figure 9(b).

This strong dependence of dislocation behaviour on details of the driving pulse envelope agrees completely with the findings of Wright & Nye (1982), and appears to be a disadvantage for NDE. A Lorentzian pulse (Wright & Nye 1982), which decays more slowly than exponential, produces dislocation confinement and additional more complicated behaviour, which is even less desirable.

#### 6. Wavefront dislocations inside the incident beam: two point scatterers

This model is difficult to analyse, so to avoid inessential complications I shall simplify the model in figure 5(b) so that  $b \equiv a$ ,  $\psi \equiv \phi$ ,  $\alpha \equiv 0$ . The total cw field is (cf. (3))

$$\sim e^{-i\omega t} (e^{ikz} + 2ar^{-1/2} \cos(\omega\Delta) e^{i(\phi+kr)})$$

where the two scattered wave functions have been combined, and interfere to give the  $\cos(\omega\Delta)$  factor, in which  $\Delta \equiv \delta \sin\theta/c$  as in §4. This cw field is very similar to that in §5, and if  $k\delta < 2\pi$  so that  $\cos(\omega\Delta) > 0$  for all  $\theta$ , the cw minima are identical for 1 and 2 point scattering. Generally, the phase-opposition condition gives

$$\phi + kr = kz + \frac{2n+1}{2n} \pi \quad \text{if } \cos(\omega\Delta) > 0 \quad (9)$$

for cw minima, which change into maxima when  $\cos(\omega\Delta)$  passes through 0. Hence it is not obvious what dislocation trajectories will do in this model.

The total pulse field is

$$\sim e^{-i\omega t} \left( f(t-z/c) e^{ikz} + a r^{-1/2} \left[ f(t-r/c-\Delta) e^{i\omega\Delta} + f(t-r/c+\Delta) e^{-i\omega\Delta} \right] e^{i(\phi+kr)} \right).$$

Let us assume that  $f(t) \equiv F(\sigma t)$  is slowly varying, i.e.  $\sigma$  is small, so that

$$f''(t) \equiv \sigma^2 F''(\sigma t) \ll f'(t) \equiv \sigma F'(\sigma t).$$

Then Taylor expanding and combining terms gives the following approximation for the scattered pulse:

$$e^{-i\omega t} 2a r^{-1/2} \left[ f(t-r/c) \cos(\omega\Delta) - i\Delta f'(t-r/c) \sin(\omega\Delta) \right] e^{i(\phi+kr)}. \quad (10)$$

Hence the total pulse field is approximately

$$e^{-i\omega t} \left( f(t-z/c) e^{ikz} + 2a r^{-1/2} f(t-r/c) R e^{i(-\Xi+\phi+kr)} \right) \quad (11)$$

where  $R^2 = \cos^2(\omega\Delta) + \Delta^2 (L(t-r/c))^2 \sin^2(\omega\Delta)$ ,  $\Xi = \arctan(\Delta L(t-r/c) \tan(\omega\Delta))$  and  $L(t) \equiv f'(t)/f(t) \equiv d \ln f(t)/dt$ . From figure 8, which applies to this model also,  $f'(t-r/c) > 0$  at a dislocation in the scattered pulse, so  $L(t-r/c) > 0$ . There are two conditions for a zero of (11). Phase-opposition gives

$$-\Xi + \phi + kr = kz + (2n+1)\pi, \quad \text{i.e. } r = z + \phi_n + \Xi/k, \quad (12)$$

where  $k\phi_n \equiv (2n+1)\pi - \phi$  just as for the single scatterer (§5). We shall see that <sup>n</sup>this phase condition determines the gross appearance of the dislocation trajectories, which seems to be generally the case (Wright & Nye 1982). The amplitude condition gives

$$f(t-z/c) = 2a r^{-1/2} f(t-r/c) R. \quad (13)$$

Equations (12) and (13) are a perturbation (in  $\Delta$ ) of those for a single scatterer, and I will use this observation to investigate their solution.

For all pulse shapes,  $\Xi$  is symmetrical in  $\Delta$  as are the cw minima, and satisfies  $\Xi = \omega\Delta$  (modulo  $\pi$ ) at  $\omega\Delta = n\pi/2$ . It looks as in figure 10a, on which the wavy lines indicate the values of  $\Xi$  that satisfy the cw minimum condition (9). As  $\Delta$  increases beyond about  $1/L(t-r/c)$ , the wiggles of  $\Xi$  go 'out of phase' with the cw steps, because the imaginary term in (10) is increasing and has no analogue for cw. Figure 10a shows that the dislocation trajectories drift smoothly across the cw extremum lines as the angle  $\theta$  varies. They cross the cw minima where  $\omega\Delta = \Xi = n\pi$ , pass inbetween the 'saddles' S where  $\omega\Delta = \Xi = (n+1/2)\pi$  so that  $\cos(\omega\Delta)$  changes sign and cw minima turn into maxima, and avoid the cw maxima. The number of cw-minimum lines crossed is  $[k\delta/\pi]$ ; maximum drift occurs on the x axis, and zero drift on the z axis and asymptotically as  $r \rightarrow \infty$ . This is sketched in figure 10b for a system with  $k\delta/\pi = 5/2$ . All these gross features of the trajectories are independent of the pulse shape.

Where a trajectory crosses a cw minimum,  $R=1$ , and the dislocation time is exactly as for the single scatterer. Otherwise, for small  $\sigma$  and  $\Delta$  ( $\Delta \rightarrow 0$  as  $r \rightarrow \infty$ ),  $R \approx 1$ , so that the dislocation times given by (13) will

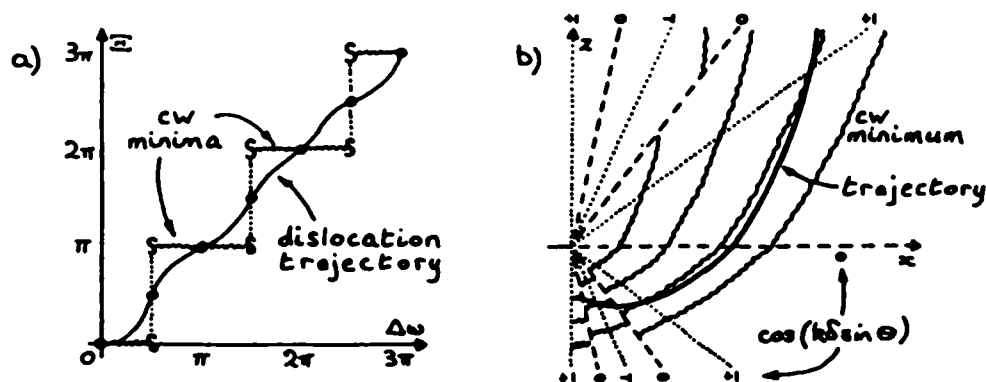


Figure 10. (a)  $\epsilon$  vs.  $\Delta$ ; (b) A typical dislocation trajectory.

be similar to those discussed in §5; further analysis is too complicated to give here.

## 7. Conclusions

Wavefront dislocations provide markers within (possibly long) pulses, that are more sharply defined than say leading edge or pulse centre, although in practice they can only be localized to an accuracy proportional to the S/N ratio. Such markers allow the 'uncertainty principle' to be beaten, and Walford (1972) used this idea to measure displacements of a glacier as small as a hundredth of a wavelength.

Dislocation trajectories are fairly easy to calculate approximately, they are closely related to cw minimum-amplitude surfaces, and only weakly dependent on pulse shape. Dislocation times along their trajectories are difficult to calculate and highly dependent on pulse shape. In realistic systems dislocations seem to occur mainly in the tail of the pulse, and if the tail does not decay sufficiently rapidly they may be confined, and never leave the scattering region. This appears to be less of a problem if there is no strong incident beam reaching the detector, so that monostatic (coincident source-receiver) geometry should be favourable. The system discussed in §4 (out of incident beam) also models the essence of this case.

We have seen that a realistic radiator itself produces wavefront dislocations that will be present in the incident pulse. Hence it will be necessary to distinguish observations of such intrinsic dislocations from the extrinsic dislocations generated by the scattering. The propagation of intrinsic dislocations has so far received only cursory attention (Wright & Nye 1982), but they could be more useful for NDE than their extrinsic counterparts.

I conjecture that more realistic models of scattering from microstructure will not show qualitatively new dislocation behaviour. For example, the piston radiator model (Wright & Berry 1984) consisted of a finite size radiator with 'infinitely sharp' edges. At quite low frequency (wavelength =  $(2\pi/10)$  radius) it showed very similar behaviour to the point scattering models, with trajectories that are roughly parabolic (figure 3b). The scattering amplitudes determining dislocation behaviour are just the usual cw amplitudes, so anything detectable using dislocations is also detectable using cw. However, dislocations convey the information

differently -- for example, cw interference fringes of negligible visibility may be pulled down nearby to actual amplitude zeros at some time during the passage of a suitable pulse, and these might be more easily detected.

#### Acknowledgement

All those people named in the reference list have contributed to my ideas about wavefront dislocations, especially Michael Berry and John Nye. I thank Ken Ashbee for suggesting the topic discussed here, and Barbara & Gerhard Dangelmayr for their hospitality and assistance, which facilitated the final preparation of this paper.

#### References

Balian, R. et al. eds. (1981), Les Houches Summer School 1980 - Physics of Defects, Amsterdam: North Holland, Vol. XXXV, pp.453-543.

Berry, MV (1978) J.Phys.A: Math.Gen. 11, 27-37.

--- (1981) in Balian et al. (1981), pp.453-543.

Humphrey, VF (1980), 'Experimental Observation of Wavefront Dislocations in Pulsed Wavefields', Ph.D. thesis, University of Bristol, UK.

Nye, JF and Berry, MV (1974) Proc.R.Soc.Lond. A336, 165-90.

Nye, JF (1981a) Proc.R.Soc.Lond. A378, 219-39.

--- (1981b) in Balian et al. (1981), pp.545-9.

--- (1983a) Proc.R.Soc.Lond. A387, 105-32.

--- (1983b) Proc.R.Soc.Lond. A389, 279-90.

Walford, MER (1972) Nature 239, 93-5.

Walford, MER, Holdorf, PC and Oakberg, RG (1977) J.Glaciol. 18, 217-29.

Wright, FJ (1979) in Structural Stability in Physics, ed. W. Güttinger & H. Eikemeier, Berlin: Springer, pp.141-156.

Wright, FJ and Nye, JF (1982) Phil.Trans.R.Soc.Lond. A305, 339-82.

Wright, FJ and Berry, MV (1984) J.Acoust.Soc.Am. 75, 733-48.

## MICROPHASE SEPARATION IN DENSELY CROSSLINKED POLYMERS

Dov Katz  
Department of Materials Engineering  
Technion, Israel Institute of Technology  
Haifa, Israel

### Abstract

Based on literature survey and on experimental work by the author and his coworkers, the phenomenon of microphase separation in densely and moderately crosslinked polymers is discussed. An attempt was made to explain in general terms the reasons for microphase separation. The presence of supermolecular structures created by agglomeration of smaller microheterogeneities into structures of the micron size, due to the action of secondary forces and displacement and changes in shape of these structures, was emphasized. It seems necessary to take into account the total morphology, namely the molecular or chemical structure of the network together with the supermolecular structures built by action of secondary forces in polymers used for matrices in composite materials and for adhesives, when their mechanical properties are considered.

### Introduction

In many polymerization reactions in which moderate or dense crosslinking takes place, the resulting polymer has a nonhomogeneous structure due to phase separation and microheterogeneities formed during the process of crosslinking. In our earlier studies, Katz and Zewi (1972, 1974, 1975) (1-4) phase separation was postulated after discovering two distinct secondary transitions in systems which contained only two reactive species participating in the network building: the basic prepolymer and the crosslinking agent. The phenomenon was related to the nature of the two components, as well as to the continuous changes occurring in the system during crosslinking. An assumption was made that formation of supermolecular structures takes place because of physical interaction between sections of the network. As a result of a fair amount of investigation done on the subject of microphase separation, mostly by use of electron microscopy, the existence of "gel-balls", Labana, Newman and Chomppf (1971) (5) or "nodules", Racich and Koutsky (1976) (6) of the size of 100-600Å was assumed by those authors and others. The phenomenon of microphase separation and formation of microheterogeneities on the molecular level, defined as "nodular morphology" can be attributed to a few factors, of which the most important seem to be:

a) syneresis, mainly microsyneresis, as suggested by Dušek (1971) (7) due to local incompatibility which may occur with the progress of polymerization because of the inhomogeneous increase of the degree of crosslinking ( $\nu$ -induced syneresis), or because of compatibility changes in polymer-monomer interaction due to changes in the nature of reaction participants ( $x$ -induced syneresis);

b) formation of polymerization "loci" with excessive intramolecular reactions within the "gel-balls" which exhaust the amount of available functional groups for crosslinking outside the "gel-balls", consequently creating nonhomogeneous networks.

In both cases regions with localized high crosslinking density are formed which are surrounded by a "matrix" with a lower density of crosslinking. The "nodulae" are interconnected since they are attached to the less dense "matrix" by chemical bonds. Both above mentioned factors influence the molecular structure and should perhaps be referred to as chemical microheterogeneity of the network. Many of the functional groups remain unreacted on pendant prepolymer or curing agent chains, because of movement restrictions imposed on these chains partially participating in the network formation, by the pronounced increase in viscosity of their surrounding due to polymerization and possible also because of physical interaction caused by strong secondary bonds. The unreacted functional groups of the pendant chains play an important role in the aging of the polymer and can be also used for chemical modification of the system, Funke (1982)<sup>(8)</sup>. Another factor contributing to formation of heterogeneities in the crosslinked polymers are differences in the chemical and physical nature of significant parts of the network. This may lead to formation of supermolecular structures as a result of the action of physical forces between certain parts of the network. Those structures are much larger than the previously described microheterogeneities and were defined by Lipatov (1975)<sup>(9)</sup> as macroheterogeneities. There exists of course, the possibility, and this is usually the case, that more than one of the a.m. factors are acting and enhancement of microphase separation occurs.

### Supermolecular Structures

Most of the following discussion will be dedicated to microphase separation due to formation of supermolecular structures. In their basic structure those heterogeneities appear as globules much larger than the "chemical" microheterogeneities randomly distributed in a structureless "matrix". Their order of organization can be increased in some cases by stretching the polymer: the globules become aligned in the direction of the acting stress and they may transform eventually into fibrilles, similar to the cases discussed by Kargin (1956)<sup>(10)</sup> with relation to some elastomers in their rubbery state. Erath & Spurr (1959)<sup>(11)</sup> while describing their studies of phenolic diallyl phthalate and some epoxy resins below their  $T_g$ , reported the existence of globular formations which are "denser than the material in which they are embedded and which may become arranged in linear arrays". In a study of the microstructure of bisphenol-A epoxy resins, published by Cuthrell (1968)<sup>(12)</sup> the presence of "two-phase systems containing floccular aggregates of higher density in a lower density interstitial phase" is described. The experimental procedure included microscopy and mapping the samples with a micropenetrometer. "Spherical floccules" in the size range from about  $2 \times 10^5$  -  $9 \times 10^5 \text{ \AA}$  randomly distributed in the interstitial phase or symmetrically arranged were noticed and their size could be made large or small by curing at low or high temperatures. Based on those and other reports, as well as on our observations, it seems that the larger supermolecular structures are built up by agglomeration and formation of aggregates of the smallest structures discussed before, the nodules. The supermolecular structures are held together by intra-and-intermolecular secondary forces and are formed or changed during and after polymerization. After polymerization the changes occur due to thermal and mechanical treatment of the polymer, physico-chemical processes which take place in the polymer on aging without or with straining, plasticizer migration, chemical attack, etc. The size and the shape of these structures seem to be influenced by many factors as discussed by Morgan and O'Neal (1977)<sup>(13)</sup>, some of them mentioned above, and they



range from a few tens of nm up to  $\mu\text{m}$ . In a latter work, reported by Aspbury and Wake (1979)<sup>(14)</sup>, on amine-cured epoxy resins used for structural adhesives, nodular structures of different sizes were noticed. The nodulae aggregate into larger structures, defined by Aspbury as "trees", which vary with the curing agent, the state of cure, specimen preparation, etc. An assumption was also made, that the fracture behavior of a polymer may be associated with the large size aggregates.

In our more recent studies of supermolecular structures and attempt was made to find a correlation between the nature of these structures in the basic polymer, or created by the action of aging and stresses, and some mechanical properties of the specimen. Most of the polymers used for this investigation were diglycidyl ether of bisphenol A (Epon Resin 826) cross-linked with diethylene triamine (DETA) or with metaphenylene diamine (MPDA), while another part of the study dealt with the behavior of a commercial structural epoxy type adhesive. Scanning electron microscopy (SEM) was used for examination of the failure surfaces topography of specimens fractured at room temperature, much below  $T_g$  of the polymers. The study included investigation at room temperature of:

I. properties and failure surfaces of unstrained and strained specimens aged in air at temperatures above  $T_g$  of the resins, Katz and Buchman (1977, 1978, 1979)<sup>(15-17)</sup>.

II. properties and fracture surfaces structure of a one component structural adhesive aged in its prepolymerized state at room temperature, Katz, Buchman and Gonen (1980)<sup>(18)</sup>.

III. topography of failure surfaces of unaged samples bent at different rates of strain at room temperature, Katz and Donnet (1982)<sup>(19)</sup>.

#### I. Aged Unstrained and Strained Crosslinked Epoxide Resins

Due to aging of X-linked Epon-DETA and Epon-MPDA systems above their  $T_g$ , profound physico-chemical changes occur in the polymers affecting their structure and properties. Application of large tensional strains, 20, 40 and 60%, during the aging process results in obtaining of specimens with different properties and a different structure than those of the specimens prepared the same way, but unstrained during aging, Fig.1. This behavior seems to be due to orientation occurring in the stretched samples during their aging and to changes in the network structure of the polymer because of orientation and different supermolecular structures, stable below  $T_g$ , which are formed in the two cases. While on SEM micrographs, Fig.2, of the external and fractured surfaces of the unaged and unstrained aged samples only large globular structures are observed, on the surfaces of samples aged while strained, also oriented sections, some of them even very highly oriented, can be seen. In spite of the fact that most of the structural changes occurred during the aging process in the "skin and intermediate layer" as shown by SEM micrographs and birefringence measurements, the mechanical properties of the specimens were affected considerably. A qualitative relation between some mechanical properties of the aged samples and their unoriented or oriented structure can be noticed. In this case, strain induced orientation in a typical amorphous crosslinked polymer led to different chemorheological aging processes in the specimens and to different network structures of the aged unstressed and stressed samples derived from the same basic polymer.

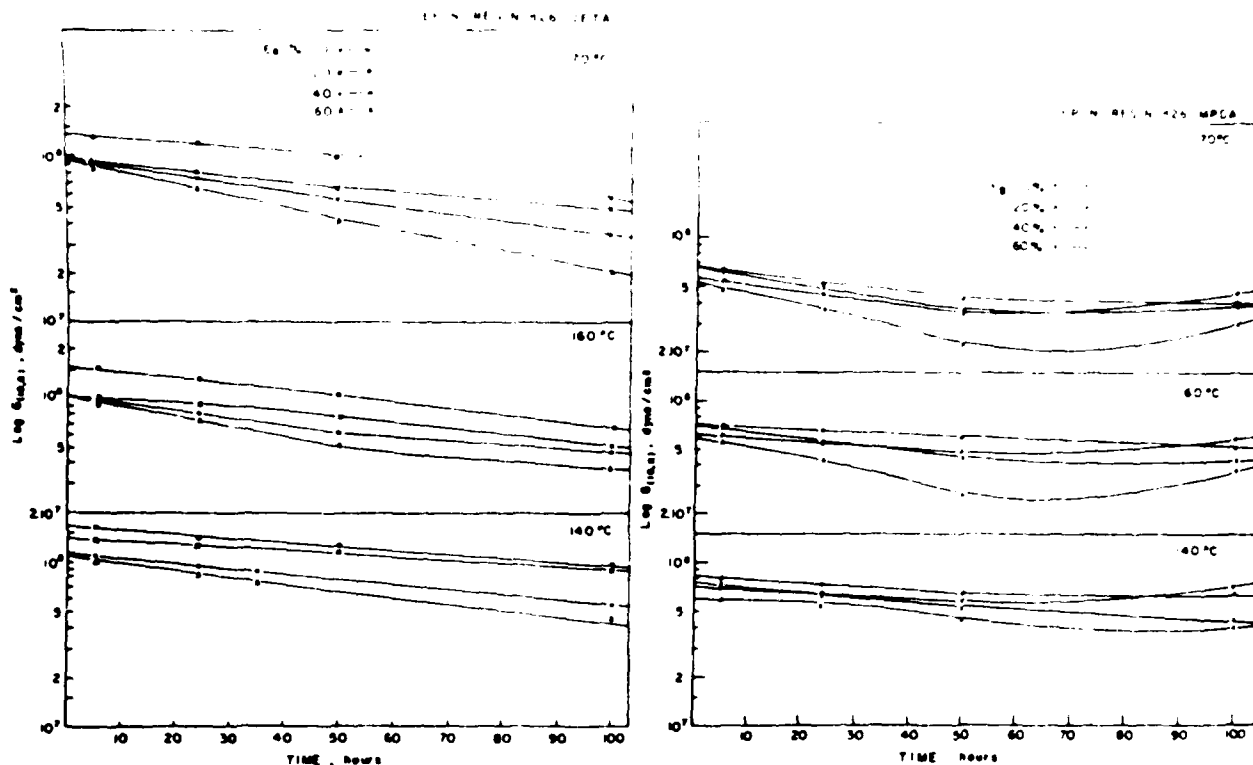


Fig.1: 10-sec torsion modulus at 200°C,  $G_{(10,R)}$  vs. time of aging at different temperatures of specimens strained to various percentages of  $\epsilon_b$ .

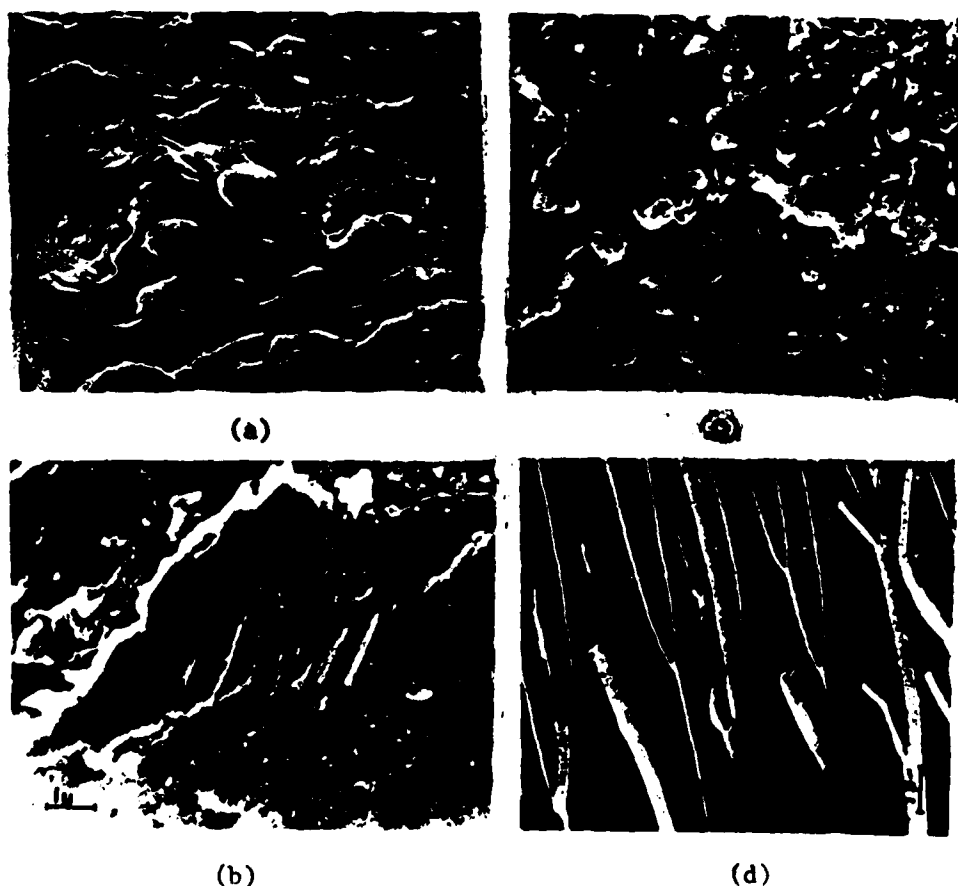


Fig.2: SEM photomicrographs of aged surface of Epon 826-MPDA specimens(x1000): (a) unstrained ; (b) strained-oriented section; (c) strained, unoriented section; (d) strained, fractured.

## II. One-component Structural Adhesive Prepolymer

In another study by Katz, Buchman and Gonen (1980)(17) which dealt with aging in storage of a one-component structural adhesive "PM-73" (manufactured by American Cynamid) in its prepolymerized state, a correlation between mechanical properties of the polymerized adhesive and its supermolecular structures as observed on SEM micrographs of the failure surfaces of the adhesive, was noticed, Table I. The adhesive unaged before

Table I. Properties of unaged and aged polymerized adhesive

Material	Aging time (days)		0	3	8	16
	Properties					
Polymerized adhesive	Swelling	Weight increase (% wt)	41.0	35.2	23.8	27.7
		Solubles (% wt)	2.72	2.73	1.78	1.41
	Tension	$\sigma_b$ (kg/cm <sup>2</sup> )	178.4	275.0	289.0	316.0
		$\epsilon_b$ (%)	3.10	2.45	2.40	2.3
	Torsion in rub- bery region	$G_{10,R}) \times 10^{-7}$ dyne/ km <sup>2</sup> )	3.1	3.1	4.5	5.4
Single lap joint	Shear	$\tau$ (kg/cm <sup>2</sup> )	256	264	262	240
		E (kg/cm <sup>2</sup> )	275	246	233	228

polymerization, had after the accomplishment of the curing cycle a lower stress at break ( $\sigma_b$ ), shear and torsion modulus but a higher strain at break ( $\epsilon_b$ ), toughness and adhesion energy, than the adhesive aged at room temperature for different lengths of time before polymerization. The SEM micrographs of the fractured surfaces, Fig.3, show clearly the presence of fibrillar structures in the first case, but only a few fibrilles and mostly globular supermolecular structures in the polymer specimens made from aged prepolymers. There seems to be a clear relation between the more ductile failure of the product obtained from the unaged prepolymer and the occurrence of fibrilles in its failure surface, while the failure surface of the more brittle material obtained from the aged prepolymer contained mainly globular structures, an occurrence which can be characteristic for the behavior of a material with a high  $\sigma_b$  and a low  $\epsilon_b$ .

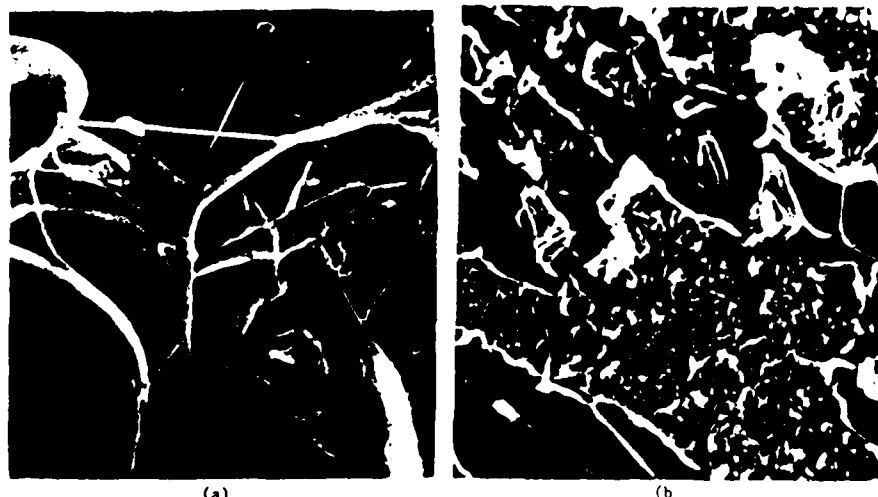


Fig.3 : SEM photomicrographs of failure surfaces in tension ( $r = 50 \text{ mm/min}$ ) of specimens prepared from an adhesive which was before polymerization: (a) unaged ( $\times 100$ ) ; (b) aged for 7 days ( $\times 150$ ).

### III. Epoxide Resins (Epon 826-DETA) Subjected to Bending at Different Rates of Strain.

This work is only in its early stages and therefore only a few qualitative results of some introductory experiments will be presented and discussed.

Samples of EPON 826 crosslinked by equivalent ratios of DETA and prepared all in one batch were bent at room temperature at different rates of strain: 50, 5 and  $0.05 \text{ mm/min}$  till fracture (by use of an Instron universal machine). The specimens were made by machining from a plate polymerized in a mold after careful mixing of the two reactants. The polymerization cycle included reaction at room temperature for 1 hr, at  $35^\circ\text{C}$  for 1 hr and postcuring for additional 2 hours at  $115^\circ\text{C}$ . The fractured surfaces coated with a thin layer ( $100\text{\AA}$ ) of Au/Pd (90/10) were studied by use of an electron scanning microscope (SEM). Since in bending experiments part of the specimen is subjected to compressive and another part to tensional stresses, the micrographs show different structures of the fractured surface in the part where compression and in the other part where tension occurred, but a large degree of orientation can be distinguished in both regions, Fig.4. The orientation effect depends on the rate of strain and so are the structures which formed mainly during the application of the bending stresses. The occurrence of fibrillar structures in the fractured surfaces is increasing with the decrease of the rate of strain and in some micrographs it can be seen clearly, that they are developing from larger globular structures in the presence of small globules.

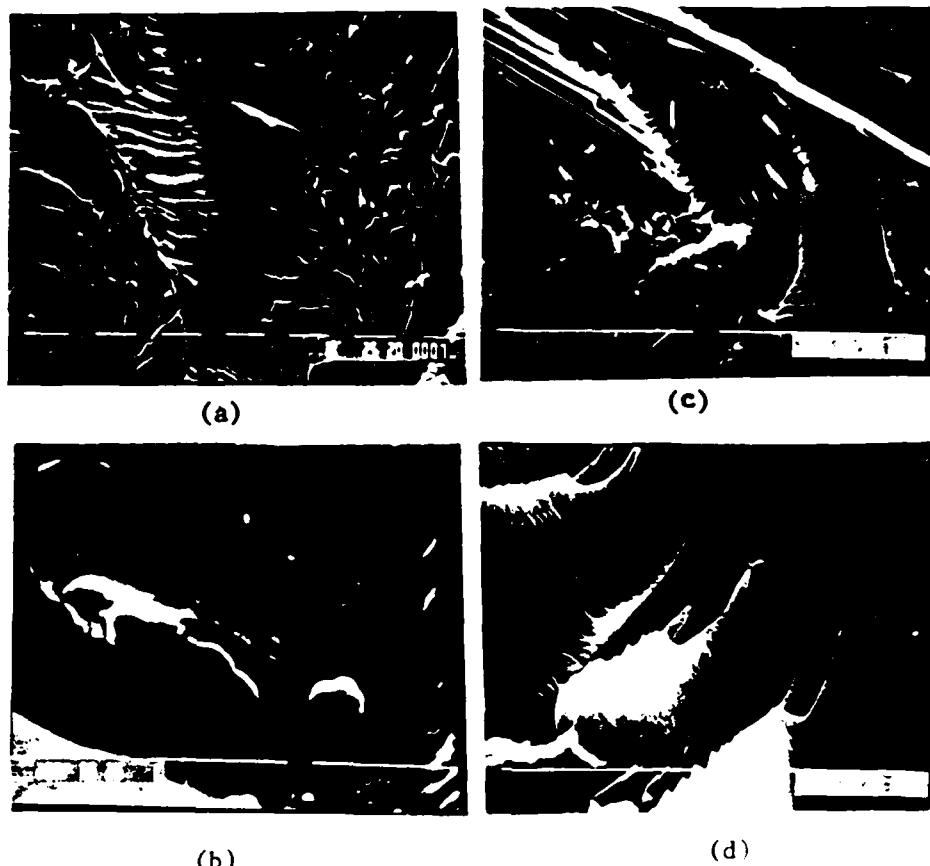


Fig.4 : SEM photomicrographs of failure surfaces of EPON 826-DETA fractured by bending at different rates of strain ( Tension region):  
 (a)  $r = 50 \text{ mm/min}$  (x400); (b)  $r = 50 \text{ mm/min}$  (x20,000) ;  
 (c)  $r = 0.05 \text{ mm/min}$  (x200) ; (d)  $r = 0.05 \text{ mm/min}$  (x2000);

Most of the fibrillar structures are not continuously smooth and uniform; they seem to be built from flattened ellipsoid shaped layers which form almost uniform parallel strata, arranged perpendicularly to the direction of the acting stress. The thickness of these layers may be of importance and can perhaps be related to the size of the globules and to the magnitude of forces acting inside the globules and between them. Much work has to be still done on this subject; we believe that micro X-ray analysis can contribute more to formation of a clearer picture of the interrelation between the structure of the polymer, its crosslinking density, efficiency of crosslinking, inter- and intramolecular forces, supermolecular structures obtained during polymerization, and the microphase structures created while acting on the polymer in controlled conditions.

#### Discussion

No serious attempt was made, neither by us, nor to the best of our knowledge by others, to correlate quantitatively or even qualitatively the occurrence of supermolecular structures with properties of the material, but one can not avoid the temptation to make a few highly speculative remarks on the subject. The explanation of the influence of new supermolecular structures obtained as a result of stretching on physico-chemical processes

(ex. aging of strained samples at high temperatures) on mechanical properties of the polymer is simpler, because of the relative easiness in recording of changes occurring in the network due to chemical reactions. The situation becomes much more complicated in the case of changes, or build-up of new supermolecular structures of nonpermanent character, due to action of physical factors only and it seems worthwhile to consider a few ideas from the point of view of structure properties correlation. By stressing a polymer specimen a higher order of organization can be induced into the material, because the globular structures will align themselves in the direction of the strain or they even transform into fibriles which may or may not interact. If no considerable creep and/or stress relaxation takes place during the straining process, and this is the case in cross-linked systems, and if the forces holding together the newly created structures are weak, after stress release, the oriented structures tend to return quickly to the lower degree of organization, namely to form again a pattern with randomly distributed globules. This will also be the situation in nonlinear highly polar noncrosslinked polymers in their transition and rubbery regions, when no strong secondary intra- or intermolecular forces are preserving the new strain created structures. Such structures can be formed in the transition, rubbery or even in the viscous flow region of certain thermoplastics and then preserved by rapid cooling of the polymer to temperatures below its  $T_g$ . Secondary forces, weakened or even nullified by high temperatures act again and preserve the new structures. Consequently the properties characteristic for the oriented structures, like the reinforcing effect, which can be observed mainly by the increase of stress at break and of the Young modulus and often by a decrease in the strain at failure, are preserved too. The shape, orientation and size of the oriented structures can be studied by use of different physical methods, like SEM, LAX-S, birefringence etc. Since the oriented structures in crosslinked polymers and in many cases in thermoplastics are not the ones with the highest entropy at temperatures below  $T_g$ , the ordered or distorted globular and fibrillar inhomogeneities in the material will tend to relax and return to their random distribution in the interstitial phase. Their relaxation process will depend on the driving force related to the surplus of free energy in the non-equilibrium state and to the magnitude of the secondary forces acting at the relaxation temperature inside and between the inhomogeneities. (This description of a polymer behavior may explain the memory effect characteristic for many polymeric products, an effect which is very marked in polymers with strong inter- and intramolecular forces). In non-polar nonlinear polymers the acting inter- and intramolecular forces are very weak; the oriented structures of the stretched polymer disintegrate easily and since the internal energy difference between the oriented and unoriented states ("the driving force") is small, no serious reinforcement effect can be observed due to creation of oriented structures, after cooling below  $T_g$  of the polymer or after the orientation-causing stress is removed. Straining below  $T_g$  will produce in crosslinked polymers with secondary inter- and intramolecular forces of different magnitude different results which demonstrate themselves in such characteristics of the material, as  $\sigma_b$ ,  $\epsilon_b$ ,  $E$  and toughness. If the secondary forces are strong and the rate of strain is high enough, one would expect that the dense globular supermolecular structures will persist, they may become aligned in the direction of the acting stress moving inside the less dense interstitial phase and the material will show a brittle behavior with relatively high  $E$  and  $\sigma_b$ , a low  $\epsilon_b$  and toughness, on the fractured surface of the polymer very few short or even no fibriles will be detected. Easiness in transition from the globular to fibrillar structures seems to be very important when

brittleness, ductility or toughness of the material are considered. The rate of strain at a certain temperature, or the temperature at a certain rate of strain doubtlessly influence the formation of different kinds of supermolecular structures in polymers. Ex. given enough time (at lower rates of strain) at a certain temperature, formation of fibrillar structures is more pronounced than in experiments performed at high rates of strain. This approach is supported by results of our experimental work and by the conclusions derived by Gladhill and Kinloch (1979)<sup>(20)</sup> from their investigation of crack growth in epoxy resins used as adhesives. According to them: "it is the flow of nodules past one another, rather than slippage of polymer chain segments, which is the mechanism involved and which is largely responsible for plastic strains observed. Further, the different plastic strains recorded may possibly be ascribed to morphological differences. Mechanisms for different modes of crack growth have been considered. It is proposed, that the amount of localized plastic deformation arising from shear yielding that occurs at the crack propagation is the controlling feature. Correlation between the mode of crack growth ability to undergo plastic straining and morphology of the adhesive have been established in support of the proposed mechanism".

#### Summary

The presence of microheterogeneities in a less dense chemically attached interstitial phase in crosslinked polymers was proven in many investigations. These microheterogeneities, from submicron nodules up to micron size structures, are held together by chemical links and by physical forces acting between parts of the network. They are formed by agglomeration of smaller heterogeneities into supermolecular structures and exist in their simplest shape as globules of different size distributed randomly in the interstitial phase. Due to the influence of different factors (temperature, magnitude of stress, rate and frequency of strain, plastification, etc.) the supermolecular structures may become aligned and change their shape from globular to fibrillar with different more or less ordered intermediate structures between the two extreme ones. When rheological properties of crosslinked polymeric matrices in composite materials or in adhesives are considered, in addition to the molecular (chemical) structure of the network, also the strength of secondary intra- and intermolecular forces, the formation and changes of supermolecular structures due to the action of these forces, in other words the total morphology of the network, should be taken into account.

#### References

1. Katz, D and Zewi, IG (1972) IUPAC 1972, Proceedings III, 365
2. Katz, D and Zewi, IG (1974) J. Polymer Sci., Part C, Polymer Symposia No.46, 139
3. Katz, D and Zewi, IG (1975) J. Polymer Sci., Chem. Ed., XIII, 654
4. Katz, D and Zewi, IG (1978) J. Polymer Sci., Chem. Ed., XVI, 597
5. Labana, SS, Newman, S and Chompff, AJ (1971) "Polymer Networks", Plenum Press. New York, 454
6. Racich, JL and Koutsky, JA (1976) J. Appl. Polymer Sci., XX, 2111

7. Dušek, K (1971) "Polymer Networks", Plenum Press New York, 245
8. Funke, W (1982) "Crosslinking and Network Formation in Polymers", The Plastics and Rubber Institute, 6
9. Lipatov, Yu S (1975) Pure and Appl. Chem., XLIII, 273
10. Kargin, VA (1958) J. Polymer Sci., XXX, 247
11. Erath, EH and Spurr, RA (1959) J. Polymer Sci., XXXV, 391
12. Cuthrell, RE (1968) J. Appl. Polymer Sci., XII, 391
13. Morgan, RJ and O'Neal, JE (1977) "Chemistry and Properties of Cross-linked Polymers" Academic Press Inc. New York, 289
14. Aspbury, PJ and Wake, WC (1979)
15. Katz, D and Buchman, A (1977) Polymer Eng. Sci., XVII, 85
16. Buchman, A and Katz, D (1979) Polymer Eng. Sci., XIX, 923
17. Katz, D and Buchman, A (1979) J. Appl. Polymer Sci., Appl. Polymer Symposium 35, 491
18. Katz, D, Buchman, A and Gonen, S (1980). VIIIth International Congress of Rheology, Proceedings, Plenum Press New York, Vol. III, 249
19. Katz, D and Donnet, JB (1980), unpublished results
20. Gledhill, RA and Kinloch, AJ (1979) Polymer Eng. Sci., XIX, 82.



## PROBING THE MESOPHASE LAYER IN POLYMERIC COMPOSITES

P.S. Theocaris

*Department of Theoretical and Applied Mechanics,  
The National Technical University of Athens  
Athens GR-157 73, Greece*

### Abstract

The structure and extent of the boundary layer developed between phases in a two-phase composite was represented by models which consider the totality of the transient phenomena taking place along this boundary layer. These models are based on the assumption that all physical and mechanical properties of the composite unfold from those existing at the inclusions, to those dominating in the matrix.

In this way a *pseudophase* was developed between main phases, consisting of an infinite number of layers each one of them having progressively varying properties from its neighbours.

The extent of mesophase was evaluated by considering the variations existing in the heat-capacity jumps  $\Delta C_p$ , of the simple polymeric substance made of the matrix material and the respective composite, appearing at the respective glass-transition temperatures of both substances. Based on thermodynamic measurements with differential scanning calorimetry the extents of these jumps were accurately measured and these define the thickness of this boundary layer.

It was, further, assumed that the abrupt variations of the mechanical properties in the mesophase follow negative-power laws, whose exponents were derived by measuring the moduli of the matrix, inclusions and the composite and assuming the validity of an improved law of mixtures.

Experimental evidence with either iron-particulates, or glass-fiber composites indicated clearly that the introduction of the mesophase yields a better and more flexible model for interpreting in a realistic manner the complicated phenomena appearing in all composites used in engineering applications.

### Introduction

The adhesion between matrix and inclusions in a fiber- or particulate-composite material is one of principal factors characterizing the mechanical and physical behaviour of the modern composite materials. All theoretical models describing these substances neglect to consider the influence of the boundary layer developed between phases during the preparation of the composite.

In reality, around an inclusion embedded in a matrix a rather complex

situation develops, consisting of areas of imperfect bonding, permanent stresses due to shrinkage, high stress-gradients or even stress-singularities, due to the geometry of the inclusions, voids, microcracks etc.

Moreover, the interaction of the surface of the filler with the matrix is usually a procedure much more complicated than a simple mechanical effect. The presence of a filler actually restricts the segmental and molecular mobility of the polymeric matrix, as adsorption-interaction in polymer surface-layers into filler-particles occurs.

The polymeric matrix, cast around the inclusions, created phenomena of physical and chemical adsorption. *Physisorbed* layers of the matrix contribute, in general, to weak mesophases. However, the physical interpenetration of the *boundary layer* of the matrix in cavities and other rough regions of the surfaces of solid inclusions, interrelated with the biased development of the molecular structure of the polymeric chains there, and any other structural variations of the adjacent layers, creates an intermixing and interpenetrating phenomenon, which influences considerably the molecular structure of the *mesophase*, thus resulting to variations of its mechanical strength. Thus, the mechanical properties of the matrix films and layers close to the interfaces, which are functions of the initial structure of the matrix, are strongly depending on the physical situation of this boundary layer.

On the other hand, *chemisorbed* (chemically adsorbed) molecules on the interfaces create structural variations, by developing beaded structures of caged molecules or ladder-like molecules. All these types of chemisorbed elements on inclusions lead to rapid variations of the properties and mechanical strength of the interface layer, close to the surfaces of inclusions.

Then, around each inclusion (fiber or particulate) a complex state is developed, which creates an *intermediate boundary layer* of variable thickness along the inclusions, where all these anomalies are concentrated and influence the physical behaviour of this layer. This zone is extended beyond the thin layer including the phenomena of *physisorption* and *chemisorption*, and it incorporates the zones of imperfect bonding and shrinkage stresses, the high stress gradients, or even stress singularities, due to geometric discontinuities of the surfaces of inclusions, to the concentration of voids and to the impurities, microcracks and other anomalies.

In this study the existence of the boundary layer, constituting the *mesophase*, and developed between the two main phases of a *two-phase composite* was taken into account for the development of a convenient model describing the thermomechanical behaviour of unidirectional fiber composites. This layer was assumed as developed entirely on the side of the softer polymeric matrix, and the harder inclusion is considered as neutral. Moreover, the mesophase was assumed as an independent pseudo-phase of variable properties, matching those of the inclusion on the one side, and the matrix on the other. The models are based on the same basic ideas as the Hashin-Rosen model (Hashin, 1962; Hashin and Rosen, 1964).

The evaluation of the characteristic properties of the mesophase was achieved by introducing two alternate expressions of an *improved law of mixtures* between phases incorporating the influence of the third phase. In both models it was assumed that the mechanical and the physical properties

of the *mesophase "unfolding"* from those of the hard-core fillers to those of the softer matrix. Thus, a multilayer model was assumed, improving the classical two-layer model, introduced by Hashin and Rosen, for the representative volume element of the composite.

The variation of the mechanical properties of the mesophase layer were considered as varying according to different negative power laws along the infinitesimal thickness of the mesophase, thus matching conveniently the properties of the inclusions with those of the polymeric matrix. The one model uses a three-term expression, whereas the other and simpler one a two-term expression for this variation of the modulus of the mesophase.

In order to define the thickness of the mesophase,  $\Delta r_i$ , Lipatov's law was considered, which interrelates this thickness to the jump in the heat-capacity values at the glass transition temperature of a polymer. According to this law the difference in heat-capacity jumps between the pure polymer of the matrix and the respective composite at their glass transition zones defines the extent of mesophase. Then, measurements with suitable samples of the matrix polymer and the composite in a differential scanning calorimetry apparatus define accurate the values of  $\Delta r_i$ .

On the other hand, accurate experimental evaluation of the modulus of the composite,  $E_c$ , yields another quantity necessary for the solution of the two versions of the improved law of mixtures considering the influence of mesophase. The solution of these equations yields the exponents of negative-power expressions for the variation of the mesophase modulus,  $E_i(r)$ , and constitute an effective means for defining the *adhesion quality* of the bonding between phases in the composite.

The models have been applied either to iron-particulates, or the glass-fiber reinforced polymers with satisfactory results (Theocaris, 1984a,b,c,d).

Both versions of the unfolding model gave reasonable thicknesses for the mesophase layer in its proper sense. Moreover, the mode of variation of the mesophase modulus in the layer indicated the role of transition, played by this layer in adapting and smoothing out the large differences in the mechanical properties of phases.

These versions of the model were based on a previous one related to a multilayer model (Papanicolaou, Theocaris and Spathis, 1980), which was an improvement of the classical Hashin-Rosen two-phase models. These new versions were already presented in previous publications by the author (Theocaris, 1984a;1984b;1984c;1984d).

### The Unfolding Models in Composites

The models introduced by Hashin (1962) for the particulates and by Hashin and Rosen (1964) for the fiber composites are of general acceptance. They assume in both cases representative volume elements (RVE) of the materials consisting of a gradation of sizes of cells, corresponding to the volume filling configuration existing in the particular material studied. Moreover, a fixed ratio of radii between the spheres or the cylinders of the inclusions ( $r_f$ ) and the respective quantities for the matrix ( $r_m$ ) are assumed, in order to have the analysis of a single representative volume element (RVE), expressing the behaviour of the entire composite.

Besides these simple geometric models, other types of models include the

so-called *self-consistent model*, according to which the average values for stresses and strains in either phase are determined by solving two separate problems, whose superposition yields the final configuration of the model. The solution of the two individual problems allows the evaluation of the average properties of the composite, by knowing the respective properties of either phase. The self-consistent model was applied to composites by *Budiansky* (1965) and separately by *Hill* (1965).

An important variation of the self-consistent model is the *three-phase model* introduced by *Kerner* (1956). In this model the inclusion is enveloped by a matrix layer, which in turn is embedded in an infinite medium with the unknown macroscopic properties of the composite. A variation of the Kerner model was introduced by *Van der Poel* (1958), which approached more correctly the problem of stress distribution in particulates. Both models were based on solutions introduced by *Goodier* (1933) and *Fröhlich and Sack* (1946) for a spherical cavity submitted, either to a hydrostatic loading, or to a pure shear loading.

While the initial Van der Poel model was valid for hard fillers and incompressible matrices, this model has been extended by *Schwarzl and Eikhoff* (1971) to incorporate the description of particulates along a wide temperature range. A further use of the Van der Poel model and the Schwarzl and Eikhoff ideas were made by *Maurer* (1983) in his interesting dissertation.

Similar attempts to study three-phase particulate composites were made by *Sagalaev and Simonov-Emiljanov* (1973) in the Kerner-Kerner model, where the classical Kerner model was used twice to cover successively by pairs the phases of a three phase composite, by *Kudykina and Pervak* (1975), by *Takano and Sakanishi* and, finally, by *Spathis, Sideridis and Theocaris* (1981). All these models yield the moduli of the particulate composites in terms of the moduli and respective volume fractions of three constituent phases of the composite, without considering, except the last one, that the middle phase is a product derived from the interaction of the two main phases and depends on their degree of adhesion. All these models have been compared previously (*Theocaris, 1984d*).

Finally, the Takayanagi model (*Takayanagi, Uemura and Minami, 1964*) should be mentioned, where the influence of the filler modulus,  $E_f$ , is taken into account for the evaluation of the respective modulus of the composite,  $E_c$ . In this model the filler volume fraction,  $u_f = \lambda\phi$ , was combined with a part  $(1-\phi)\lambda u_m$  of the matrix-volume fraction,  $u_m$ , which had a different influence on  $E_c$  than the rest of the matrix volume fraction  $(1-\lambda)u_m$ .

These three elements, that is the filler-volume fraction  $u_f = \lambda\phi$  (represented as an orthogonal of sides  $\lambda$  and  $\phi$ , quantities which represent the state of mixing), the connected to  $u_f$  part of the matrix  $(1-\phi)\lambda u_m$ , and the rest of the matrix  $(1-\lambda)u_m$ , were arranged in convenient combinations. The model A consists of the  $u_f$ - and  $(1-\phi)\lambda u_m$ -elements in parallel and then the  $(1-\lambda)u_m$ -element in series, whereas the model B contains the  $u_f$ - and  $(1-\phi)\lambda u_m$ -elements in series and the  $(1-\lambda)u_m$ -element in parallel with the previous unit. Both models gave satisfactory approximations, either for the composite compliance,  $D_c$ , of a particulate (model A), or for the composite modulus,  $E_c$ , of a fiber composite (model B).

While the Takayanagi model was designed mainly for two-phase materials, it could be extended to incorporate the influence of mesophase (*Spathis, Kontou and Theocaris, 1984*).

It seems that a further extension of the concept of using mixed-mode connections, that is in series and in parallel, for the elements contained in such models is very promising.

In a similar context a series of models was recently introduced by *Theocaris* (1984a,b,c and d) which approaches better the real situation in the composites. The novel element in these models is the introduction of a third phase in the Hashin-Rosen models, which lies between the two main phases (inclusions and matrix) and contributes to the progressive unfolding of the properties of the inclusions to those of the matrix, without discontinuities. Then, these models incorporate all transition properties of a thin boundary-layer of the matrix near the inclusions. Thus, this pseudo-phase characterizes the effectiveness of the bonding between phases and defines an *adhesion factor* of the composite.

For the model valid for particulate composites the component-phases are interconnected through consecutive spherical interfaces of the filler, mesophase and matrix. The dominant transverse interconnection through shear, holding for the fiber-composites, is in this case insignificant, the adhesion being now achieved by a continuously varying combination of shear and normal forces at the interfaces. Thus, variable components of the hydrostatic and shearing loadings were developed between these surfaces. Then, it is closer to the real situation of force-distribution to assume that the contributions of phases are done by superposed in series layers of the phases, lying the one on the top of the other in the direction of the application of the external load. (Fig.1a).

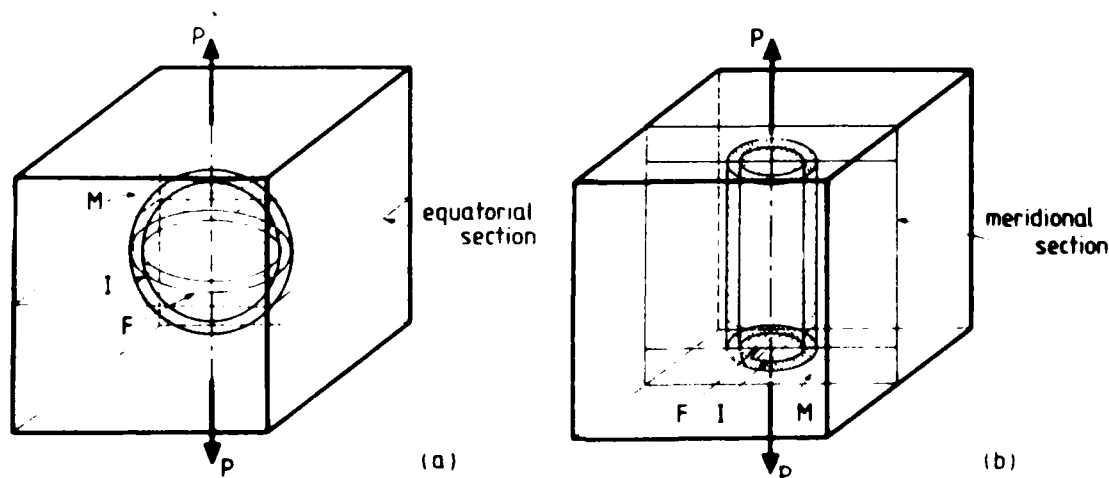


Fig.1. Configurations of the representative volume elements for particulates (a) and fiber-reinforced composites (b).

In this case, the compliances, instead of the moduli, should be added to derive the compliance of the composite, since now the capacitances of the respective electrical analogy, corresponding to the moduli of the elements, are connected in series. This argumentation explains the necessity of adding in this case the compliances of phases, instead of moduli.

However, since the approximation of superposed flat layers is again far away from reality, because of the average sphericity of the layers, the expressions for the bulk compliance of the composite should be expected to be expressed by complicated expressions of the constituent compliances.

It has been shown that the bulk compliance  $B_c = 1/K_c$  of the composite is expressed in terms of the bulk and shear moduli of the filler (denoted with subscript f), the mesophase (denoted with subscript i) and the matrix (denoted by subscript m) by:

$$\begin{aligned} \frac{1}{K_c} = & \frac{u_f}{K_f} \left( \frac{\lambda_{fi}}{\lambda_{im}} \right)^2 + \frac{3u_f^2}{4BG_i u_i} \left[ \frac{1-\lambda_{fi}}{\lambda_{im}} \right]^2 + \frac{u_f^2}{K_i u_i} \left[ \frac{\lambda_{fi}}{\lambda_{im}} - \frac{1}{B\lambda_{im}} \right]^2 + \\ & + \frac{3u_f}{4BG_m u_m} \left[ 1 - \frac{1}{\lambda_{im}} \right]^2 + \frac{1}{K_m u_m} \left[ \frac{u_f}{B\lambda_{im}} - 1 \right]^2 \end{aligned} \quad (1)$$

where the coefficients  $\lambda_{fi}$  and  $\lambda_{im}$  are expressed by:

$$\lambda_{fi} = \frac{p_f}{p_i}, \quad \lambda_{im} = \frac{p_m}{p_i} \quad \text{and} \quad \frac{p_f}{p_m} = \frac{\lambda_{fi}}{\lambda_{im}} \quad (2)$$

and:

$$r_i^3/r_m^3 = u_f + u_i, \quad r_f^3/r_m^3 = u_f \quad (3)$$

Moreover, it is valid that,

$$r_i^3/r_f^3 = \frac{u_f + u_i}{u_f} = \frac{1}{B} \quad (4)$$

Equation (1) yields the bulk modulus,  $K_c$ , of the composite in terms of the bulk and shear moduli of the phases and the stress-ratios  $\lambda_{fi}$  and  $\lambda_{im}$  which, on the other hand, depend on the elastic moduli and Poisson's ratios of the phases. These stress ratios are expressed by (Theocaris, 1984b):

$$\lambda_{fi} = \frac{3(1-\nu_i)(u_f + u_i)E_f}{2u_i E_i (1-2\nu_f) + [3u_f(1-\nu_i) + u_i(1+\nu_i)]E_f} \quad (5)$$

and:

$$\lambda_{im} = \frac{3(1-\nu_m) - 2u_m(1-2\nu_m)}{3(1-\nu_m)} - \frac{E_m u_m}{E_i} \frac{(1+\nu_i)}{3(1-\nu_m)} \quad (6)$$

For the complete solution of the problem, a relation between the Poisson ratios of the composite and its constituent phases is needed. Since the

mesophase is derived from the matrix material, it is reasonable to accept that:

$$v_i \approx v_m \quad (7)$$

whereas for the Poisson ratio  $v_c$  of the composite we use a modification of relationship given by Jones (1975) interconnecting the values of Poisson's ratios. This relationship was found satisfactory for our purposes and is given by:

$$\frac{1}{v_c} = \frac{u_f}{v_f} + \frac{u_i}{v_i} + \frac{u_m}{v_m} \quad (8)$$

The last equation completes the number of relationships, necessary for evaluating the characteristic properties of the particulate.

The model expressed by relations (1) and (8) yields accurate results, if the constituent phases of the particulate composite are accurately defined. However, it should be mentioned that its validity holds only in the purely elastic behaviour of the composite, since viscoelastic effects have not been encountered in this model. To this aspect the model is similar to all other models and especially the most sophisticated Kerner-Kerner, Krauss, Takayanagi, Van der Poel and Maurer models. Furthermore, it contains an additional advantage that it, alone, incorporates the influence of the mesophase developed between phases, which depends on the adhesion quality of their bonding and in some regions it plays an important and regulating role to the mechanical behaviour of the composite.

Indeed, in all previous models the boundaries of their phases were assumed as smooth surfaces. In reality, around an inclusion a complex state develops, which consists of areas of imperfect bonding, permanent stresses, due to shrinkage of the polymer phases, during the curing and aftercuring periods, and the change of the thermal conditions there, high stress-gradients and stress-singularities, due to the complicated geometry of the interfaces, voids, impurities and microcracks, appearing at the vicinity of these boundaries.

Moreover, the interaction of the matrix polymer, during its aftercuring period, with the surface of the solid inclusion is always a complicated procedure. Indeed, the presence of the filler restricts the free segmental and molecular mobility of the polymeric matrix, as adsorption interaction between phases occurs. This phenomenon influences considerably the quality of adhesion between phases, contributing to the development of a hybrid phase between main phases, which is called *interphase*, or, better, *mesophase*.

The existence of mesophase was proved experimentally and its extent was evaluated by a theory developed by Lipatov (1977). Similar evaluations of the extent of mesophase were established by calculating, through dynamic measurements of the storage moduli and the loss factors at the vicinity of  $T_g$ 's of the matrix and the composites the differences of these quantities for the composite and the matrix materials (Theocaris, Kefalas and Spathis, 1983). Finally, the mesophase volume fraction,  $u_i$ , may be evaluated by executing measurements of the strain magnification factor for the unfilled and filled polymer, as it has been nicely advanced by Ziegel and Romanov (1973a;1973b), on a theory based on the concept of line-fraction introduced by Bucche (1960).

For the case of unidirectional fiber-reinforced composites a multi-layer model was initially introduced by *Theocaris and Papanicolaou* (1979). In this model influence of the mesophase on the properties of the composite was studied. Another model was afterwards presented, where the variable with polar distance elastic modulus of the mesophase was expressed as sum of a constant term and two variable terms, expressed as modifications of the moduli of the filler and the matrix by negative power laws (*Papanicolaou, Theocaris and Spathis*, 1980). The inconsistencies of this model were remedied by a new version of the model introduced by *Theocaris* (1984a to e) containing either two, or three terms.

However, the situation with unidirectional composites appears to be much simpler. In this case and when the fibers of the composite are oriented parallelly to the externally applied load an improved law of mixtures holds, where the contribution of the mesophase is taken into account. This law is expressed by:

$$E_c = E_f u_f + E_i u_i + E_m u_m \quad (9)$$

where the  $u$ 's are expressing the respective volume fractions.

Relation (9) may be considered as satisfactory for fiber-reinforced composites because, the individual moduli of phases in the RVE should cooperate through their interfaces, which are assumed parallel to the direction of application of the external load, this cooperation being achieved by the lateral surfaces of cylinders developing shears between phases. Thus, this model necessitates an addition of the moduli of the phases multiplied by weight-factors, which are simply their respective volume contents. In an electrical analogy scheme then, the weighted moduli constitute capacitances connected in parallel, which explains the validity of relation (9). This relationship was found to yield satisfactory results in the applications (*Theocaris and Papanicolaou*, 1979).

The representative volume element for unidirectional fiber-reinforced composites, see Fig.1b, consisting of a cluster of three co-axial cylinders of the same height equal to unity, has volume fractions  $u$ 's for its phases given by:

$$u_f = \left( \frac{r_f^2}{r_m^2} \right), \quad u_i = \left( \frac{r_i^2 - r_f^2}{r_m^2} \right) \quad \text{and} \quad u_m = \left( \frac{r_m^2 - r_i^2}{r_m^2} \right) \quad (10)$$

Assuming the appropriate boundary conditions between the internal cylinder and any number of annuli surrounding it in the RVE of the composite, which assure continuity of radial stresses and displacements, according to the loading case considered, we may establish readily, by an energy balance between phases, the well-known law of mixtures, valid for the longitudinal modulus  $E_{cl} = E_c$  of the composite:

$$E_c = E_f \left( \frac{r_f^2}{r_m^2} \right) + E_i \left( \frac{r_i^2 - r_f^2}{r_m^2} \right) + E_m \left( \frac{r_m^2 - r_i^2}{r_m^2} \right) \quad (11)$$

If we assume further that the interphase annulus consists of a material having progressively variable mechanical properties, in order to match the respective properties of the two main phases bounding the mesophase, we can define a



variable elastic-modulus for the mesophase,  $E_j(r)$ , which, for reasons of symmetry, depends only on the polar distance from the fiber-interphase surface. In other words, we assume that the mesophase layer consists of a series of elementary layers, whose constant mechanical properties differ to each other by a quantity (small enough) defined by the law of variation of  $E_j(r)$ .

#### Definition of the Thickness of the Mesophase

It has been observed that, for the same volume fraction  $u_f$  of the filler, an increase of  $T_g$  indicates an increase of the total surface of the filler (Voyutsky, 1960). This is because an increase in  $T_g$  may be interpreted as a further formation of molecular bonds and grafting between secondary chains of molecules of the matrix at the solid surface of inclusions, thus restricting significantly the mobility of neighbour chains. This increase leads to a change of the overall viscoelastic behaviour of the composite, by increasing the volume fraction of the strong phase of inclusions.

The variation of the properties of polymers along their interfaces with inclusions is extended to layers of a, sometimes, significant thickness. This follows from the fact that, if only a thin surface-layer of the polymer was affected by its contact with the other phase, then the change in  $T_g$  should be insignificant, since the level of the glass transition temperature is associated with the bulk of the polymer, or, at least, with a large portion of it.

If calorimetric measurements are executed in the neighbourhood of the glass transition zone, it is easy to show that jumps of energies appear in this neighbourhood. These jumps are very sensitive to the amount of filler added to the matrix polymer, and they were used for the evaluation of the boundary layers developed around fillers.

The experimental data show that the magnitude of the heat capacity (or similarly of the specific heat), under adiabatic conditions, decreases regularly with the increase of filler content. This phenomenon was explained by the fact that the macromolecules appertaining to the mesophase layers are totally or partly excluded to participate in the cooperative process taking place in the glass-transition zone, due to their interactions with the surfaces of the solid inclusions.

Lipatov (1977) has indicated that a relation holds between a *weight constant*,  $\lambda$ , defining the mesophase volume-fraction  $u_j$ , and the jumps of the heat capacity  $\Delta C_p^f$  of the filled-composite and  $\Delta C_p^0$  of the unfilled polymer for particulate composites:

$$\lambda = 1 - \frac{\Delta C_p^f}{\Delta C_p^0} \quad (12)$$

where  $\lambda$  is a factor multiplying the filler volume fraction  $u_f$ , in order to take into consideration the contribution of the mesophase-volume fraction  $u_j$  to the mechanical behaviour of the composite.

In order to define the volume-fraction  $u_j$  of the mesophase for the particular composite studied, a series of dilatometric measurements were executed in a differential scanning calorimeter, over a range of temperatures including the glass transition of the matrix, and the composites containing different amounts

of fillers. The variation of the heat capacity  $C_p$  of the samples per mole versus temperature was plotted automatically in a differential scanning calorimetry. All  $C_p=f(T)$  curves plotted for pure polymers and composites presented a typical jump  $\Delta C_p$  in heat capacity at the glass transition zone. Fig.2 presents schematically the variation of  $C_p$  at this zone versus temperature.

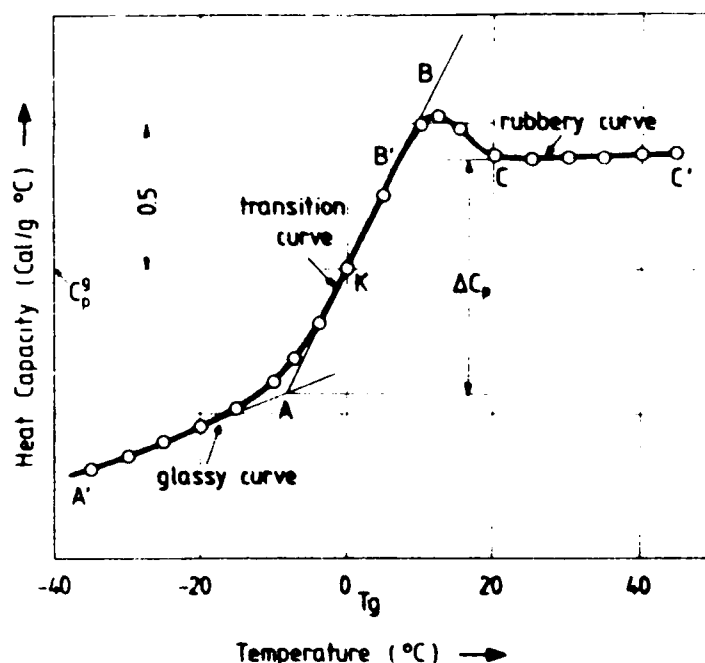


Fig.2. Typical DSC traces for the specific-heat jumps at the glass-transition regions of E-glass fiber-epoxy resin composites and the mode of evaluation of  $\Delta C_p$ 's.

The  $\Delta C_p$ 's were calculated by ignoring the smooth protrusions B'BC appearing in the  $C_p=f(T)$  curves (see Fig.2) and measuring the distance of the intersection A of the tangents AA' of the glassy curve and AB of the transition curve from the horizontal tangent CC' of the rubbery part of the curve  $\Delta C_p=f(T)$ .

In order now to define the radius  $r_i$  of the layer corresponding to the mesophase, we express it as  $r_i=(r_f+\Delta r)$  and we introduce this value into the relations expressing the respective volume fractions  $u_i$  for the particulates, or the cylindrical inclusions. For particulate composites, which will be used in the applications of the method, use will be made of the Lipatov formula, valid for particulates (Lipatov, 1977). This relation for particulate composites takes the form:

$$\frac{(r_f+\Delta r)^3}{r_f^3} - 1 = \frac{\lambda u_f}{1-u_f} \quad (13)$$

Relation (13) yields:

$$B = \frac{u_f}{u_f + u_i} = \frac{u_f}{1 - u_m} = \frac{1 - u_f}{1 - u_f(1 - \lambda)} \quad (14)$$

The real constant  $B$  depends only on the filler-volume fraction and the coefficient  $\lambda$ . Introducing the values of  $\lambda$  derived from relation (12) we can define the values of  $\Delta r_i$  for the various filler-volume contents  $u_f$  of the composite.

In order to define the volume-fraction  $u_i$  of the mesophase for the particular composite studied in the experimental part of this study, which was an iron-epoxy particulate, a series of dilatometric measurements were executed in a differential scanning calorimeter (DSC) over a range of temperatures including the glass transition of a pure epoxy polymer used as matrix, and a series of samples of composites containing different amounts of iron-particles of three different diameters  $d_f=150, 300$  and  $400\mu\text{m}$ ., varying between  $u_i=5$  percent to  $u_i=25$  percent.

The graphs of all the data presented shapes, which were qualitatively similar to one another. They consisted of two linearly increasing regions separated by the glass transition zone. While the glassy linear regions presented a positive and significant slope, the rubbery linear regions were, all of them, almost horizontal.

The  $\Delta C_p$ 's were calculated by ignoring the smooth protrusions  $B'BC$  appearing in the  $C_p=f(T)$  curves, as indicated in Fig.2. The variation of the specific heat, and its jumps at the region of glass-transition temperatures  $T_g$ , versus temperature was plotted for an iron-epoxy particulate with  $d_f=400\mu\text{m}$  and for various  $u_f$ 's in Fig.3. Then, by measuring the distance of the intersection  $A$  of the tangents  $AA'$  of the glassy curve and  $AB$  of the transition curve from the horizontal tangent  $CC'$  of the rubbery part of the curve  $\Delta C_p=f(T)$ , the values of  $\Delta C_p$ 's for the different composites are found and they are included, among others, in Table 1.

Fig.4 presents the variation of the differences,  $\Delta r_i$ , of the radii of the mesophases and inclusions, ( $\Delta r_i=(r_i-r_f)$ ), versus the filler-volume content  $u_f$  for the three different types of iron-epoxy particulates with diameters of fillers  $d_f=150, 300$  and  $400\mu\text{m}$ , as they have been derived from relation (13).

Fig.5 presents the variation of the heat-capacity jumps,  $\Delta C_p^f$ , at the respective glass-transition temperatures of the particulates, versus the filler volume content  $u_f$ , for the three different diameters of the fillers ( $d_f=150, 300$  and  $400\mu\text{m}$ ). In the same figure the variation of the coefficient  $\lambda$  and the volume fractions for the mesophase and the matrix, versus  $u_f$  were plotted, as they have been derived from relation (14). It is apparent from these graphs, that the mesophase-volume content  $u_i$  for the three different diameters of inclusions were varied only insignificantly and, therefore, they may be assumed as independent of the diameters of the fillers.

It may be concluded from Fig.5 that the variation of the heat-capacity-jump curves are smoothly decreasing curves, as the filler-volume content is increased. This behaviour is logical, since addition of iron particles makes the composite more rigid (Lipatov, 1977).

It is also interesting noting that, for various diameters of the fillers,

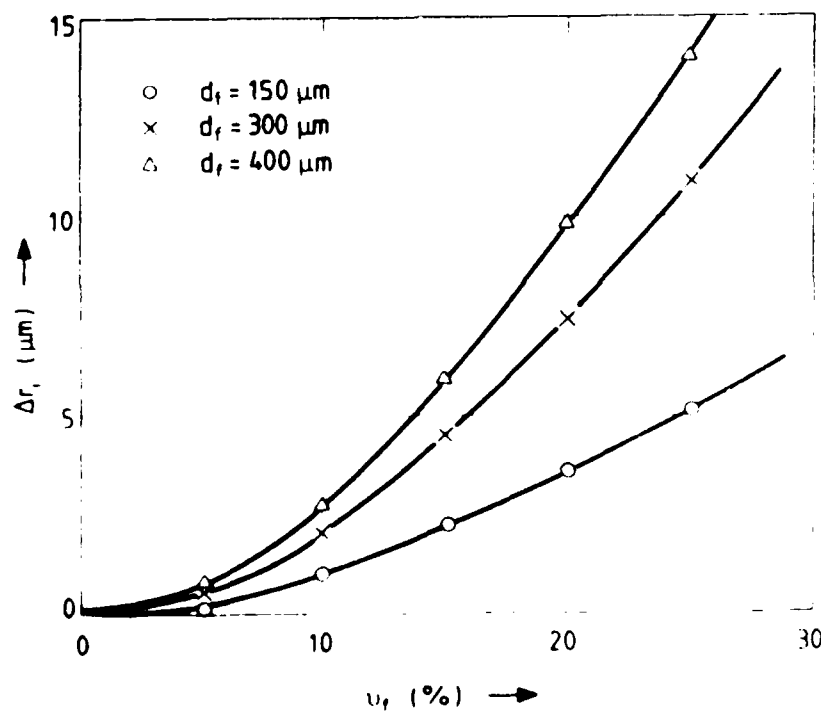
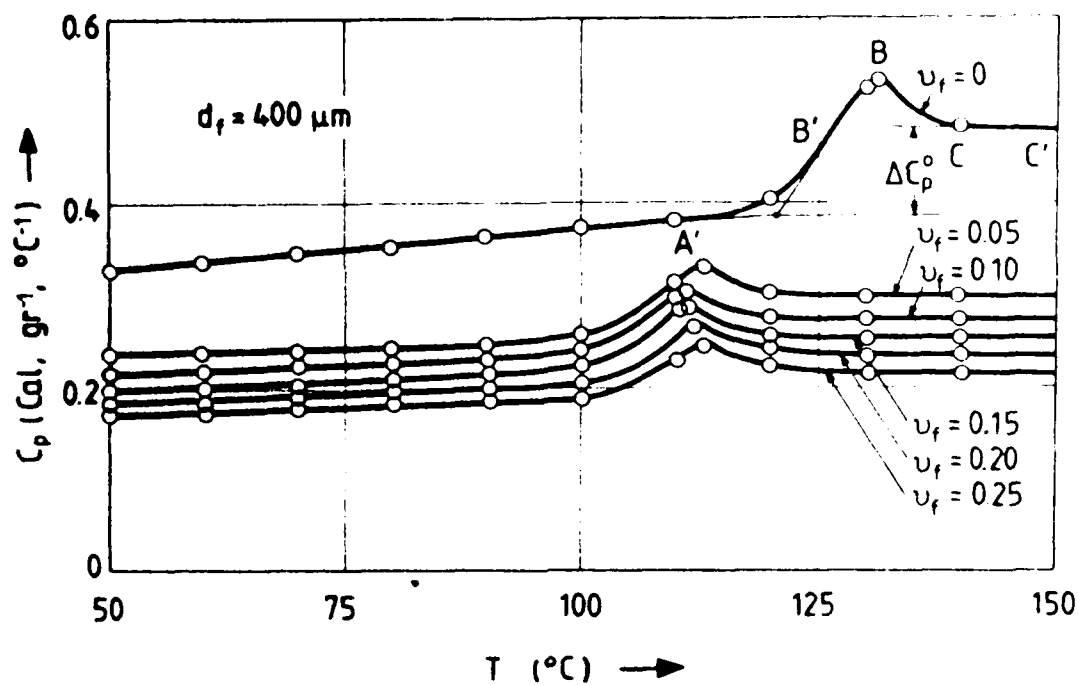


Fig.4. The variation of the differences  $\Delta r_i$  of the radii of

mesophases and inclusions ( $\Delta r = (r_i - r_f)$ ), versus the inclusion volume content  $u_f$  for three different diameters of inclusions of iron-epoxy particulates.

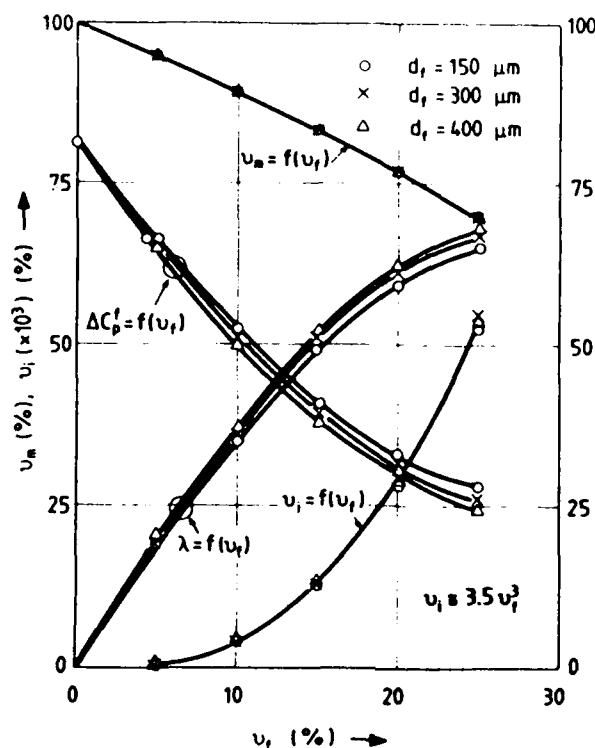


Fig.5. The variation of the specific heat jumps at glass-transition temperature of iron-epoxy particulate composites, versus the filler volume content  $u_f$ . The values for the factor  $\lambda$ , the mesophase ( $u_i$ )-, and the matrix ( $u_m$ )-volume fractions versus  $u_f$ , as derived from the values of the respective  $\Delta C_p^f$ 's are also plotted.

the  $\Delta C_p^f = f(u_f)$ -curves differ only slightly, with the respective curves for different filler-diameters, mutually intertwining. This fact indicates that the size of diameter of the filler plays only a secondary role on the influence of the heat-capacity jumps, which are primarily influenced by the filler-volume content. A similar behaviour is expected for the variation of the coefficient  $\lambda$ , as indeed it is indicated in Fig.5.

It is worthwhile indicating that the values for  $u_i$ 's fitted excellently a third degree curve expressed by:

$$u_i = C u_f^3 \quad (15)$$

where the constant  $C$  was evaluated experimentally to be equal to  $C=3.5$ .

The values of  $u_i$ 's, together with the respective values for  $E_c$ 's, were introduced in the respective models and gave excellent coincidence with their experimental values, based on the cubic relation between  $u_i$  and  $u_f$ .

Table 1. The values of the characteristic parameters of a series of iron-epoxy particulate composites for various fiber-volume contents  $u_f$

$u_f$	$u_i$	$u_m$	$\Delta C_p$	$\lambda$	$r_f$	$r_i$	$E_{CL}$	$E_i^a$	$\eta_1$	$\eta_2$	A	$2n$
	Percent	Cal/g °C			$\mu m$	$\mu m$	$10^9 NM^{-2}$	$10^9 NM^{-2}$				
5	0.048	94.95	0.0660	0.185		75.24	3.60	7.60	14239	12976	1263	11114
10	0.386	89.61	0.0525	0.352		75.96	4.22	12.50	1783	1464	319	1520
15	1.270	83.73	0.0410	0.494	75	77.12	4.75	19.34	459	313	146	424
20	2.828	77.17	0.0330	0.593		78.53	5.34	30.00	163	75	88	158
25	5.098	69.90	0.0280	0.654		80.10	6.06	43.00	74	12	62	74
5	0.052	94.48	0.0650	0.198		150.5180	3.98	11.00	7981	6796	1185	6584
10	0.413	89.59	0.0505	0.377		152.0632	4.37	17.00	1108	809	299	1002
15	1.348	83.65	0.0385	0.525	150	154.4935	4.82	25.00	317	179	138	302
20	2.968	77.03	0.0305	0.623		157.4199	5.38	36.00	125	41	84	124
25	5.457	69.54	0.0240	0.704		160.9148	6.11	49.00	63	1	62	64
5	0.050	94.95	0.0655	0.191		200.6691	4.09	15.00	5354	4131	1223	4744
10	0.399	89.60	0.0515	0.364		202.6621	4.20	20.00	935	626	309	866
15	1.333	83.67	0.0390	0.519	200	205.9229	4.84	27.00	293	153	140	282
20	2.940	77.06	0.0310	0.617		209.7998	5.39	38.00	119	34	85	118
25	5.280	69.72	0.0260	0.679		214.0751	6.10	51.00	62	2	60	58

The values of the characteristic quantities for the three-term unfolding model, as derived by this procedure, were included in Table 1.

### The Three-Term and Two-Term Versions of the Unfolding Models

In order to make compatible the variation of the  $E_i(r)$ -modulus with its neighbour phases, this modulus should be expressed by three terms, that is a constant one and equal to the  $E_m$ -modulus and two variable terms depending on the moduli of the filler,  $E_f$ , and the matrix,  $E_m$ , respectively.

The two variable terms should yield very abrupt variations in the  $E_i(r)$ -modulus, since the generally large differences between the moduli of the inclusions and the matrix must be accommodated in very thin layers of the mesophases. The appropriate functions for such steep variations are power functions of  $r$  with large negative exponents. Then, the  $E_i(r)$ -modulus may be expressed by:

$$E_i(r) = E_m + E_f \left( \frac{r_f}{r} \right)^{\eta_1} - E_m \left( \frac{r_f}{r} \right)^{\eta_2} \quad (16)$$

Expression (16) may be interpreted by the fact that the variable  $E_i(r)$ -modulus, which connects two phases with highly different mechanical properties and elastic moduli, must interconnect and span these differences. Indeed, for hard-core composites it is valid that  $E_f \gg E_m$ , whereas for rubber reinforcements we have the opposite relation  $E_m \gg E_f$ . However, never happens that  $E_f \sim E_m$ .

If we assume that the longitudinal displacements along each of the three phases (filler-mesophase-matrix) are, in an average, equal and if we neglect transversal effects we can reason that, since longitudinal displacements and strains are equal, the stresses developed in these phases should be proportional to their respective moduli. It has been established that, for singular regions in elastic stress fields, singular distributions may be approximated by negative powers of the radial distances from the singular points. Then, it is reasonable to accept in this case also as appropriate functions, expressing the transfer of moduli from fillers to matrix, forms described by the terms of relation (16).

The second right-hand term in Eq.(16) expresses the contribution of the  $E_f$ -modulus to the variation of  $E_i(r)$ -modulus, whereas the third right-hand term defines the counterbalancing contribution of the  $E_m$ -modulus, to correct the contribution of the  $E_f$ -modulus, and insert the influence of the matrix to the outer layers of the mesophase-layer.

From the compatibility conditions for the moduli at the filler-mesophase and mesophase-matrix boundaries, it may be derived that for  $r=r_f$  we have:

$$E_i(r_f) = E_f \quad (17)$$

which indicates the automatic satisfaction of the boundary condition for this interface, and similarly, for  $r=r_i$  we have:

$$E_i(r_i) = E_m + E_f \left( \frac{r_f}{r_i} \right)^{\eta_1} - E_m \left( \frac{r_f}{r_i} \right)^{\eta_2} = E_m$$

which yields:

$$(\eta_1 - \eta_2) = \log\left(\frac{E_f}{E_m}\right) : \log\left(\frac{r_i}{r_f}\right) \quad (18)$$

Putting:

$$A = \frac{\log(E_f/E_m)}{\log(r_i/r_f)} \quad (19)$$

we have:

$$\eta_1 = (\eta_2 + A) \quad (20)$$

where A is a real constant, depending on the ratio of the moduli of the two phases and the ratio of the radii of the fiber and the interphase. This constant is called the *adhesion parameter* of the model.

As soon as the radius of the extent of mesophase is defined, the parameter A is immediately defined and fixes the constant difference between the exponents  $\eta_1$  and  $\eta_2$ .

Higher values of A indicate better adhesion for a particular composite, because they imply small differences in the values of  $r_i$  and  $r_f$ . For hard-core materials, where  $E_f \gg E_m$ , the radius  $r_i$  must be always larger than  $r_f$ , and  $E_f \gg E_m$ , therefore the logarithm of the ratio  $r_i/r_f$  is a positive number and since  $\log(E_f/E_m) > 0$  the values of A are always positive. This means for a hard-core composite it is always valid that  $\eta_1 > \eta_2$ . On the contrary, for rubber-core composites  $\log(E_f/E_m)$  is also negative and therefore it is valid that  $\eta_1 < \eta_2$ .

Since the third term of the right-hand side of Eq.(16) takes care of the influence of the matrix modulus  $E_m$  to the variation of  $E_i(r)$ -modulus and since always for strong-core composites this contribution is secondary, relation (16) may be somehow relaxed by assuming that this third term varies linearly with the radius  $r$  along the mesophase. This means, in other words, that the exponent  $\eta_2$  may be assumed equal to unity, without losing generality, and imposing to the first right-hand side term to take care of the totality of the change of slope of the  $E_i(r)$ -modulus.

Then, relation (16) may be written as follows:

$$E_i(r) = E_f \left(\frac{r_f}{r}\right)^{2\eta} + \left\{ E_m - E_f \left(\frac{r_f}{r_i}\right)^{2\eta} \right\} \frac{(r - r_f)}{(r_i - r_f)} \quad (21)$$

It is easy to show that the boundary conditions for this equation are automatically satisfied. Indeed, for  $r=r_f$  we have the second right-hand term of Eq.(21) equal to zero and the first term equal to the  $E_f$ -modulus. Moreover, for  $r=r_i$  equation (21) yields automatically  $E_i(r)=E_m$  and this satisfies the exterior boundary condition.

Relation (21) has the advantage to contain only one unknown exponent and therefore simplifies considerably the evaluation of the unknown quantities in the definition of the variable  $E_i(r)$ -modulus. Then, in this two-term unfolding model remains to define this exponent  $2\eta$ , since all other quantities and especially the  $r_i$ -radius are either given, or evaluated from



the thermodynamic equilibrium relations.

In this model the  $2\eta$ -exponent is the characteristic parameter defining the quality of adhesion and therefore it may be called the *adhesion coefficient*. This exponent depends solely on the ratios of the main-phase moduli ( $E_f/E_m$ ), as well as on the ratio of the radii of the filler and the mesophase.

#### Evaluation of the Adhesion Exponents $\eta_1, \eta_2$ and $\eta$ of the Unfolding Models

As soon as the  $\Delta r_i$ s were determined and the values of  $r_i$ s are found, the values of the *adhesion parameter*  $A$  may be readily defined by using relation (19). For the evaluation of the exponents  $\eta_1$  and  $\eta_2$  in the three-term model it is necessary to dispose one more equation. This equation is derived from the values of the modulus of the composite which may be measured experimentally. In the case of particulates use then should be made of relation (1).

However since relation (1) is a complicated expression for the compliances of the composite and its phases in which is difficult and time consuming to introduce the variable modulus or compliance of the mesophase  $E_i(r)$ , use is made of the notion of the average value of the modulus of the mesophase,  $E_i^a(r)$ , which is expressed by:

$$E_i^a(r) = E_m + E_f \left( \frac{r_f}{r} \right)^{\eta_1} - E_m \left( \frac{r_f}{r} \right)^{\eta_2} \quad (22)$$

for the three-term model and by a similar expression for the two-term model. Then, as soon as this value is derived from relation (1) valid for particulates the mode of variation of these modulus inside the mesophase may be derived from relation:

$$E_i^a u_i = \frac{3}{r_m^3} \int_{r_f}^{r_i} \left[ E_m + E_f \left( \frac{r_f}{r} \right)^{\eta_1} - E_m \left( \frac{r_f}{r} \right)^{\eta_2} \right] r^2 dr \quad (23)$$

for the three-term model, and from relation:

$$E_i^a u_i = \frac{3}{r_m^3} \int_{r_f}^{r_i} \left[ E_f \left( \frac{r_f}{r} \right)^{2\eta} + \left\{ E_m - E_f \left( \frac{r_f}{r_i} \right)^{2\eta} \right\} \frac{r - r_f}{r_i - r_f} \right] r^2 dr \quad (24)$$

for the two-term model.

Both above relations, integrated in the interval between  $r=r_f$  and  $r=r_i$ , yield respectively:

$$E_i^a u_i = E_m u_i + \frac{E_f u_f}{\left( \frac{\eta_1}{3} - 1 \right)} \left\{ 1 - B \left( \frac{\eta_1}{3} - 1 \right) \right\} - \frac{E_m u_f}{\left( \frac{\eta_2}{3} - 1 \right)} \left\{ 1 - B \left( \frac{\eta_2}{3} - 1 \right) \right\} \quad (25)$$

and:

$$E_i^a u_i = \frac{E_f u_f}{\left(\frac{2\eta}{3} - 1\right)} \left\{ 1 - B^{\left(\frac{2\eta}{3} - 1\right)} \right\} - \frac{u_f}{4} \left( E_m - E_f B^{\frac{2\eta}{3}} \right) \left\{ 1 - B^{-1/3} + B^{-2/3} - 3B^{-1} \right\} \quad (26)$$

Relation (25) uses the value of  $E_i^a$ , derived from Eq.(1), and it constitutes one equation interrelating the two unknown exponents  $\eta_1$  and  $\eta_2$ . Then, relations (19) and (25) form a system of two equations and two unknowns, which can be solved, and yields the values of the exponents  $\eta_1$  and  $\eta_2$  and their difference  $A$ , which expresses the quality of adhesion and it is called the *adhesion coefficient*. The values of the exponents  $\eta_1$  and  $\eta_2$ , as well as of their difference are given in Table 1 and plotted in Fig.6 for the iron-epoxy particulate composites.

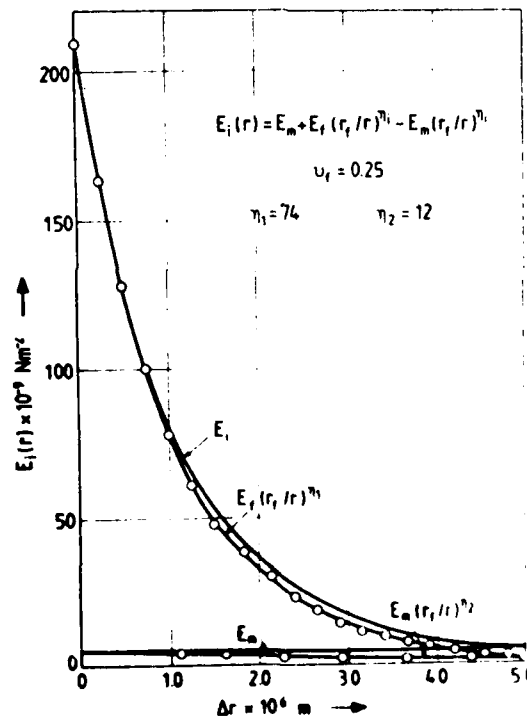


Fig.6. The mode of evolution of the variable terms  $E_f(r_f/r)^{\eta_1}$  and  $E_m(r_f/r)^{\eta_2}$ , contributing to the definition of the mesophase modulus, versus the polar distance from the filler boundary for a 25% iron-epoxy particulate composite.

Fig.7 presents the variation of the terms  $E_f(r_f/r)^{\eta_1}$  and  $E_m(r_f/r)^{\eta_2}$  in the mesophase layer for a 25 percent iron-epoxy particulate, as they have been derived from Eq.(22). It is worthwhile indicating the smooth transition of the  $E_i$ -modulus to the  $E_m$ -modulus at the region  $r \approx r_i$ . Similar behaviours present all other compositions.

It is interesting plotting the variation of the  $E_i(r)$ -modulus, versus polar distance around a typical filler. Fig.8 presents this transition of the moduli from the fibers to the matrices, exemplifying the important role

played by the mesophase layer to the overall mechanical behaviour of the composite.

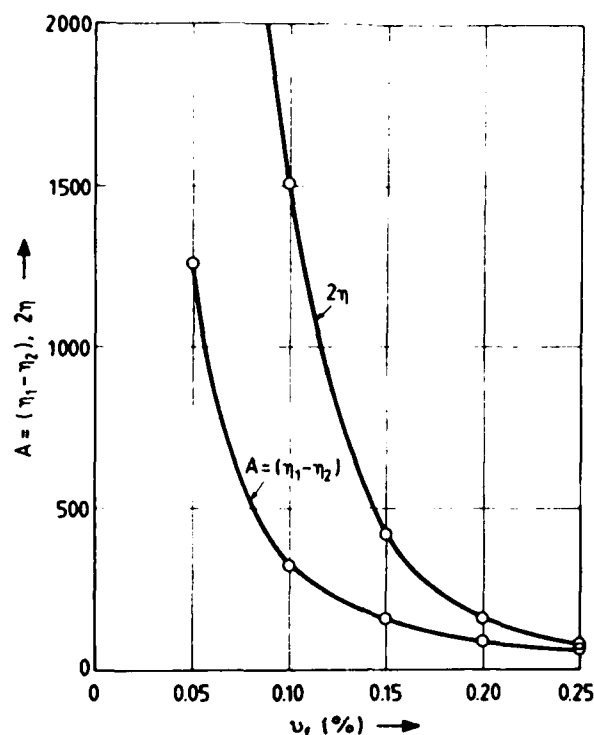


Fig.7. The variation of the adhesion parameter  $A$  for the three-term unfolding model, and the adhesion coefficient  $2\eta$  for the two-term model, versus the filler volume fraction  $u_f$ .

Fig.9 presents the variation of the various moduli of the composite and its constituents for various volume fractions of the series of iron-epoxy particulates. It is of interest to point out the small variation of the average value of the variable  $E_j(r)$ -modulus of the mesophase, which reflects the uniformity of the adhesion quality of these series of composites, which is also indicated by the almost linear variation of the longitudinal composite modulus, versus the filler-volume content.

For the case of the two-term unfolding model use should be made of Eq.(26) instead of Eq.(25). Then, the system of equations (1) and (26) yields the values of the exponent  $2\eta$  and the radius  $r_j$  of the mesophase. Fig.6 contains also the plot of the adhesion coefficient  $2\eta$ , versus filler volume fraction for all iron-epoxy particulates studied.

It is worth mentioning here that the three  $2\eta=f(u_f)$  curves for the three different diameters of the fillers are almost coincident. Furthermore, there is an equivalence between the mode of variation of the two adhesion coefficients  $A$  and  $2\eta$  corresponding to the two versions of the unfolding model.

Fig.10 presents the variation of the interphase moduli  $E_j(r)$  for the various inclusion-volume fractions, versus the extent of the interphase  $\Delta r$ , normalized to the highest inclusion-volume fraction of 25 percent.

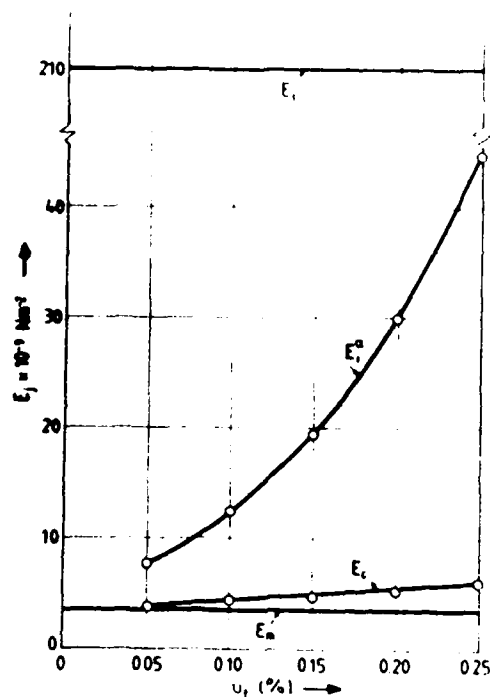


Fig.8. The variation of the moduli of the particulate composite,  $E_c$ , versus the filler-volume fraction,  $u_f$ , and the mode of variation of the average mesophase modulus,  $E_i^a$ , as derived from the models.

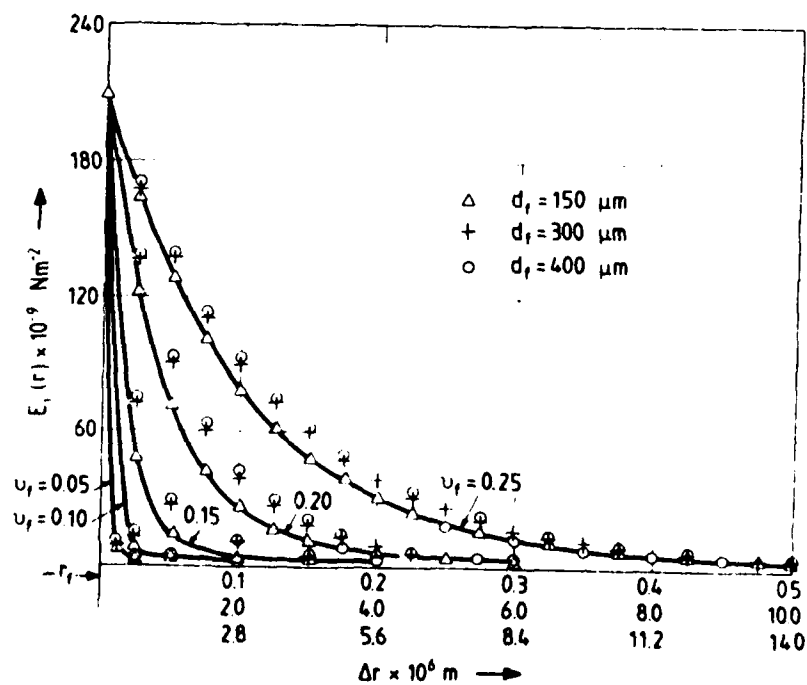


Fig.9. The variation of the mesophase moduli, versus polar

distance  $r$  for different filler-volume contents  $u_f$  for the three-term unfolding model.

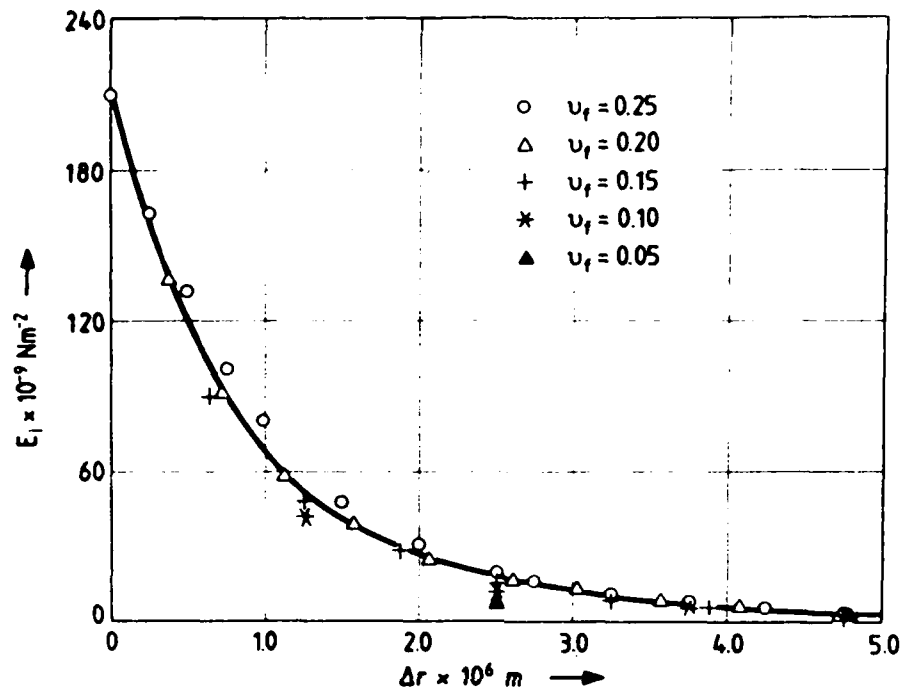


Fig.10. The variation of the mesophase moduli, normalized to the mesophase thickness  $\Delta r$  for the 25 percent filler-volume content composite versus polar distance  $r$  for the two-term unfolding model.

This was done in order to show the similarity of variation of the  $E_i$ -modulus for the various values of  $u_f$  for this series of composites, possessing the same adhesion properties between them. These normalized patterns are equivalent with those presented in Fig.9 for the three-term unfolding model, since the differences between corresponding values of the two versions of the model are insignificant.

### Conclusions

The theoretical models describing the physical and mechanical properties of composites consider the surfaces of the inclusions as perfect mathematical surfaces. Thus, the transition of the mechanical properties from the one phase to the other is done by jumps in the characteristic properties of either phase. This fact introduces high shear straining at the boundaries.

In order to alleviate this singular and unrealistic situation two versions of a model were presented, in which a third pseudo-phase was considered, as developed along a thin boundary layer between phases during the polymerization of the matrix, and whose properties depend on the individual properties of the phases and the quality of adhesion between them.

The two versions of this unfolding model consider that the mesophase layer

possesses varying physical and mechanical properties, assuring a smooth transition from the properties of the fillers to the properties of the matrix. In this manner a progressive change of the mechanical properties from the filler to the matrix is achieved in a very short distance, corresponding to the thickness of this boundary layer.

By using Lipatov's theory, interrelating the abrupt jumps in the specific heat of composites at their respective glass transition temperatures with the values of the extents of these boundary layers, the thickness of the mesophase was accurately calculated.

Assuming in the one version of the model a three-term representation of the unfolding value for the elastic modulus of the interphase, where each variable term is expressed as a negative power function of the polar distance from the inclusion, the variation of the elastic modulus of the mesophase was accurately determined.

The second version of the unfolding model uses, instead of three, two terms, one of which is a negative power function of the polar distance, acting upon the inclusion modulus, and the other one, acting upon the matrix modulus, is expressed as a linear function of  $r$ .

Both versions of the unfolding model gave satisfactory results for the evaluation of the variation of modulus of mesophase, with the second one (the two-term model) yielding always more stable results.

The difference in the exponents  $\eta_1$  and  $\eta_2$  in the three-term model and the exponent  $2\eta$  in the two-term model, gave a measure of the quality of adhesion between phases and they may be considered as *adhesion coefficients*, since higher values of these coefficients characterize a better adhesion, whereas, as these values are diminished, the adhesion becomes less and less effective.

Both types of the unfolding model describe satisfactorily the state of transition of the mechanical and physical properties of the composites from its fillers to the matrix, with the two-term version yielding more stable and, therefore, more reliable results than the three-term model.

#### References

- Budiansky, B. (1965) Jnl. Mech. Phys. Sol., 13 (3), 223.
- Bueche, F. (1960) J. Appl. Polym. Sci., 4, 107.
- Fröhlich, H. and Sack, R. (1946) Proc. Roy. Soc. Lond. (A) 185m, 415.
- Goodier, J.N. (1933) Jnl. Appl. Mech., Trans. ASME, APM-55-7, 39.
- Hashin, Z. (1962) Jnl. Appl. Mech., 29 (2), 143.
- Hashin, Z. and Rosen, B.W. (1964) Jnl. Appl. Mech., 31 (3), 223.
- Hill, R. (1965) Jnl. Mech. Phys. Sol., 13 (3), 213.
- Jones, R. (1975) Mechanics of Composite Materials, McGraw-Hill, N. York.
- Kerner, E.H. (1956) Proc. Phys. Soc. London, 69B, 808.

Kudykina, T.A. and Pervak, I.G. (1975) Ukransky Fizichesky Zhurnal 20, 1664.

Lipatov, Yu. (1977) Physical Chemistry of Filled Polymers, Engl. Trans. by Moseley, R.J., Intern. Poly. Sci. and Techn. Monograph No.2, Khimiya, Moscow.

Maurer, F. (1983) Ph. D. Thesis, University of Duisburg FRG.

Nielsen, L.E. (1966) Jnl. Appl. Polym. Sci. 10, 97

Papanicolaou, G., Thecaris, P.S. and Spathis, G. (1980) Kolloid Zeitsch. and Zeit für Polym., 258 (11), 1231.

Sagalaev, G. and Simonov-Emiljanov, I. (1973) Platinassy, N2, 48.

Schwarzl, F.R. and Eikhoff, J. (1971) Central Lab. TNO Rep.CL71/55.

Spathis, G., Sideridis, E. and Theocaris, P.S. (1981) Intern. Jnl. Adhesion and Adhesives 1 (2), 195.

Spathis, F., Kontou, E. and Theocaris, P.S. (1984) Jnl. of Rheology, 28 (2), 161.

Takayanagi, M., Uemura, S. and Minami, S. (1964) Jnl. Polym. Sci., Part C, No.5, 113.

Theocaris, P.S. and Papanicolaou, G. (1979) Fiber Sci. and Technology, 12 (6), 421.

Theocaris, P.S., Kefalas, B. and Spathis, G. (1983) J. Appl. Polym. Sci., 28 (12), 3641.

Theocaris, P.S. (1984a) New Developments in the Characterization of Polymers in the Solid State, Advances in Polymer Science, Kausch H.H. and Zachmann H.G. Editors, Springer Verlag.

Theocaris, P.S. (1984b) Jnl. Reinfor. Plastics and Composites, 3 (4), 286.

Theocaris, P.S. (1984c) Jnl. Reinf. Plastics and Composites (in press).

Theocaris, P.S. (1984d) Jnl. Appl. Polymer Sci. (in press).

Theocaris, P.S. (1984e) Proc. Nat. Acad. of Sci. (Athens) 59(I), 327.

Van der Poel, C. (1958) Rheol. Acta 1, 198.

Voyutsky, S.S. (1960) Adhesion and Autohesion of Polymers, English Trans. Interscience Publ. (1963).

Ziegel, K.D. and Romanov A. (1973a) J. Appl. Polym. Sci. 17, 1119.

Ziegel, K.D. and Romanov, A. (1973b) J. Appl. Polym. Sci., 17, 1133.

## Discussion of Session I

Direct observations of wavefront dislocations have been made for ultrasound, for example in two experiments by D R Andrews and in an independent experiment by G J Hardy. All three experiments make use of a light-emitting diode as a stroboscopic light source (Andrews and Wallis, 1977), in a schlieren system by Andrews (1983) and in a photoelastic system by Hardy et al (1978).

Figure 1 is a schlieren image (Andrews, 1983) of a pulse of approximately 15 wavefronts of compressional ultrasonic waves that have been reflected by the curved boundary seen at the bottom of the photograph. This image bears direct comparison with Wright and Nye's (1982) Figure 13 (larger scale) which is reproduced here as Figure 2. In Figure 3, Figure 1 is reprinted with 3 non-circular loops sketched on it to draw attention to the extents of the three regions of strong contrast at waves. These regions, or lobes, correspond to the amplitude "hills" in Figure 2; in the photograph, each hill is traversed by some 5-10 bright contrast waves. The cusp also sketched in Figure 3 is the cusp caustic shown as a dot-dash line in Figure 2. The two dots in Figure 3 identify the dislocations corresponding to the two lowest filled circles in Figure 2. The spatial structure of these dislocations is sketched in Figure 4 and is asymmetric. This asymmetry can be explained by a 2-beam model (see Figure 2 of Wright and Nye (1982)) in which are superposed two envelopes with a delay time. Referring to Figure 5, subtracting envelope B from envelope A (destructive interference) gives C which is very bright and short in front, and long and weak behind.

Figure 6 is also a schlieren image (Andrews, 1983) this time of waves scattered by a cylindrical object. The occurrence of a dislocation is indicated by an arrow.

The above are examples of dislocations generated in the visualising medium. If wavefront dislocations are to be fully exploited in order to obtain the microstructural information which they carry, it is necessary that they be visualized, or otherwise detected and recorded, outside the medium in which they are formed. One method by which direct visualization has been achieved (Hardy et al, 1978) is to transmit the pulse of ultrasound from the solid of



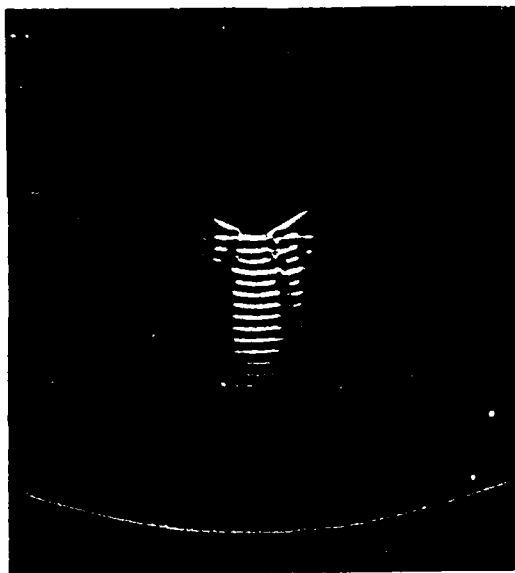


Figure 1. Schlieren image of a pulse of ultrasound reflected by a curved boundary

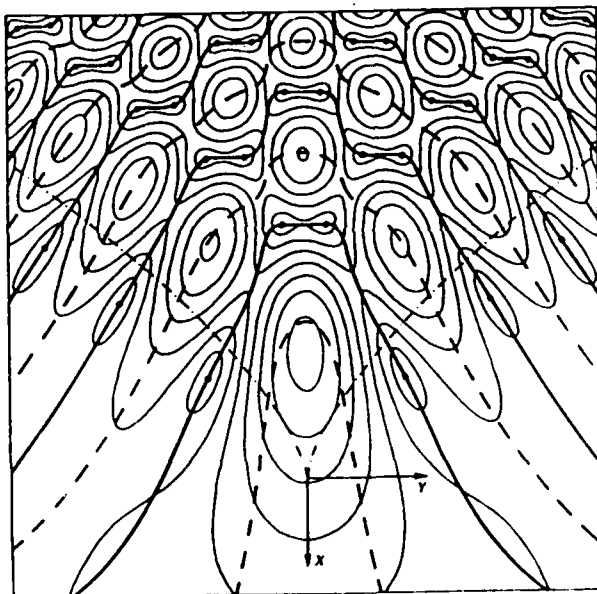


Figure 2. Amplitude contours of the cusp diffraction catastrophe. The loci of frequency minima  $\mathcal{S}$  (thick solid lines) link the c.w. nulls (filled circles) and contain the approximate pulse dislocation trajectories for small bandwidth. The loci of frequency maxima (thick broken lines) approximately link the spatial maxima. The cusp caustic is shown as a dot-dash line

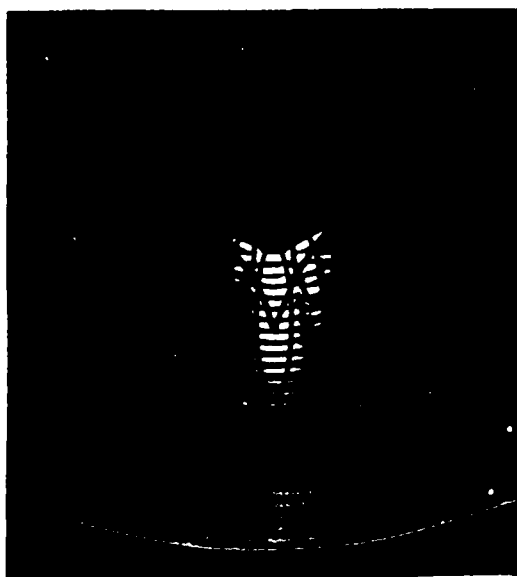


Figure 3. Same as Figure 1 (see text)

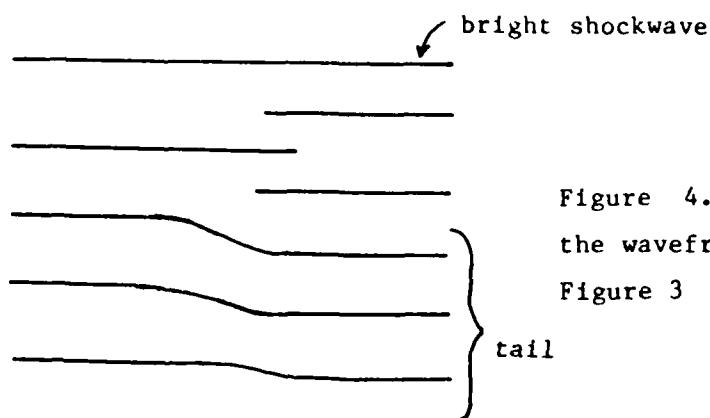


Figure 4. Spatial structure of the wavefront dislocations seen in Figure 3

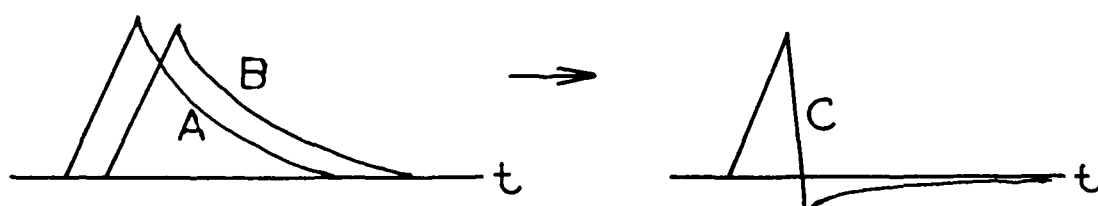


Figure 5. 2-beam explanation for the asymmetry of the dislocations in Figure 3

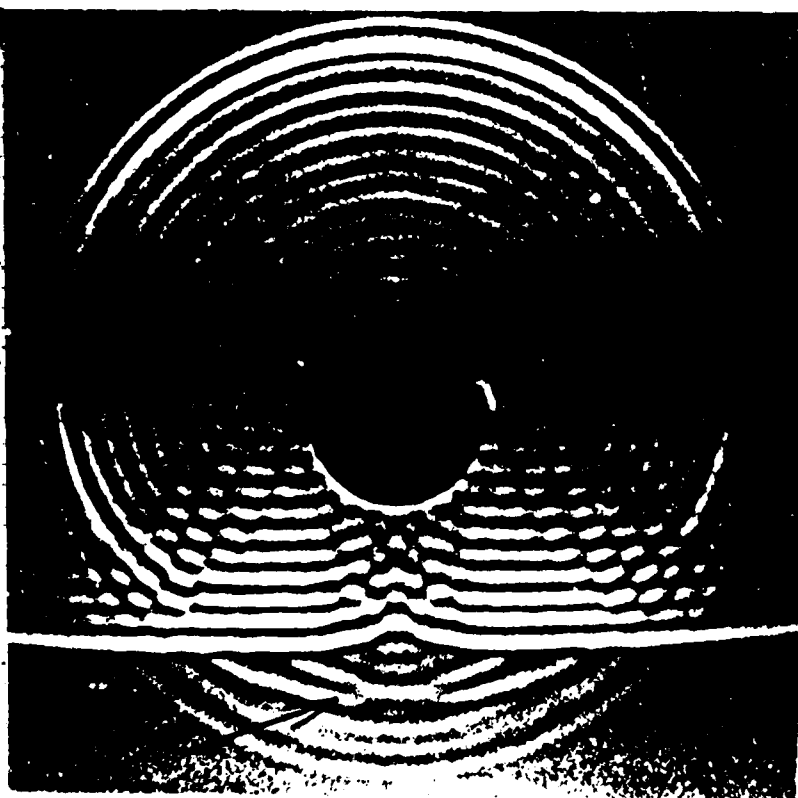


Figure 6. Schlieren image of dislocations associated with scattering by a cylindrical object

interest and into an adjacent block of annealed glass where, by using stroboscopic illumination, it can be seen by virtue of its associated photoelasticity. Figure 7 is an image obtained by passing a 2 MHz pulse of 7 wavefronts through a block of steel containing a 1 mm radius hole (arrowed). The consequent wavefront dislocation structure is clearly resolved in the upper part of the photograph.



Figure 7. Photoelastic image in glass of dislocations in a pulse of ultrasound which has been scattered by a circular hole in an adjacent block of steel

The radius of the defect detected in Figure 7 is similar in magnitude to the wavelength of the radiation used and this led to discussion of exactly what radiations might be best suited for exploitation of wavefront dislocations as a tool for NDE. Assuming that objects cannot be detected if they are smaller than the wavelength of the radiation used to detect them then, for polymers, microwaves might be an ideal radiation for defects of the order of 1cm in size and infra-red radiation for defects smaller than this.

#### References

- D R Andrews and L J Wallis (1977) J Phys E 10 95
- D R Andrews (1983) 15th Intl Congr on High Speed Photography and Photonics, Soc of Photo-Optical Instrumentation Engrs 348 565
- F J Wright and J F Nye (1982) Phil Trans Roy Soc Lond A305 339
- G J Hardy, T W Turner and K H G Ashbee (1978) Metal Sci 12 406

Session II: Molecular orientation

# CONTRIBUTION OF NEUTRON SCATTERING TO THE DETERMINATION OF CHAIN TRAJECTORY IN SEMI-CRYSTALLINE ISOTACTIC POLYSTYRENE.

J.M. Guenet.

Centre de Recherches sur les Macromolécules, CNRS, 6, rue Boussingault,  
67083 Strasbourg, Cédex France.

**ABSTRACT :** The chain trajectory in semi-crystalline polymers is a topical subject. One way of determining it directly is to use the neutron scattering technique. In this paper, after a short description of this technique, the results obtained on semi-crystalline isotactic polystyrene are given. They show that the trajectory is mainly governed by the competition between crystals growth rate and chain mobility in the original melt.

## INTRODUCTION.

Since the end of the fifties where the lamellar character of the structures in crystalline polymers<sup>1</sup> has been recognized and the chain folding concept<sup>2</sup> put forward, scientists working in this field of polymer science have been steadily concerned with the trajectory of a chain once crystallization has been achieved. As at the time there was no way of determining it directly from the available experimental techniques, the scientific community soon divided into two schools each propounding its own model. Schematically speaking, on one hand was standing the switch-board model which was reminiscent of the gaussian character of the chain in the molten state and to some extent an up-to-date adaptation of the fringed-micelle model to requirements imposed by the existence of lamellae. On the other hand, was standing the model of adjacent reentry along an  $hk0$  plane which conveyed the idea of regularity in crystalline polymers. While morphological evidence rather supported the second type of model especially in single crystals grown from dilute solutions, no definite answer could be provided.

In the early seventies, the successful investigations of chain statistics in bulk amorphous polymer by neutron scattering<sup>3-4</sup> nourished great hopes for elucidating the chain trajectory in crystallizable polymers and thus for definitively settling a twenty-years-old dispute. The principle of the technique is at first sight quite appropriate for answering the question. By mixing some deuterium-labelled chains in an hydrogenated matrix, one should be able to easily determine their conformation in the semi-crystalline state. Unfortunately, polyethylene which was the first polymer studied<sup>5</sup> proved to be virtually inadequate on account of the fact that in the course of crystallization isotopic segregation takes place.

In spite of this major impediment to a thorough study some virtually unsmearred results were gained on quickly quenched samples which showed an absence of variation of chain dimension after crystallization.<sup>5-6</sup> This particular point was soon interpreted differently and thus revived with renewed vigour the controversy.<sup>7</sup>

Alternatively, some polymers such as isotactic polystyrene<sup>8</sup> (iPS) or isotactic polypropylene (iPP)<sup>9</sup> were fortunately found free of segregation phenomenon between protonated and deuterated species after crystallization. As a result more extensive studies have been performed on these polymers. In this paper, after a short description of the neutron scattering technique, results gathered on isotactic polystyrene in the semi-crystalline state are reported.

## PRINCIPLE OF NEUTRON SCATTERING EXPERIMENTS.

The use of neutron scattering to study chain trajectories, with parti-

cular emphasis on bulk samples, relies upon the large difference of interaction of a neutron with hydrogenated or deuterated matter.<sup>10</sup>

Whereas, chemically speaking, there is virtually no difference between protonated and deuterated species, their neutronic contrast  $b$  is quite unlike ( $b_H = -0.374$ ,  $b_D = +0.67$ ). In addition, protonated chains scatter neutrons mainly in an incoherent manner as opposed to deuterated chains. Accordingly, these essential differences enable to "visualize" by small angle neutron scattering deuterated chains imbedded in a protonated matrix.

# I) Theoretical.

## 1. Intensity scattered by a mixture of protonated and deuterated chains.

The intensity scattered by a blend of protonated and deuterated chains generally reads :

$$S(q) = (\bar{a}_D - \bar{a}_H)^2 S_D^{coh}(q) + (\bar{a}_H - \bar{a}_m)^2 S_H^{coh}(q) + 2(\bar{a}_H - \bar{a}_m)(\bar{a}_D - \bar{a}_m) S_{DH}^{coh}(q) + N_H \bar{z}_H 4\pi a_{inc,H}^2 + N_D \bar{z}_D 4\pi a_{inc,D}^2 \quad (1)$$
 where  $N_H, \bar{z}_H$  and  $N_D, \bar{z}_D$  are respectively the number and the polymerization degree of the protonated and deuterated chains,  $\bar{a}_D, \bar{a}_H, \bar{a}_m$  are the mean average scattering lengths of a deuterated chain, a protonated chain and of their blend. Finally,  $a_{inc,H}^2$  and  $a_{inc,D}^2$  are the incoherent cross-section with obvious meaning for the subscripts. The diffusion functions  $S_D^{coh}(q)$ ,  $S_H^{coh}(q)$  and  $S_{DH}^{coh}(q)$  read :

$$S_D^{coh}(q) = \sum_i \sum_j \sum_s \sum_t \langle \exp i\vec{q} \cdot (\vec{r}_{is} - \vec{r}_{jt}) \rangle = N_D \bar{z}_D^2 P_D(q) + N_D^2 \bar{z}_D^2 R_{DD}(q) \quad (2)$$

$$S_H^{coh}(q) = N_H \bar{z}_H^2 P_H(q) + N_H^2 \bar{z}_H^2 R_{HH}(q) \quad (3)$$

$$S_{DH}^{coh}(q) = N_H \bar{z}_H N_D \bar{z}_D R_{HD}(q) \quad (4)$$

where  $P(q)$  is the form factor of a molecule and  $R(q)$  the Fourier transform of the radial distribution function.

By introducing  $\bar{z}_H = M_H/M_{oH}$  and  $\bar{z}_D = M_D/M_{oD}$  where  $M$  is the chain molecular weight and  $M_o$  the monomer molecular weight and also  $N_H = C_H N_A / M_H$  and  $N_D = C_D N_A / M_D$  where  $C$  is the concentration of the species in  $g/cm^3$ , one ends up with :

$$S(q) = (\bar{a}_D - \bar{a}_m)^2 \left[ \frac{C_D N_A}{M_{oD}^2} M_D P_D(q) + \frac{C_D^2 N_A^2}{M_{oD}^2} R_{DD}(q) \right] + (\bar{a}_H - \bar{a}_m)^2 \left[ \frac{C_H N_A}{M_{oH}^2} M_H P_H(q) + \frac{C_H^2 N_A^2}{M_{oH}^2} R_{HH}(q) \right] + 2(\bar{a}_D - \bar{a}_m)(\bar{a}_H - \bar{a}_m) \frac{C_H C_D N_A^2}{M_{oH} M_{oD}} R_{HD}(q)$$

Two cases are now to be considered :

i) Protonated and deuterated species are identical (same molecular weight and same conformation) and their solid solution is homogeneous.

ii) Protonated and deuterated chains have different molecular weight and as previously their mixture is homogeneous.

In the first case, the following relations can be written down<sup>11</sup> :

$$\text{molecular weight identity : } M_H = M_D \quad \text{and} \quad P_H(q) = P_D(q) \quad (6)$$

$$\text{homogeneity : } R_{DD}(q) = R_{HH}(q) = R_{HD}(q) \quad (7)$$

The mean scattering length of the blend then reads :

$$\bar{a}_m = x_D \bar{a}_D + (1-x_D) \bar{a}_H$$

$S^{coh}(q)$  eventually reads :

$$S^{coh}(q) = \rho \frac{N_A}{M_o} x_D (1-x_D) (\bar{a}_D - \bar{a}_H)^2 P(q) \quad (8)$$

Relation (8) shows that  $S^{coh}(q)$  is at a maximum for  $x_D = 0.5$ . However, the possible presence of microvoids or heterogeneities (crystalline polymers are heterogeneous in nature) has been so far overlooked. These heterogeneities

lead to density fluctuations hence a parasitic coherent signal enhanced by increasing the amount of deuterated species. In addition, it happens to be quite difficult, even impossible, to prepare samples of crystallizable polymers having rigorously the same molecular weight and the same molecular weight distribution. As a result, it seems more realistic to work with samples containing only a few amount of deuterated species (say 1 to 2 %) to avoid the afore-mentioned problems.

Under these conditions,  $S(q)$  becomes :

$$S(q) = c_D \frac{N_A M_0}{M_{00}} (\bar{a}_D - \bar{a}_H)^2 \rho_D(q) + 4\pi \frac{c_H N_A}{M_{0H}} a_{inc,H}^2 \quad (9)$$

where the following approximations have been made :

$$1 - x_D \approx 1, \quad \bar{a}_H \approx \bar{a}_H, \quad \frac{c_D N_A}{M_{00}} 4\pi a_{inc,D}^2 \approx 0$$

## 2. Analysis of the scattering intensity.

The intensity found experimentally is the Fourier transform of the conformation investigated. Instead of taking the inverse Fourier transform to determine the conformation, a method which might prove very tedious in the end, it is more convenient to examine the scattered intensity in different domains of scattering vectors (or more precisely transfer momentum). Usually two domains are considered :

i) The Guinier range where  $qR_g < 1$ ,  $R_g$  being the radius of gyration of the chain.

ii) The intermediate range where  $qR_g > 1$ .

In the Guinier range, the intensity reduces to :

$$I(q) \sim M_w \left( 1 - \frac{q^2 R_g^2}{3} \right) \quad (10)$$

By plotting  $I^{-1}(q)$  as function of  $q^2$ , both the radius of gyration and the molecular weight can be measured. Consequently, determining the variation of  $R_g$  with molecular weight brings useful information on the chain conformation.

In the intermediate range, the intensity takes the form :

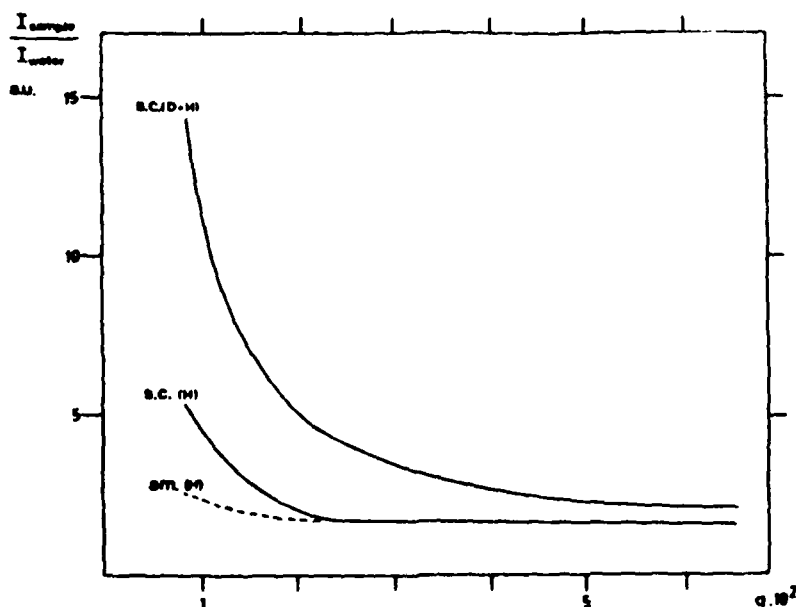
$$I(q) \sim q^{-\eta} \quad (11)$$

where  $\eta$  is a exponent depending on the conformation which is however not univoque. For instance, a gaussian conformation and a thin sheet both give an exponent  $\eta = 2$  in spite of their unlikeness.

## II) Experimental.

If, theoretically, neutron scattering seems to be simple, experimentally some problems have to be solved so as to obtain the true intensity scattered by the label species. The case of isotopic segregation will be ignored here. Unless the degree of segregation is known by a separate method it is impossible to get correct results under these circumstances.

The main constraint in a neutron scattering experiment is to remove the incoherent background arising from the protonated chains which should be flat (no angular dependence). Normally, this is done by measuring the intensity scattered by a sample containing the same number of protons by unit volume. For instance, pure water could do the trick. However as shown on Fig.1, this background is far from being flat. An upturn at small angle is visible which comes from the residual coherent scattering due to inhomogeneities. Fig.1 shows that as the size of these inhomogeneities is increased the upturn becomes more prominent. (Note that a crystalline sample is inhomogeneous since there is an alternation of amorphous and crystalline domains



Intensities in arbitrary units normalized by H-water spectrum: [am. (H)] = amorphous matrix; [S.C. (H)] = single crystal blank, [S.C. (H+D)] = single crystal sample containing about 1% of D species.

Figure 1.

that have different densities). As a consequence, to obtain correct results, one has to remove a background measured on a blank sample prepared under the same conditions that is, in the case of crystalline polymers, crystallized at the same temperature for the same time.

Another problem consists of determining the absolute intensity, chiefly to measure the molecular weight so as to check that isotopic segregation is absent. This is usually achieved by dividing the intensity scattered by the sample once the incoherent background is subtracted by the intensity scattered by protonated water. The normalized intensity  $I_N(q)$  then reads:

$$I_N(q) = 4\pi d \frac{c_D M_D N_A}{M_D^2} \frac{(\bar{\alpha}_D - \bar{\alpha}_H)^2}{(1-T)} P_D(q) \quad (12) \quad \text{where } d$$

is the thickness of the water sample and  $T$  its transmission. Through this technique one can measure intensities within 30% to 50%. The discrepancy stems from the fact that inelastic scattering takes also place which is not accounted for by the above relation and is difficult to estimate. In our experiments, we preferred in addition to water normalization to use a reference sample containing the same labeled chains but imbedded in an atactic polystyrene matrix wherein no segregation occurs whatsoever. This sample enables to determine the true value of  $I(0)$  and then to renormalize again the experiments.

#### EXPERIMENTAL RESULTS ON SEMI-CRYSTALLINE SAMPLES.

##### 1. Samples preparation.

Protonated and deuterated isotactic polystyrenes have been synthesized according to the Natta<sup>12</sup> method. Particular care has been taken with the deuterated material to fractionate it so as to obtain fractions whose polydispersity is lower than 1.2. Blends of H and D polymers have been obtained by dissolving them together in boiling chlorobenzene then coprecipitating in methanol. H-matrices of different molecular weight were used. Bulk crystallized samples have been prepared in two steps. The mixture has been moulded at 250°C then quenched in iced-water in order to obtain amorphous



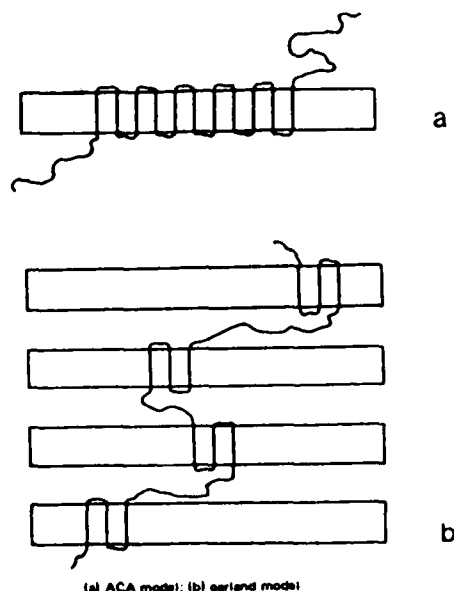
samples. Finally these samples have been annealed for various times at the desired temperature  $T_c$  to achieve crystallization. (In these experiments  $T_c = 140, 185, 200, 220^\circ\text{C}$ ). Single crystals have been grown from dilute solutions in dibutyl phthalate at  $130^\circ\text{C}$  through the use of the self-seeding technique.

## 2. Neutron scattering set-up.

Neutron scattering experiments have been carried out at the "Institut Laue-Langevin" in Grenoble (France). Two devices have been employed D11 ( $5 \cdot 10^{-3} < q < 10^{-2}$ ) and D17 ( $10^{-2} < q < 7 \cdot 10^{-1}$ ) allowing to investigate the Guinier and the intermediate domains. A rotating monochromator providing a width at half-height  $\frac{\Delta h}{h} \approx 9\%$  was used.

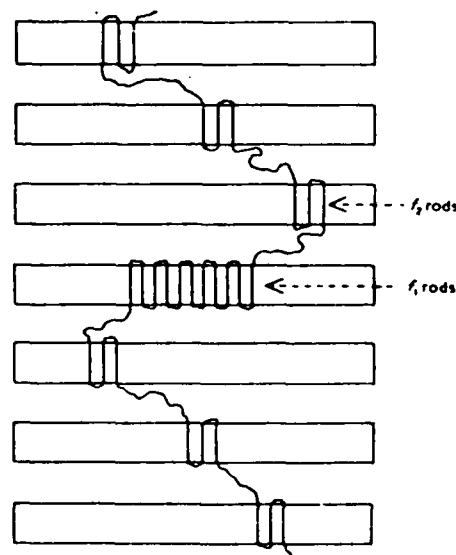
## 3. Results.

All the results presented here have been interpreted with four basic models : the sheet-like model arising from incorporation of a chain along an  $hk0$  plane, the ACA model made up with a long sheet and two amorphous wings (Fig.2a), the "garland" model composed of very short crystalline sequences alternating with short amorphous sequences (Fig.2b) and the "central core" model which is an intermediate between the latter ones (Fig.3).



(a) ACA model; (b) garland model

Figure 2.



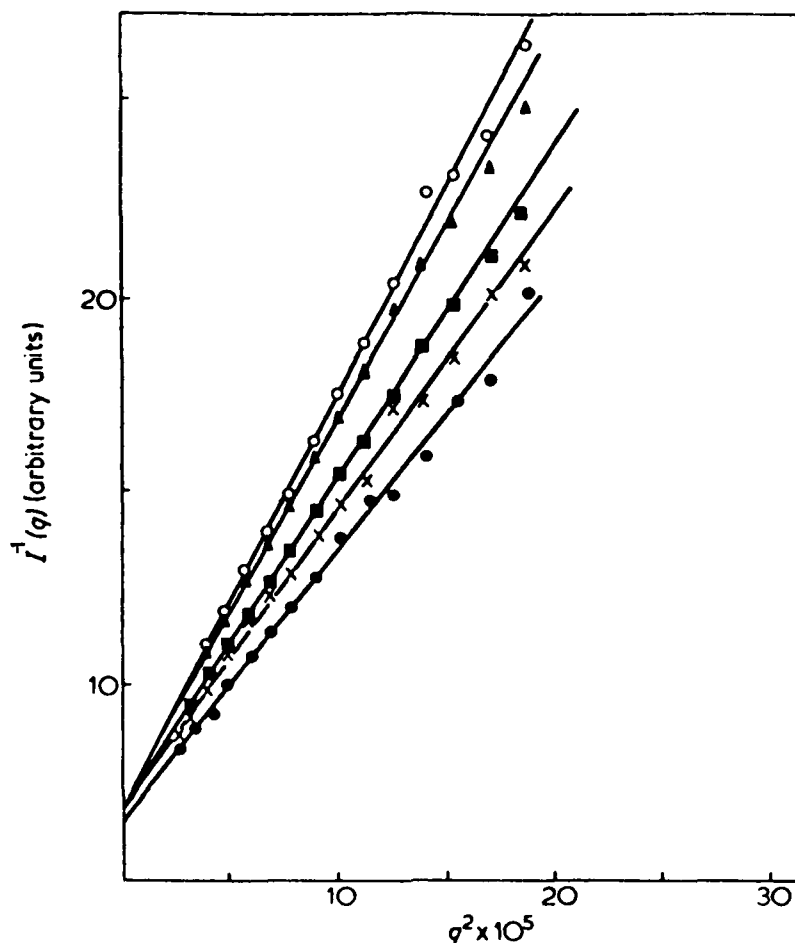
Central core model

Figure 3.

In the following, results are given for the different crystallization temperatures. Here only a brief summary of the results is reported. Detailed information will be found in references , 8 and 13 to 17.

### a) $T_c = 185^\circ\text{C}$ .

Two matrix molecular weights have been employed. For  $M_w = 4 \cdot 10^5$ , an increase of the radius of gyration  $R_g$  has been observed (see Fig.4). (Note the invariance of  $I^{-1}(0)$  which is proportional to  $M_w$ ). The variation of  $R_g$  with molecular weight of the labelled species gives  $R_g \sim M_w^{0.78}$  for  $x_c = 30\%$ . These results are consistent with the ACA model. Data in the intermediate range are in agreement with this model as well (Fig.5). Conversely by increasing the molecular weight of the matrix ( $M_w = 1.7 \cdot 10^6$ ) (hence augmenting the viscosity in the molten state)  $R_g$  does not vary by increasing the crystallinity and  $R_g \sim M_w^{0.5}$  is found as opposed to previously. A "Garland" model is appropriate in this case to account for the results. Data in the intermediate range (Fig.5) although giving a  $q^{-2}$  behavior for both samples



$I^{-1}(q)$  vs.  $q^2$  ( $\text{\AA}^{-2}$ ) for different degrees of crystallinities.  
 $\circ = 0.35$ ,  $\triangle = 0.3$ ,  $\blacksquare = 0.25$ ,  $\times = 0.22$ ,  $\bullet = 0.16$ . The slopes are directly related to  $R_g^2$

Figure 4.

have different shapes and therefore support the results in the Guinier range and the existence of two types of models.

b)  $T_c = 200^\circ\text{C}$ .

At this crystallization temperature for a matrix molecular weight  $M_w = 8 \cdot 10^5$ ,  $R_g$  varies like  $M^{0.78}$  as previously, a result consistent with the ACA model. Intermediate behavior of the form factor is also in agreement with this model.

c)  $T_c = 140^\circ\text{C}$ .

As with samples crystallized at  $185^\circ\text{C}$ , two matrices have been used. In the middle molecular weight matrix ( $M_w = 4.2 \cdot 10^5$ , sample C-140-HM1),  $R_g$  varies like  $M^{0.63}$ , a result accounted for by considering in that case a "central core" model. With the high molecular weight matrix ( $M_w = 1.7 \cdot 10^6$ , sample C-140-HM3),  $R_g$  varies like  $M^{0.5}$  which is consistent with the "Garland" model. Results in the intermediate range (Fig.6) clearly show two types of behaviour consistent with the models deduced from the variation of dimensions with the molecular weight of the labeled species.

d) Solution grown crystals ( $T_c = 130^\circ\text{C}$ ).

Certainly the most interesting and decisive results have been obtained

on single crystals. The variation of  $R_g$  with molecular weight gives an exponent  $\nu = 0.91$  (Fig.7) which indicates that the chain folds along the 330 plane with an average distance between stems of about 13 Å. Data gained at larger angles confirm this interpretation. As a matter of fact two types of behaviour appear (Fig.8) for  $q < q^*$  ( $q^* \approx 3 \times 10^{-3}$ )  $I(q) \sim q^{-1}$  and for  $q > q^*$   $I(q) \sim q^{-2}$ . Examining the form factor of a sheet with length  $L_c$  and width  $l_c$ :

$$P(q) = \frac{2}{qL_c} \left[ \frac{\pi}{qL_c} \left( \int_0^{qL_c} \frac{J_0(x)}{x} dx \right) + \frac{1}{qL_c} \left( \frac{\sin \frac{qL_c}{2}}{\frac{qL_c}{2}} \right)^2 - \frac{\sin qL_c}{(qL_c)^2} \right] \quad (13)$$

two regimes are expected:

for  $qL_c > 1$  and  $ql_c < 1$

$$P(q) \sim q^{-1}$$

for  $qL_c > 1$  and  $ql_c > 1$

$$P(q) \sim q^{-2}$$

Therefore the results both in the Guinier and the intermediate ranges are definitely consistent with a sheet which irretrievably leads to the dismissal of the switch-board model.

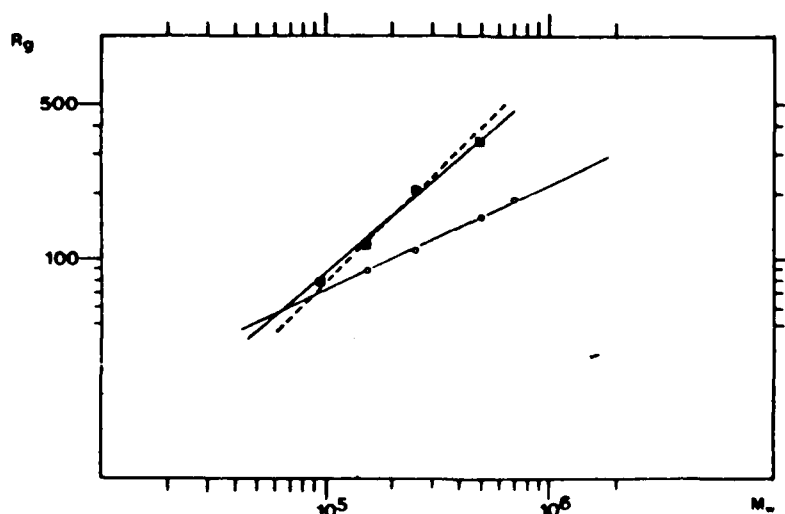


Figure 7

Plot of  $\log R_g$  vs.  $\log M_w$ : (■) Tagged chains in single crystal, (○) amorphous sample molded at 250 °C (previous results available in ref 14). The dotted line stands for theoretical variations derived from relation 5 with  $(l^2)^{1/2} = 12.6$  Å.

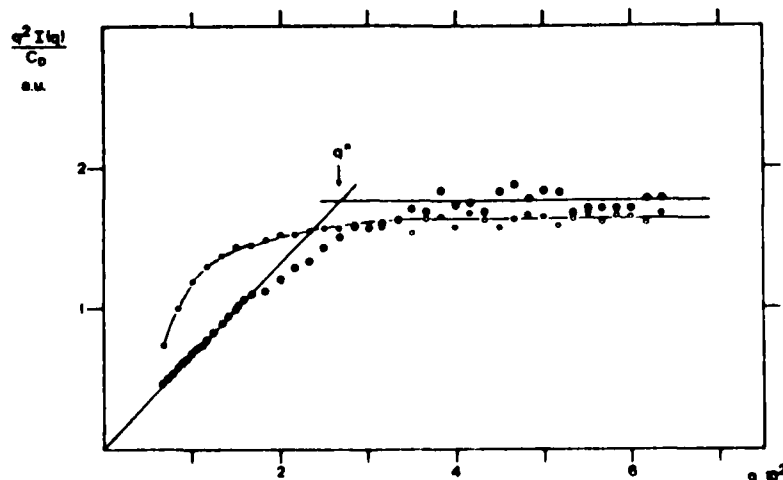
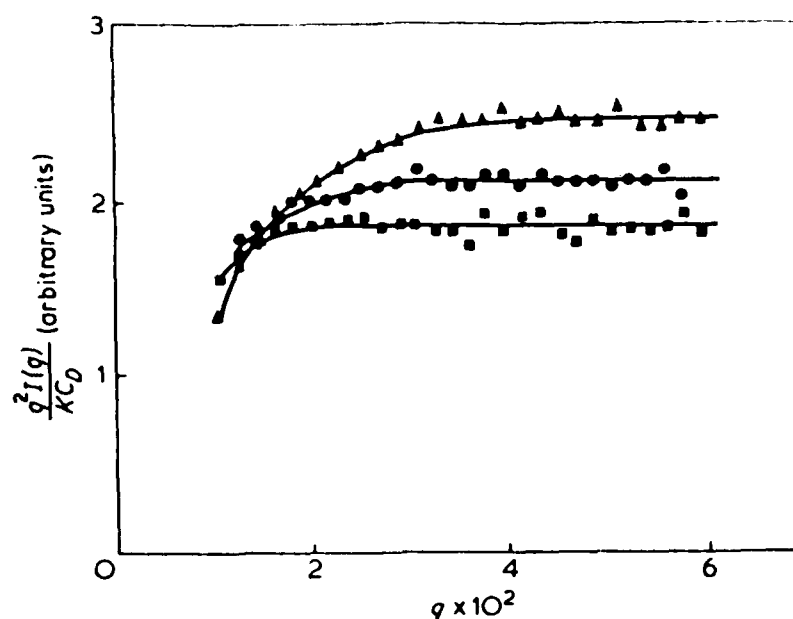


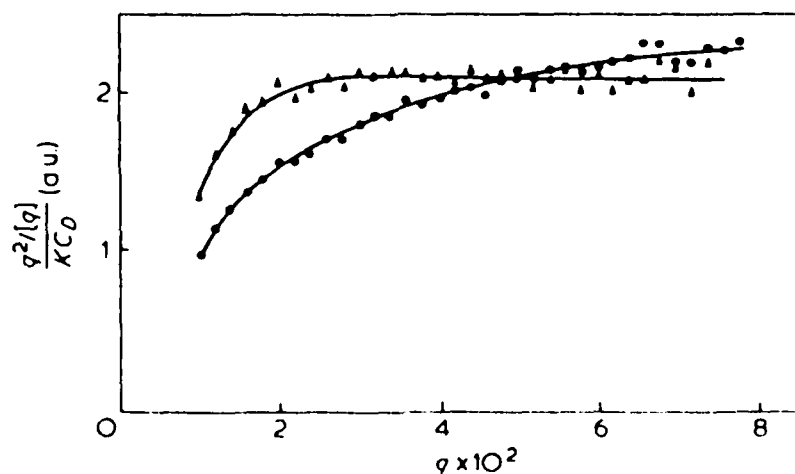
Figure 8

Kratky plot  $q^2 I(q)$  vs.  $q$ . Full and opened circles correspond respectively to single crystal and amorphous samples. In both cases  $M_{w,IPSD} = 5 \times 10^6$ . For  $q < q^*$ ,  $I(q) \sim q^{-1}$ , and for  $q > q^*$ ,  $I(q) \sim q^{-2}$ .



Kratky-plot  $q^2 I(q) / K C_D$  vs.  $q (\text{\AA}^{-1})$  in arbitrary units,  $\blacktriangle$ , 0.35-crystallized sample in IPSH matrix of molecular weight  $M_w = 1.75 \times 10^6$  (From series D);  $\bullet$ , amorphous sample,  $\blacksquare$ , 0.35-crystallized sample in IPSH matrix of molecular weight  $M_w = 4 \times 10^5$  (from series A)

Figure 5.

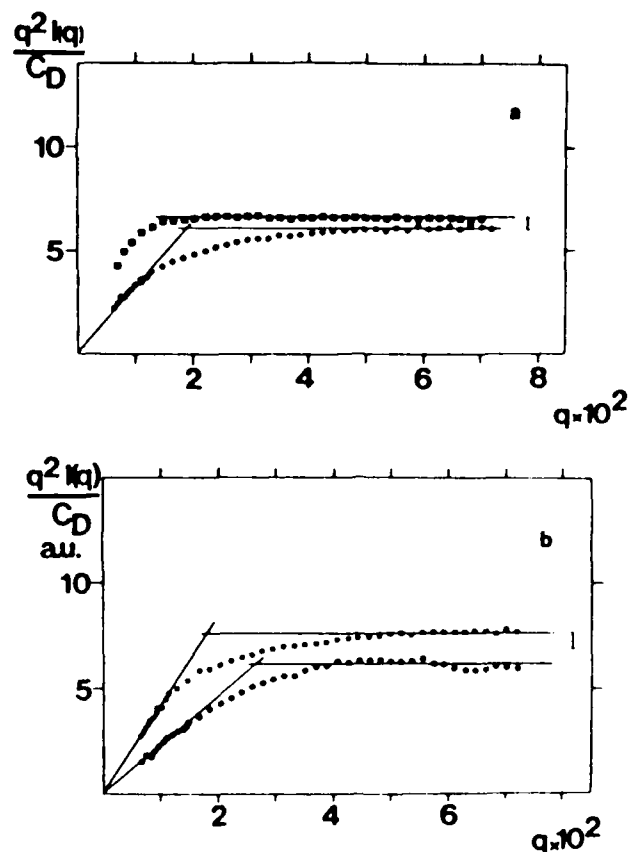


Kratky plot,  $q^2 I(q)$  vs.  $q$ .  $\blacktriangle$ , C-140-HM1,  $\bullet$ , C-140-HM3. In both cases  $M_{wIPSD} = 5 \times 10^5$

Figure 6.

e) Bulk-crystallization at  $T_c = 220^\circ\text{C}$ .

Although crystallization is achieved in the bulk, hexagonal crystals as in dilute solution grow under these conditions. Thermal analysis reveal however a residual content of amorphous chains independent of the crystals. Taking this into account, SANS results giving  $R_g \sim M^{0.78}$  are consistent with a sheet-like conformation as in crystal grown from dilute solution. Data of Fig.9 show the similarities of the intensities scattered in the intermediate range for both type of crystals. As a consequence, regular folding in one lamella is not the prerogative of crystals formed in dilute solutions.



(a) Kratky representation of the reduced intensity in the intermediate range ( $q^2 I(q)/C_D$  vs.  $q$ ). Circles stand for the  $220^\circ\text{C}$  crystallized samples, where  $M_w(\text{IPSD}) = 5 \times 10^5$  (opened circles stand for the highest angles on D11). Black squares stand for  $M_w(\text{IPSD}) = 5 \times 10^5$  in APSH matrix molded at  $220^\circ\text{C}$ . For clarification of the figure the upper curve has been shifted upward by a factor of 1.1. (b) Same representation as Figure 5a. Circles stand for solution-grown single crystals with  $M_w(\text{IPSD}) = 5 \times 10^5$ . Squares stand for  $220^\circ\text{C}$  crystallized sample with  $M_w = 7 \times 10^5$ . The upper curve has been shifted upward by a factor of 1.1 to clarify the figure (opened circles and squares stand for highest angle on D11).

Figure 9.

#### 4. Consistency of the SANS results.

If these results might appear as interesting, they however need be confirmed or at least get support. One way of testing the validity of the interpretation given here is to look into viscoelastic properties. A criterion proposed by Flory<sup>18</sup> can be invoked in that respect. It consists of comparing the long relaxation time  $\tau_m$  of a molecule in the melt to the envelopment time  $\tau_e$  which is defined as the time needed by the crystalline growth front to overlap the molecule ( $\tau_e \sim Rg/G$ ,  $G$  being the radial growth rate). If  $\tau_m < \tau_e$  the chain has time to rearrange so as to fold in a regular way. Conversely, if  $\tau_m > \tau_e$ , only small portions of the chain have time to rearrange leading to an irregular folding ("Garland" model for instance). Applying this criterion to <sup>13</sup>C iPS ( $\tau_m$  have been obtained from long relaxation time of atactic polystyrene) one is led to :

$T_c = 185^\circ\text{C}$	matrix with $M_w = 4.2 \cdot 10^5$	$\tau_m \approx \tau_e$	(ACA)
	" with $M_w = 1.7 \cdot 10^6$	$\tau_m \gg \tau_e$	(Garland)
$T_c = 200^\circ\text{C}$	" with $M_w = 8 \cdot 10^5$	$\tau_m \approx \tau_e$	(ACA)
$T_c = 140^\circ\text{C}$	" with $M_w = 4.2 \cdot 10^5$	$\tau_m > \tau_e$	(Central core)
	" with $M_w = 1.7 \cdot 10^6$	$\tau_m \gg \tau_e$	(Garland)
$T_c = 220^\circ\text{C}$		$\tau_m \ll \tau_e$	(Sheet-like)
Solution grown		$\tau_m \ll \tau_e$	(Sheet-like)

These comparisons support both the neutron scattering results and their interpretation. From this, it can be safely concluded that chain mobility with respect to crystal growth rate determines the chain trajectory. The higher the "mobility", the more regular the chain-folding.

#### CONCLUSION.

Small angle neutron scattering happens to be a powerful tool for investigating polymer conformation in bulk-samples provided that isotopic segregation does not take place. In the case of iPS, the technique has enabled a successful determination of the chain trajectory in a crystalline medium. From this investigation we have been able to show that the competition between the crystal growth rate and the chain mobility in the surrounding melt monitors the final conformation in crystals.

#### REFERENCES.

- 1) P.H. Till, J.Polym.Sci., 17, 447 (1975) ; E.W. Fischer, Z.Natur Forsch., 12a, 753 (1957).
- 2) A. Keller, Phil.Mag., 2, 21 (1957).
- 3) R.G. Kirste, W.A. Kruse and J. Schelten, Makromol.Chem., 162, 299 (1972).
- 4) J.P. Cotton et al., Macromolecules, 7, 863 (1974).
- 5) J. Schelten, G.D. Wignall and D.G.M. Ballard, Polymer, 15, 682 (1974).
- 6) G. Lieser, E.W. Fischer and K. Ibel, J.Polym.Sci., Polym.Lett.Ed., 13, 39 (1975) ; D.M. Sadler and A. Keller, Macromolecules, 10, 1128 (1977).
- 7) See J. of Faraday Discussion n°68, "Order of Macromolecules in the Condensed Phase".
- 8) J.M. Guenet and C. Picot, Polymer, 20, 1483 (1979).
- 9) D.G.M. Ballard, P. Cheshire, C.W. Longman and J. Schelten, Polymer, 19, 379 (1978).
- 10) See for example : J.P. Cotton, B. Farnoux and G. Jannink, J. de Physique, 32, C 5A, 283 (1971).
- 11) F. Boué, M. Nierlich and L. Leibler, Polymer, 23, 29 (1982).
- 12) G. Natta, J.Polym.Sci., 16, 143 (1955).
- 13) J.M. Guenet, Polymer, 21, 1385 (1980).
- 14) J.M. Guenet, Macromolecules, 13, 387 (1980).
- 15) J.M. Guenet and C. Picot, Polymer, 20, 1473 (1979).
- 16) J.M. Guenet, Polymer, 22, 313 (1981).
- 17) J.M. Guenet and C. Picot, Macromolecules, 16, 205 (1983).
- 18) P.J. Flory, and D.Y. Yoon, Nature, 272, 226 (1978).
- 19) S. Suzuki, Thèse Université Strasbourg (1972).

# MOLECULAR EXTENSION AND ORIENTATION IN A CRYSTALLINE POLYMER

D. M. Sadler

Institut Laue-Langevin,  
BP 156X-38042, Grenoble Cedex, France

## Abstract

This paper is centred on the capability offered by neutron scattering and isotope labelling to obtain directly the degree of molecular extension. The method has been successfully applied to a crystalline polymer (polyethylene). Two systems have been selected as extreme cases: viz stretched crystalline material where the molecules both extend and align, and solution grown crystals where, although the chains are again oriented, the molecule is restricted in length to the thickness of the lamellar crystallite.

## Introduction

In crystalline polymers, chain extension has often been inferred from orientation, since until recently only the latter has been accessible experimentally. The distinction between the two is illustrated in Figure 1, where two oriented stacks of lamellae are shown schematically (in two dimensions).

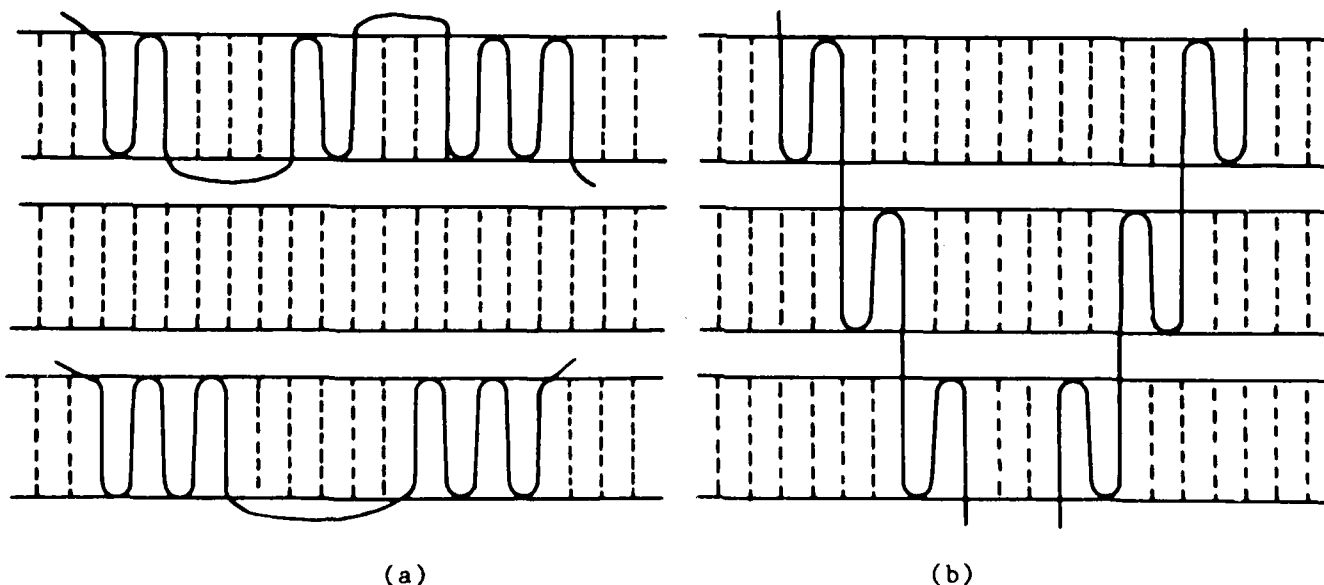


Figure 1. Schematic two dimensional representations of hypothetical single chain conformations in a stack of crystalline lamellae. Broken lines indicate parts of neighbouring molecules. (a) Each molecule participating in only one lamella (b) Each molecule distributed between several lamellae, giving covalent links between lamellae.



Individual chains are indicated by the continuous lines, and parts of other neighbouring molecules by broken ones. In (b) there are links involving covalent main chain bonds between the lamellae, whereas in (a) these are absent, at least as concerns the molecule "labelled" in these diagrams. The properties of (a) and (b) should be very different, in particular how they deform under mechanical load. Neutron scattering using isotope labelling is enabling, for the first time, molecular extension to be measured experimentally so as to distinguish (a) from (b).

Neutron scattering has not been used as a method of routine testing, but is not primarily because of excessive cost. For example, the low angle scattering facility D11 at the Institut Laue Langevin is shared between so many research groups and projects that each of these probably costs no more than one requiring substantial use of electron microscopy. D11 can be hired on a daily basis. Clearly however the logistics involved with an instrument requiring a reactor and a sample-detector distance of 10m is very restrictive. Nevertheless, neutron scattering is relevant to the interpretation of many other techniques, e.g. to assess over what condition there may be a correlation between chain orientation and extension, and this is currently the justification of its consideration for NDE.

The neutron scattering method has been developed over about ten years and has been reviewed elsewhere. Discussion of this basic material will be mainly restricted to a reminder of the degree of information loss involved where imaging is not possible, and where scattering is used as opposed to microscopy. The basic equations are very well understood and can be written in terms of a powerful and flexible Fourier transform formalism. The interference (diffraction) effects in the intensity scattered are obtained by summing scattering contributions over an "assembly" (in the present case this is an individual molecule, see below):

$$nI(q) = \langle \text{Fourier transform } (g(r)) \rangle \quad (1)$$

$$= \text{Fourier transform } (\langle g(r) \rangle) \quad (2)$$

where  $nI(q)$  is the intensity per molecule,  $|q| = 4\pi \sin\theta/\lambda$  where  $2\theta$  is the scattering angle and  $\lambda$  the wavelength, and  $g(r)$  is the (intramolecular) correlation function.  $g(r)$  is most usefully thought of as a histogram of the number of times a separation vector  $r$  occurs between scattering centres (labelled hydrogen atoms in the present case). It is important to realize that although  $g(r)$  contains less information than in a focussed image, there is often still enough to distinguish physically different models. For example, if the stems, corresponding to the crystalline traverses of crystal lamellae, are arranged in rows (e.g. adjacently re-entrant folding)  $g(r)$  is quite different from models where stems are in two dimensional clusters (e.g. fully random folding). Hence the ability to distinguish these two examples is not limited by the lack of imaging lenses.

The averaging indicated by  $\langle \rangle$  includes not only different molecules but different orientations. Averaging over orientations depends on the "texture" of the sample, e.g. isotropic or fibre-like, and most of this paper will be concerned with the latter and the additional information which is available as compared with the former.

The reason why the scattering of individual molecules is accessible is best

expressed as "partial incoherence": scattering contributions from correlations between different molecules cancel if deuterium labelled molecules are mixed randomly with similar unlabelled ones. This is why neutron scattering is unique in separating  $g(r)$  (intramolecular) from  $g(r)$  (intermolecular). For polyethylene isotope mixing is sometimes not entirely random, and the corresponding intermolecular terms at very low  $q$  limit to some degree the experiments possible.

This paper is further restricted to sufficiently small  $q$  that only the overall size of the molecule governs the scattering (the "Guinier" range). The size is expressed as  $R_z$  ( $\equiv \langle z^2 \rangle$  where  $z$  is distance of a D atom from the centre of gravity of the molecule along the fibre axis, axis of symmetry,  $z$ ) and  $R_{xy}$  ( $\equiv \langle x^2 \rangle = \langle y^2 \rangle$  where  $x$  and  $y$  are at right angles to  $z$ ). In this case, by expanding the complex exponentials in the Fourier transform:

$$I(0)/I(q) = 1 + d^2 q^2 \quad (3)$$

where  $d$  is the analogue of  $R_z$  and  $R_{xy}$  along any measurement direction  $q$ . For example,  $R_z$  can be measured directly if intensity data can be collected for  $q$  along  $z$ .

Two examples will now be given for polyethylene corresponding to 1(a) and 1(b): solution grown crystals and fibres respectively.

#### Solution Grown Crystals

Figure 2 shows the model derived a series of experiments not specifically concerned with orientation (Sadler and Keller, 1977, Sadler and Keller, 1979, Spells and Sadler, 1984): (a) shows a folded ribbon along the crystal growth face which folds back on itself ("superfolding"). (b) shows the stems in projection down the chains, showing a statistical preference (of 75%) for adjacent re-entry. A method of analysing oriented samples (Sadler, 1983) has now been developed which can extract  $R_z$  values so as to test an important feature shown in 2(a): the restriction of molecules to single lamellae.

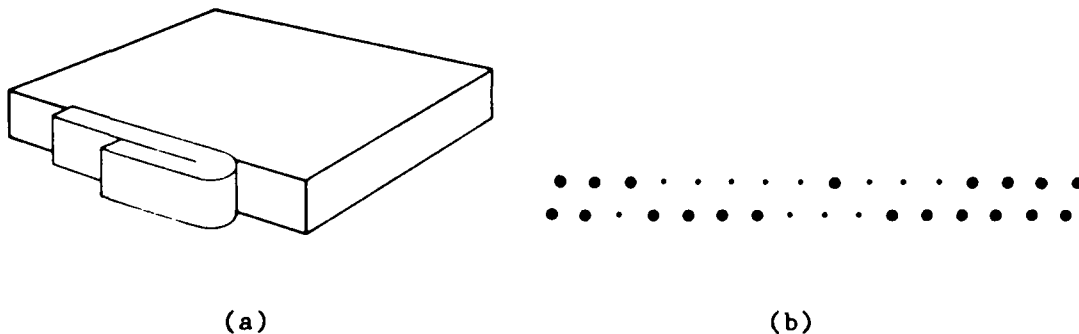


Figure 2. Schematic representations of the conformation in solution grown crystals, based on measurements not specifically concerned with orientation. (a) Perspective view showing the folded ribbon itself folding back (b) projected view down the chains.

The coordinates for displacements from the centre of gravity of a molecule can be expressed using polar coordinates  $|r|$  and  $\beta$  where  $\beta$  is the angle between  $\underline{r}$  and the measurement direction  $\underline{q}$ . The dimension obtained by using plots according to equation (3) depends on distances as projected on to  $\underline{q}$ .

Hence  $\langle r^2 \cos^2 \beta \rangle = d^2$  is accessible experimentally.

This dependence on  $\cos^2 \beta$  recalls the formalism used for optical dichroism.  $\beta$  depends not only on the molecule, but also on the way the platelet crystals are held in the diffractometer and the spread of platelet normals with respect to the symmetry axis of the sample. A concise way to combine these orientation distributions is to make use of order parameters:

$$P_2(\beta) \equiv (3\langle \cos^2 \beta \rangle - 1)/2 \quad (4)$$

For convoluting different orientation distributions together, the corresponding  $P_2$  are simply multiplicative. The result is a linear dependence of  $d^2$  on  $\cos^2 \alpha$ , where  $\alpha$  is the angle between the sample axis and  $\underline{q}$ , and Figure 3 shows two examples of plots.

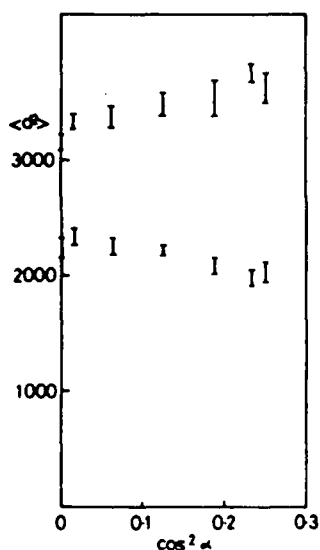
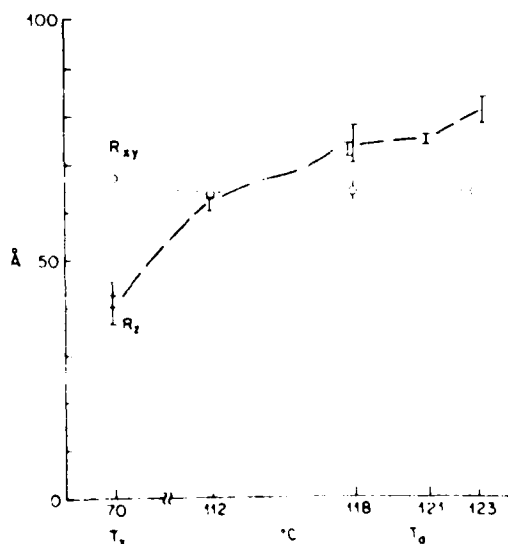


Figure 3. Orientation plot of  $d^2$  (obtained from plots according to equation (3)) versus  $\cos^2 \alpha$  where  $\alpha$  is the angle between the measurement direction and sample axis of symmetry. Molecular weight 90000, crystallization 343K from xylene solution. Upper points: as crystallized, lower points: heat treated at 396K (dry). The 7 independent measurements come from dividing the detector into 15 segments. The error bars are derived assuming  $I(0)$  is independent of  $\alpha$ .

Figure 4. Results of  $R_z$  and  $R_{xy}$  for samples as in Figure 3, versus heat treatment temperature



Three technical points are worth mentioning:  $R_z$  values are accessible even though measurements are not possible along  $z$ ;  $z$  data from the whole of the two dimensional detector can be used (cf. using only horizontal and vertical "slices" on the detector corresponding to  $\cos^2\alpha = 0$  and  $\cos^2\alpha = 0.3$ ); textures with lack of complete orientation are usable. As a result, data with rather low basic precision can be exploited to the full.

The result is rather simple: for crystals as grown  $R_z < R_{xy}$  (lower points in Figure 3) but after heat treatment involving crystal thickening  $R_z > R_{xy}$  (upper points). In both the cases quoted here the  $R_z$  agree with the molecules being in single lamellae, i.e. no interlamellar links as in Figure 1(a). However, when results for a range of heat treatment temperatures are considered (Figure 4) there are  $R_z$  values at intermediate temperatures greater than implied for restriction to single lamellae (e.g. for  $112^\circ\text{C}$  the average lamellar thickness has only increased slightly above the initial,  $70^\circ\text{C}$ , value). The implication is heterogeneity: the rims of crystals, probably D rich, thicken at lower temperatures than the centres. Heterogeneity has been clearly indicated previously. The approximate constancy of  $R_{xy}$  during heat treatment is intriguing and has obvious implications on the mechanism(s) for changes in molecular conformations.

#### Deformation Studies

Another type of analysis, applicable in cases of very high anisotropy has also been developed (Sadler and Barham, 1983). Melt quenched polyethylene was stretched in an Instron tensometer to draw ratios in the range 5-10, so that the samples had tape geometry (i.e. "fibre" axis in the plane of a sheet sample). Figure 5 shows a contour plot of (difference) intensity as recorded on the two dimensional counter (64x64 elements, each 10mm square; here the detector - sample distance was 9.14m and the  $\lambda = 8\text{\AA}$ ).

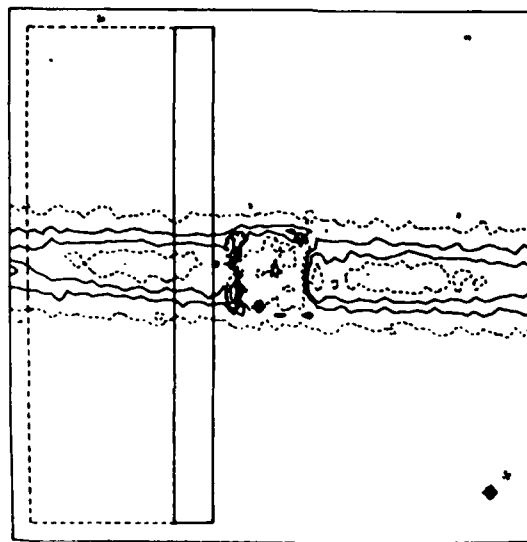


Figure 5. Contour plot of difference intensity for stretched polyethylene (fibre axis vertical, further details given in the text)

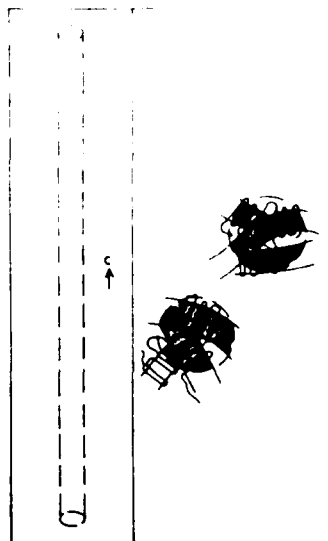


Figure 6. Schematic views of initial conformation prior to deformation of melt quenched crystals, and the approximate shape of the molecular envelope assuming molecular deformation is affine with sample (see text).  $c$  crystal axis is along the chain.

The fibre axis  $z$  is vertical in the diagram and since small  $q$  correlates with large distances, we can see directly that intensities fall quickly with  $q$  along  $z$  (i.e.  $R_z$  is large) but slowly with  $q$  along  $x$  (i.e.  $R_{xy}$  relatively small). For  $R_{xy}$  measurements equation (3) is used for intensities along "x" (horizontal in Figure 5). For  $R_z$  it is not possible to plot intensity through the origin  $q_z = q_x = 0$  (the centre of Figure 5), so we use the approximation that holds good for  $R_z \gg R_{xy}$ , that a plot along  $z$  at finite  $q_x$  (e.g. along rectangles in Figure 5) will give the appropriate  $q_z$  dependence. In this way very high  $R_z$  values are obtainable. For three molecular weights,  $R_{xy}$  decreased approximately as predicted according to molecular deformation being affine with the sample (e.g. for a molecular weight of 62000 the initial "R value" is 100Å whereas the final  $R_{xy}$ , both measured and predicted, was 31Å).  $R_z$  however increases less (to 500Å in the example chosen) than for affine deformation (1000Å).

For a second set of experiments, solution grown crystals were drawn at about 100°C, to draw ratios near x20. In these cases the changes in dimensions are far less than predicted by affine deformation (e.g.  $R_{xy} = 104$ Å compared with 11Å predicted, and  $R_z$  140Å compared with 1000Å). Two explanations are possible for the difference in molecular deformation between melt and solution grown crystals. Firstly, if in the original crystals there are few interlamellar links (Figure 6(a)) the deformation could move the molecules without unduly distorting them (solution grown crystal case). If, however, there are such links even before deformation (Figure 6) then as the crystals distort different parts of the molecules will be pulled apart. Incidentally, the somewhat confused arrangement of bowed crystals shown in Figure 6 is taken from a micrograph of a melt quenched sample, and should be contrasted with the idealized flat parallel lamellae shown in Figure 1 and in many other publications. The second possibility is that the higher temperature used during deformation for solution grown crystals has enabled the molecule to relax during deformation so as not to reach full "affine dimensions". Experiments have been carried out on higher temperatures of deformation for melt grown crystals where the draw ratios are higher. A preliminary analysis suggests that indeed, as expected for the second explanation, the changes in R values for high temperatures are more significantly different from the affine predictions than is the case for cold deformation.

### Conclusions

Neutron scattering using isotope labelling is enabling molecular extension in solid polymer materials to be measured. The relevance to deformation

mechanisms is clear from the discussion above. Although the technique is not likely to become suitable for routine testing, there is a need for more experiments along the lines of the preliminary ones described here. The significance of results from other techniques (e.g. for measuring orientation) can then be used with more confidence in assessing molecular events under various conditions (e.g. as temperature of fabrication is changed).

#### Addendum

Computer simulation studies (Sadler and Gilmer, 1984) are now indicating a new explanation for the why molecular shapes should differ between melt (high temperature) and solution (low temperature) growth. Figure 7 shows the result of such a simulation, showing (left to right) the initial "seed" crystal used, and two crystals after growth with different  $\epsilon/kT$  values, where  $\epsilon$  is the energy of bonding between units (each unit corresponding to several chemical repeats but less than a complete crystal traverse). Both these crystals have fairly rough growth surfaces (pointing towards the bottom left of the diagram). In such cases the fold re-entry would be fairly random, whereas if the growth surface were to be smoother, adjacent re-entry would be promoted. The latter is probably the case for solution growth (Figure 2).

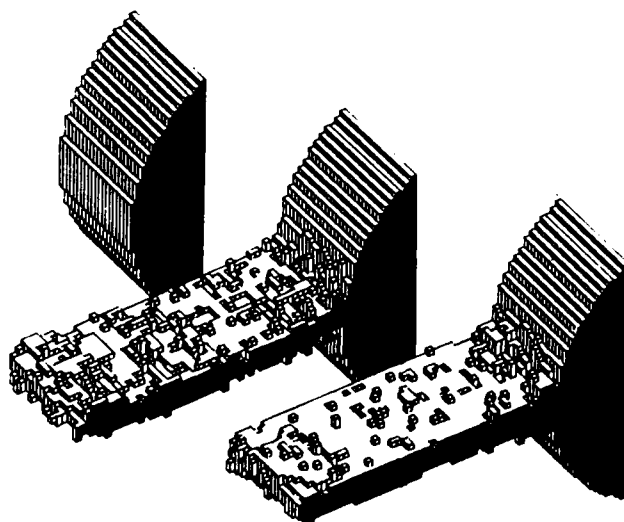


Figure 7. Results of computer simulated crystal growth, with the initial seed on the left. Shaded areas are linked to opposite faces by cyclic boundary conditions. Molecular direction is vertical, with non-crystalline sequences omitted.

#### References

- Spells, S.J. and Sadler, D.M. (1984) *Polymer* 25, 739
- Sadler, D.M. (1983) *J. Appl. Cryst.* 16, 519
- Sadler, D.M. and Gilmer, G.H. (1984) *Polymer* (in press)
- Sadler, D.M. and Barham (1983) *J. Polym. Sci. (Phys. Ed.)* 21, 309
- Sadler, D.M. and Keller, A. (1977) *Macromolecules* 10, 1128
- Sadler, D.M. and Keller, A. (1979) *Science* 203, 263

## Discussion of Session II

It is evident that the nature of certain fabrication defects in polymers can be investigated only by resorting to neutron scattering. When discussing the prohibitively high cost implied by the desirability to subject polymers to neutron scattering, even for specialised polymer components, Dr R E Green Jr pointed out that the US ceramics inspection industry now uses transporter carried neutron sources.

Session III: NDE of laminates



## QUALITY CONTROL AND LIFETIME PREDICTION OF RUBBER FABRIC COMPOSITES

D M Turner, Director,  
New Projects, Avon Rubber plc, Melksham, Wiltshire

### ABSTRACT

The rubber industry has been manufacturing composites from its inception over one hundred years ago. The pneumatic tyre is a highly sophisticated composite where great care is taken to ensure that the fibre reinforcements are precisely located. These and many other products have a high degree of reliability. For a number of reasons NDE techniques have been difficult with rubber so reliability has been attained by attention to manufacturing methods and quality control.

In this paper, as a case history, the problems of design, manufacture and quality control are considered for the very large bearings required by Tension Leg Platforms (TLPs). Currently a multi-layer spherical laminate bearing is being used which does present problems in manufacture and evaluation. An alternative is proposed making use of polyaramid tyre cord where specialised X-ray and ultrasonic techniques developed for the tyre industry may be applied.

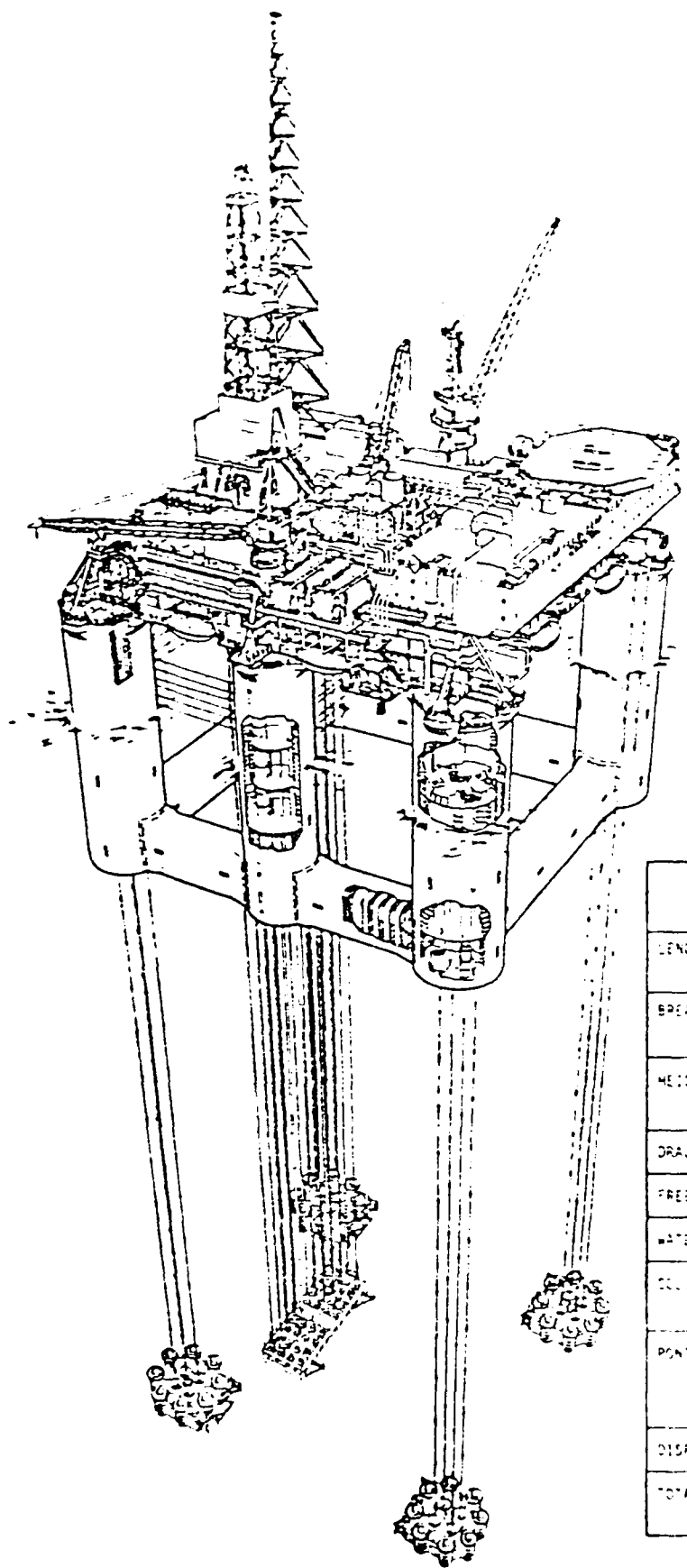
.....

Figure 1 illustrates the layout of the Hutton Tension Leg Platform

Leece M J (1983) 'Hutton TLP Mooring System Flexjoint' Paper presented at 'Rubber in Offshore Engineering' Conference, PRI London 13th April, 1983.

At each corner there are 4 legs which are terminated at each end with a flexible bearing so that the whole rig can respond to wind and tide motion by parallelogram motion. Good working conditions on the platform are provided as the horizontal resonant frequency will be below that of the wave frequency whilst the vertical is above. The total vertical upthrust on the legs is 13,000 tons but allowing for 100 year storms and conditions where one of the legs may be out of action, the maximum load required on an individual leg is 2,400 tons. The maximum angular offset is  $16.6^\circ$ .

The Hutton TLP uses a multi-laminate spherical bearing which is illustrated in Figure 2. The actual bearing is composed of successive layers of stainless steel 6 mm thick and rubber of 4 mm thickness. Bearings of this principle have been used for many years for the blades of helicopters and more recently for the thrusters of space rockets. Thus the knowledge was present to calculate the strains and loadings throughout the bearing and comparisons were available to make realistic predictions of the expected fatigue life.



GEOMETRY		
All dimension to moulded lines		
LENGTH	- Between column centres	78.00 M
	- Overall	95.70 M
BREADTH	- Between column centres	74.00 M
	- Overall	91.70 M
HEIGHT	- Keel to main deck	57.70 M
	- Main deck to weather deck	11.35 M
DRAUGHT	- Operating	30.00 M at L
FREBOARD	- To underside of main deck	24.50 M at L
WATER PLANE	Area	7324.00 M <sup>2</sup>
COLUMN	- 4 Corners	11.10 M Dia
	- 2 Centre	8.50 M Dia
PILON	- Height	11.80 M
	- Width	8.00 M
	- Corner radius	50 M
DISPLACEMENT	Approx	6.50 Tonnes
TOTAL WEIGHT	Including riser tension (Approx)	5910 Tonnes

THE TENSION LEG PLATFORM

FIG 1

# FLY JOINT

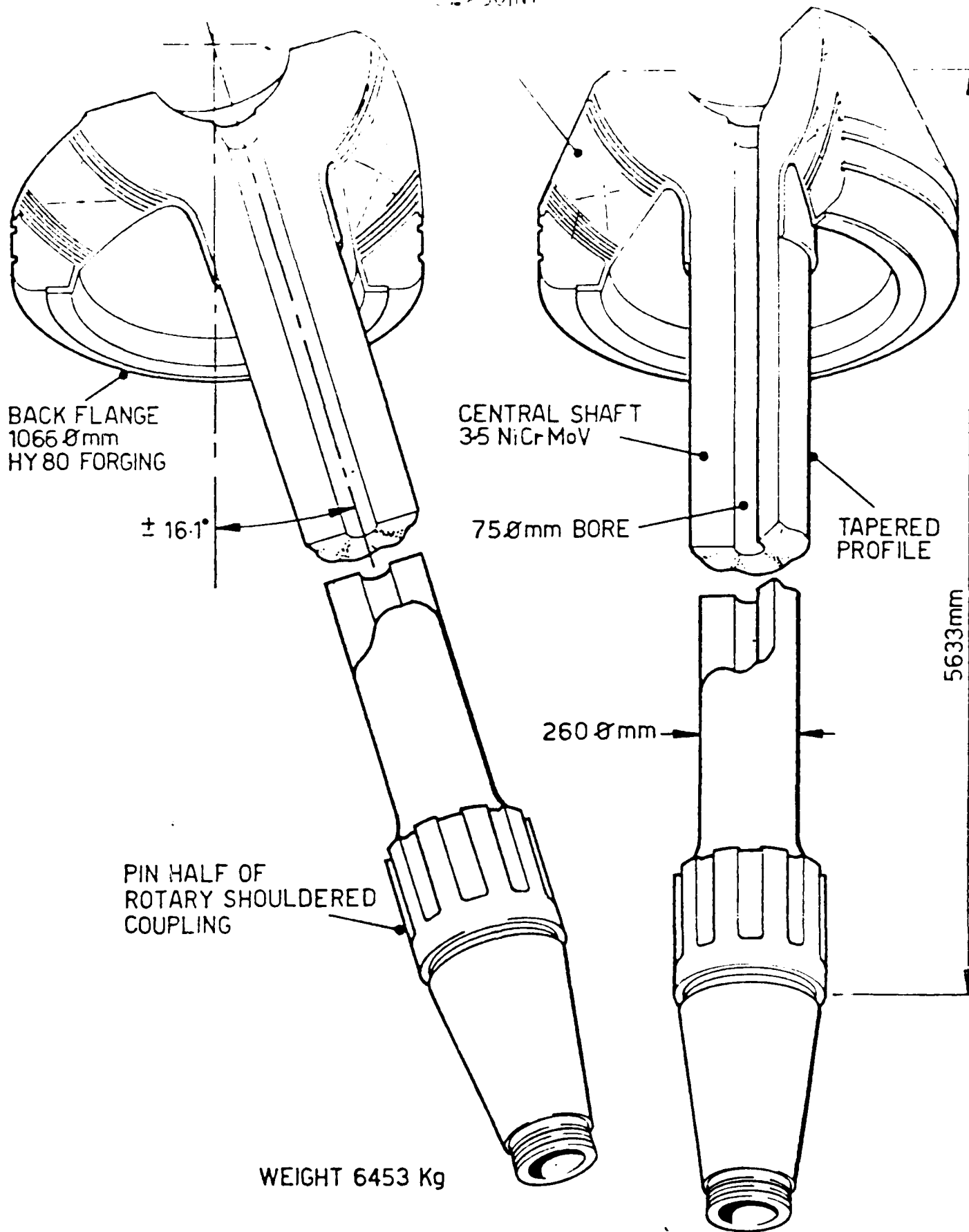


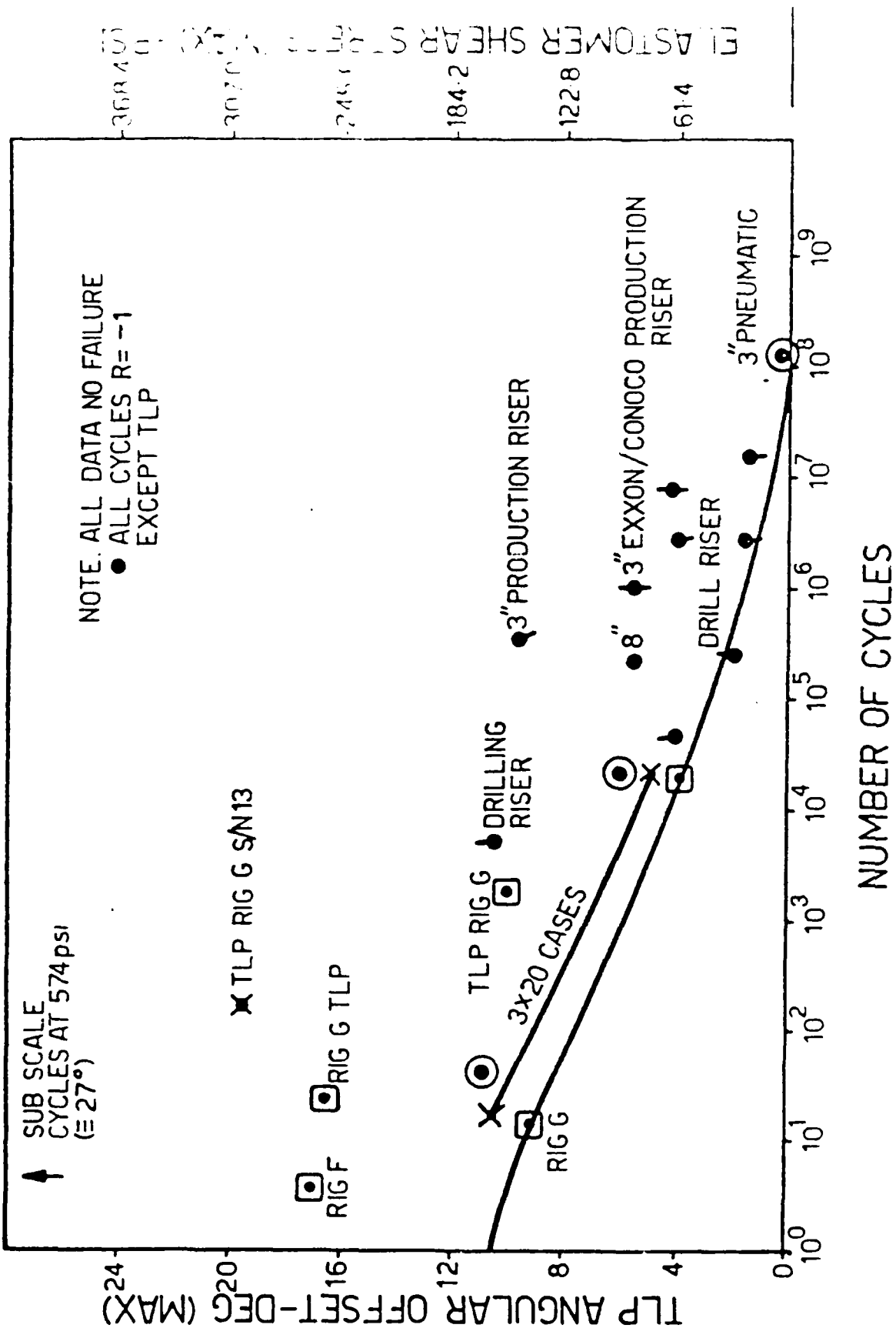
Figure 3 shows some of the results which have been obtained on various rigs and some riser bearings in service which suggest a minimum achievement in number of cycles expected at various angular displacements. By the application of Miner's Rule, this information can be used to predict a life against a history imposed by wave conditions.

The performance of such a product does depend on a good bond between the rubber and the steel. Proprietary bonding agents have been found to be remarkably reliable but in a product such as this where the rubber layers are only 4 mm thick and the individual plates are 350 mm wide and a metre in circumference, it is far from easy to ensure that the rubber is properly distributed to create the correct contact pressure throughout during the moulding process. Any void in the rubber will act as an initiator for crack growth and will upset the distribution of strains in the remaining part of the rubber. Such voids even with the geometry like this can be detected ultrasonically. More difficult, however, is where sufficient rubber was present to prevent the formation of a void but was not sufficient to ensure a satisfactory bond. Ultrasonic methods under these conditions would only be able to locate actual voids, and not incipient weaknesses. For products such as engine mounts for the automotive industry, all bondings are checked with shear loadings 50% greater than they would experience in service and if there was an unbonded area, there would be an increase in deflection. This technique will only eliminate really bad bonds as it is difficult to control the elastic modulus of rubber to better than 6% so that only bondings with unbonded areas of greater than 10% of the total are likely to be detected. After such tests the products are inspected closely to see whether there are any cracks on the surface as in fact the stresses are going to be highest at the edges. Elimination of products even with the smallest of cracks on the surface is justified and it does ensure maintenance of a reasonable quality level.

Because of the reported difficulties with the spherical laminated bearing, Avon Rubber plc decided to investigate the possibility of a different concept of bearing making use of polyaramid tyre cord. The essential features seen in Figure 4 are:

- 1 The main body of the bearing which is effectively a tube composed of plies of polyaramid tyre cord set at an angle of 25° to the axis but in alternating directions.
- 2 A large and a small diameter termination which transfer the tensions in the tube to the internal and external rings or members.
- 3 A core which creates the necessary pressure to prevent the tube from collapsing under the external tension.

It can be shown that such a bearing under tension will deflect exponentially with the line of action of the tension being close to the centre line at the small end and still being within the base of the bearing at the large end. The principle of asymmetric ends was chosen on the grounds for a viable production process which enables the tube to be built and cured on a mandrel and then permit the

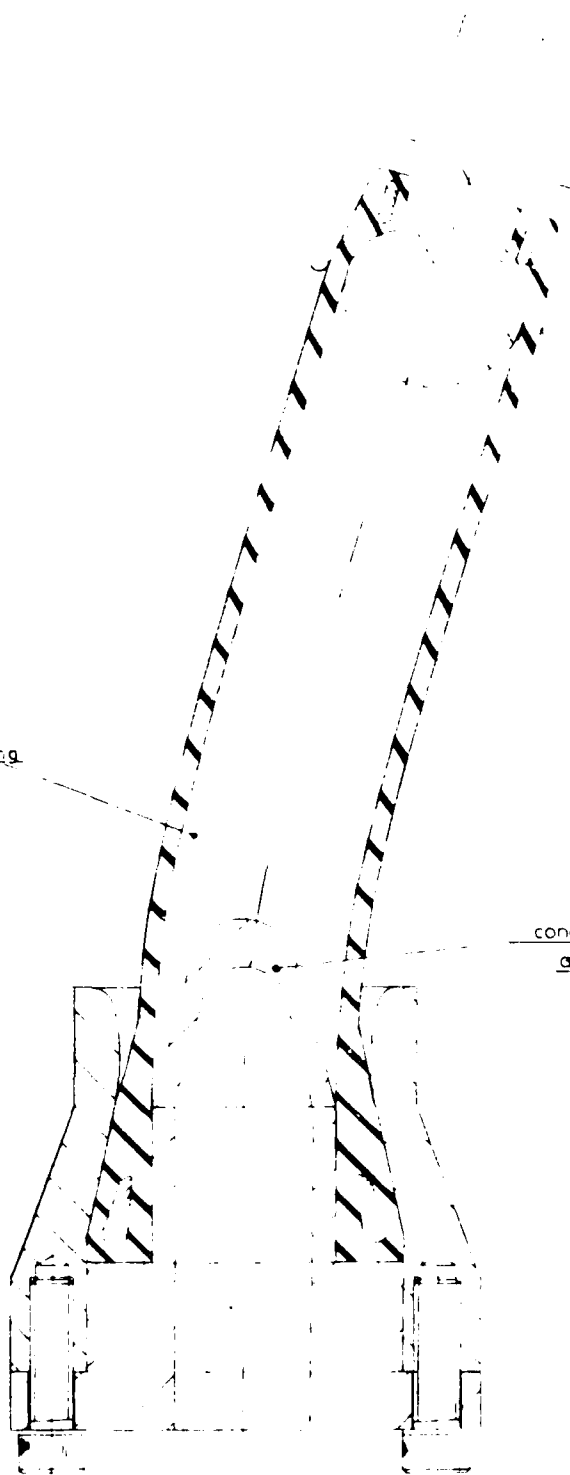


FATIGUE LIFE EXPERIENCE DIAGRAM

ANGLE OF TILT = 17°

solid rubber filling

cone to control curvature  
at base



# HELICAL TENSION LINK

prototype model

The copyright in this drawing is the property of Avon Tyres Limited. It must not be copied, used or copied in whole or in part or used as a basis for any other drawing or other work reproduced in any material form whatsoever without the consent in writing of Avon Tyres Limited. It is the property of Avon Tyres Limited and must be returned to them on demand.

**AVON**  
DESIGN  
DEPARTMENT

SCALE full size  
Dwg. 4-1182 by  
2/107

AD-A153 204

PROCEEDINGS OF THE WORKSHOP ON NDE OF POLYMERS HELD AT  
VIMEIRO PORTUGAL ON 4-5 SEPTEMBER 1984(U) BRISTOL UNIV  
(ENGLAND) H H WILLS PHYSICS LAB 05 SEP 84

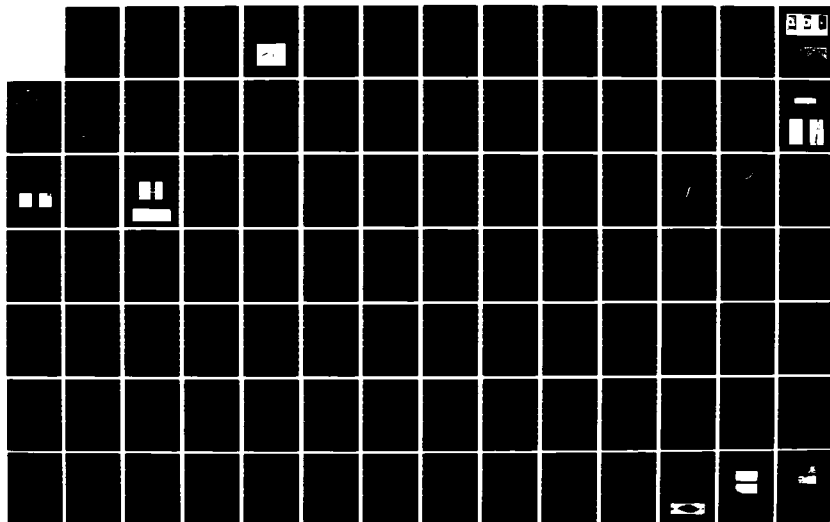
2140

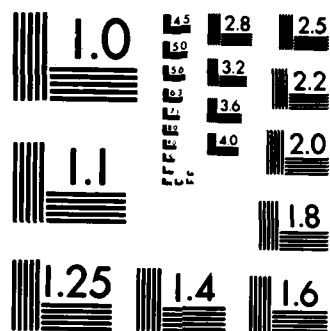
UNCLASSIFIED

DAJA45-84-M-0182

F/G 11/9

NL





MICROCOPY RESOLUTION TEST CHART  
NATIONAL BUREAU OF STANDARDS-1963-A



mandrel to be withdrawn.

A development programme has been proceeding on a small scale model tube of 55mm diameter. The intention is to complete a dynamic programme so that the fatigue lives can be determined for various strain levels. The actual test programme consists of applying 20% extensions to gas filled tubes set at a pressure to give the required loading. The results from this can be related bending as of course bending involves compression on one side and extension on the other.

The first part of a programme was to establish a specification which could withstand a 9 ton static load. In fact to achieve this, considerable attention had to be paid to the shape of the ring in the small end and Figure 5 shows the progressive evolution of the design. It was originally thought that the greatest interaction between the ring and the cord would be at the top end but in fact the more important factor was the high compression set up between the bead ring and the inner termination and progressive increases in the ring radius led to 9 tons being achieved consistently. The next feature which emerged was that if the load was held at 9 tons, failures would occur after a few minutes. Reducing the load to 8 tons produced failures in between 10 minutes and 1 hour.

This brought home the realisation that polyaramid cord behaves like conventional plastic materials and has a time dependent strength. Thus the dynamic programme could only commence at loads which were below those which would be influenced by the static loading. Lives are now being obtained at 5 ton and 4 ton loadings. Lower loadings would involve tests lasting several weeks. This example underlines the difficulty in establishing reliable SN data. If it is assumed that the shape of the curve is similar to that obtained from rubber fatigue testing where, in particular, small amplitude cycles have negligible fatigue effects, some reasonable estimates can be made of the life. In Table 1 a prediction is made for the life of an extensible mooring tube of similar construction to the tension link.

TABLE 1

<u>EXTENSION</u>	<u>FATIGUE LIFE OF RUBBER</u>	<u>NO OF CYCLES IN RANGE</u>	<u>1/1000's OF FATIGUE LIFE USED</u>
8	6 E 8	1.5 E 5	.25
10	1 E 8	6 E 4	.6
12	1.3 E 7	3 E 4	2.26
14	4 E 6	1 E 4	2.50
16	1.7 E 6	3 E 3	1.76
18	8 E 5	8 E 2	1.0
20	4 E 5	1.8 E 2	.45
22	2.5 E 5	3 E 1	.12
24	1.6 E 5	6 E 0	.04
26	1 E 5	1 E 0	.01

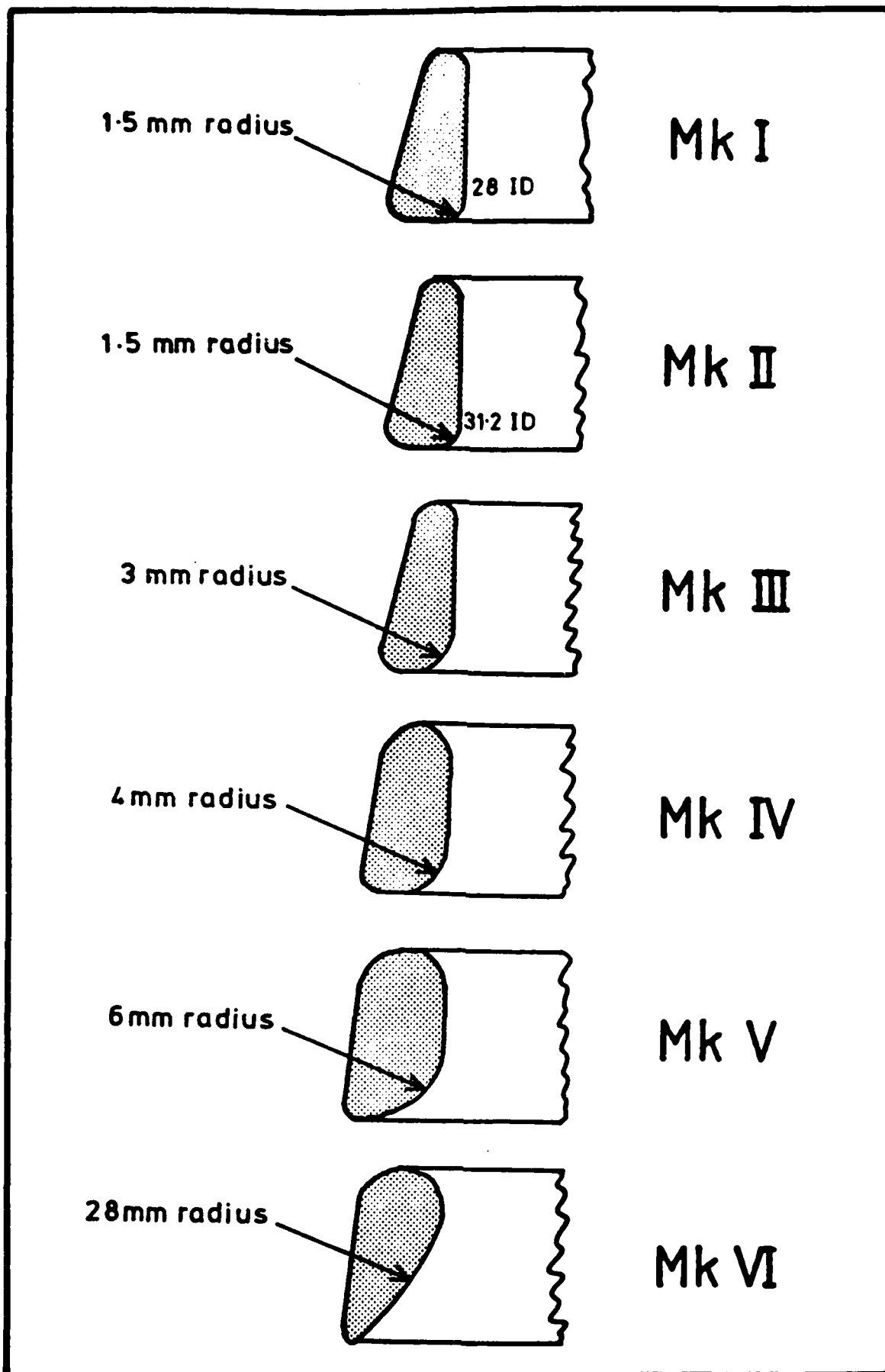


Figure 5: Development of the small bead ring.

The above Table shows the expected fatigue life of rubber under the strain imposed by the stated extension of the tube related to the number of cycles experienced in service at that extension in the course of one year. The proportions of the fatigue life used are summed to give 8.9/1000 which is equivalent to a life of 111 years.

The philosophy of the manufacturing process will be similar to that used in tyres where great care is taken to ensure that the textile or steel reinforcement is placed exactly where it is required. The basic material which consists of unidirectional cords embedded in rubber is amenable to precise location during the building process and in the case of a large bearing, the correct application of the material would be checked layer by layer. The curing process should not encourage any movement of the cord and material. In the curing of tyres it is also hoped that cords do not shift position but, in fact, some movement does occur. Factories making steel radial tyres are all nowadays equipped with X-ray equipment. Monsanto manufacture a specialised X-ray system where the emitter can be placed inside the tyre. Successive portions of the tyre are scanned by rotation of the tyre and the images presented on a television monitor. Figure 6 is the X-ray picture of a test piece containing all the normal types of tyre reinforcements.

No 2

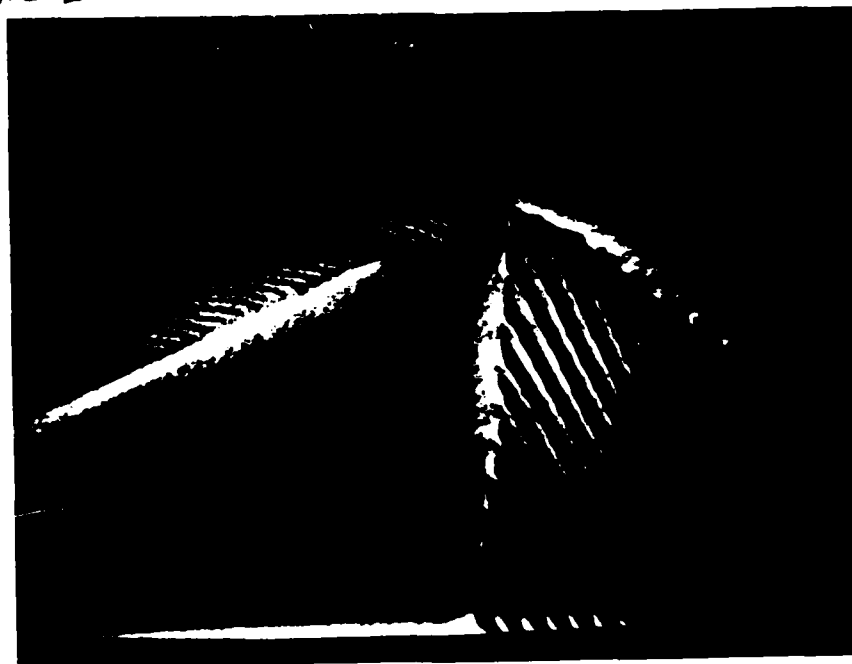


Fig. 6 This is a test piece called a pie with a sample of all the common materials used for tyre reinforcement sandwiched in a tread compound. It gives some indication of how well a system can resolve these materials. Clockwise, starting at bottom right the materials are: 1 Steel, 2 Rayon, 3 Kevlar (Aramid), 4 Fibreglass, 5 Polyester, 6 Nylon.

Clearly there is extremely good resolution for the steel cord and glass fibre and reasonable resolution for the aramid and nylon. The technique has no difficulty in identifying some of the faults which occur with radial tyres such as open splices or distorted cord paths.

A major difficulty with using ultrasonics on rubber components has been the presence of a large number of fine air bubbles on the rubber surface during immersion in water. Sonatest Schlumberger have overcome this by developing a dry coupling system using PVC covered wheels as transmitters and receivers. Thus a tyre can be set up with the wheels located at selected positions on the tyre and then the whole tyre scanned by rotation. 125 MHz is used in short pulses which permits resolution of defects down to 1 mm in size. With this technique it is evident that any small areas of separation or lack of bond can be detected between the rubber surface and the outer ply. Once the basic technique can be made to work then many developments are possible by computer processing of the received signals which can lead to ultrasonics providing valuable information on the integrity of a full scale multi-ply tube.

#### CONCLUSION

The purpose of this paper has been to examine some of the design and quality control requirements for two products which typify the new uses of rubber components in the offshore market. The main quality problems will be solved by the traditional approach to ensure that all constituents have been correctly prepared and are positioned accurately during assembly. However, the industry is continually examining new techniques such as X-rays and ultrasonics where current development activity will improve the interpretation of results and the engineering development permits their use in the production line.

The work on the Helical Tension Link has been assisted by a grant from the Department of Energy.

# Feasibility of Useful Real-time In-process Evaluation of Laminates

by  
Kenneth L. Reifsnider

Reynolds Metals Professor  
of Engineering Science and Mechanics  
Virginia Polytechnic Institute and State University  
Blacksburg, Virginia 24061-4899 USA

## Abstract

Composite materials are not ideal materials in the classical sense, i.e., they are anisotropic, nonuniform and inhomogeneous. This situation is further complicated by the fact that these materials are usually used in laminar form with different layers having different properties in a given direction. Consequently, when these materials are loaded, the damage development process is very complex, consisting of a variety of combinations of damage events such as cracking, debonding, micro-flaw growth and internal stress redistribution. It is generally not possible to characterize these events or the combinations thereof as a real or effective single through crack, as one might do for common metals. Therefore, it is not possible to follow the damage development process by measuring something as simple as a single crack length. The present paper describes three experimental methods which can be used to follow and quantitatively characterize the severity and extent of damage development, in real-time, in composite laminates. Moreover, these methods are chosen because of their relationship to the physics and mechanics of the damage development process and the subsequent mechanical properties of the laminates. The methods are vibrothermography, tensor stiffness change, and ultrasonic stress wave analysis. Concepts, applications and feasibility of in-process use will be discussed.

## Vibrothermography

We will be concerned below with thermographic techniques which depend upon the manner in which materials dissipate energy during mechanical excitation. In particular, we will address the method called "vibrothermography", a term coined by the authors to describe the concept and related techniques whereby the internal integrity and uniformity of materials and components is interrogated by observing the heat pattern produced by the energy dissipation which occurs when a specific vibratory excitation is applied to the test piece. Vibrothermography, then, consists of the study of thermographic (heat) patterns which are recorded or observed in-process during such an excitation. It has been observed that the details of the mechanisms which produce such dissipative heat are directly related to the mechanisms of material deformation and degradation in several important ways, a fact that provides the basis for the use of the scheme as a nondestructive test and evaluation method and general philosophy. This technique was introduced in 1974 by Reifsnider and Stinchcomb and is unique in the sense that it uses heat patterns produced by the specimen itself rather than introduced from an outside source. The heat so produced under cyclic loading is proportional to the energy dissipated by the material at each point which is, in turn, proportional to the material deformation at that point. Hence, it is possible to

determine the severity and distribution of damage by observing the severity and distribution of local deformation as indicated by the heat pattern [1-3]. An example is provided by Fig. 1 which shows progressive heat patterns developed in a notched graphite/epoxy specimen under cyclic loading at three different times during the loading process. The heat patterns do not provide a description of each individual damage site or event, but rather describes the cumulative damage in some local region and its collective effect. In that sense, vibrothermography provides an interpretation of the complex damage patterns. As is the case for many nondestructive test techniques, a major challenge is the specific interpretation of the thermographic heat patterns in terms of strength and life. This interpretation requires that precise associations be made between the heat patterns that are produced and the micro-states of stress and states of material that control the strength of the laminate and correspond to the heat patterns observed. Efforts to make such associations are underway. An example is provided by Fig. 2 which shows a super-position of ultrasonic C-scan inspection (gray and black) and vibrothermographic inspection (white isotherm lines indicating degree C rise over reference temperature) of a random fiber glass/epoxy sheet molding compound specimen with a region of delamination on the right-hand edge. We have found that internal free surfaces such as delaminated sites provide major sources of energy dissipation under cyclic loading; vibrothermography is an excellent method to locate and characterize such delaminations. However, a major part of the energy dissipation in many polymeric matrix materials is also due to viscoelastic nonlinearity in the constitutive behavior so that local gradients and stress fields caused by damage disruptions of integrity of the specimen are also potential sources of heat.

One of the particular advantages of vibrothermography is its ease of applicability to large-scale structural examinations. An example of this is provided in Fig. 3 which is a thermographic pattern observed during the cyclic loading of a full-scale rotor blade which was about 3' wide and 30' long. The image of the rotor blade runs from the lower left to upper right of the photograph and a pattern of increased heat is shown by the elliptical image shown in the center of the picture. This pattern was observed in the early part of the life of the blade at a time when no other nondestructive testing technique indicated that damage had occurred. Subsequent loading produced failure of the blade in this location. Hence, vibrothermographic techniques are quite applicable to full-scale and in-process monitoring of damage development in composite laminates and components.

### Stiffness Change Methods

The notion of stiffness is the fundamental idea on which the concept of elasticity was constructed by Robert Hooke in the mid sixteen-hundreds. The corresponding mathematical statement followed the definition of stress and strain by Augustin Cauchy in the early eighteen-hundreds and the introduction of an elastic constant of proportionality by Thomas Young in 1807. (References 4-6 treat various details of related history.) While the idea of a "modulus of elasticity" as a material property is defined by the elastic stress-strain relationship known as Hooke's Law, the concept of stiffness is usually more broadly interpreted to include the load-displacement record of response of a specimen or component. No other concept is more basic to the mechanical response of materials. The

interpretation, measurement and understanding of stiffness has been developed over more than 330 years.

The idea of relating stiffness to the internal integrity of materials, and to the process of damage development when a component is subjected to continuing load histories is a much more recent concept. (Some details can be found in a summary article by O'Brien [7]. Salkind, et al., appears to be the first investigator to discuss stiffness change during fatigue loading as a characteristic of composite materials [8-9]. In the early 1970's the present investigators reported large stiffness changes in notched composite specimens (both polymer and metal matrix systems) and associated those changes with damage zone development, acoustic emission, heat emission, fatigue life and residual strength [10-15]. Over the last several years, the present authors have conducted a number of investigations which specifically focus on the association of stiffness change with damage development in composite laminates [16-20]. The results of those investigations will form the basis for the present discussion.

Figure 4 shows three illustrative examples of stiffness change during fatigue loading taken from Ref. [21]. Curve A for a  $[0,90_2]_s$  laminate cycled at a maximum stress of 67% of the static strength in a tension-tension test shows an initial drop in stiffness associated primarily with matrix cracking. The same type of change occurs for curve B (which is from a test of a  $[0,90,\pm 45]_s$  laminate) and curve C (for a  $[0,\pm 45]_s$  laminate) cycled at the same relative amplitudes. There is also a second range wherein very little additional damage or stiffness change is observed in curves A and B but edge delamination in the quasi-isotropic laminate is revealed by stiffness change in that region for curve B. In later stages, longitudinal splitting of  $0^\circ$  plies causes step reductions in curve A, delamination causes further reductions in curve B, and the final coalescence of damage causes a very abrupt drop in curve C. These associations of stiffness change with microdamage development events, which was established in the investigation reported in Ref. [21], provide an excellent foundation for the interpretation of stiffness changes during in-process monitoring in a quantitative way. In fact, stiffness changes can be used to determine the collective effect of complex patterns of microevents on the global response of a component as we will show with a few examples below.

The stiffness response of a unidirectional reinforced composite lamina can be characterized by four independent in-plane constants, the tensor stiffness values. When the continuity of the material is interrupted by matrix cracking, debonding, fiber fracture, and combinations of damage events the lamina becomes more compliant. The specific type of damage is reflected in the specific type of changes induced in each of the tensor stiffness moduli. The amount of damage is indicated by the amount of the stiffness changes. An example of this latter fact is provided by Fig. 5. That figure shows the changes observed in the axial stiffness of a cross-ply glass/epoxy laminate induced by cyclic loading as a function of the number of cracks observed in the  $90^\circ$  plies. The monotonic decrease (which is nicely matched by our analysis) appears to be bounded by a simple estimation obtained from laminate analysis by discounting the in-plane shear modulus and transverse stiffness of the broken plies. The amount of stiffness caused by matrix cracking or other damage modes is directly controlled by the nature and amount of local stress

redistribution associated with the damage event. For commonly used engineering laminates, for example, damage modes such as matrix cracking and delamination may be fairly pervasive and influence significant volumes of material, causing substantial stiffness changes which are easily measured and monitored. However, fiber fractures tend to be relatively isolated in small volumes of material throughout a major part of the life of the specimen and are generally associated with relatively little global stiffness variation.

Perhaps the most important aspect of the use of stiffness change as an indicator of fatigue damage development is the power of interpretation associated with the concept. While it is not clear how information from many other nondestructive measurement schemes should be used to anticipate strength and life, stiffness is more directly associated with those ideas. Any analysis of stress states involves stiffness components as a direct input. Also, micro-mechanical models of damage events can be used to directly associate global specimen stiffness changes with the remaining strength of the laminate by calculating the local stress redistribution associated with the damage event. Since fatigue life is defined by the incidence of identity between the residual strength and the applied stress amplitude, such a scheme can also be used to predict fatigue life. The author has recently developed a cumulative damage theory which uses such a model [22].

It should also be mentioned that changes in other components of the stiffness tensor may be larger and more useful than the load-direction modulus. Highsmith, et al., have shown that changes of 74% are predicted and observed in cross-ply glass/epoxy laminates, for example [23]. Large changes in other in-plane and bending stiffness values were also predicted and observed.

### **Stress Wave Analysis**

Ultrasonic test methods have traditionally played a major role in the field of nondestructive testing and evaluation. Ultrasonic waves have the capability to travel through materials in a manner which is sensitive to the integrity and the anisotropy of the constituents and the boundary geometry of the component. While the complexity of the constituent phases and their boundaries (and the damage states that develop in such materials) greatly complicate the mechanics of stress wave propagation, nondestructive testing and evaluation techniques based on the interpretation of such propagation generally provide highly sensitive and very practical methods of investigating such materials.

One such method, to be discussed here, was originally suggested and described by Vary [24-26]. The technique employs both a sending and a receiving ultrasonic transducer that are in contact with the same surface of the object being examined as shown in Fig. 6. A train of ultrasonic pulses is introduced into the specimen and the resultant stress wave detected by a receiver. A number of oscillations received in a period of time which have an amplitude which exceeds a specified threshold value is used to define a "stress wave factor" (SWF) which is a product of the oscillation count, the total time of counting, and the repetition rate of the sending transducer as shown in Fig. 6. Hence, the principle of operation of the device depends upon the manner in which acoustic energy is transmitted from the sending to the receiving transducer. As a



consequence, the technique is particularly sensitive to the internal microstructure of the constituent phases of the composite material, lamina interfaces between plies of a laminate, and the properties of the composite materials in each ply of a laminate including the anisotropic nature and orientation of those plies. It should be noted that it is possible to interrogate composite materials in various directions which may be of special interest because of specific loading or material characteristics. In the intuitive sense, it is clear that "poor" material will be a "poor" conductor of acoustic energy from one transducer to the other. As is frequently the case for nondestructive test methods, the difficulty lies in attempting to be more precise and quantitative about the influence of material properties and arrangements on the energy transmission process; it is especially difficult to anticipate the absolute value of changes in the amplitude of a transmitted stress wave caused by specific types of changes in material properties and arrangement. While continuing progress is being made in this area, we will be satisfied at this writing with descriptions of relative changes and comparisons.

As suggested by the arrangement shown in Fig. 6, the SWF is quite convenient for practical applications. The method requires access to only one surface of the material to be examined. Transducers may be permanently fixed or moved about to examine various areas. In-process monitoring requires only that adequate recording and interpretation instrumentation be available.

The type of information that can be obtained with this technique is illustrated by Fig. 7. That figure shows comparison data for stress wave changes and stiffness changes observed during the cyclic loading of a quasi-isotropic graphite epoxy laminate. As we explain in a previous section, stiffness changes are reliable quantitative indicators of damage development during fatigue loading. For the particular test shown in Fig. 7, a stiffness change of about 15% was observed over the 70,000 cycle life of that laminate. However, the SWF recorded during the same damage development process showed a change of over 90% for the experimental arrangements and conditions used for that test. Figure 7 represents a typical experience, the SWF is extremely sensitive to damage development in composite laminates and provides an excellent in-process method of monitoring such development.

Another important point can be made with the data shown in Fig. 7. Stress wave propagation in materials is controlled by the same tensor stiffness quantities that we have shown can be used as damage monitors in composite materials. Hence, one would expect, for example, to be able to obtain independent indications of material integrity in different directions in an anisotropic material by making independent measurements of the SWF in those directions. It is indeed so. However, it should also be noted that the transmission of stress wave energy from one transducer to another depends more strongly on material volumes close to the surface of the specimen being examined than it does on material elements further into the bulk of the specimen. Hence, the technique is best exploited for use on relatively thin laminates.

Instead of holding the sending and receiving transducers in one position to measure changes in the properties of that region over a period of time as shown in Fig. 7, it is also possible to make comparative readings over

an area of material at a given instant of time as shown in Fig. 8. The glass epoxy cross-ply laminate used for that series of measurements eventually fractured in the position shown by the shaded region at the bottom left of the figure. It is seen that the SWF had a low value (poor energy transmission) in that area, although the SWF data were recorded before the specimen was loaded. This peculiar, and somewhat unique, characteristic ability to locate a region which eventually is associated with the fracture event appears to be related to the fundamental association of this technique with local stiffness values [27]. This conclusion was reached by employing the technique of moire interferometry to obtain the full-field in-plane axial displacement as a function of position along the length of a specimen during quasi-static tensile loading.

In summary, the stress wave analysis technique as described in the above paragraphs is a highly practical in-process method which can provide reliable comparison data concerning the initial and eventual condition of composite laminates which is highly sensitive to constituent properties, orientations, and geometries and well correlated with performance.

### References

1. Reifsnider, K. L., Henneke, E. G. II and Stinchcomb, W. W., "The Mechanics of Vibrothermography," in Mechanics of Nondestructive Testing, W. W. Stinchcomb, Ed., (Plenum Press, 1980) pp. 249-276.
2. Reifsnider, K. L. and Williams, R. S., "Determination of Fatigue-Related Heat Emission in Composite Materials," J. of Experimental Mechanics 14, no. 12 (1974) pp. 479-485.
3. Reifsnider, K. L., Henneke, E. G., Stinchcomb, W. W. and Duke, J. C., "Damage Mechanics and NDE of Composite Laminates", Mechanics of Composite Materials, Z. Hashin and C. T. Herakovich, Eds. (Pergamon Press, New York, 1983) pp. 399-420.
4. Love, A. E. H., The Mathematical Theory of Elasticity, (Cambridge University Press, 1 ed. 1892, 1893; 4th ed. 1927). Reprinted (Dover Publications, New York, 1944), pp. 1-31.
5. Westergaard, H. M., Theory of Elasticity and Plasticity, (Harvard University Press, Cambridge, MA, 1952), Chapter 2.
6. Timoshenko, S. P., History of Strength of Materials, (McGraw Hill, New York, 1953).
7. O'Brien, T. K., "Stiffness Change as a Nondestructive Damage Measurement," Mechanics of Nondestructive Testing, W. W. Stinchcomb, ed., (Plenum Press, New York, 1980), pp. 101-121.
8. Salkind, M. J., "Fatigue of Composite Materials," Composite Materials: Testing and Design (Second Conf.), ASTM STP-497, (American Society for Testing and Materials, Philadelphia, PA, 1972).
9. Nevadunsky, T. T., Lucas, T. T. and Salkind, M. J., "Early Fatigue Damage Detection in Composite Materials," J. Composite Materials 9, (1975), p. 394.
10. Reifsnider, K. L., Stinchcomb, W., Williams, R. and Marcus, L., "Heat Generation in Composite Materials During Fatigue Loading," VPI-E-73-21, May 1973, (AFOSR TR-73-1961).
11. Reifsnider, K. L., Stinchcomb, W., Marcus, L. and Williams, R., "Effects of Cyclic Frequency on the Mechanical Properties of Composite Materials," VPI-E-73-25, June 1973, (AFOSR TR-73-1907).

12. Reifsnider, K. L., Stinchcomb, W. W., Williams, R. S. and Turgay, H., "Influence of Cyclic Frequency on Composite Fatigue Reliability," AFOSR-TR-74-1201, May 1974.
13. Reifsnider, K. L., Stinchcomb, W. W., Williams, R. S. and Turgay, H. M., "Frequency Effects on Flawed Composite Fatigue Reliability," Composite Reliability ASTM STP 580, (American Society for Testing and Materials, Oct. 1975), pp. 425-442.
14. Williams, R. S. and Reifsnider, K. L., "Investigation of Acoustic Emission During Fatigue Loading of Composite Specimens," J. Composite Mat'l's, 8, (Oct. 1974), pp. 340-355.
15. Williams, R. S. and Reifsnider, K. L., "Determination of Fatigue-Related Heat Emission in Composite Materials," J. of Experimental Mechanics 14, no. 12, (1974), pp. 479-485.
16. Reifsnider, K. L. and Highsmith, A. L., "The Relationship of Stiffness Changes in Composite Laminates to Fracture-Related Damage Mechanisms," Proc. 2nd Int'l. US-USSR Conf. on Fracture of Composite Materials, Lehigh University, Mar. 1981.
17. Highsmith, A. L. and Reifsnider, K. L., "Measurement of Nonuniform Microstrain in Composite Laminates," Composites Technology Review 4, no. 1, (1982), pp. 20-21.
18. Jamison, R. D., Highsmith, A. L. and Reifsnider, K. L., "Strain Field Response of 0° Glass/Epoxy Composites Under Tension," Composites Technology Review 3, no. 4, (1981), pp. 158-159.
19. Reifsnider, K. L. and Highsmith, A. L., "Stress Redistribution in Composite Laminates," Composites Technology Review 3, no. 1, (1981), pp. 32-34.
20. O'Brien, T. K. and Reifsnider, K. L., "Fatigue Damage Evaluation Through Stiffness Measurements in Boron-Epoxy Laminates," J. Composite Materials 5, (Jan. 1981), pp. 55-70.
21. Jamison, R. D. and Reifsnider, K. L., "Advanced Fatigue Damage Development in Graphite Epoxy Laminates," AFWAL-TR-82-3103, Dec. 1982.
22. Reifsnider, K. L. and Stinchcomb, W. W., "Cumulative Damage Model for Advanced Composite Materials," Phase II Final Report, Contract No. F33615-81-C-5049, Wright-Patterson AFB, OH, Aug. 1984.
23. Highsmith, A. L. and Reifsnider, K. L., "The Effect of Fatigue-Induced Defects on the Residual Response of Composite Laminates," Proc. ASTM Symp. on 'Effect of Defects in Composites', San Francisco, CA, Dec. 1982.

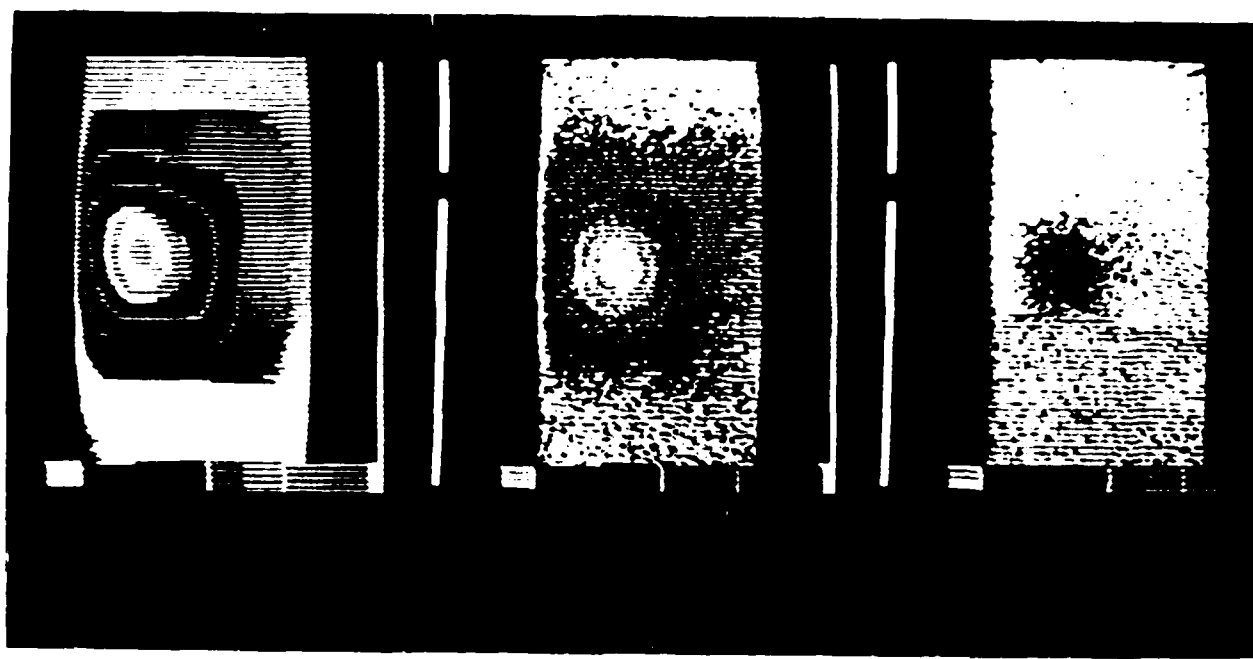


Fig. 1. Dissipated heat patterns observed during cyclic loading of a center-notched graphite/epoxy laminate (maximum cyclic stress was 130% of the static ultimate strength).

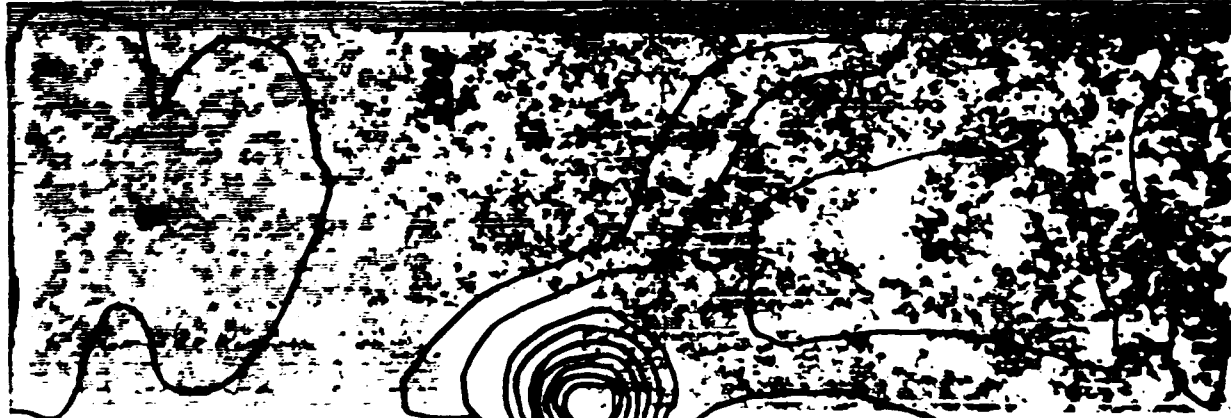


Fig. 2. Superposition of an ultrasonic f-scan pattern and a vibrothermographic pattern for a couple of sheet molding compound after cyclic loading.



Fig. 3. Thermographic pattern of heat dissipated during the full-scale in-process testing of a helicopter rotor blade.

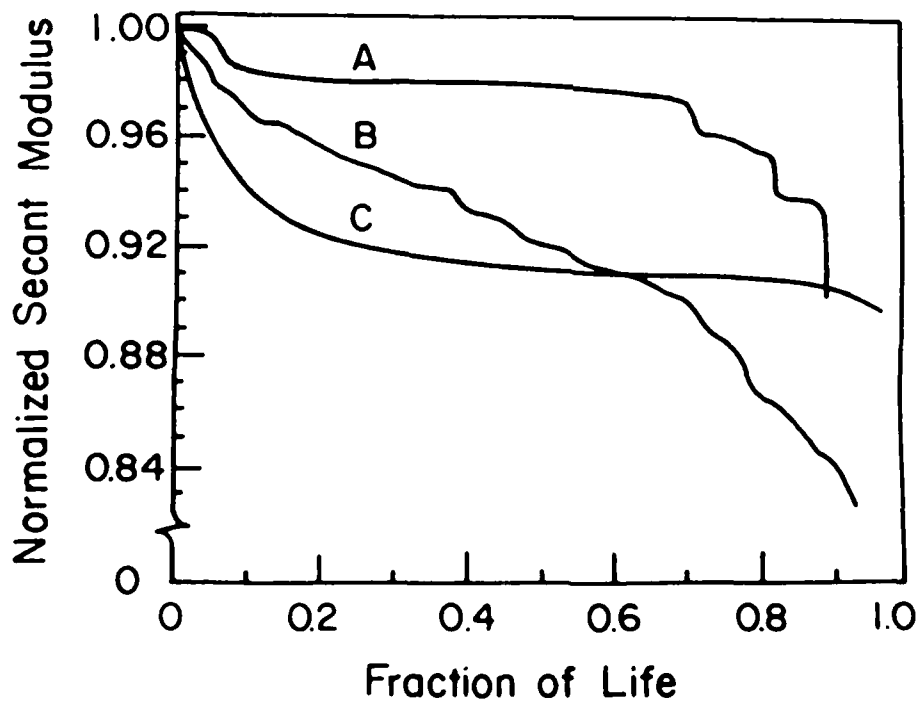


Fig. 4. Stiffness reduction as a function of the number of applied cycles for three graphite/epoxy laminates.

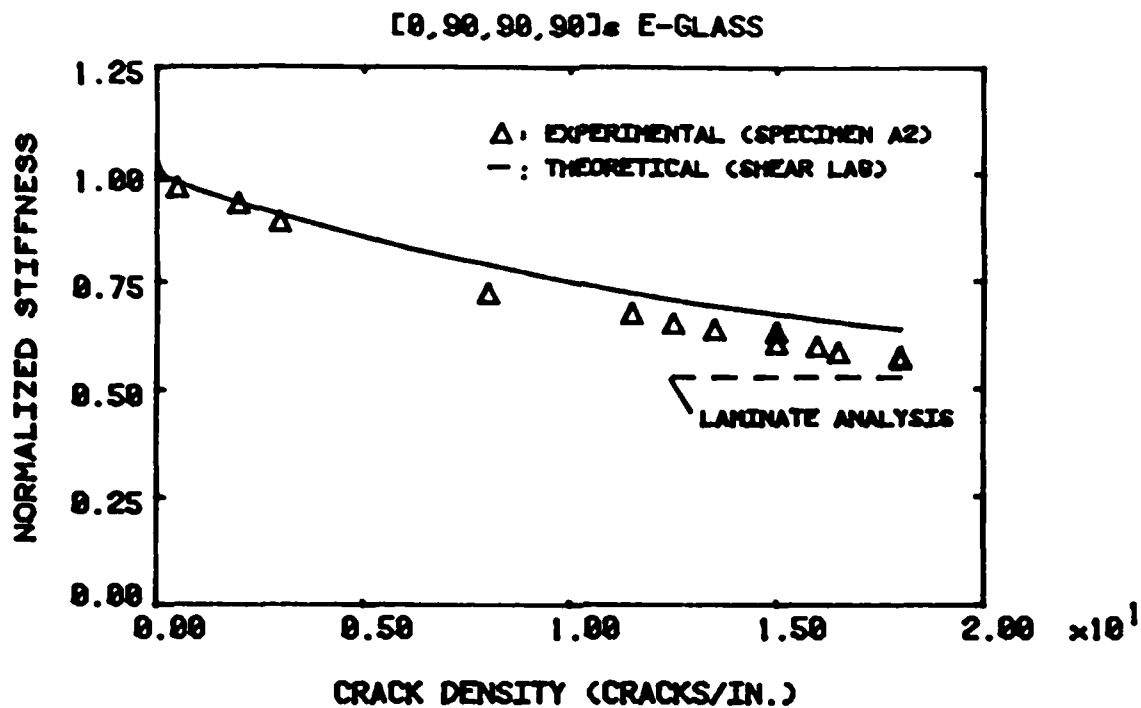


Fig. 5. Change in (normalized) axial stiffness of a fatigue-loaded specimen as a function of matrix crack density in the 90° plies.

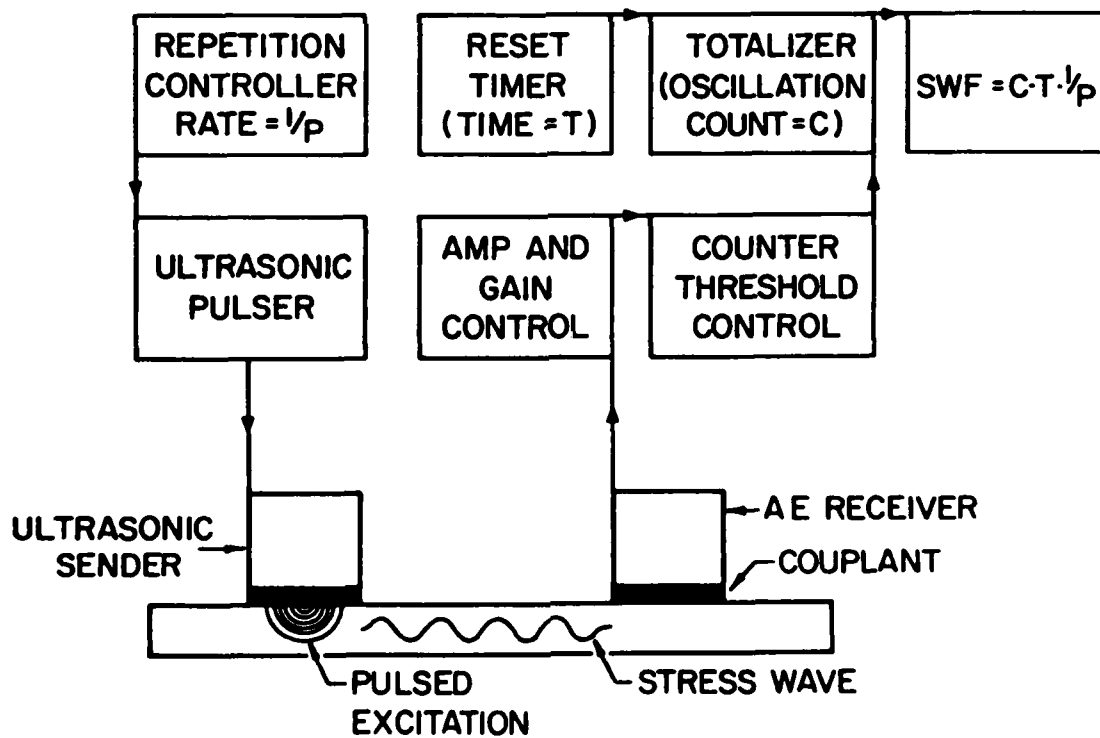


Fig. 6. Schematic diagram of an arrangement for evaluating the transmission of ultrasound through materials.

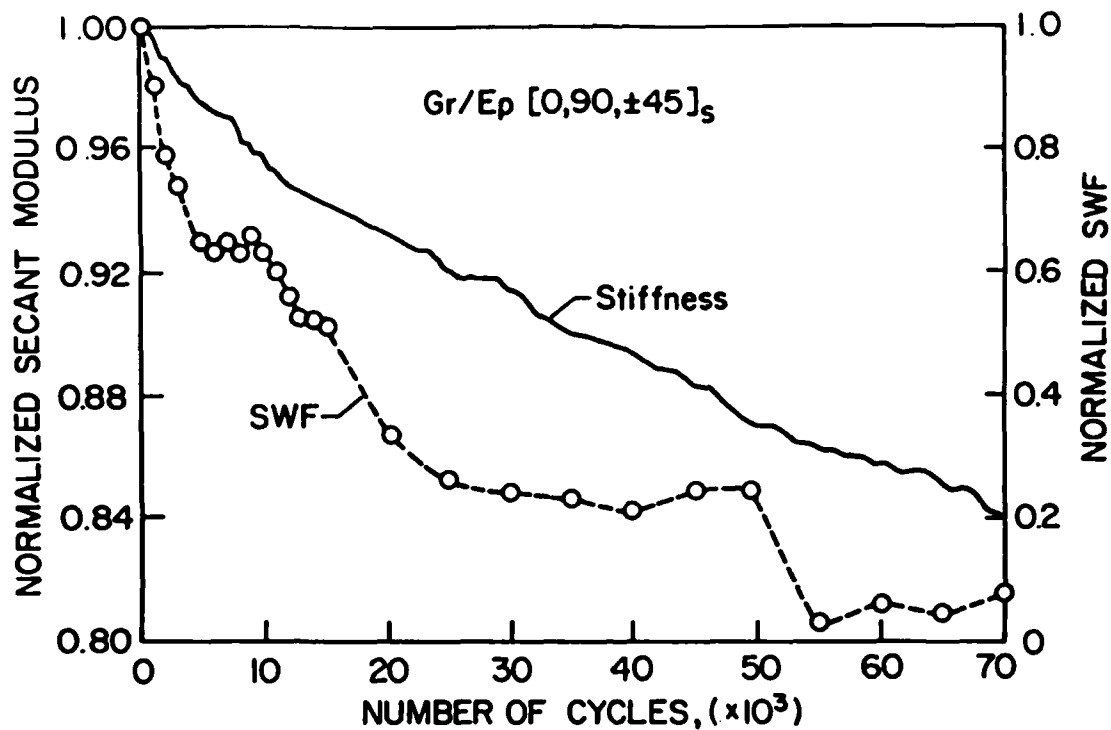


Fig. 7. A comparison of SWF changes and stiffness changes observed during the cyclic loading of a quasi-isotropic graphite/epoxy laminate.

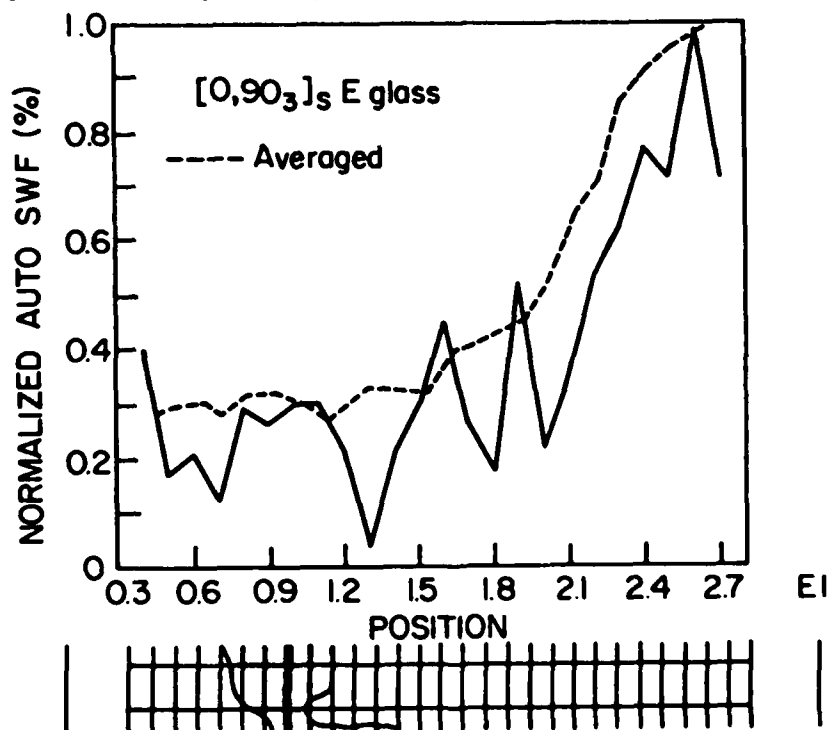


Fig. 8. Measured values of the SWF along the length of a specimen compared with the eventual region of failure (shaded region on the bottom left).

### Discussion of Session III

The consensus of opinion is that a major remaining problem for the NDE of rubber coated fabrics is detection of inadequate adhesion between fabric and rubber. At the present time, only proof testing appears to have met with any real success.

There followed a lengthy discussion on the sizes of the defects which are important in laminates. On the one hand, there is no doubt that delamination is a problem, that it can be extensive on a macro-scale and that on that scale it can be satisfactorily detected and sized using conventional ultrasonic C-scans. However, theories for in-service dynamic fatigue of fibre reinforced laminates are modelled on the accumulation of micro-scale damage, some of which is attributable to the fabrication process and most of which involves such molecular level phenomena as the debonding and breakage of individual fibres.

In respect of possible in-process detection of poor interfacial bonding between fibres and matrix, there was discussion of the virtues of simple mechanical testing accompanied by the detection and analysis of the associated adiabatic heating. Since it is conceivable that measurement of the latter could make use of existing commercially available equipment, the following written discussion was solicited.

That the interface between fibre and matrix materials is an important location for dissipation of energy during cyclic deformation of composite materials is best demonstrated by carrying out identical tests on a range of specimens, each specimen fabricated using fibres of constant but different diameter from the rest in the range. Figure 1 shows data reported by D Short (1970) for glass reinforced polyester resin.



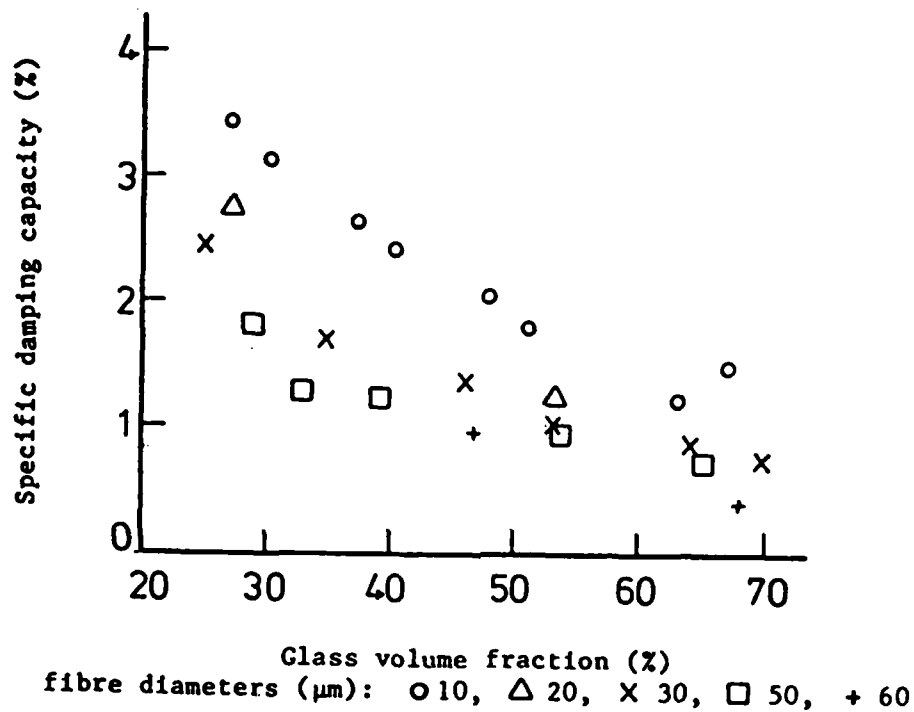


Figure 1

The energy is dissipated as heat which arises adiabatically as the instantaneous consequence of application of stress. In Fig. 2 consider a length  $l_0$  of glass fibre which is suddenly subjected to a load  $W$ .

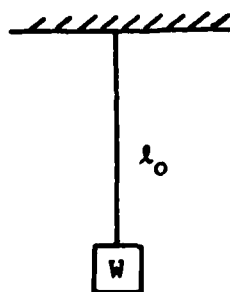


Figure 2

The immediate response is adiabatic although, after a time, the wire will reach equilibrium with the surrounding air.

$$dU = Wdl + TdS$$

We can write, for the temperature change for adiabatic reversible change,

$$\begin{aligned} \left( \frac{\partial T}{\partial W} \right)_S &= - \left( \frac{dl}{dS} \right)_W \\ &= - \left( \frac{\partial l}{\partial T} \right)_W / \left( \frac{\partial S}{\partial T} \right)_W \end{aligned}$$

for small loads, the numerator is a thermal coefficient of expansion and the denominator is  $1/T$  multiplied by a specific heat at constant pressure.

Assuming a linear coefficient of expansion and Hooke's law, we have a linear relationship between length, temperature and load, viz

$$l = l_0 (1 + \alpha(W)T + \beta(T)W)$$

$$\text{so } \frac{\partial l}{\partial T} = l_0 \left( \alpha + W \frac{\partial \beta}{\partial T} \right)$$

To obtain an expression for  $\left( \frac{\partial S}{\partial T} \right)_W$  we make use of the Maxwell relationship

$$\left( \frac{\partial S}{\partial W} \right)_T = \left( \frac{\partial l}{\partial T} \right)_W = l_0 \left( \alpha + W \frac{d\beta}{dT} \right)$$

Integrating with respect to  $W$ , we find

$$S = S_0 + l_0 \left[ \int_0^W \alpha dW + W^2 \frac{d\beta}{dT} \right]$$

Hence

$$\begin{aligned}\left(\frac{\partial S}{\partial T}\right)_W &= \frac{dS_0}{dT} + \lambda_0 \frac{1}{2} W^2 \frac{d^2 \beta}{dT^2} \\ &= \frac{\lambda_0 a_0 \rho_0 c_p}{T} + \lambda_0 \frac{1}{2} W^2 \frac{d^2 \beta}{dT^2}\end{aligned}$$

where  $a_0$  is the cross-section of the fibre and  $\rho_0$  is its density

Therefore

$$\left(\frac{dT}{dW}\right)_S = - \frac{\alpha + W \frac{d\beta}{dT}}{\frac{a_0 \rho_0 c_p}{T} + \frac{1}{2} W^2 \frac{d^2 \beta}{dT^2}}$$

or

$$\left(\frac{dT}{d(W/a_0)}\right)_S = - \frac{\alpha + W \frac{d\beta}{dT}}{\frac{\rho_0 c_p}{T} + \frac{1}{2a_0} W^2 \frac{d^2 \beta}{dT^2}}$$

$W/a_0 = \sigma$  is the applied stress,  $\alpha$  is the thermal expansion coefficient,  $\rho_0 c_p$  is a volumetric specific heat and  $d\beta/dT$  and  $d^2\beta/dT^2$  are temperature coefficients of elastic compliance.

At low loads

$$\left(\frac{dT}{d\sigma}\right)_S = - \frac{\alpha T}{\rho_0 c_p}$$

For fibreglass,  $\alpha \sim 4 \times 10^{-6}$  fractional extension per Kelvin,

$$\rho_0 \sim 2.2 \times 10^3 \text{ kgm}^{-3} \text{ and } c_p \sim 500 \text{ Jkg}^{-1}\text{K}^{-1}$$

Hence

$$\left( \frac{dT}{d\sigma} \right)_s \sim 10^{-9} \frac{\text{K}}{\text{Nm}^{-2}}$$

At 300K, the strength of fibreglass is  $\sim 3 \times 10^9 \text{ Nm}^{-2}$ , so adiabatic loading up to the elastic limit would change the temperature by about three degrees.

In practice, fibres would be loaded to less than their breaking strength so the momentary temperature change is expected to be a fraction of a degree. A camera and processing system developed by Sira Institute and known as SPATE registers temperature changes by remote measurement of infrared emission with a discrimination of about one-thousandth of a degree and spatial resolution of 0.5mm. With such a temperature sensitivity, the consequences of stress changes of the order of  $10^6 \text{ Nm}^{-2}$  should be detectable.

#### Reference

D Short (1970) "Effect of fibre diameter on the specific damping capacity of glass fibre reinforced polyester resin" M Sc Thesis, University of Bristol

Session IV: Acoustic emission

THE VALUE OF IN-PROCESS MONITORING OF ACOUSTIC EMISSION  
DURING PARTIAL PRESSURIZATION OF PRESSURE VESSELS

G. Marom, A. Mittelman and I. Roman  
Graduate School of Applied Science and Technology  
The Hebrew University of Jerusalem  
91904 Jerusalem, Israel

ABSTRACT

The paper describes the conceptual framework and the corresponding research stages of a project destined to develop a non-destructive procedure for the evaluation of filament-wound pressure vessels. In general, the establishment of a non-destructive technique is a two-phase process consisting of a systematic identification of the fundamental failure modes, fracture mechanisms and of the relevant defects, followed by correlating a particular non-destructive output with a specific defect or mechanism. To increase the reliability of the technique a characterization of a variety as wide as possible of fracture mechanisms is essential.

The procedure chosen for investigation in the present study is based on detecting specific acoustic emission data generated during a series of partial pressurization cycles, and interpreting the data in terms of specific material damage.

The research programme included three-point bend testing employed to generate failure modes such as tensile, compression and delamination, each comprising a sequence of fracture mechanisms. A correlation between those mechanisms and acoustic emission data was established. Tensile testing was carried out to examine in detail tensile and delamination failures typical of pressure vessels. Tensile specimens containing artificially implanted damage were also tested to verify the concept of the proposed non-destructive procedure. Presently, testing is extended to filament-wound pipes under NOL type loading and to ASTM pressure vessels.

1. INTRODUCTION

Poly (p-phenylene terphthalamide) fibres (Kevlar 49) have recently become a major reinforcement material in high performance filament-wound pressure vessels. Simultaneously with the technical development of the new product it is essential that reliable non-destructive quality control techniques be developed. Such techniques should provide tight rejection/certification criteria for advanced materials in critical applications.

Acoustic emission (AE) was chosen in the present study because of its reportedly high relevance to pressure vessels, see for example SPI (1983). Acoustic emission has been shown to be a most promising technique for failure monitoring of composite materials. Substantial contributions to the understanding of failure of these materials have been made using AE equipment based on simple analogue processing. The commercial computer-based AE systems which are now available generally report a wide range of parameters for the AE signal. Hence, it is now possible to obtain additional information regarding the nature of the source event. In addition, those

systems are now employed to identify source-events during partial, non-destructive loading of composite materials.

It is therefore clear that an AE-based technique has become a natural candidate in the present study whose task has set to develop a non-destructive procedure for the evaluation of filament-wound pressure vessels.

## 2. A FRAMEWORK FOR NDT

Our proposal of a conceptual framework for non-destructive testing had to consider three main parameters and prerequisites. We proposed to rely on an AE-based technique; we assumed that a monovalent correlation between AE signals and source events could be established; and the test procedure had to be integrated in the production line. It was assumed that a technique that utilizes the Felicity Effect would in fact fulfill these requirements and produce an appropriate solution.

The proposed procedure is based on subjecting the pressure vessel to 2-3 successive partial pressurization cycles. The first cycle will produce acoustic emission signatures of the perfect or the defective vessel. The subsequent cycles according to the Felicity Effect, will result in the perfect part in no or very little acoustic emission as long as the first pressure level (threshold level) is not surpassed; the defective part will continue to produce AE even under pressures below the threshold level. This AE signal will result from interactions (source events) between a defect and the stress field, and it will enable to identify the type of defect present. The pressurizations can be carried out in the production line immediately after removing the vessel from the mandrel.

## 3. PROGRAMME STAGES

In general, the establishment of a non-destructive technique requires simultaneously two parallel research paths. The first consists of a systematic identification of the fundamental modes of failure and of the relevant fracture mechanisms and related defects; the second path consists of receiving, storing and analyzing of some non-destructive output such as acoustic emission. These are followed by establishing a monovalent correlation between the non-destructive signals and specific mechanisms or defects. In order to increase the reliability of the technique a variety as wide as possible of fracture mechanisms should be characterized, leading towards a thorough understanding of the failure processes.

The actual research programme emerged from this background as follows. The call for a total characterization of the fracture mechanisms of Kevlar-reinforced composites resulted in selecting flexural testing for the first stage. Bending of composite materials may produce one or a combination of failure modes, namely, tensile, compressive and delamination. Each of these failure modes comprises a sequence of fracture events and fracture mechanisms related to the reinforcement (fibres), the matrix and the interface. In addition, extraneous fracture mechanisms also take place due to the physical conditions which derive directly from the loading technique. As a result a wide variety of fracture mechanisms may be generated by flexural testing.

The focal point of the second stage was the investigation of failure

modes with particular relevance to failure of Kevlar-reinforced pressure vessels, namely, tensile and delamination failures. This was carried out by axial and transverse tensile testing of unidirectional coupons of a wide range of fibre contents.

The Felicity Effect was tested through a comparison between perfect and damaged unidirectional specimens, containing either a notch or a delamination. Between 2 to 3 successive tensile loading cycles to 60% of the ultimate stress were performed.

Presently, testing is extended to filament-wound pipes under NOL type loading and to ASTM pressure vessels.

#### 4. RESULTS OF FLEXURAL TESTING

##### 4.1 Modes of Failure

The failure of Kevlar-reinforced epoxy composited in 3-point bending occurred by either one of two modes being failure by longitudinal fracture of fibres in the tensile side, or by shear delamination in the neutral plane. Each of these failure modes was preceded by compressive yielding in the compressive side typical of Kevlar composites. The first failure mode was typical of the lower volume fraction composites, and the second was typical of the higher, with a distinct transition in the volume fraction range 45-48%. With interlaminar loading the transition occurred at the lower end of the transition range, ~45%, and with translaminar loading the transition occurred at the higher end, ~48%.

Fig. 1 is a qualitative representation of the load-deflection curves for the respective failure modes. The curve of the fibre fracture mode is characterized by a yielding stage and a longer ultimate deflection. These result from compressive failure occurring in the compressive side of the specimen as discussed below. The curve of the delamination mode is characterized by a main delamination event followed by a number of secondary delaminations.

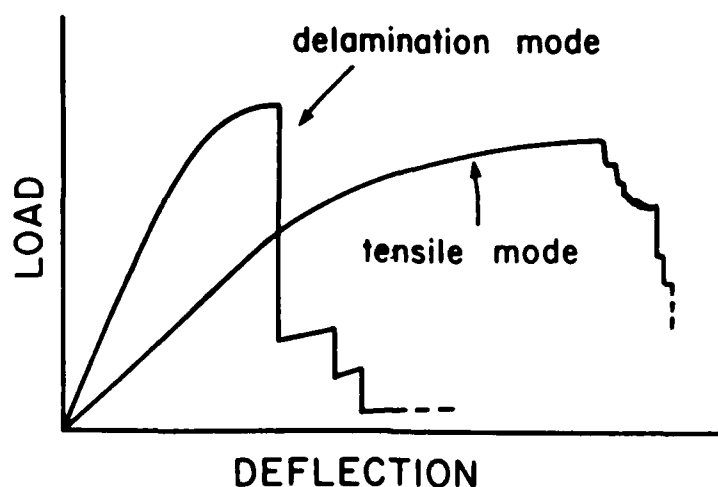


Fig. 1 Load-deflection curves for delamination and tensile failures



The transition from failure by fibre fracture to failure by delamination was governed by the fibre volume fraction. It was therefore detectable by monitoring various mechanical properties and plotting them versus the fibre volume fraction. Figure 2 presents the transition as reflected by strength measurements. The results show that the transition occurs around  $\phi_f = 0.45 - 0.48$ . Although the ultimate strength values,  $\sigma$ , were calculated for the entire  $\phi_f$  range, only those below the mode transition points are appropriate. Hence, in view of the observed transition to a delamination mode controlled by the shear stress at the neutral plane, the ultimate shear strength values,  $\tau$ , were calculated for  $\phi_f$  values above the transition point. These are shown in Fig. 2.

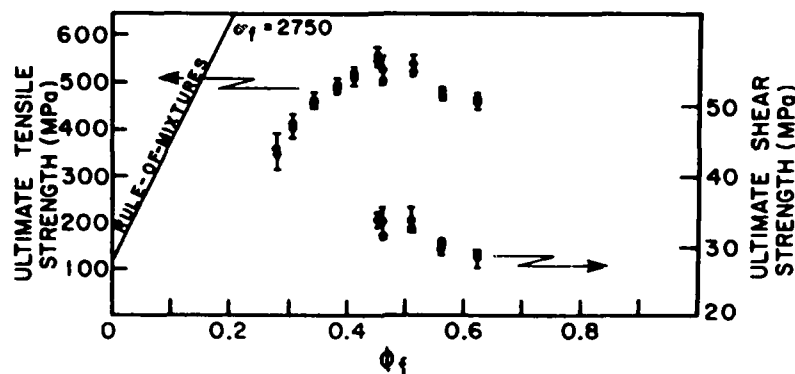


Fig. 2 Ultimate tensile and shear strength values

The reason for the mode transition at a critical  $\phi_f$  point lies with the different functions that  $\sigma$  and  $\tau$  have in  $\phi_f$ . Whereas  $\sigma$  increases linearly with  $\phi_f$ ,  $\tau$  decreases due to increasingly high proportions of interface at the shear plane. In fact, at high  $\phi_f$  values  $\tau$  is governed by fibre-fibre contacts of zero strength and by the fibre-matrix interfacial strength being relatively weak with Kevlar fibres. Hence, the critical  $\phi_f$  point is the value of  $\phi_f$  for which  $\sigma$  and  $\tau$  attain their ultimate values simultaneously. In the translaminar case  $\tau$  may be higher due to the action of misaligned fibres, resulting in a somewhat higher critical  $\phi_f$ .

Regarding the actual values of  $\sigma$  up to the transition point, they indeed seem to increase linearly with  $\phi_f$ . However, they are smaller compared with the rule-of-mixtures values calculated with  $\phi_f = 2.75$  GPa. The lower values derive from a calculation assuming both tensile and compressive elastic behaviour of the Kevlar-reinforced composites. As a matter of fact these composites exhibit non-linear compressive behaviour, resulting in a different stress distribution, as discussed in detail by Fischer and Marom (1984), producing the rule-of-mixtures values for  $\sigma$ . Another important outcome of the non-linear compressive behaviour is that stresses above the compressive yield stress shift the neutral axis downward. The marking of this shifting is obtained by the onset of delamination failure, taking place within the neutral plan in its ultimate new location away from the

centroidal axis. This is shown in Fig. 3 with four specimens representing different fibre volume fractions above the critical  $\phi_f$ , which sets the failure mode transition.

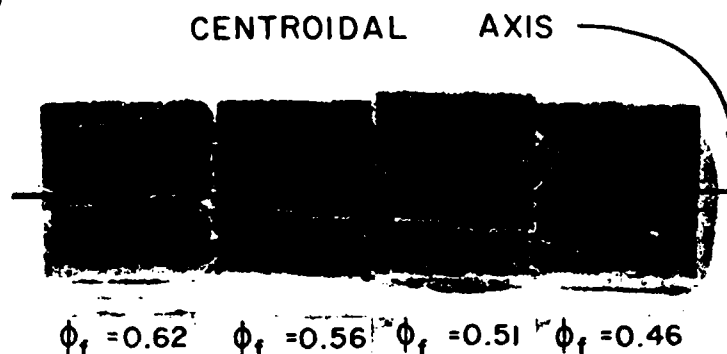


Fig. 3 The displacement of the neutral plane (marked by delamination) from the centroidal plane as affected by the fibre volume fraction

#### 4.2 Fracture Mechanisms

Fractographic examinations of the fractured specimens revealed typical features of the two observed modes of failure. Fig. 4 contains examples of scanning electron fractographs showing the details of a tensile failure



Fig. 4 Scanning electron fractographs of tensile failure related fracture mechanisms



Fig. 5 Scanning electron fractographs of delamination failure related fracture mechanisms

mode. The important observation concerns the fracture of the Kevlar fibres and their pull-out from the fractured matrix. It is seen that the fracture of the Kevlar fibres occurs through an axial splitting mechanism, followed by a pull-out stage of the two opposing split portions.

Examples of the details of the delamination failure mode are presented in Fig. 5 by scanning electron fractrographs showing the final shear damage in the matrix typical of the delamination mode, and the typical splitting of the fibre. Although fibre splitting occurs under both tensile and delamination failure modes, fracture proceeds differently in each case. Three typical fibre failure events under the delamination mode may be observed. The most interesting and unique is the shear failure of an individual filament also shown in Figure 5. The other two events are the tearing off in the axial direction of the fibre skin to form a continuous ribbon, and the production of deformation kink bands on the compression side of a sharp bend. For a more comprehensive examination of the fracture mechanisms see Davidovitz et al (1984).

Additional fracture mechanisms studied were those related to compressive failure and to transverse failure (obtained by transverse 3-point bending). Figures 6 and 7 present examples of corresponding micrographs related to these respective failures.



Fig. 6 A kink bend formed on the specimen surface in the compression side



Fig. 7 A typical transverse fracture surface

#### 4.3 Preliminary AE Results

Figure 8 presents acoustic emission amplitude distributions obtained for 3 different failure modes. It is obvious that the different modes are distinguishable by their typical acoustic responses. Moreover, the tensile-delamination mode transition is also detectable through the AE data. This is exemplified in Figure 9 by plotting the ratio of the event count in the amplitude range 10-20 dB to the total event count

versus the fibre content. The preliminary AE results already indicate that matrix fracture events probably occur in the amplitude range of 10-40 dB, while fibre fracture events occur in the amplitude range 45-65 dB.

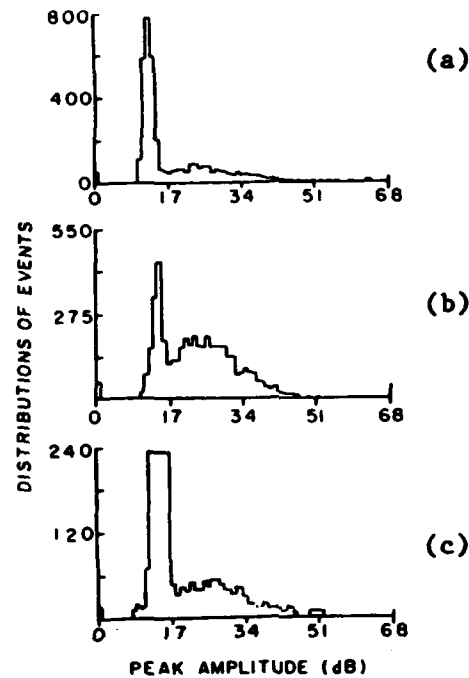


Fig. 8 AE amplitude distributions by a 375 kHz sensor; (a) tensile; (b) delamination; (c) transverse failure modes

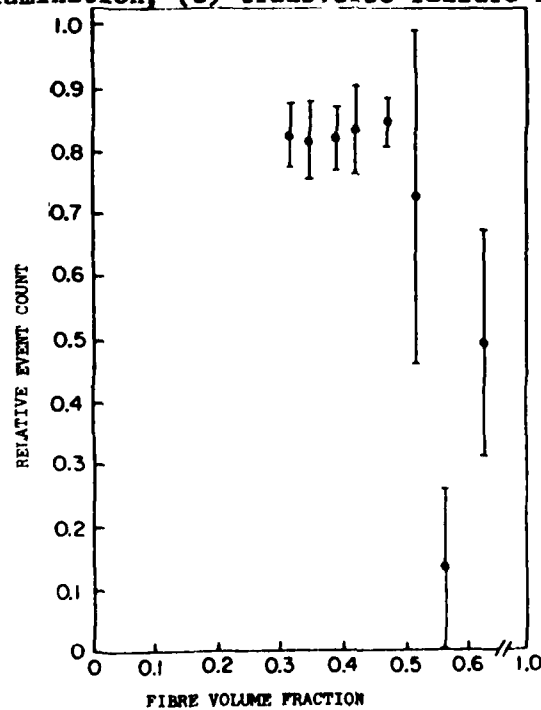


Fig. 9 Event count ratio as a function of the fibre content, showing the failure mode transition at  $\phi_f = 0.50$

## 5. RESULTS OF TENSILE TESTING

### 5.1 Fracture Mechanisms

Failure under tensile loading occurred by a combination of fibre fracture and longitudinal matrix and interfacial shear failure. The first occurred progressively with the loading of the specimen, and the latter occurred at the onset of failure. The mechanism of fibre fracture exhibited the typical splitting process regardless of the fibre content. The matrix and interfacial shear failure events exhibited strong dependence on the fibre content, with the longitudinal shear damage increasing as the fibre content is increased. This is seen in Figure 10, where only one longitudinal shear crack is observed in 27% fibre content, while multiple longitudinal shear is observed in 73% fibre content.

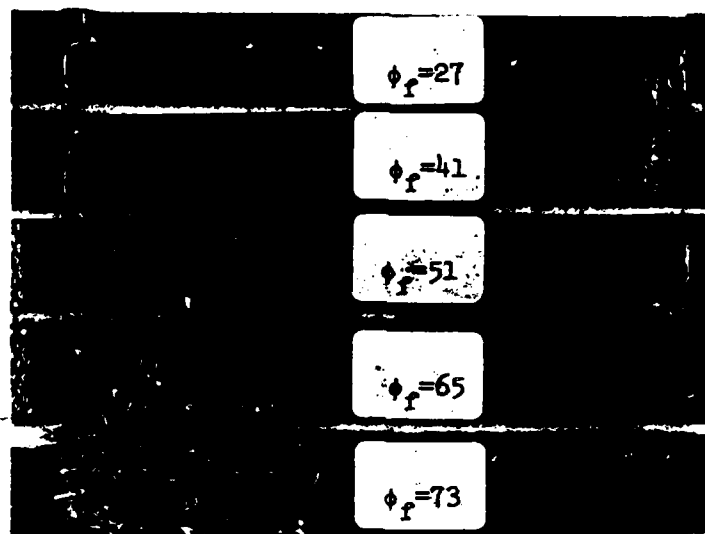


Fig. 10 Longitudinal shear damage in fractured tensile specimens as a function of the fibre content

Typical details of tensile failure-related fracture mechanisms are shown by the scanning electron micrographs of Figure 11.



Fig. 11 Tensile failure of unidirectional Kevlar-reinforced composite: (a) longitudinal shear damage; (b) fractured fibres; (c) matrix and interfacial shear damage.

## 5.2 AE Data

The AE information was analyzed at a number of points during the loading of the specimen. This enabled to establish a correlation between the acoustic signal and the source event. Some of the AE results are presented in Figure 12. On the left hand side of this figure we see amplitude distributions for the events which occurred up to 95% of the ultimate load. The amplitudes appear in the range 39-65 dB and result from fibre breakage which occurs progressively with the loading. On the right hand side of Figure 12 we see the amplitude distribution of the total events at the instant of failure. The high fibre content composites exhibit an addition of events in the range 18-38 dB, related to matrix and inter-facial failure.

These partial AE results already indicate that amplitude distribution ranges may be correlated with source events such as fibre or matrix fracture, with a high degree of confidence. Additional information obtained for instance, by tensile testing of transverse specimens strengthens this picture. A fuller account of the AE results is in preparation.

## 6. RESULTS OF CYCLIC LOADING

In this phase of the research 3 loading cycles to 60% of the ultimate load were applied to 3 types of specimens, two of which containing a notch or delamination. The results reported below were obtained with an insufficient number of specimens to allow a thorough statistical analysis, and at this stage they should be considered as of indicative value only. A number of AE transducers were used; the 375 kHz transducer for example provided the following information.

---

	Av. No. of events			Count ratio	
<u>Specimen</u>	<u>1st cycle</u>	<u>2nd cycle</u>	<u>3rd cycle</u>	<u>2nd/1st</u>	<u>3rd/1st</u>
Original	13926	1208	621	8.7%	4.5%
Delamination	19876	1483	753	7.5%	3.8%
Notch	39483	4485	3407	11.4%	8.6%

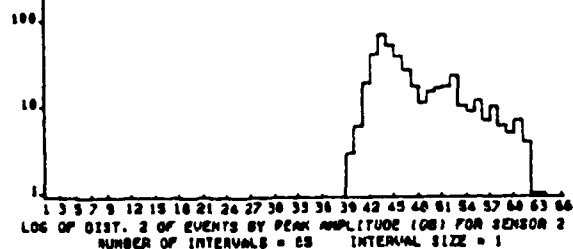
---

It is seen that the presence of a notch results in a drastic increase in the total event count in the first loading cycle, and the count ratio after the 3rd loading cycle is almost twice that of the undamaged specimen. Delamination seems to be a less noticeable damage under tensile loading, however, the total picture obtained with more specimens and transducers points in the same direction as that of the notched specimens. It is also thought now that a lower load level of about 30% of the ultimate would result in a more significant picture. It is clear though, that such AE data as presented above is indicative of the presence of damage and of its type.

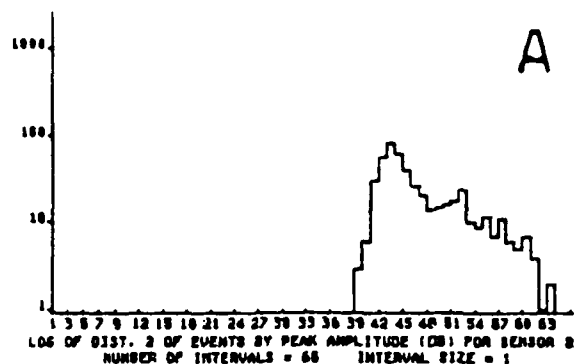
MAY 12 10:53:21 ELAPSED TIME = 00:06:52

DEGEN 200  
STATISTICS FOR SENSOR -0  
DEGEN 200

RUN TIME	EVENTS	TOT REJ	% LOST
00:06:33	8851	0	0
00:06:56	431	0	0
00:01:29	2319	0	0
00:01:27	71	0	0



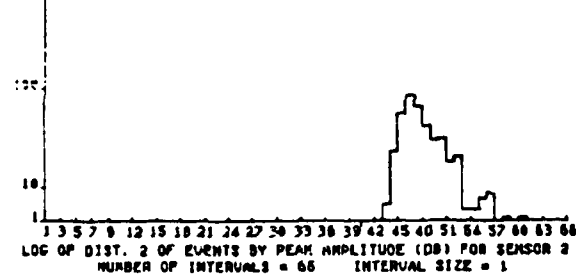
MAY 12 10:57:08 ELAPSED TIME = 00:07:50  
DEGEN 200 LAST



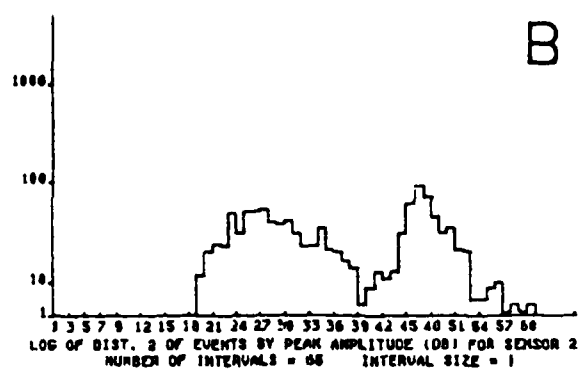
MAY 12 12:00:24 ELAPSED TIME = 00:11:45

DEGEN 500 (22)  
STATISTICS FOR SENSOR -0  
DEGEN 500 (22)

RUN TIME	EVENTS	TOT REJ	% LOST
00:11:47	17190	0	0
00:11:49	447	0	0
00:01:27	1543	0	0
00:01:25	81	0	0



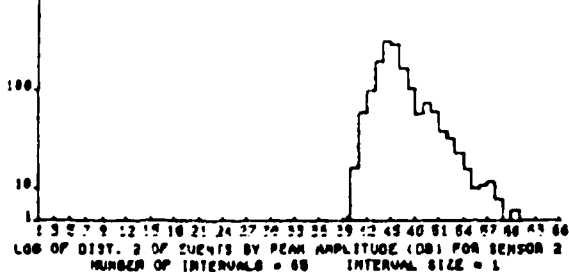
MAY 12 12:11:18 ELAPSED TIME = 00:12:26  
DEGEN 500 LAST (22)



03 MAY 12 13:16:46 ELAPSED TIME = 00:09:40

DEGEN 600 (24)  
LIST STATISTICS FOR SENSOR -0  
DEGEN 600 (24)

SEN	RUN TIME	EVENTS	TOT REJ	% LOST
1	00:09:49	18864	0	0
2	00:09:50	1689	0	0
3	00:01:52	2336	0	0
4	00:01:50	319	0	0



MAY 12 13:23:59 ELAPSED TIME = 00:11:48  
DEGEN 600 LAST (24)

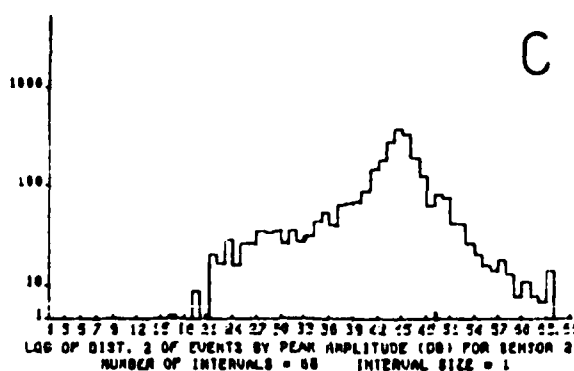


Fig. 12 Amplitude Distributions for fibre volume fractions 71% (A), 65% (B), and 65% (C); From left to right: distributions at 95% of ultimate load, and the instant of failure, respectively.

## 7. CONCLUSIONS

Two major conclusions that reflect on future progress of this study are as follows:

- (i) Specific fracture mechanisms and failure modes may be identified at a high level of confidence by AE data.
- (ii) AE during non-destructive partial loading produces information regarding presence and type of material damage.

## REFERENCES

Davidovitz, M., Mittelman, A., Roman, I. and Marom, G., (1984) J. Mater. Sci., 19, 377-384.

Fischer, S., and Marom, G., (1984) Fibre Sci. Tech., 20, 91-98.

SPI (1983), 1st International Symposium on AE from Reinforced Plastics, San Francisco, July 19-21, Society of Plastics Industry.



THE STRAIN RATE DEPENDENCE OF ACOUSTIC EMISSION, INCLUDING THE  
DETECTION AND NON-DETECTION OF DEFECTS KNOWN TO BE SUBJECTED TO  
INTERNAL STRESS.

Jan-Fredrik Jansson and Henrik Sundström.

Department of Polymer Technology  
The Royal Institute of Technology  
S-100 44 Stockholm, Sweden

ABSTRACT

The initiation and growth of cracks in CSM laminates have been studied using stress-strain relations, hysteresis, mechanical loss factor, laser light scattering and electron microscopy in combination with acoustic emission. In tensile tests three regions of fracture initiation and crack growth have been defined. The strain limits as well as the acoustic emission event rate and energy per event of these regions changes with the type of composite as well as with the strain rate. The changes have been analysed with respect to the defects in the composite. It is shown that acoustic emission is unable to detect some types of fracture mechanisms at low strain rates and thus the influence of the defects on those mechanisms.

DEFECTS IN CSM POLYESTER/GLASS FIBER LAMINATES

The fracture long term loading capacity of CSM laminates is limited by a large number of different types of defects. These defects not only have their origin in the heterogeneous structure of the composite itself but also in the imperfection of the laminating methods and in the processing properties of the raw materials.

Most CSM polyester/glass fibre laminates are made either by hand lay up, by spray up of chopped rowing followed by manual rolling or by resinject techniques. All these different methods involve risks in producing incomplete wetting of the fibres resulting in poor bonding between the fibres and the matrix, flaws, gas inclusions etc.

The glass fibre strands are often built up by several hundreds of fibres. To prevent the rowing formed in this way of being splintered during the handling, the fibres are usually held together by a binder of high molecular weight polyester, polyvinyl acetate or the like. The idea is that this binder should be dissolved in the polyester resin, allowing the fibres to be reasonably well distributed throughout the laminate.

However, due to the relatively high viscosity of the resin and the small local shear flow that can be achieved around the bundles during the normal fabrication of the laminates the fibres also stick together in the composite. This results in large variations in the fibre content reaching more than 60 % by volume within the strands although the average value might be as low as 15 - 20 %. The effect is of course, an increased strain magnification within and around the bundles in addition to the generally non-uniform local stress distribution in the composite.

It is also reasonable to expect the binder to affect the properties of the cured polyester. Due to the imperfect mixing which can be expected around the bundles, the binder will be included in different amounts and in different ways in the polyester network. The result might be a lowered  $T_g$  and either degraded or enhanced fracture properties.

The properties of the polyester matrix itself vary through the laminate. Thus, the number and length of the styrene bridges (the crosslinks) vary due to the curing conditions. The chemical structure of the network and the degree of crosslinking are influenced by fillers, fibres etc. Some authors, e.g. Katz et al (1980, 1982) and Sperling et al (1978) have reported substantial local variations in the crosslinking degree and a globular structure of highly crosslinked material surrounded by areas with lower degrees of crosslinking.

Internal stresses are built up because of the shrinkage of the matrix around the fibres while curing and the larger thermal contraction of the matrix when the laminate is cooled down from the curing temperature. These stresses can locally exceed the strength of the matrix to cause cracks.

It is obvious that all these defects will influence the fracture properties and especially the fracture initiation in different ways and to different extents. It is also well known that the viscoelasticity as well as the time and strain rate dependent fracture properties of the polymer matrix affect the fracture behaviour of the composite and also the influence of the defects on the fracture initiation and growth.

Therefore, a NDE method for control of the loading capacity due to fracture has to be capable of distinguishing defects which are active to the fracture processes from "passive" defects, also taking into account the deformation and fracture properties of the matrix.

At least to some extent, Acoustic Emission used for the indication of the fracture initiation seems to fulfill these conditions.

## FRACTURE PROCESSES IN SCM LAMINATES - RELATIONS TO DEFECTS.

There is no single method available at present which is capable of both the identification of the different types of fracture initiation and crack growth mechanisms in composites, and of the measurement of their intensity.

Fig.1 shows the acoustic emission event rate,  $AE(N)$ , i.e. the number of events per time unit for a CSM, E-glass/polyester laminate during tensile test at a strain rate of 20% per hour, Sundström and Jansson (1984).

The curves show three distinct regions:

- I, which ranges from 0.1% strain, at which the acoustic emission appears, to approximately 0.35% and is characterized by a slow increase in the event rate,
- II, where the acoustic emission event rate is multiplied and
- III, which ranges from approximately 0.9% strain up to the final failure which occurs at about 1.5% strain and is characterized by a constant or even decreasing event rate.

This means that the accumulated number of event follows an S-shaped curve starting at 0.1% strain and having its inflection at about 0.8%.

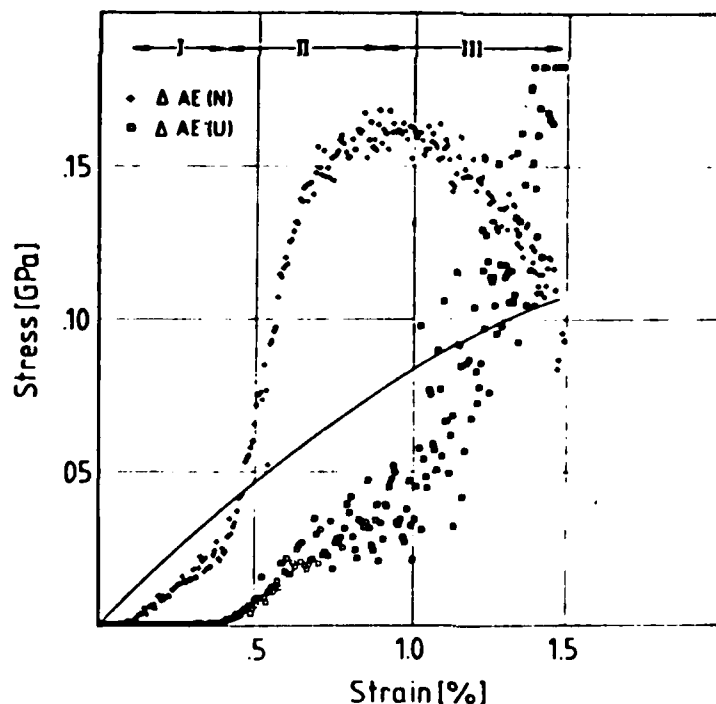


Fig.1 The stress, event rate and energy rate vs strain for a CSM laminate ( $V_f=17\%$ ) at 20% per hour strain rate. The arrows show the regions I-III defined in the text.

A few events of high energy occur already at very low strain, although a more continuous high energy emission does not appear until above approximately 0.4% strain.

In Fig.2 the rate of the average energy per event is plotted for two different strain rates. The behaviour seems to be composed by several mechanisms. Appearing at about 0.4% strain for 20% per hour strain rate, the average energy per event increases up to a plateau,  $3 - 5 \mu V^2$  per sec, in region II. An additional, superimposed mechanism, which gives an exponentially increasing energy per event rate, seems to dominate the behaviour above 0.9% strain in region III. A more detailed study shows a further plateau below 0.35% strain at about  $5 \cdot 10^{-2} \mu V^2$  per sec for the very low energy fracture processes in region I.

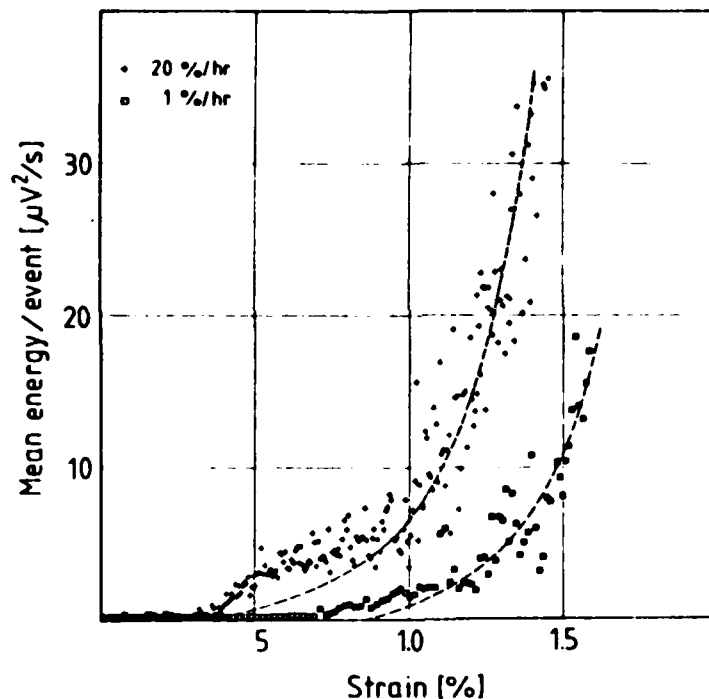


Fig.2 The average energy per event vs strain for CSM laminates tested at 20 and 1% per hour strain rate, respectively. The dotted lines represent the exponentially increasing part of the curves in region III.

Using measurements of stress strain relations, hysteresis, mechanical loss factor, laser light scattering and electron microscopy in combination with acoustic emission, the following fracture sequences have been detected in CSM laminates with a plain polyester matrix, Sundstrom and Jansson (1984).

The failure is initiated at very low strains, region I, by debonding between the fibres and the matrix within the strands. With increasing strain, transverse intra-strand matrix cracks are formed by the growth and coalescence of the debonds, region II. The size of these cracks increases until they are temporarily arrested at the edges of the fibre bundles. At still higher strains, region III, a few of the intra-strand cracks proceed into the matrix rich regions between the strands. The final catastrophic crack growth occurs when a few of these cracks have reached a critical size.

Thus, the fracture initiation is strongly dependent on those defects which determine the stress and strain conditions within the fibre bundles: local fibre distribution, wetting of the fibres, internal stresses, local matrix properties etc. In the same way, the different fracture mechanisms preceding the final crack growth are influenced by the fibre distribution and other large scale defects.

The detailed influence of the different defects on the initiation and growth of the fracture has been studied only in a few cases, although many general relations can be formulated. Therefore, very little is known in what way the different defects will appear in NDE methods capable of predicting fracture behaviour and loading capacity.

In the following, a few relations of this type have been listed.

#### Dependence on fibre content.

As can be expected, the numbers of debonded fibres, intra-strand matrix cracks and cracks in the inter-strand matrix rich regions increase with increasing fibre content. For very low fibre content, only very few cracks are induced in the inter-strand regions and, in principle, the final failure is caused by the growth of only one matrix crack.

The strain of approximately 0.1% for the initiation of the debonding does not seem to be much affected by the fibre content, at least in the region 10 - 25 % by volume. On the other hand, the formation of the intra as well as of the inter strand matrix cracks is shifted towards lower strains at increasing fibre content. In contrast to this, the strain at the final failure increases when the fibre content is increased from 10 to 25 %, due to the larger number of matrix cracks formed before the final failure

### Influence of fibre distribution.

The number of debonds as well as the number of intra-strand matrix cracks are reduced as can be expected due to the more favourable stress distribution in laminates made from strands which include only a few fibres. Besides, both the strain at the formation of the large scale matrix cracks as well as their number increase. At constant fibre content, this improves the loading capacity of the composite.

### INFLUENCE OF STRAIN RATE.

Fig.3 and 4 show the effect of strain rate on the event rate and average energy per event rate.

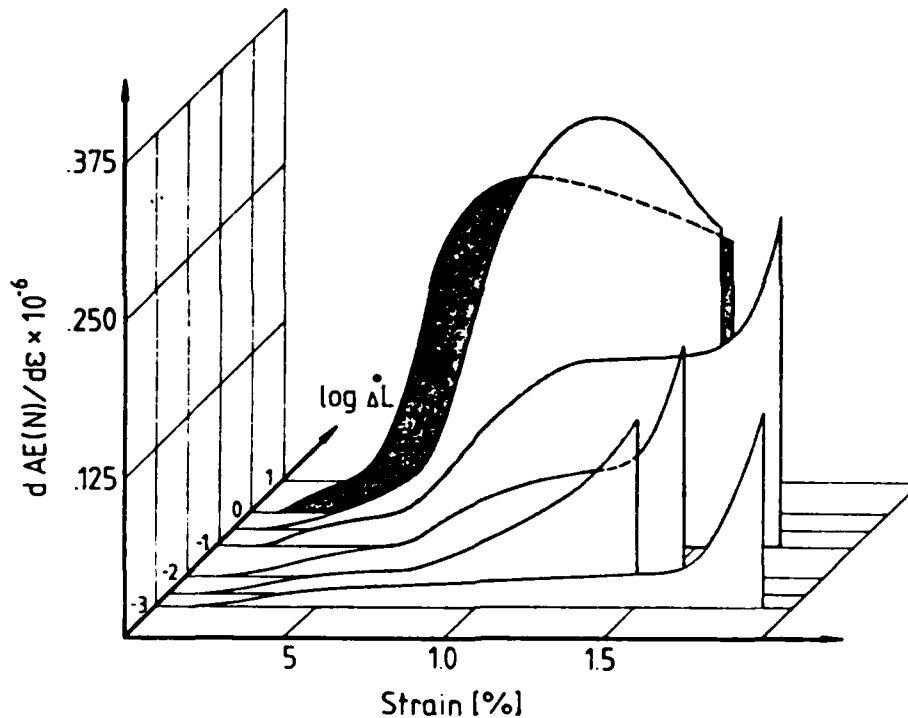


Fig.3 The event rate vs strain for CSM laminates ( $V_f = 17\%$ ) at different draw rates, sample length 170 mm.

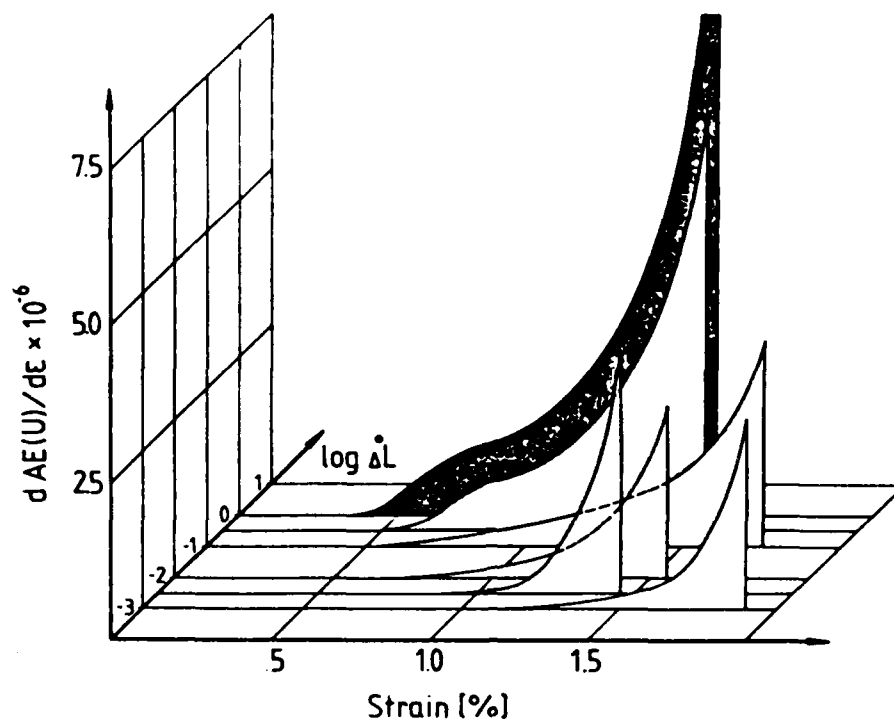


Fig.4 The energy rate vs strain for CSM laminates ( $V_f 017Z$ ) at different draw rates, sample length 170mm .

At reduced strain rate both the event rate and the energy rate, decrease. Also the characteristics of the fracture regions defined above change:

- The strain at which AE(N) appears remains mainly constant, while the level of the plateau in region I decreases slightly.
- The increase of AE(N) and the appearance of the AE(U) in region II is shifted towards higher strains and their levels are slightly reduced.
- The event rate preceding the final failure is not influenced to any higher extent. Due to the decreasing intensity in region II, the effect of this will be that the intensity in region III decreases, however.

At very low strain rate AE(U) in region II is suppressed and the exponential part of the curve in region III is shifted towards still higher strain levels.

Fig.5 shows the rate dependence of the strain limits for the different regions as it appears in both the event rate and the energy per event rate. When the strain rate is decreased from 20 to 0.005% per hour the transition: I - II is shifted from about 0.3 to 0.65% and the transition: II - III from 0.9 to 1.2% strain.

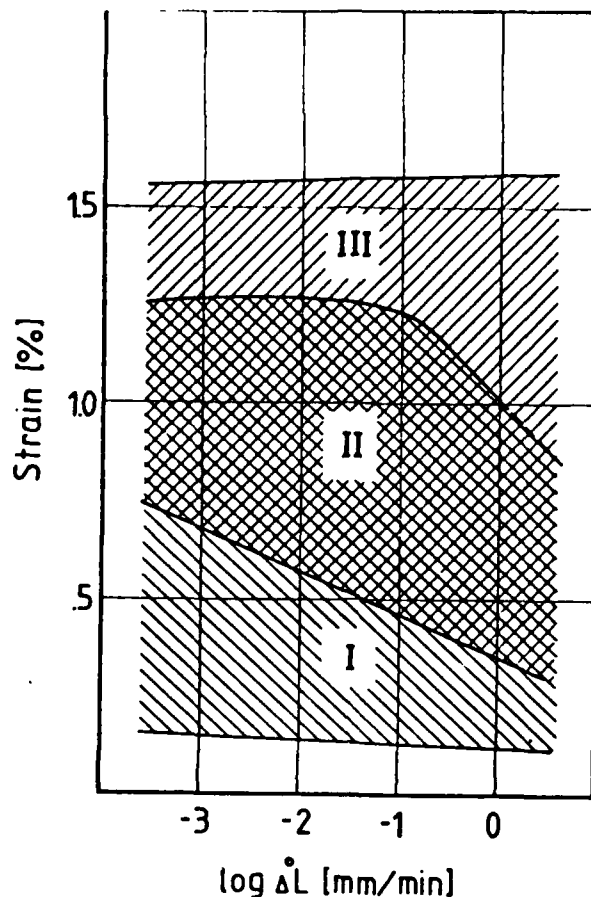


Fig.5 Effect of draw rate on the strain limits of the three regions defined in Fig.1.

Thus, the strain at the initiation of the debonding does not vary significantly with the strain rate in the region 0.005 - 20 % per hour.

On the other hand, the number and size of the debonds, as well as the conditions for the intra-strand matrix cracking seem to vary in a rather complex way with the strain rate. Different techniques, for instance light scattering and acoustic emission, also give different information on the kinetics of these processes.

The exact behaviour is not known at present. Thus, while the effect of the strain rate on the number of debonds is not clear, it is obvious that the number of intra-strand matrix cracks initiated before the development of the large scale cracks in the matrix rich regions, increases with decreasing strain rate. On the other hand, the number of cracks formed in the matrix rich inter-strand regions before the final failure decreases with decreasing strain rate. This implies that a smaller number of the formed intra-strand cracks continue to grow out into the matrix rich regions.



The explanation of these phenomena may be found in the visco-elastic-plastic behaviour, in the strain rate dependent fracture mechanisms of the matrix and in the relaxation of the stresses around the induced cracks. During the slow deformation, a general smoothing of the stress distribution takes place in the composite due to the visco-elastic behaviour of the matrix. Furthermore, local stress relaxation will occur in the matrix when the debonds are formed. This changes the conditions for the growth and coalescence of the debonds and thus, those of the formation of the matrix cracks. In the same way, the larger number of intra-strand cracks produces a more favourable stress distribution around the strands which will delay the initiation of the large scale matrix cracks. The phenomena will be strengthened still more by the changes which might take place in the fracture mechanisms in the polyester matrix. Thus, the ability of the matrix to form oriented structures absorbing part of the fracture energy during the crack growth is strongly dependent on the strain rate.

At high strain rates, all the different techniques mentioned above give similar results with respect to the nature and intensity of the different fracture processes. In this case, the intensity of the acoustic emission will give an indirect measurement of the influence of the different active defects.

Also at low strain rates, the initiation and growth of the debonds and the intra-strand matrix cracks are easily detected by a continuous increase in the  $45^\circ$  vertical light scattering and by a whitening of the laminate.

Also, acoustic emission seems to give an adequate measure of the initiation and growth of the debonds, despite the very low acoustic energy that can be expected to be emitted at low strain rates.

However, the energy emitted by the initiation and growth of the matrix cracks within the strands seems too low for the acoustic emission to be detectable. This means that both this special mechanism as well as the defects behind are not immediately detectable by acoustic emission.

#### REFERENCES

Misra S.C., Manson J.A. and Sperling L.H., Epoxi Resin Chemistry, p. 157, (1978).

Katz D., Buchman A and Gonen S., Eighth Intern. Congr.on Rheology, 3, p. 249, (1980)

Katz D., 28 th IUPAC Macromol. Symp. Amherst, Ma. USA, p 691, (1982)

Sundström S. and Jansson J.-F., Intern. Symp. Composites: Materials and Engineering, Newark, Delaware, USA, 1984.

QUALITATIVE AND QUANTITATIVE EVALUATION OF DAMAGE IN C F R P BY  
ACOUSTIC EMISSION DURING STRUCTURAL LOADING

D. VALENTIN, B. PONSOT, A.R. BUNSELL

Ecole Nationale Supérieure des Mines de Paris  
Centre des Matériaux  
B.P. 87  
91003 EVRY Cédex  
FRANCE

**Abstract**

A major hindrance to the wide use of advanced composites is the absence of proof testing and life prediction techniques and these require an understanding of the way damage accumulation occurs. The acoustic emission technique is an attractive means for damage investigation. Our approach was on the one hand qualitative as it involved a statistical analysis of the amplitude of the recorded signals without differentiating them and on the other hand quantitative by counting events under different loading conditions. It has been found possible to correlate different damage mechanisms with typical acoustic patterns on amplitude histograms and also to develop an understanding of damage kinetics which are useful for determining as in a proof test, the longterm reliability of structures.

**Introduction**

The impressive mechanical properties of C F R P are coupled with a low density. As a consequence it is often used for structures requiring low weight or inertia and for this type of application it is clearly desirable to be able to subject the material to as high a load as is safely possible. There are, however, difficulties in replacing traditional materials by new ones and not least of these is the lack of long term experience and the necessity of developing new methods of control adapted to the new material. The lack of a proof testing technique or a means of determining the long term reliability of composite structures is inhibiting their adoption for applications for which a cursory glance at their short term properties would indicate their imminent suitability. The acoustic emission technique has proved to be a useful tool with which it is possible to monitor the processes of damage in composites. The usefulness of the results which are obtained depends on the theoretical means of analysis and modelling.

### Experimental details

Experiments have been conducted on flat unnotched plate specimens made from different types of prepreg. They were Ciba Geigy Fibredux 914 CTS, which has a curing temperature of 180°C, and resins obtained by mixing the Ciba Geigy systems - CY 205 and CY 208 - in different proportions. The component CY 208 is a plastifier and can be mixed in any proportion with the CY 205 resin. The cure temperature was 120°C in the latter case. Some unidirectional carbon fibre reinforced polystyrylpyridine were also tested. The P S P specimens were made by the Société Nationale des Poudres et Explosifs, the cure temperature was 250°C. In all cases, the reinforcement was Toray T300 carbon fibres.

All acoustic emission monitoring was made with a 3000 series Dunegan Endevco system. A PZT differential transducer type D140 B was employed with a dominant frequency at 200 kHz. The system consisted of a 40 dB preamplifier with a frequency range of 100-300 kHz, an amplifier with adjustable gain and an impulse detector transforming all peaks exceeding the threshold (25 dB) at the output into digital pulses. The dB measurements were given in reference to a 1  $\mu$ V signal at the transducer. The analysis system was set to have a dead time of 100  $\mu$ s which allowed one event only to be counted for each series of pulses separated by less than 100  $\mu$ s. During creep tests, as earlier studies [1] had revealed a nearly logarithmic stabilisation of acoustic emission as a function of time, counts were recorded on an X-Y plotter which allowed a direct trace of  $\log \frac{dN}{dt}$  as a function of N. Tests were conducted using a total gain of 80 dB.

### Qualitative evaluation

The damage produced in composite materials may be of a complex nature, and thus, the problem of discrimination between the different and often simultaneous mechanisms arises. Several parameters may characterise an acoustic signal, amplitude, energy, duration etc.. Experimental results obtained on different materials have shown that statistical analysis based on the distribution function of certain of those parameters might allow the discrimination of different mechanisms and leads to the identification of the physical sources of the detected acoustic emission. Amplitude analysis enables such an approach to be attempted [2-3]. To describe the amplitude distribution, we can choose a differential function  $f(V)$  defined by the number of emissions at the amplitude  $V$  or a cumulative function  $g(V)$  defined by the number of emission above the amplitude  $V$ . To a first approximation this last function  $g(V)$  can be written equal to :

$$g(V) = N_0 \left( \frac{V}{V_0} \right)^{-b} \quad (1)$$

where  $V_0$  is the smallest detected amplitude,  $N_0$  the total number of events and  $b$  a parameter which may be a function of damage mechanisms for a given material [4]. On logarithmic scales the corresponding histogram will give a gradient the value of which is  $-b$ . As a consequence, the appearance of several mechanisms will divide the histogram into several linear zones.

#### a. First ply failure

Considering cumulative histograms on logarithmic scales obtained at rupture with unidirectional and cross plied composite  $(0, 90^\circ)_s$ , we can see that there is a very clear difference in the curves obtained from each type of specimen (Fig. 1). For the unidirectional case, we can only distinguish one linear part ( $b \approx 2$ ) and most of the amplitudes are lower than 65 dB. For  $(0^\circ, 90^\circ)_s$  materials, two straight lines can be clearly seen, one for amplitudes  $S$  lower than 65 dB and another for amplitude higher than 65 dB. So if the curve is approximated by two straight lines, it can be seen that the initial gradient  $b_1$  is close to those obtained with unidirectional composite ( $b_1 = 1,7$ ) followed by a second gradient giving  $b_2$  which is considerably lower ( $b_2 = 0,3$ ). Since it has been shown that matrix failure parallel to fibres produced large proportion of high amplitude ( $0,3 < b < 0,7$ ) [5], we can deduce that first ply failure may be responsible for the appearance of the second mechanisms of emission at high amplitude.

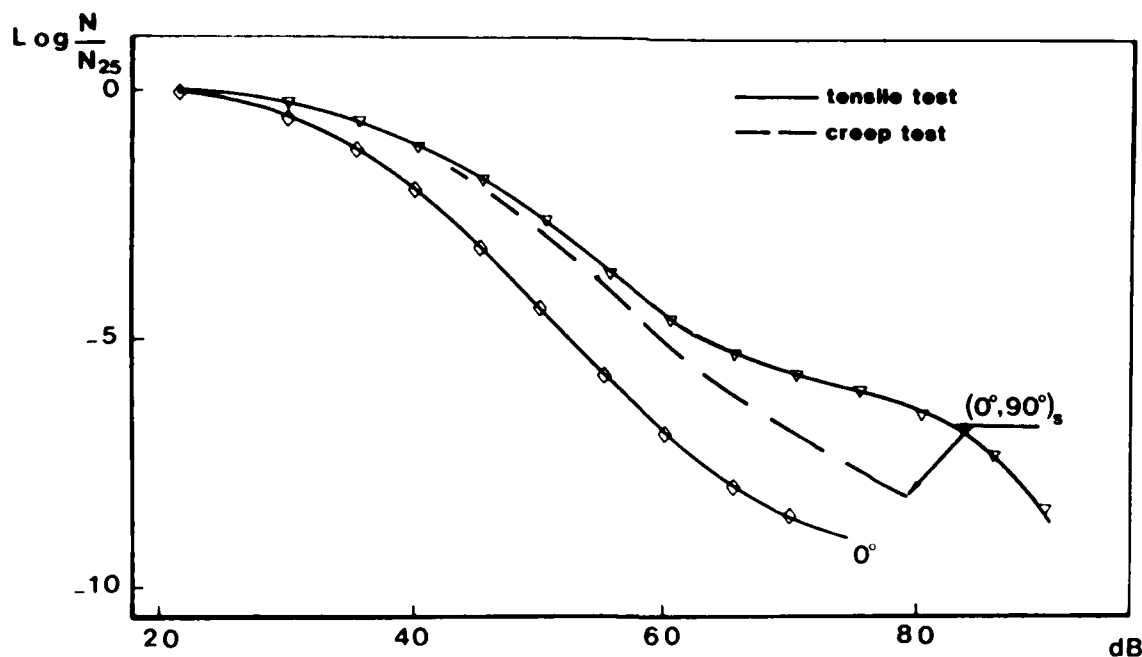


Fig. 1 : Cumulative histogram of acoustic emission amplitude of  $(0^\circ, 90^\circ)_s$  and unidirectional specimen at rupture.

It is then possible to detect the first ply rupture or its initiation with the appearance of the second distribution at high amplitudes (Fig. 2). A correlation has been made with calculated values of first ply failure using the Tsai-Hill criteria and also by visual observation (optical microscopy and X-ray) on a wide range of lay-ups. The results are in good agreement with acoustic emission detection (Fig. 3) when the ply rupture is activated by tension in the layer. If shear stress dominates, as for  $(45^\circ)_S$  composites for example, we detect the initiation of the ply rupture, that is to say the decohesion of fibres and matrix [6].

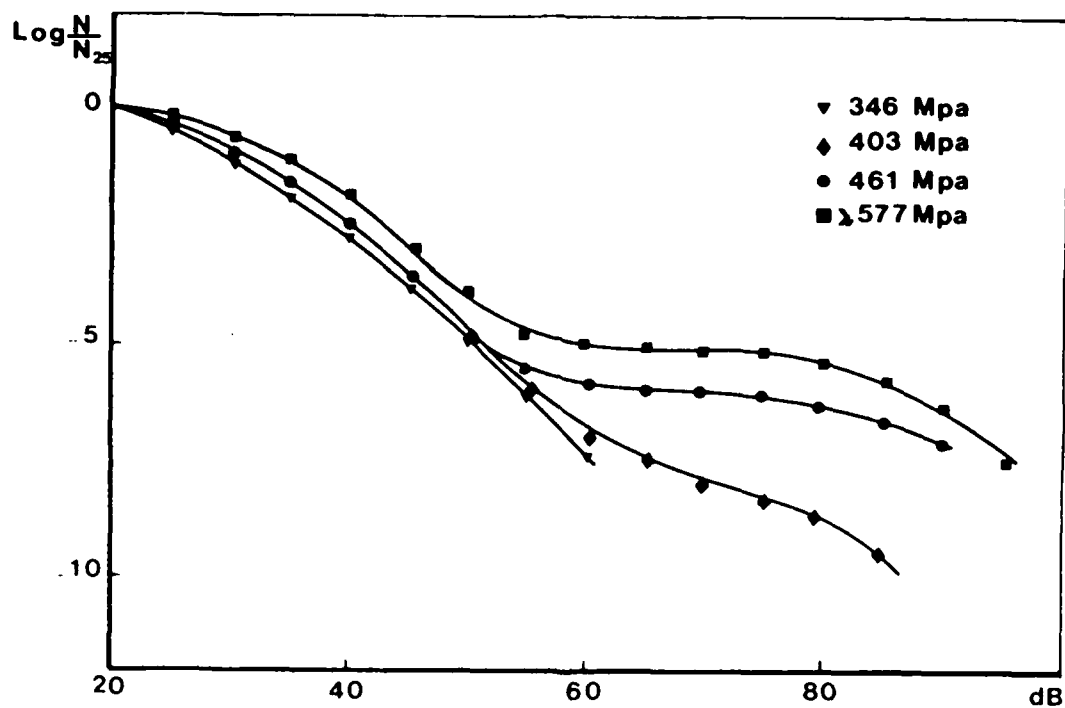


Fig. 2 : Evolution of the cumulative histogram of acoustic emission amplitude of  $(0^\circ, 90^\circ)_S$  specimen as a function of stress during tensile testing.

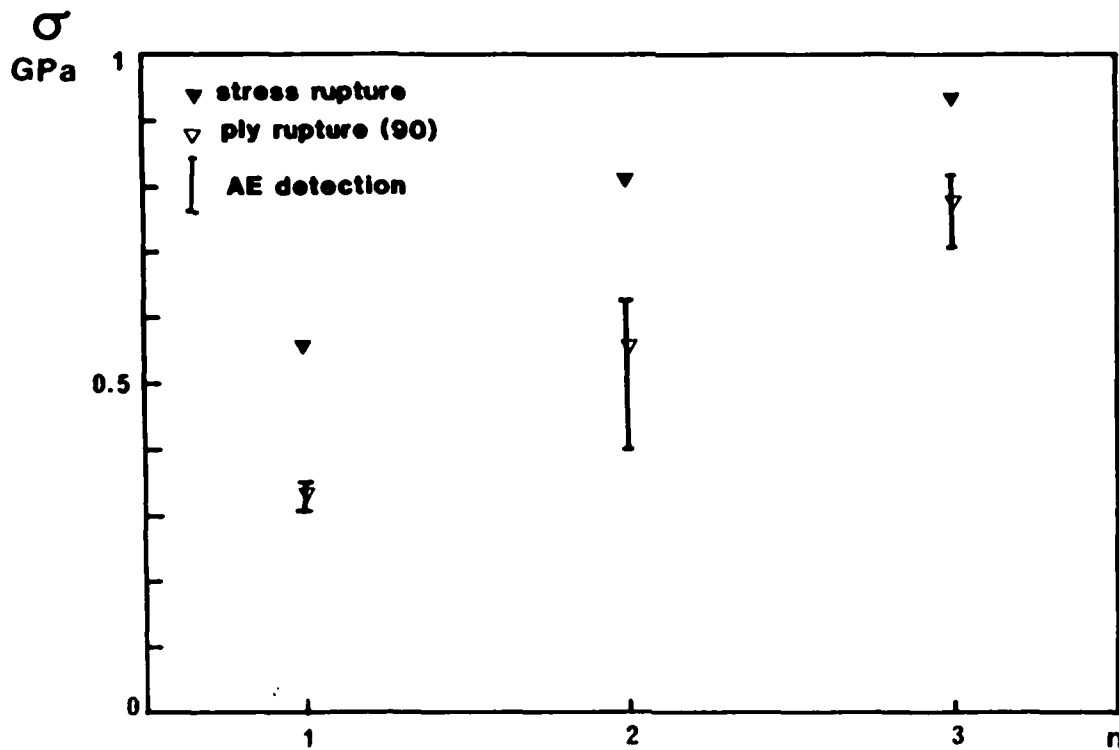


Fig. 3 : First ply failure detection by acoustic emission compared to the theoretical determination for  $(0_n, 90, \pm 45^\circ)_s$  composites ( $n = 1, 2, 3$ ).

#### b. Fibre breakage and matrix microcracking

The usefulness of the statistical analysis of the signal amplitudes depends on the theoretical means of modelling and analysis of damage accumulation. A new method of analysis could be based on a spectral approach of the differential histogram. For this, we use a new function for the cumulative histogram :

$$g(V) = N_0 \left( \frac{V}{V_0} \right)^{-b} \frac{V_a^{-b} + V_0^{-b}}{V_a^{-b} + V^{-b}} \quad (2)$$

For amplitudes such that  $V \gg V_0$  and  $V_0 \gg V_a$  we have :

$$\frac{V_a^{-b} + V_0^{-b}}{V_a^{-b} + V^{-b}} \approx \frac{V_a^{-b}}{V^{-b}} = 1 \quad (3)$$

which lead to the Pollock law (1) which is a limiting case of this function. The main advantage of the equation (2) is to give a corresponding symmetrical differential histogram with a maximum  $n_o$  at  $V_a$  [7]. When the amplitude is expressed in dB we have :

$$g(x) = N_o \left[ \frac{1 - \text{th } B \left( \frac{x - x_a}{2} \right)}{1 - \text{th } B \left( \frac{x_o - x_a}{2} \right)} \right] \quad (4)$$

with  $B = \frac{b \text{ Log } 10}{20}$ .

From equation (4) we can deduce :

$$\frac{1}{N_o} \frac{dg(x)}{dx} = \frac{n(x)}{N_o} = \frac{B}{4} (1 - \text{th}^2 B \left( \frac{x - x_a}{2} \right)) \frac{1}{1 - \text{th } B \left( \frac{x_o - x_a}{2} \right)} \quad (5)$$

Putting

$$\frac{n_o}{N_o} = \frac{B}{4} \frac{1}{1 - \text{th } B \left( \frac{x_o - x_a}{2} \right)} \quad (6)$$

We have :

$$f(x) = n_o \left[ 1 - \text{th}^2 B \left( \frac{x - x_a}{2} \right) \right] \quad (7)$$

On logarithmic scales, the differential histogram will be represented by two symmetrical linear parts of slope  $B$  and  $-B$  about  $x_a$ . Hence each observed peak can be deconvoluted and correlated with a particular degradation mechanisms.

This approach has enabled the detection of several mechanisms which produced emissions during tensile tests of P S P based unidirectional composites as several peaks were found with different values of  $B$  (Fig. 4). We can attribute these results, to microcracking of the matrix ( $x_a = 25$  dB and  $x_a = 34$  dB), fibre breakage ( $x_a = 40$  dB) and interfacial debonding ( $x_a = 47, 55$  and  $60$  dB). Compared to more conventional composite materials (Fig. 5), we can see a high proportion of events at low amplitude for the P S P composite. This can be attributed to microcracking of the resin

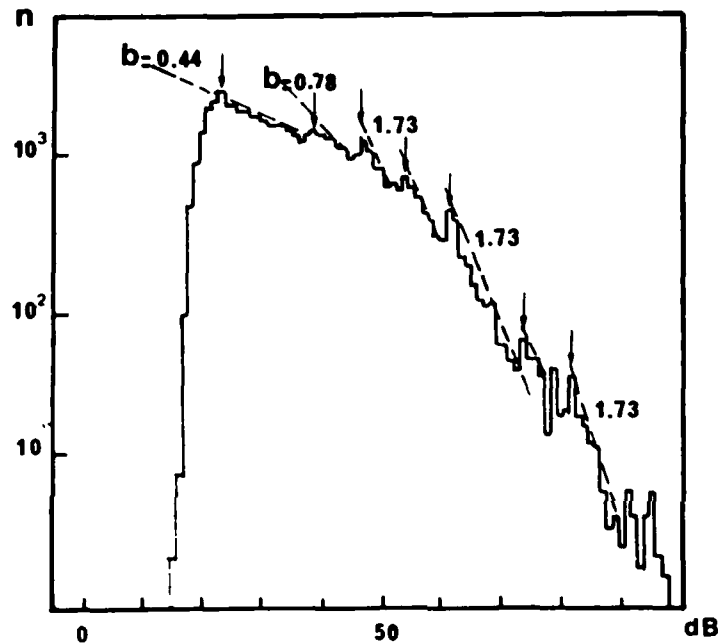


Fig. 4 : Representation on logarithmic scales of the normal amplitude histogram obtained on P S P unidirectional composite material ( $\sigma = 588$  MPa).

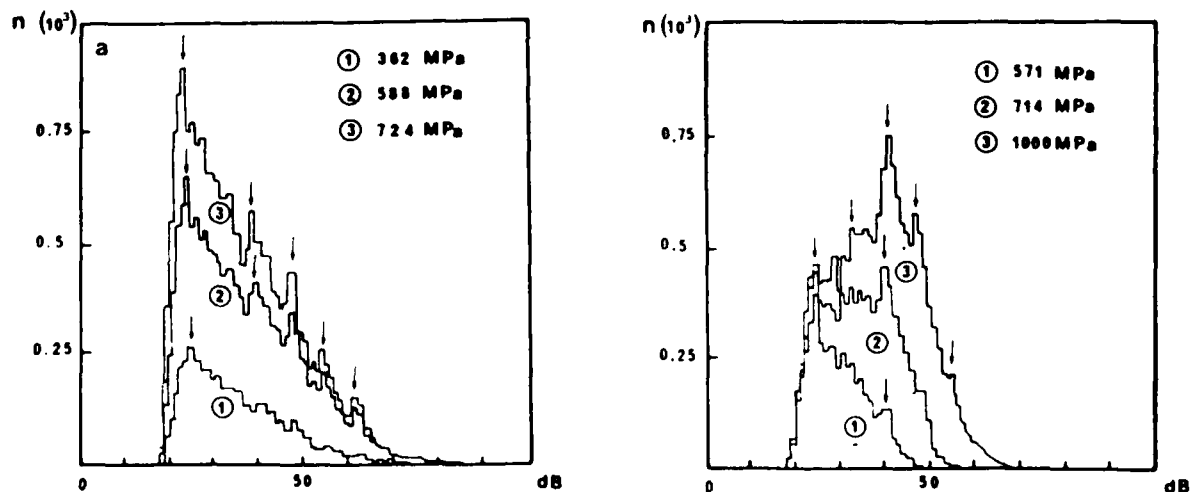


Fig. 5 : Comparison of the differential amplitude histogram for  
a) P S P and b) epoxy based unidirectional composite material.



due to internal stresses enhanced by the curing cycle. In fact, the P S P matrix is very brittle ( $K_{IC} = 0,28 \text{ MPa}$ ) and the triaxial state of stress due to the difference of the coefficients of expansion of the matrix and the fibres is very important when the composite undergoes temperature variations between 200 or 300°C as is the case during its elaboration.

## Quantitative evaluation

### a. Life prediction

A model of damage accumulation in unidirectionnal C F R P loaded in the fibre direction has been proposed and shown to be applicable to a number of different structures including filament wound tubes [1, 8]. It is assumed that the carbon fibres are perfectly elastic and that an unidirectionnal C F R P specimen can be considered to be a fibre bundle embedded in a viscoelastic matrix. The effect of load transfer by the shear of the matrix isolates fibre breaks in a narrow section of the composite so that the Rosen model of a chain in which the links are fibre bundle. Their lengths are determined by the load transfer between a broken fibre and unbroken fibres [9]. It has been shown that as damage is accumulated in a fibre bundle, the load which can be safely supported without causing catastrophic failure passes through a maximum [1]. At loads lower than the simple tensile strength of the bundle, the specimen can support a greater degree of damage than at the maximum load given by :

$$P = (N_o - N_f) f_o \left[ \frac{N_o - N_f}{N_o - N_f} \right]^{1/\delta} \quad (8)$$

where  $P$  is the applied load,  $N$  the number of broken fibres,  $N_o$  the total number of fibers,  $f_o$  a constant and  $\delta$  the Weibull shape parameter characterizing the failure probability of fibres. Figure 6 shows the curve given by equation 8. If at a given steady load  $P_1$ , a mechanism

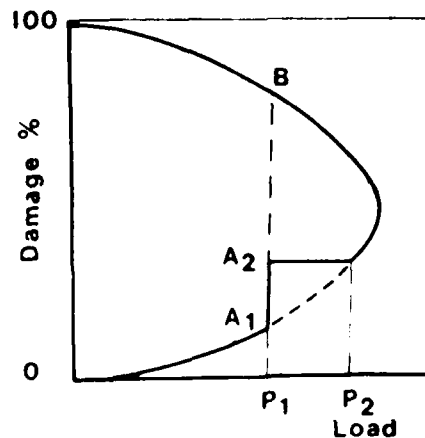


Fig. 6 : Evolution of the load bearing capacity of a bundle as fibres are broken in order at increasing strength while it is held under constant load.

of degradation produces further fibre failures, even though the load remains steady, damage will be accumulated along the line A, B. Acoustic emission reveals that further damage is accumulated at constant load and that if further loading takes place after reaching the damage level  $A_2$  no emissions are recorded when greater load is applied. It has been shown [1] that this observation demonstrates that the accumulated damage is the progressive failure of the weakest fibres in the composite. Under steady loading damage accumulation evolves in a quasi logarithmically decreasing fashion :

$$\frac{dN}{dt} = \frac{A}{(t+\tau)^n} \quad (9)$$

in which  $N$  is the number of events,  $t$  the time,  $\tau$  a time constant,  $n$  a power close to one ( $n = 0,99$  for 914 CTS unidirectional composites) and  $A$  a parameter which depends only on the applied load.

The combination of the damage accumulation model for composites and the analytical description of the acoustic emission recorded under steady loads permits minimum lifetimes to be calculated. In order to be able to calculate the residual life of structures it is necessary to obtain the master curve shown in Figure 6. This has been possible for prepreg specimen but not for cured specimens as failure is of a too brittle nature. The first part of the curve is easily obtained however as are the number of emissions to failure and the mean value of breaking load. As the damage level at the breaking load is a minimum level which must be exceeded at all lower loads, a calculation of the time necessary to reach that level will give a minimum life time prediction.

The rate of damage accumulation must depend on the viscoelastic properties of the matrix. This can be observed when less rigid epoxy based composites are under creep condition. In Fig. 7, the evolution of the compliance  $D(t)$ , for two resins is represented. The first resin system contains 70 % of CY 208 and 30 % of CY 205 whereas the second contains 30 % of CY 208 and 70 % of CY 205. The first matrix is much more compliant than the second one which leads to values of  $n$  lower than for the second material itself lower than the obtained value for 914 CTS composites (Table I).

$$D(t) \cdot 10^4 \text{ (Mpa}^{-1}\text{)}$$

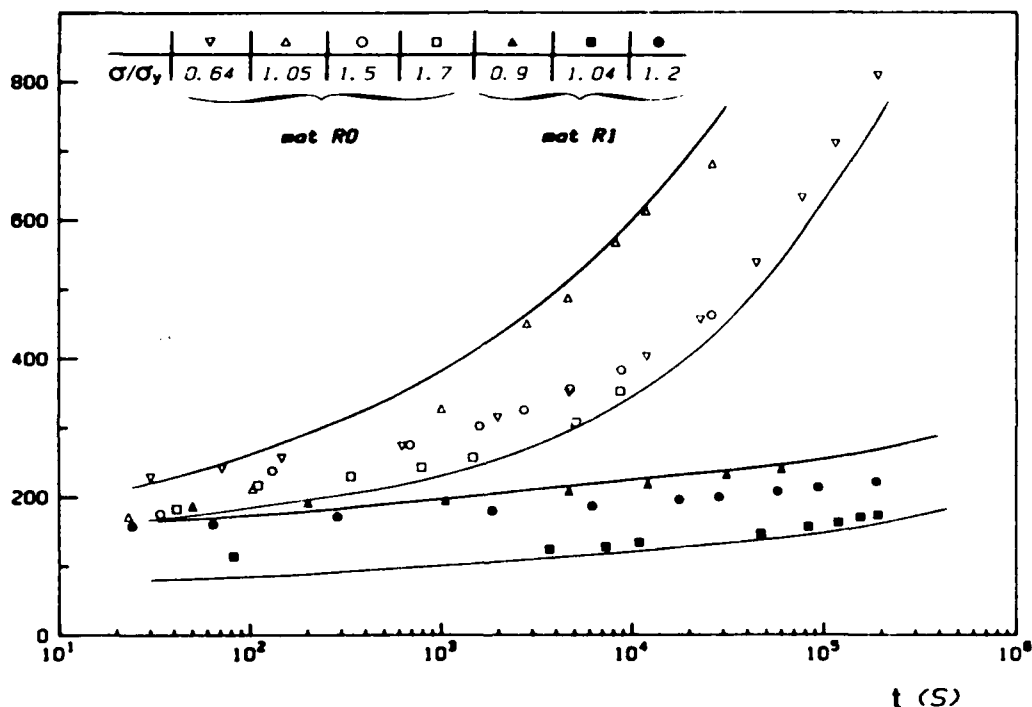


Fig. 7 : Influence of plastifier percentage (CY 208) on the compliance of the matrix.

Specimen	914	70 % CY 205 30 % CY 208	30 % CY 205 70 % CY 208
$n$	0,99	0,97	0,77

Table I : Values of  $n$  for different type of unidirectional composite.

This shows less tendency for the composites to stabilize. It follows that the coefficient  $n$  can be an indication of the degree of polymerisation of the system. This coefficient is also a function of the fibre volume fraction  $V_f$ , thus for a rigid matrix (914 CTS)  $n$  decreases to 0,97 if  $V_f$  is equal to 30 % instead of 0,99 for  $V_f$  equal to 60 %. This may be due to a greater freedom of movement of the resin. The coefficient  $n$  could therefore be indicative of good elaboration : good cure cycle, good volume fraction etc. At first glance, the difference of 0,02 in the value of  $n$  appears small, however in reality it is highly significant. In fact, if  $n$  is put equal to 1 and equation (9) integrated we see that :

$$N = A \log \frac{t + \tau}{\tau} \quad (10)$$

so that from equation (9) and (10) we have :

$$\log \frac{dt}{dN} = \frac{N}{A} + \log \frac{\tau}{A} \quad (11)$$

The function  $\log \frac{dt}{dN}$  is therefore a linear function of the accumulated number of emission  $N$  but any derivation of  $n$  from unity will result in a non linear curve for  $\log \frac{dt}{dN}$  which will become progressively noticeable with time (Fig. 8). The variation from linearity is shown to be strongly dependant on  $n$  [7].

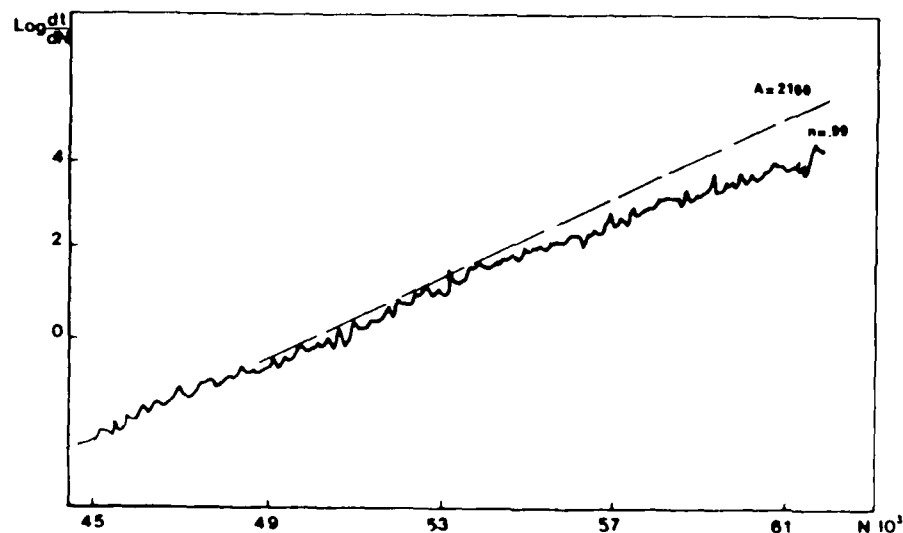


Fig. 8 : Evolution of the acoustic activity versus the accumulation of emissions during a constant load test on 914 CTS unidirectional composite.

For laminates, it has been shown that when the failure is fibre rupture dominated, the acoustic emission rate can be described analytically in the same way as for unidirectional composites. In that case, the coefficient  $n$  which are obtained, are generally lower than those obtained with unidirectional composite (Table II). The values of the parameter

Specimen	$0^\circ$	$(0^\circ, 90^\circ)_S$	$(\pm 15^\circ)_S$	$(0^\circ, 90^\circ, T)_S$
$n$	0,99	0,98	0,95	0,96

Table II : Values of  $n$  for each type of specimen

$n$  is then an indication of macroscopic effects (ply ruptures) which do not evolve. This has been verified by the analysis of amplitude histograms during creep conditions on  $(0^\circ, 90^\circ)_S$  and  $(0^\circ, 90^\circ, T)_S$  materials,  $T$  stands for cloth layer oriented at  $45^\circ$ . In these conditions, the cumulative amplitude histograms are very similar to those obtained on unidirectional composites and do not show high amplitude distribution (Fig. 1) as has been noticed during tensile testing. Then the existence of ply cracks in a  $90^\circ$  layer in a  $(0^\circ, 90^\circ)_S$  composite, for example, will lead to a change of  $n$  signifying greater damage accumulation in the  $0^\circ$  layers while the damage in the  $90^\circ$  layer does not progress but has an influence on the activity of the  $0^\circ$  layer.

#### b. Proof Testing

The variation of coefficient  $A$  as a function of applied stress can be obtained by applying steady loads at increasingly high loads long enough to determine the rates of emission as well as the precise value of  $n$ . The parameter  $A$  has been found to obey the relationship :

$$A = A_0 e^{k \sigma} \quad (12)$$

where  $A_0$  and  $k$  are constants and  $\sigma$  the applied stress.

A number of properties are inherent in composites and then the only recourse for their analysis is a statistical approach. With

reference to equation (12), it can be seen from Fig. 9 that there is an inverse relationship between the parameter  $k$  and the breaking strength. The coefficients  $k$  have been obtained with two creep tests at 800 and 1200 MPa. It is also possible to correlate the stress at failure and the time constant  $\tau$  for given specimens. From equation (11) we see that :

when  $\text{Log} \left( \frac{dt}{dN} \right) = 0 :$

$$\tau = A e^{-N_0/A} \quad (12)$$

where  $N_0$  is the number of emissions at  $\text{Log} \frac{dt}{dN} = 0$ .

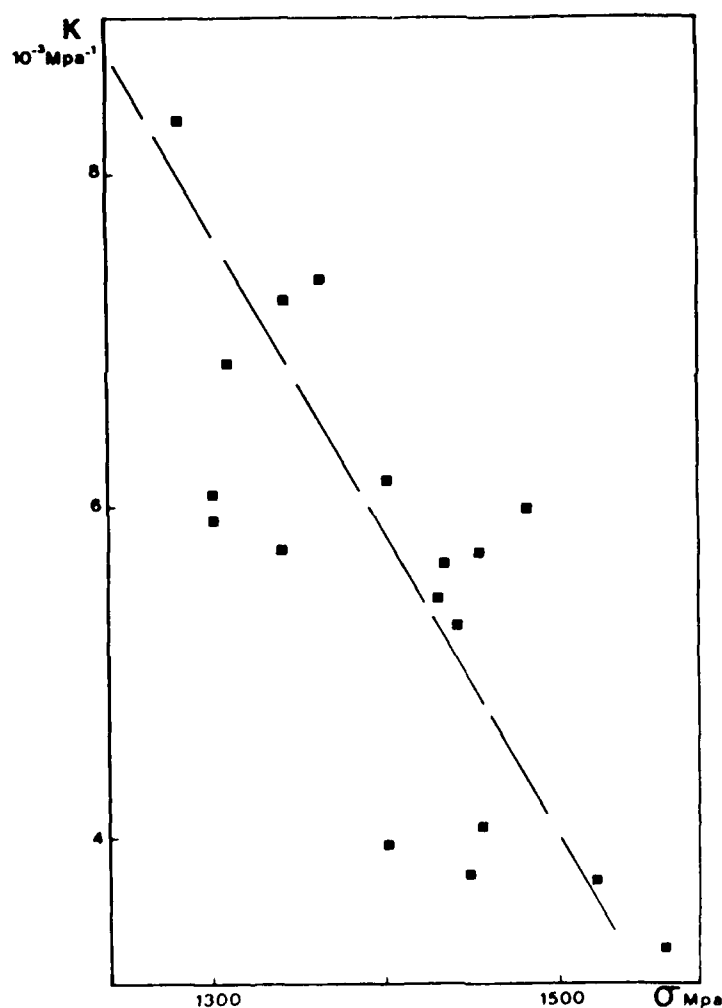


Fig. 9 - Correlation of the coefficient  $k$  and stress at failure for GFR/epoxy unidirectional composite materials.

It can be seen that the time constant  $\tau$  is a function of the total number of emissions, including the emissions produced during initial loading until the condition  $\log \frac{dN}{dt} = 0$  is reached at the rate given by the coefficient A. There appears to be little correlation between  $N_0$  and the breaking strength but there is reasonable correlation between  $\tau$  and the stress at failure, as it can be seen from Fig. 10. The coefficient k and  $\tau$  can be obtained during proof testing at low loads which allows an extrapolation of the behaviour during service condition and using the life prediction model as a statistical treatment of these parameters, a better prediction of the stress at rupture could be obtained.

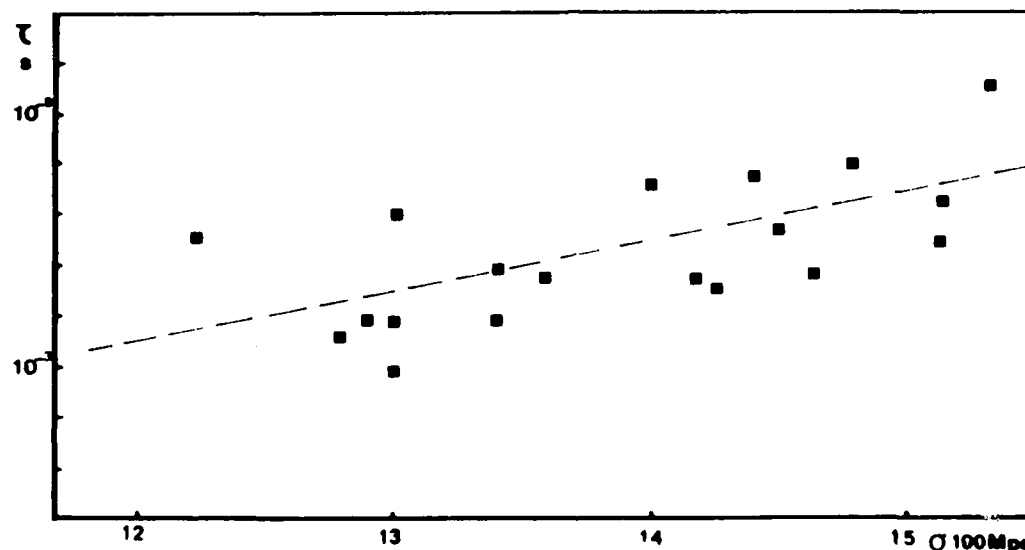


Fig. 10 : Correlation of the coefficient  $\tau$  obtained during a creep test (1200 MPa) and stress at failure for 914 CTS unidirectional composite materials.

## Conclusion

Although acoustic emission is a global and indirect technique, it is possible to use it in both a qualitative and a quantitative way to define the accumulated damage in CFRP. Amplitude analysis enables first ply failure detection and also discrimination between fibre breakage, matrix cracking or interfacial failure and so reveals the effect of internal stress which can be due to the curing cycle on different unidirectional CCFRP specimens. When it is fibre failure dominated, counting events enables damage to be quantified as well as the definition of damage kinetics. These are related to the rheology of the matrix but also to macroscopic defects (first ply failure) which do not progress. Statistically, certain of the parameters characterizing the kinetics can be related to the breaking strength of the material. All these results might be taken into account, for example, during proof testing after fabrication.

## References

1. A.R. BUNSELL, D. LAROCHE, D. VALENTIN  
"Damage and failure in carbon fibre-reinforced epoxy resin".  
Long term behavior of composites. ASTM STP 813 T.K. O'Brien. Ed.,  
American Society for Testing and Material, Philadelphia 1983, pp.  
38-54.
2. A. ROTEM, E. ALTUS  
"Fracture modes and acoustic emission of composite materials".  
J. of Testing and Evaluation, 137 n° 1 (Jan. 1979) pp. 33-40.
3. J.T. RYDER, J.R. WADIN  
"Acoustic emission monitoring of a quasi isotropic graphite epoxy  
laminate and fatigue loading".  
A S N T Spring Conf. (San Diego 1979), pp. 9-22.
4. A.A.B. POLLOCK  
"Acoustic emission amplitudes".  
Non destructive testing, 6 n° 5 (Oct. 1983) pp. 63-78.
5. D. VALENTIN, P. BONNIAU, A.R. BUNSELL  
"Failure mechanism descrimination in carbon fibre reinforced epoxy  
composites".  
Composites, Vol. 14? n° 4 (Oct. 1983), pp. 345-351.
6. B. BOUTIN, D. VALENTIN, F. PEREZ.  
"Study of the first layer rupture in fibre reinforced composites by  
non-destructive evolution".  
European Mechanics Colloquium 182, Mechanical characterisation of  
Load bearing fibre Composite laminates. Brussels, 29-31, Aug. 1984,  
C, II.4.
7. D. VALENTIN  
"A critical analysis of amplitude histograms obtained during acoustic  
emission tests on unidirectional composites with an epoxy and P S P  
matrix".  
to be published.
8. D. VALENTIN, A.R. BUNSELL  
"A study of damage accumulation in carbon fibre reinforced epoxy  
resin structures during mechanical loading monitoring by acoustic  
emission".  
J. Reinforced Plastics and Composites, 1-4 (1982), pp. 314-334.
9. B.W. ROSEN  
"Tensile failure of fibrous composites".  
AIAA Journal, 1964, Vol. 2, p. 1985.



#### Discussion of Session IV

Strictly speaking acoustic emission is a destructive rather than non-destructive technique. However, since acoustic emission is widely used to monitor the properties and behaviour of fibre composite materials, it was decided to include it in this workshop.

Y L Hinton, R J Shuford and W W Houghton of the Composites Development Division, Army Materials and Mechanics Research Center, Massachusetts 02172 have investigated acoustic emission during cure of fibre reinforced composites, and conclude that acoustic emission is a potential in-process quality control technique for resin-based materials. Acoustic emission data (including events, counts, count rate, rms and amplitude distribution) and dc-resistance data were collected during the cure (heating) and cool-down of 6-ply SP250/S glass and Fiberite 934/kevlar 49 prepreg laminates. Acoustic emission appears to be very sensitive to microstructural changes in laminates occurring during the cure. The acoustic emission observed during the heating phase is thought to be due partly to outgassing of the resin and partly to cure shrinkage (caused by polymerization/cross-linking), whereas the acoustic emission during cool-down is attributed to the creation of residual stresses associated with mis-match of thermal expansion coefficients between fibre and matrix materials. Under identical experimental conditions, kevlar/epoxy laminates produced significantly more counts with higher amplitudes than the glass/epoxy laminates. Correlations were found between the acoustic emission activity, the dc-resistance and the resultant residual stresses. A preliminary account of this work has been published in US Army publication AMMRC MS 82-3, May 1982).

Session V: Control of fibre orientation in short fibre composites

A NON-DESTRUCTIVE CONTROL OF FIBER CONTENT AND ORIENTATION  
IN SMC-ARTICLES

G Menges and H Cherek

Institut für Kunststoffverarbeitung (IKV), TH Aachen, West Germany

Fiber reinforced compression moulded parts with complex geometries show a wide variation in their mechanical behaviour. The reason for this is the undefined flow direction, which changes from cycle to cycle and produces different fiber orientations and different fiber contents at critical points in the moulding. With manually operated moulds and presses these differences have to be tolerated. It is evident that there exists an urgent need for non-destructive quality control of critical points on every part produced.

We now suggest that this quality control is best achieved by an X-radiographic method in conjunction with automated optical assessment. Hitherto we have used the birefringence of a laser beam transmitting an X-radiograph (Menges and Geisbusch 1979). It is demonstrated that information about the average fiber distribution and fiber orientation is thus obtained.

NONDESTRUCTIVE QUALITY CONTROL OF HEAVY-DUTY COMPONENTS

Variable flows of mat packets and resultant undesirable orientations and separations must always be expected. In shaped components which have supporting functions, e.g. in aircraft and automobile construction, it is especially not possible to do without quality control in respect of quantity and direction of fiber. Such tests may be either destructive or nondestructive. Since destructive tests, because of the lack of repeatability, are unable to supply representative findings for the manufacturing process, nondestructive tests methods are of special interest.

Work on a variety of nondestructive testing methods is being done at the Institute. Thus, the measurement of several characteristic mechanical properties, such as deflection under load or the like, permits conclusions to

be drawn as to the quantity and position of fibers in the component. This method, however, is specific to the component and must still be confirmed by practical experience.

A method is presented here which permits the quantitative determination of fiber orientations and local fiber contents by means of X-radiographs. The reinforcing fibers appear on the radiographs as transparent rectangles on a dark background which, upon irradiation with coherent light, generate special diffraction effects. Evaluation of the resultant diffraction pattern by computer, permits exact calculation of relative local fiber contents and orientations in the X-rayed sector of the component. The mathematical bases and derivation of the method of evaluation are explained in the Appendix to this report. Studies relating to this subject area will also be found in Meyer and Erber (1977), Polato, Panini and Gianotti (1980), Lipson and Lipson (1969) and Kreis (1984).

### 1.1 Instruments

Figure 1 shows the test setup for the evaluation of diffraction images of radiographs.

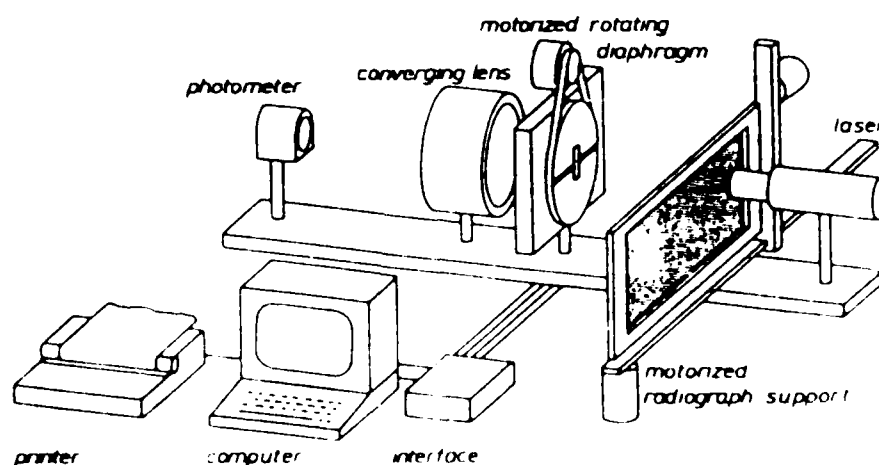


Figure 1. Optical bench for the evaluation of radiographs

An unpolarized He-Ne laser beam with wavelength 632.8 nm and power 5 mW serves as the light source. The beam diameter of 0.83 mm is expanded to 8.3 mm by means of a beam expansion adapter. The collecting lens located behind the diffracting object in the standard test setup for the visualization of diffraction images (compare for example Lipson and Lipson, 1969) is omitted in the present case. Instead, a slightly convergent bundle of rays is produced by reducing the focal length of the optical expansion system to 800 mm, this sharply images the diffraction pattern in the focal plane of the optical expansion system and focusses the diffuse beam to a point.

The photographic film holder for the radiographs is moveable in both horizontal and vertical direction by way of computer-controlled stepping motors, so that each point of the picture can be moved into the path of the laser beam.

A rotating slit diaphragm, likewise computer-controlled, is located in the focal plane of the optical beam expansion system (Figure 2).

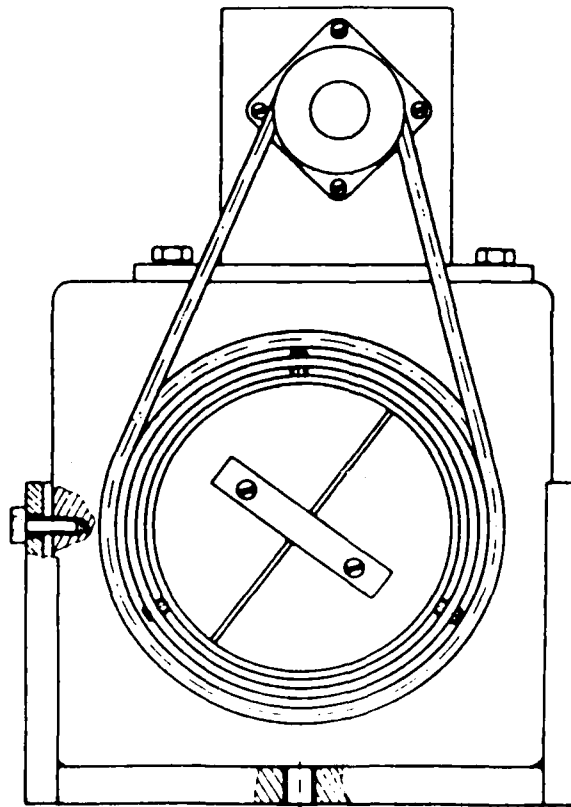


Figure 2. Rotating rectangular diaphragm

Because of the very high light intensity (see Appendix), the diffuse beam concentrated on the focal point is screened out of the continuing path of rays for all angles of rotation  $\psi$  of the diaphragm. Hence a considerably smaller measuring range and a correspondingly higher resolution may be selected on the photometer.

The smallest step width of the stepping motor operating the diaphragm is  $0.9^\circ$ . With the speed reduction ratio of 4:1 between motor and diaphragm drive this results in a resolving power of the angle of rotation  $\psi$  of  $0.225^\circ$ , or, expressed in another way, 800 test positions during a half-turn of the diaphragm. Each test value  $\hat{I}(\psi)$  thus obtained then corresponds to the light intensity of the portion of the diffraction image passed by the diaphragm. It is shown in the Appendix that the intensity  $\hat{I}(\psi)$  thus measured for the diaphragm angle  $\psi$  is directly proportional to the number  $N(a)$  of the glass fibers oriented at the angle  $a = \psi - 90^\circ$ .

$$\hat{I}(\psi) = N(a) \quad (1)$$

For reasons of symmetry,

$$\hat{I}(\psi) = \hat{I}(\psi + 180^\circ)$$

also applies, so that only a half turn of the diaphragm is ever required in order to plot all the data.

A microprocessing system based on Motorola's 68000 is used to control and evaluate the measurements. By means of suitable interfaces and stepping motors, the computer is able to position the radiograph, preset the angle of rotation of the diaphragm and read in the intensities measured on the photometer. In addition, a printer with graphics capabilities is added for printing out the results. With a view to easy expansion and good maintainability, the evaluation programs have been written in the high-level structured programming language "SOBAS".

On scanning of the diffraction image the large number of positions of diffraction pattern relative to diaphragm slit produces geometric fuzziness in

the measured intensity values and this prevents direct conclusions as to the numbers of fibers. This fuzziness is the result of optical interference attributable to the test set-up. Figure 3 shows the influence of this fuzziness on the intensity distribution for an ideal lattice of rectangles with direction of orientation  $\alpha = 0^\circ$ . The reproducibility of these influences, however, makes it possible for the computer to eliminate them from the intensity distribution. The result of this process for an ideal diffraction lattice having the two orientation directions  $\alpha_1 = 170^\circ$  and  $\alpha_2 = 0^\circ$  and a line ratio of 2:1 is shown in Figure 4. The relative percentages of fiber in the two directions of orientation can now be read off directly on the diagram.

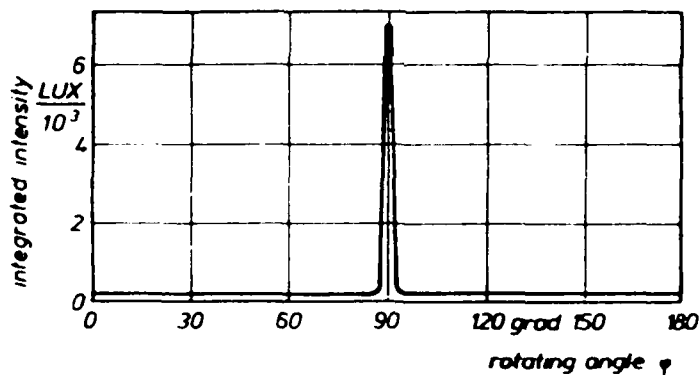


Figure 3. Integrated intensity of a lattice of rectangles

Because of the many unknown influences on the proportionality factor (X-ray conditions, film density, scattered light, laser intensity, etc.), the proportionality of the intensity test values to the numbers of fibers (Equation (1)) does not lend itself to determination of the absolute number of fibers oriented at the angle  $\alpha$ . The relative number of fibers oriented at each angle may, however, be determined very accurately by means of the computer. The reference area for measurement of this orientation parameter is then in no way limited by the diameter of the laser beam. Owing to the

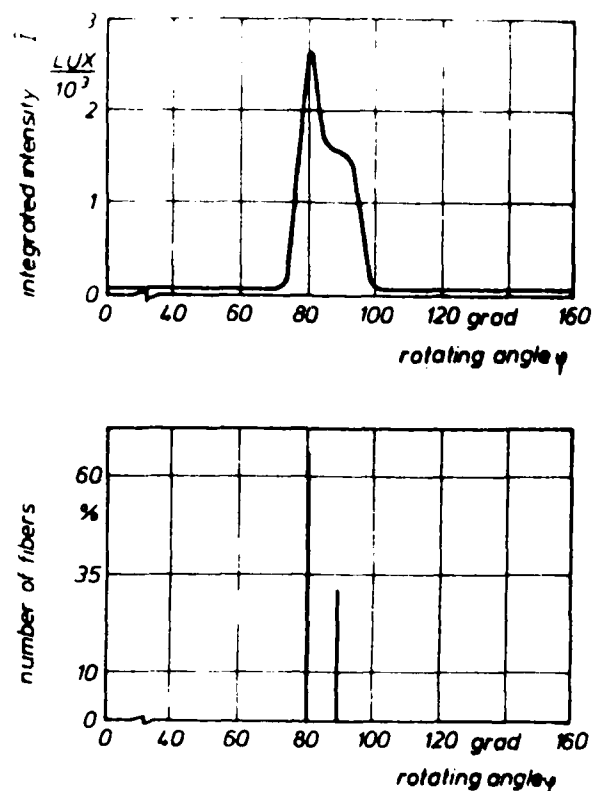


Figure 4. Integrated intensity and number of fibers of a cross lattice

facility for displacement of the photographic film holder, the entire radiograph can be read point by point in successive measurements and reconstructed in the computer program. By this method the intensity distribution of the respective diffraction image is plotted by way of the angle of rotation  $\psi$  of the diaphragm for each point. If attention is paid to even illumination of the film when the X-radiograph is photographed, and the photograph is properly developed, the proportionality constant in Equation (1) may be regarded as constant over the entire film so that test values of various points on the picture can also be compared directly with each other. Flow-induced separations ("resin pits") or accumulations of fiber can thus be reliably detected. The resolution of the method is thereby determined in advance by the area sampled, i.e. by the diameter of the laser beam. Local differences within a sample area cannot be detected because of the integrated character of the measurements.

To assist interpretation of the results, a graphic presentation is generated by the computer, representing an idealized image of the fibers in the sector of the component inspected. Although no direct correlation exists with the



actual location of the fiber, these graphics have proved to be very good for analysis of orientational states and detection of mechanically weak points.

An orientation parameter, independent of direction, which reflects the degree of fiber alignment in freely selectable sectors, serves for the general description of orientational states in the component. Application of the method will now be demonstrated for several practical examples.

## 2. Examples of application

"Acceptable" radiographs, which of course are not always obtained are naturally always a pre-requisite for the determination of fiber orientations by this method. The results of studies in this subject area, together with general instructions for X-radiography of SMC components, are summarized by Nottrott (1983) so details of the technique will not be discussed.

In many practical cases of application, for example in two-dimensional components having a wall thickness of several millimeters, the preparation of radiographs presents no great difficulties.

### Example 1

Figure 5 is a schematic drawing of an automobile bumper (fender) produced in the molding process, with the location of insertion of a blank identified by the shaded rectangle, and the sector inspected by X-radiography identified by the broken rectangle.

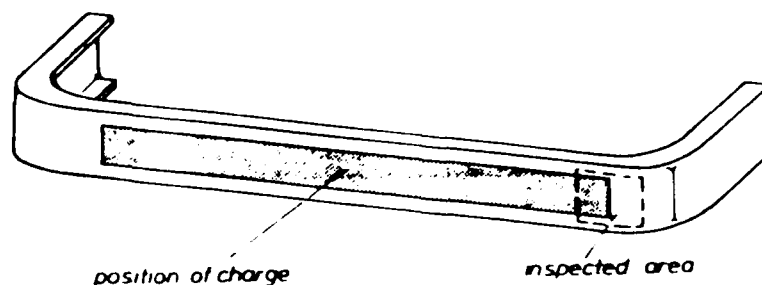


Figure 5. HMC bumper

The raw material consisted of a pre-preg layer with unidirectional continuous fiber reinforcement and two surface layers with random short fiber reinforcement (HMC). The fiber image generated by the computer and the intensity distributions of two test points are shown in Figure 6.

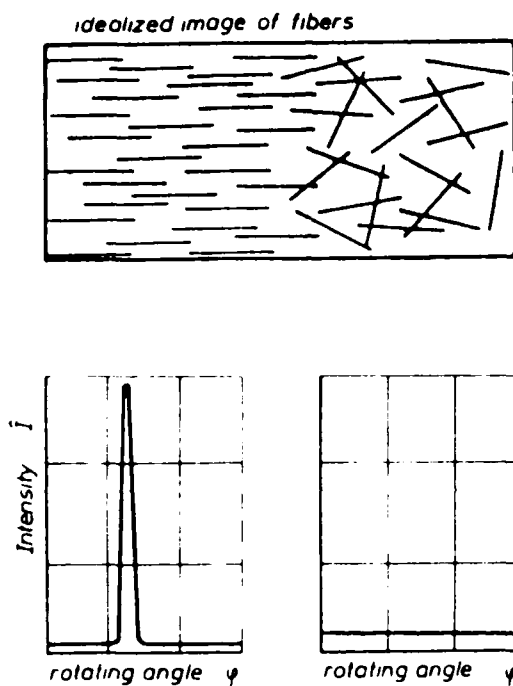


Figure 6. Fiber distribution in an HMC bumper

Here only the relative number and the orientational state of the fibers can be obtained from the image. In the left half of the ideal fiber image the aligned continuous fibers do not appear as continuous fiber images. Instead they appear as highly oriented short fibers.

In this case the blank packet inserted into the die turned out to be too short. Since the unidirectional layer is not capable of flow in the direction of orientation, the critical boundary regions of the bumper were filled only with the irregular fiber layers flowing off the surface layers.

### Example 2

In a rectangular plate of SMC, a region with mould boundary lying parallel to the direction of flow was inspected. Figure 7 shows the flow rate in the center of the flow channel and the resulting fiber orientations in the finished part.

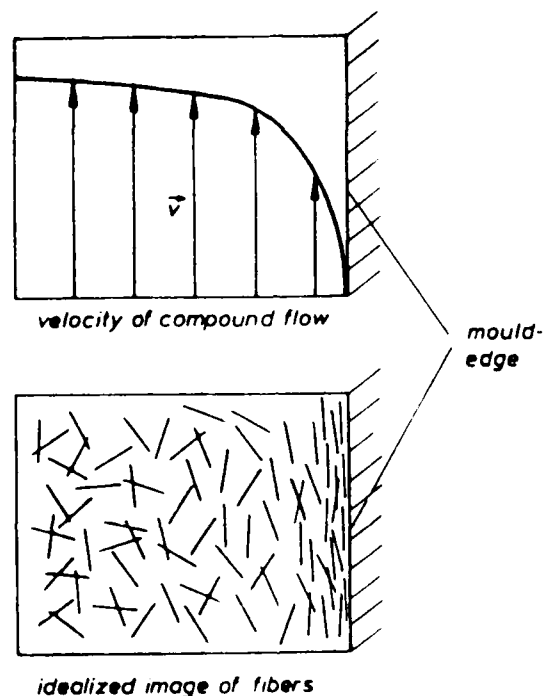


Figure 7. Origin and nature of fiber orientations in SMC parts.

Here the preferred orientations in the region of the mould edge are attributable to excessive shear stress of the material due to adhesion to the wall in the mould-filling process.

However, a similar fiber image is also obtained in the case of unfavorable flow-front travel in the filling phase. When blanks are not centered in the mould, in some cases the main flow front is surrounded by flow from already filled mould regions. In addition to the strong orientations which, owing to the high shear of the detoured flow front are produced in the narrow flow channel between main flow front and mould boundary, a bond line results. Bond line fractures on removal of the moulded part are the inevitable consequence.

### Example 3

An unfavourable flow may lead to strength problems in the case of inserts too. In this example a mounting strap about 4 cm wide was reached transversely by the flow front. The resin pits produced behind the strap in the direction of flow are clearly detectable in the fiber image (Figure 8).

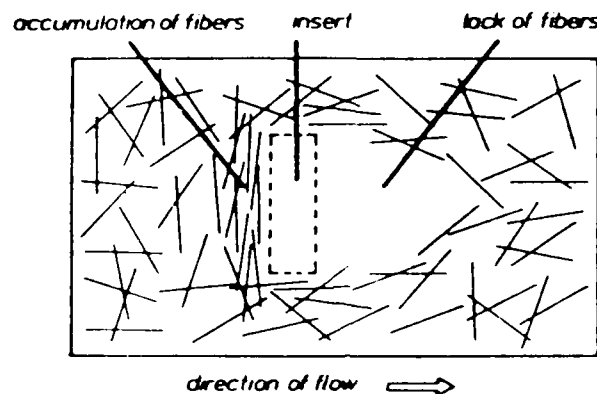


Figure 8. Lack of fibers caused by inserts

When their cause is known, such weak spots can usually be eliminated by alterations to the geometry of the blank and/or of the place of insertion of resin mats.

### Example 4

Accumulations of fibers before dummy areas which are reached by the flow front only in the process of filling the mould are another frequently observed problem. In the worst case such fiber accumulations hinder the transport of fibers past the dummy area to more distant regions of the shaped part. This was the case in the component whose fiber distribution is shown in Figure 9.

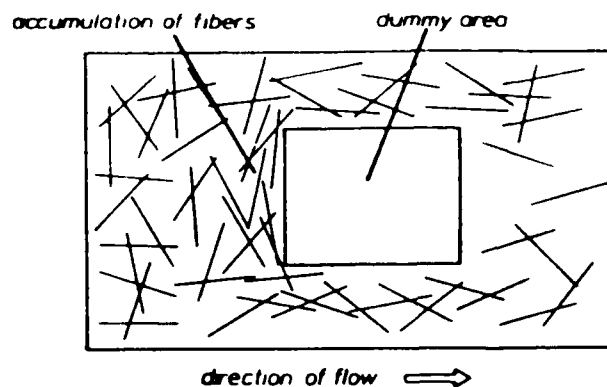


Figure 9. Fiber accumulation at a dummy area

If the problem cannot be solved by altering the location of the insert, which frequently the case in practice, checking of the suspect regions of the shaped part is especially important.

#### Example 5

In all cases the flow distance influences fiber orientation and hence the strengths of SMC components. Figure 10 shows the curve of the orientation parameter, independent of direction, over the flow distance  $l$  in a SMC part which was moulded at a constant compression rate.

In this case the increase of orientations with growing flow path is explained by the elevation of shear rates in the moulding material at decreasing flow channel height and almost constant compression rate of the press. Not until the end of the flow path at the mould boundary is there again a decrease in the orientation parameter, owing to turbulences in flow of the fibers.

The examples presented show how important fiber orientation and distribution measurements are for quality control and calculations of the strength of SMC parts. But in addition, such measurements also permit an increase in the quality of moulded parts generally. On modern presses, for example, the compression rate can be varied over the flow path. Owing to the possibility to control the positions of fibers in the component, the compression rate can then be optimized so that the strength-reducing orientations shown in the last example become minimal.

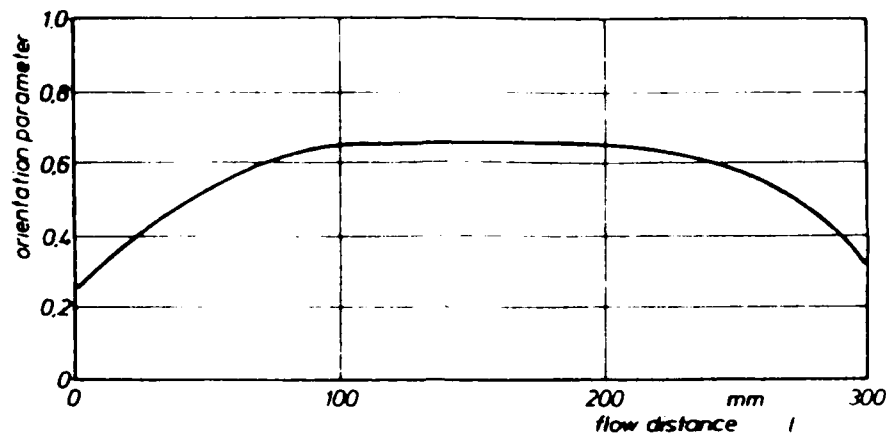


Figure 10. Orientation parameter as a function of flow distance

#### References

- Menges G and Geisbüsch P (1979) Die Glasfaserorientierung und ihr Einfluß auf die mechanischen Eigenschaften thermoplastischer Spritzgießteile Mitteilung aus dem IKV, Aachen
- Meyer F and Erber H (1977) Vergleichende Beobachtungen zur Glasfaseranordnung in spritzgegossenem Prüfkörpern, Modellkörpern und Formteilen aus GFT Problemseminar Konstruieren mit verstärkten Plasten II H 4/77, Tech. Universität Dresden
- Polato F, Panini P and Gianotti G (1980) A new technique for the measurement of glass fiber orientation in composite materials Istituto Guido Domjani S.p.A., Novara
- Lipson S G and Lipson H (1969) Optical Physics, Cambridge University Press, Cambridge
- Kreis G (1984) Rechnerunterstützte Auswertung von Röntgenaufnahmen zur Bestimmung von Faserorientierungen in GFK-Bauteilen Diplomarbeit am IKV, Aachen Betreuer: H Cherek

Nottrott A (1983) Untersuchungen zur Röntgendurchstrahlungsprüfung von SMC-  
Teilen Studienarbeit am IKV, Aachen Betreuer: H Cherek

Derek H (1982) Zur Technologie der Verarbeitung von Harzmatten Dissertation an  
der RWTH Aachen

Hafer U (1981) Geschwindigkeits- und Druckprogrammierung für die SMC-  
Verarbeitung Diplomarbeit am IKV, Aachen Betreuer: H Derek

## Appendix

For a wave diffracted by a slit, the amplitude given by Fourier theory is

$$\psi(\bar{u}) = \int_{-a/2}^{+a/2} e^{-i\bar{u} \cdot x} dx$$

where the phase shift

$$\bar{u} = \frac{2\pi}{u} x \sin \theta$$

$u$  = wavelength

$\theta$  = diffraction angle

$a$  = slit width

Hence

$$\psi(\bar{u}) = \frac{1}{i\bar{u}} \left[ e^{-i\bar{u}x} \right]_{-a/2}^{+a/2} = \frac{a \sin \frac{a \cdot \bar{u}}{2}}{\frac{a \cdot \bar{u}}{2}}$$

And the intensity is

$$I(\bar{u}) = |\psi(\bar{u})|^2$$

For a slit with a definite length  $b$ , we use the two-dimensional Fourier transformation:

$$\phi(\bar{u}, \bar{v}) = \int_{-\infty}^{\infty} \int_{-\infty}^{\infty} f(x, y) e^{-i\bar{u}x} \cdot e^{-i\bar{v}y} dx \cdot dy$$

For more than one slit in the plane the amplitude will be

$$f(x, y) = \sum_{j=1}^N \hat{f} \operatorname{rectf} \frac{(x - x_j)}{a} = \begin{cases} 1 & \text{for } |x| \leq a/2 \\ 0 & \text{for other cases} \end{cases}$$

With this the diffraction pattern of the plane with many rectangular slits of dimensions  $a \times b$  corresponds to

$$\phi(\bar{u}, \bar{v}) = \hat{f} \cdot a \cdot b \cdot \frac{\sin \frac{a \cdot \bar{u}}{2}}{\frac{a \cdot \bar{u}}{2}} \cdot \frac{\sin \frac{b \cdot \bar{v}}{2}}{\frac{b \cdot \bar{v}}{2}} \cdot \sum_{j=1}^N e^{-i\bar{u} \cdot x_j} \cdot e^{i\bar{v} y_j}$$



And for whole intensity

$$I(\bar{u}, v) = |\psi(\bar{u}, v)|^2$$

$$= \left[ \hat{f} \cdot a \cdot b \cdot \frac{\sin \frac{a \cdot \bar{u}}{2}}{\frac{a \cdot \bar{u}}{2}} \cdot \frac{\sin \frac{b \cdot v}{2}}{\frac{b \cdot v}{2}} \right]^2$$

$$\sum_{j=1}^N \cdot \sum_{l=1}^N \cdot e^{-i\bar{u}(x_j - x_l)} \cdot e^{-iv(y_j - y_l)}$$

The summation on the basis of probability gives finally for the intensity for cases  $(\bar{u}, v) \neq (0, 0)$

$$I(u, v) = \left[ \hat{f} \cdot a \cdot b \cdot \frac{\sin \frac{a \cdot \bar{u}}{2}}{\frac{a \cdot \bar{u}}{2}} \cdot \frac{\sin \frac{b \cdot v}{2}}{\frac{b \cdot v}{2}} \right]^2$$

## ORIENTATION MAPPING

F.C.Frank

H.H.Wills Physics Laboratory  
Tyndall Avenue, Bristol BS8 1TL, England.

### Abstract

The orientational statistics of uniaxial objects (e.g. chopped fibres, discs, or crystallographic poles) can be fully displayed in a two-dimensional map: customarily in the stereographic projection. Essentially triaxial objects, on the other hand (e.g. crystal lattices, or chopped ribbon) require three parameters to specify their orientation, and therefore require a three-dimensional orientation map. It can be presented on the printed page as a stereoscopic pair.

This poses the question: What are the best coordinates for the three-dimensional orientation map? The answer is that there are several, with various alternative merits, all of them founded on Euler's "Nova Methodus.." of 1776 (not the Euler angles) which utilizes the theorem that any change of orientation of a rigid body can be represented as a single rotation through an angle  $\omega$  ( $0 < \omega < \pi$ ) about an axis represented by the unit vector

$$\underline{l}^0 = (l_1, l_2, l_3): l_1^2 + l_2^2 + l_3^2 = 1$$

On this basis, choosing a standard orientation to be represented by the point at the origin, any other orientation will be represented as a point at:

$$\underline{\Lambda} = \underline{l}^0 \cdot f(\omega)$$

where  $f(\omega)$  is some function of  $\omega$ , monotone increasing in ( $0 < \omega < \pi$ ) and preferably antisymmetric ( $f(-\omega) = -f(\omega)$ ). Choices with particular advantages are:

- (I)  $t(\omega) = k\omega$  ,  
 (II)  $t(\omega) = \sin \frac{1}{2}\omega$  ,  
 (III)  $t(\omega) = \tan \frac{1}{2}\omega$  ,  
 (IV)  $t(\omega) = [\frac{3}{4}(\omega - \sin \omega)]^{1/3}$

These functions are sketched in figure 1.

(I) has the merit of crude simplicity: it suffices for purely topological arguments.

(II) is algebraically advantageous. The Cartesian components of  $\underline{A}$  :

$$(\xi, \eta, \zeta) = (l_1, l_2, l_3) \sin \frac{1}{2} \omega$$

together with

$$\chi = \cos \frac{1}{2} \omega$$

form the real and imaginary components of elements of the unitary  $2 \times 2$  complex Cayley-Klein matrix which affords the most efficient way of calculating a combination of rotations  $(\xi, \eta, \zeta, \chi)$ , though never actually used by Euler are called the Euler parameters by Whittaker (1904).

(III) yields correspondingly the parameters of Rodrigues (1840):

$$\begin{aligned} (R_1, R_2, R_3) &= (\xi / \chi, \eta / \chi, \zeta / \chi) \\ &= (\omega_1, \omega_2, \omega_3) \tan \frac{1}{2} \omega , \end{aligned}$$

which give the geometrically most advantageous map: because the trajectory of the map-point for a continuing rotation  $\underline{R}_B$  about one axis following a rotation  $\underline{R}_A$  about another axis is a straight line: and the orientationally equidistant surface between two given orientations is a plane. Rotations  $\underline{R}_A$  followed by  $\underline{R}_B$  are combined by Rodrigues' vectorial formula (given originally, of course, in a different notation).

$$\underline{R}_C = \frac{\underline{R}_A + \underline{R}_B - (\underline{R}_A \times \underline{R}_B)}{1 - \underline{R}_A \cdot \underline{R}_B}$$

The demerit of this map compared with the other three is that the complete orientation map space extends to infinity.

(IV) yields the statistically advantageous map, in which a perfectly random orientation population would produce a perfectly uniform density of map-points.

### Stereoscopic presentation

Having determined coordinates in the orientation-map,  $x^i, y^i, z^i$  (e.g. Cartesian components of the Rodrigues vector) for each of the members of a population, a stereoscopic presentation is obtained by plotting, for the left picture

$y^i + x^i/10, z^i$  and for the right picture

$y^i - x^i/10, z^i$ . Other combinations give other stereoscopic views.

### Symmetries

If the objects under consideration have discrete rotational symmetries (e.g. when they are crystal lattices) one orientation will be represented by more than one point in the orientation map: e.g. 24 points, for cubic symmetry, or 4 for orthorhombic symmetry (chopped ribbon). The advantageous convention then is to choose from these alternatives the point with least  $\quad$ , so utilizing only a fraction of the whole space of the orientation map, in a cell around the origin. In the Rodrigues map this cell is a polyhedron with plane faces. For orthorhombic symmetry it is a cube: for cubic symmetry it is a semi-regular (Schläfli  $8^2_3$ ) truncated cube.

For certain problems, e.g. considering the relative orientations of the cubic lattices of neighbouring pairs of grains in a polycrystalline metal we can make a further reduction of the utilized space in the orientation map;

first, changing the signs of coordinates to make all positive, and then permuting them so that

$$x^i > y^i > z^i > 0.$$

The utilized space is thus reduced to a pentahedron (a singly truncated tetrahedron) which is  $1/48$  of the truncated cube.

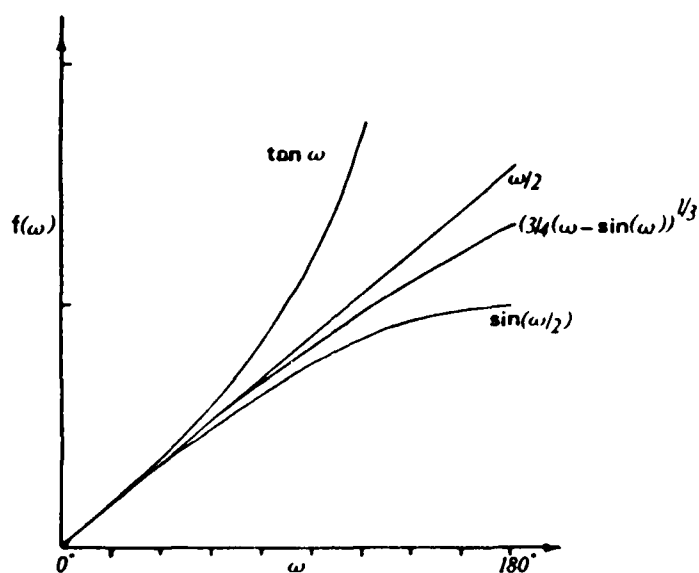


Figure 1. The four choices for the radial scaling function  $f(\omega)$

## Text

In the context of this workshop my contribution is largely Zukunftsmusik, because in the context of plastics, with or without reinforcement, I do not yet know of a case where full three-dimensional information about the orientational statistics of its anisotropic components is available. When the reinforcing components are needles, e.g. chopped fibres, or discs, two parameters suffice to define their orientation, and a two-dimensional map (customarily in stereographic projection) suffices to display the orientational distribution. For objects, all similar, but lacking uniaxial symmetry (e.g. chopped ribbons as reinforcing elements, or crystal lattices) this map cannot display the full information.

The problem is familiar in metallurgy, in which the properties depend on the lattice orientations in the grains, but the metallurgists must usually content themselves with the less complete information given by pole-figures, which are two-dimensional stereographic maps showing the statistics of orientation of particular crystallographic planes.

I was first presented with the problem nearly 30 years ago by Cecil Dunn, who was professionally engaged in determining pole-figures, but, realizing the incompleteness of this information had gone to the trouble of using a finely collimated X-ray beam to obtain the complete crystallographic orientation of 200 grains, one at a time, in a specimen of steel. He raised the question, what was the best way to display the result? He was aware that he would need a three-dimensional map, and proposed to use the Euler angles defining rotation from one standard orientation as mapping coordinates. I told him he should not use these, and showed him how to define a more symmetrical set of three coordinates. The matter has remained dormant because the experimental side of the problem was too time-consuming: the back-reflection Laue technique required an exposure of about  $\frac{1}{2}$  an hour per grain, and Dunn's 200 was not enough for real statistical significance. Today, using Kikuchi patterns produced in the electron-microscope, with an on-line micro-computer, more than one grain-orientation can be determined

per minute (and the time is capable of being shortened), so the problem becomes a practical one, at least in the domain of metallurgy. The same technique should be applicable whenever crystals are used as reinforcing components in an amorphous matrix, and other rapid techniques should be devisable for other cases where the orientation of components can be of importance for the macroscopic behaviour of a material.

What I did not know when Dunn consulted me was that had he been able to consult Euler he would have received just the same advice: don't use the Euler angles. In 1776 Euler published two successive papers in *Novi Commentarii Petropolis*. In the first of these "Formulae generales...", treating generally the mathematics of displacement of rigid bodies in three dimensions, rotations are parameterized by use of the Euler angles. It will be appreciated that given a mathematical way of specifying rotations we obtain immediately a way of specifying orientations by adding a conventional choice of one standard orientation: any other orientation is then specified by its rotation from the standard orientation. In the second of these papers of 1776, "Nova methodus..." Euler introduces another and more symmetric way of parameterizing rotations by use of his theorem that the rotation from any one orientation to another can be specified by an axis of rotation, and an angle of rotation  $\omega$  about that axis, uniquely apart from multiples of  $2\pi$  in  $\omega$ . Accordingly, he recommends as parameters to define a rotation the three direction cosines (only two of which are independent) of the rotation axis, together with the angle  $\omega$ . Neither Euler, nor any of the early writers on the subject, speak of mapping, but in the spirit of Euler's "New Method" we may take as a mapping vector for rotations (or orientations, if we represent the standard orientation by the point at the origin) the product of the unit vector  $\underline{l}^0$  corresponding to the rotation axis (whose components are the aforesaid direction cosines), with  $f(\omega)$  which is some function of  $\omega$ , monotone increasing up to  $\omega = \pi$ , and desirably an odd function. All maps in which the representative point is removed from the origin by the vector:

$$\underline{\Lambda} = \underline{l}^0 \cdot f(\omega) \quad (1)$$

i.e. in a direction corresponding to the rotation axis by a distance signifying the rotation angle, may be justly called Eulerian orientation maps.

The whole subject of the mathematics of rotation is much bedevilled by arbitrary conventions of sign. For this, and other related reasons, there are hardly two text-books which agree on the standard form for the Euler angles, use of which we are here avoiding. Even those authors who carefully emphasize anticlockwise omit to say whether this is seen from the origin, or from an external viewpoint. When returning to the subject after an interval I habitually write at the top of the page my mnemonic ALI-CLO. A positive rotation is anticlockwise as seen looking in to the origin, clockwise as seen looking out from the origin.

Just as in mapping the Earth on to a plane no one projection combines all possible advantages, so in orientation mapping there are several different advantageous choices for the radial scaling function  $f(\omega)$ . Four which can be recommended are:

$$(i) \quad f(\omega) = k\omega \quad (2)$$

(with  $k = \frac{1}{2}$  for agreement with the others near the origin)

$$(ii) \quad f(\omega) = \sin \frac{1}{2}\omega \quad (3)$$

$$(iii) \quad f(\omega) = \tan \frac{1}{2}\omega \quad (4)$$

$$(iv) \quad f(\omega) = \left[ \frac{3}{4} (\omega - \sin \omega) \right]^{1/3} \quad (5)$$

(i) has the merit of crude simplicity. It is the mapping I recommended to Dunn. With  $k = \frac{1}{2}$ , all possible orientations are mapped within the sphere of radius  $\pi/2$ .

(ii) maps all possible orientations within the sphere of radius unity. Diametrically opposite points (rotations of  $+\pi$  and  $-\pi$ ) must be deemed equivalent to each other. This scheme has geometrical advantages over (i) but its chief advantage is algebraic because the Cartesian components of  $\Lambda$ :



$$(\xi, \eta, \zeta) = (\ell_1^0, \ell_2^0, \ell_3^0) \sin \frac{1}{2}\omega \quad (6)$$

together with

$$\chi = \cos \frac{1}{2}\omega \quad (7)$$

form the real and imaginary components of elements of the Cayley-Klein matrix, to be considered further below. The parameters  $\xi, \eta, \zeta, \chi$  appear in German literature as A, B, C, D.

The proper name for these parameters is a matter of some dispute. Whittaker (1904) calls them the Eulerian parameters, giving reference to Euler's two papers of 1776 in which, however, they do not appear. They are called the Eulerian symmetric parameters in the publisher's note which appears as an introduction to Klein and Sommerfeld's "Theorie des Kreisels" (1897): but in a footnote (p60 of that book) this name is given to the Rodrigues parameters  $\lambda, \mu, \nu$  (which does Rodrigues less than justice). In the main text of that book they are called the quaternion magnitudes (Quaterniongrößen). That name, or perhaps preferably quaternion parameters, is correct. But one need not infer from this a need to learn quaternion theory: a knowledge of the rules of matrix multiplication will suffice.

(iii) yields the parameters of Rodrigues (1840), components of what we shall call the Rodrigues vector:

$$\begin{aligned} \underline{\Lambda} &= (\Lambda_1, \Lambda_2, \Lambda_3) = (\lambda, \mu, \nu) \\ &= (\xi/\chi, \eta/\chi, \zeta/\chi) = (A/D, B/D, C/D) \\ &= (\ell_1^0, \ell_2^0, \ell_3^0) \tan \frac{1}{2}\omega \end{aligned} \quad (8)$$

(These parameters  $\lambda, \mu, \nu$ , differ by a factor 2, advantageously omitted, from those of Rodrigues).

Apart from the demerit that for all possible orientations it extends to infinity, a demerit which disappears when the objects considered possess rotational symmetries, this gives the geometrically most advantageous of orientation maps. The fact that the earlier writers were more concerned

with algebra than with geometry, and did not think in terms of mapping, has caused excessive disregard for Rodrigues' admirable paper. It was the first full development after Euler of his "new method", and the first to make systematic use of functions of the half angle. As a sample I give his construction (which would surely have pleased Euclid) to find the resultant rotation axis for two successive rotations, represented by Rodrigues vectors  $\underline{P}$  and  $\underline{Q}$ . Incidentally it will show how the half-angles naturally enter the problem. Let  $OP$ ,  $OQ$ , be lines from the origin corresponding to the axes of the two successive rotations. Cast a plane  $OPR$  through  $OP$  making an angle  $-\frac{1}{2}\omega_P$  with the plane  $OPQ$ , and another plane  $OQR$  through  $OQ$  making an angle  $+\frac{1}{2}\omega_Q$  with the plane  $OPQ$ : they intersect in  $OR$ . The first rotation carries  $OR$  to  $OR'$ , its mirror image in  $OPQ$ . The second rotation carries  $OR'$  back to  $OR$ .  $OR$  is therefore the line in the rigid body which is in the same position after the two rotations as it was before: it is therefore the axis of the resultant rotation.

I omit Rodrigues derivation of the magnitude of the resultant rotation. Throughout his paper one perceives formulae which would have been simplified by use of vector notation, which, however had not yet been invented. This is most striking in his expression for the resultant Rodrigues vector  $\underline{R}$ , from successive rotations expressed by their Rodrigues vectors  $\underline{P}$  and  $\underline{Q}$ , which, so written, becomes

$$\underline{R} = \frac{\underline{P} + \underline{Q} - \underline{P} \times \underline{Q}}{1 - \underline{P} \cdot \underline{Q}} \quad (9)$$

a valuable formula, much less widely known than it ought to be. It makes plainly visible the non-commutative nature of rotations, and the fact that this is a second order property, disappearing for infinitesimal rotations.

One important geometrical property of the Rodrigues map follows immediately from this formula, namely that for a continuing rotation  $\underline{Q}$  (now, of varying magnitude about a fixed axis) following on an arbitrary fixed rotation  $\underline{P}$  the trajectory of the representative point  $\underline{R}$  is a straight line. This is self-evident when  $\underline{Q}$  and  $\underline{P}$  are orthogonal, i.e. when  $\underline{P}$

lies anywhere in the plane through the origin orthogonal to  $\underline{Q}$ : but since the set of trajectories from all such points  $\underline{P}$  for a given direction of  $\underline{Q}$  reach all points in the infinite map space the same must be true for any direction of  $\underline{P}$ .

A second most valuable geometric property of the Rodrigues map is that the orientationally equidistant surface between two orientation points  $\underline{P}$  and  $\underline{Q}$ , that is, the locus of points  $\underline{R}$  representing orientations from which equal magnitudes of rotation,  $|\omega|$ , are required to reach orientations  $\underline{P}$  and  $\underline{Q}$ , is a plane. This is most easily proved algebraically by way of the parameters of system (ii) and use of Cayley-Klein matrices.

The best introduction to Cayley-Klein matrices is probably that given in the first chapter of Klein and Sommerfeld's book "Theorie des Kreisels" ("Theory of the Top") (1897). This begins from a consideration of stereographic projection. If  $(x,y,z)$  is an arbitrary point on the sphere  $x^2+y^2+z^2 = 1$ , its stereographic projection, from the centre of projection  $(0,0,1)$  on to the plane  $z=0$  is  $(u,v,0)$  where:

$$u = \frac{x}{1-z}, v = \frac{y}{1-z} \quad (10)$$

Form the complex number

$$W = u + iv. \quad (11)$$

Then it can be shown that if the sphere is given an arbitrary rotation, bringing  $(x,y,z)$  to  $(x',y',z')$  then

$$W + W' = \frac{\alpha W + \beta}{\gamma W + \delta} \quad (12)$$

(which should probably be called the Riemann-Klein fractional linear transformation) and the complex parameters  $\alpha, \beta, \gamma, \delta$  which define the rotation are related to the real parameters  $\xi, \eta, \zeta, \chi$  defined above by

$$\begin{aligned} \alpha &= \chi + i\zeta, & \beta &= -\eta + i\xi, \\ \gamma &= \eta + i\xi, & \delta &= \chi - i\zeta. \end{aligned} \quad (13)$$

Now perform a second arbitrary rotation:

$$\begin{aligned}
 W' \rightarrow W'' &= \frac{\alpha' W' + \beta'}{\gamma' W' + \delta'} \\
 &= \frac{\alpha'' W + \beta''}{\gamma'' W + \delta''}
 \end{aligned} \tag{14}$$

By substitution one finds that

$$\begin{pmatrix} \alpha'' & \beta'' \\ \gamma'' & \delta'' \end{pmatrix} = \begin{pmatrix} \alpha' & \beta' \\ \gamma' & \delta' \end{pmatrix} \cdot \begin{pmatrix} \alpha & \beta \\ \gamma & \delta \end{pmatrix} \tag{15}$$

Thus the combination of rotations is represented by multiplication of matrices. These 2x2 complex matrices, each of which represents a rotation, are Cayley-Klein matrices. Among other properties they have determinant 1 (because  $\xi^2 + \eta^2 + \zeta^2 + \chi^2 = 1$ ) and the inverse matrix, representing the opposite rotation, corresponding to changing the sign of either  $\underline{l}^0$  or  $\omega$ , is obtained by transposing the matrix and taking its complex conjugate.

Given the Cayley-Klein matrix defining a rotation, Eq (12) affords a prescription for the way the rotation operates on any vector in the rigid body. From this we can readily derive the customary real 3x3 matrix for transformation of vectors by rotation, in which the elements are made of squares and products of the parameters  $\xi, \eta, \zeta, \chi$ .

Just as combination of rotations in the plane can be expressed either by multiplication of complex numbers, or by multiplication of 2 x 2 real matrices, so in three dimensions rotations can be combined either by multiplying 3 x 3 real matrices or 2 x 2 complex matrices: and the latter is more economical of effort, requiring in a numerical example less than half as much arithmetic.

The Cayley-Klein matrix can be expanded as a sum of four simpler matrices:

$$\begin{pmatrix} \alpha & \beta \\ \gamma & \delta \end{pmatrix} = \begin{pmatrix} \chi + i\zeta & -\eta + i\xi \\ \eta + i\xi & \chi - i\zeta \end{pmatrix} \quad (16)$$

$$= i\xi \begin{pmatrix} 0 & 1 \\ 1 & 0 \end{pmatrix} - i\eta \begin{pmatrix} 0 & -i \\ i & 0 \end{pmatrix} + i\zeta \begin{pmatrix} 1 & 0 \\ 0 & -1 \end{pmatrix} + \chi \begin{pmatrix} 1 & 0 \\ 0 & 1 \end{pmatrix} \quad (17)$$

One of the first three terms plus the last makes the Cayley-Klein matrix for rotation about the x, y, or z axis. The first three of these simple matrices (the last being just the unit matrix) are called the Pauli matrices. They are regularly used for calculating rotations in quantum mechanics. They are accordingly often called the spin matrices, a name which regrettably conceals the fact that they afford the most economical means of calculating rotations of any objects in three dimensions.

When the objects to be mapped possess rotational symmetries there are several indistinguishable orientations, to be represented by different points in the orientation map. For example for chopped ribbons, or for ellipsoids, or crystals with orthorhombic symmetry (i.e. objects with 3 2-fold axes of symmetry) there are four indistinguishable orientations: if one is represented by the point at the origin, the other three are at points on the x, y, and z axes at distances corresponding to rotations of  $\omega = \pm\pi$ : each of these pairs is to be counted as one. In the case of cubic symmetry the 4-fold, 3-fold and 2-fold axes generate 24 equivalent points. It is needless to plot all equivalent points in the map, and it is an advantageous convention to choose that one which is nearest the origin, i.e. which has the smallest value of  $\omega$ . Under this convention all points plotted will fall within a domain around the origin bounded by portions of surface each of which is orientationally equidistant from the standard orientation and one of its equivalents.

We may calculate the orientationally equidistant surface between any two orientation points P and Q by use of Cayley-Klein matrices. Denoting by  $K_{AB}$  the Cayley-Klein matrix for rotation from A to B, by requiring equal values of  $\chi$  in

$$\underline{\underline{K}}_{PR} = \underline{\underline{K}}_{OR} \underline{\underline{K}}_{OP}^{-1} \quad (18)$$

$$\text{and } \underline{\underline{K}}_{QR} = \underline{\underline{K}}_{OR} \underline{\underline{K}}_{OQ}^{-1} \quad (19)$$

we obtain an equation in  $\xi, \eta, \zeta$  defining the locus of R on this orientationally equidistant surface. It is found to be a complete hemispheroid spanning a diametral plane of the bounding sphere. On transforming to Rodrigues coordinates it becomes an infinite plane. Thus all orientationally equidistant surfaces between pairs of points in the Rodrigues map are planes. This makes it the geometrically most advantageous map, and the presence of rotational symmetries avoids its one serious disadvantage, namely its infinite extent.

In the case of orthorhombic symmetry the basic domain is a cube with faces normal to the x, y, and z axes, at a distance  $\tan \frac{1}{4}\pi = 1$  from the origin. The corners of this cube, at a distance  $\sqrt{3}$  from the origin, represent rotations about  $[1,1,1]$  of  $2 \arctan \sqrt{3} = 120^\circ$ , the greatest possible disorientation between two orthorhombic objects, orientationally equidistant from all four equivalents of the standard orientation. In the case of cubic symmetry the basic domain has bounding surfaces normal to x, y and z at a distance  $\tan \frac{1}{8}\pi = \sqrt{2}-1$  from the origin, and normal to  $[1,1,1]$  axes at  $\tan \frac{1}{6}\pi = 1/\sqrt{3}$ , forming a Schläfli  $8^2_3$  semi-regular truncated cube, the faces of which are regular octagons and equilateral triangles, so that all edges are equal. The vertices are at  $(\sqrt{2}-1, \sqrt{2}-1, 3-2\sqrt{2})$  and symmetrically equivalent points (24 in all) at a distance of  $(23-16\sqrt{2})^{1/2}$  from the origin, corresponding to rotations of  $2 \arctan (23-16\sqrt{2})^{1/2} = 62.7994..^\circ$  about  $\langle 1,1,\sqrt{2}-1 \rangle$  axes: the greatest possible disorientation between two cubes.

In some metallurgical uses of the stereographic projection it is appropriate to use less than the whole of the projection, using symmetry properties to plot all poles within one fundamental triangle between (100), (110) and (111) poles in the case of a cubic crystal. A similar reduction can be appropriate in orientation mapping, particularly when we are only interested in the relative orientations of neighbouring pairs of objects of orthorhombic cubic symmetry.

This reduction is effected by changing the signs of all negative coordinates in the orientation space to positive, and permuting them into an order of descending magnitude:

$$x \geq y \geq z \geq 0.$$

This places all plots within a sector which is only 1/48 of the basic domain, itself 1/4 for objects of orthorhombic symmetry or 1/24 for objects of cubic symmetry, of the whole orientation space. In a metal we might be looking for special crystallographic relationships between the orientations of neighbouring grains. The ordinary twins of a cubic metal would appear as points at one vertex of this fully reduced zone - the centre of a triangular face of the truncated cube. The principal Kronberg-Wilson relationships would appear as particular points along [111], [100] or [110] axes.


To display population statistics on a map of the Earth, one preferably uses an equal area projection, so that a random distribution of population gives a statistically uniform distribution of points. The radial scaling function of mapping scheme (iv) provides the corresponding equal volume orientation map. When the map is transformed by an arbitrary change of the standard orientation, any volume element migrates with change of shape but not change of volume. It will, however, be a long time before in any practical case we acquire orientation statistics deserving the use of this refinement.

It finally remains to make the three-dimensional map visible. This can only be done on the printed page by use of stereoscopic pairs. A stereoscopic pair for a view looking in along the x-axis is obtained by plotting  $z$  against  $y + 0.1x$  for the left and  $z$  against  $y - 0.1x$  for the right member of the pair.

$z$  versus  $.636x + .778y$  for the left, and  $z$  versus  $.778x + .636y$  for the right gives a stereoscopic pair for the view looking in along [110]. A stereoscopic pair for the view looking in along [111] is obtained by plotting  $0.4083(-x-y+2z)$  against  $0.8660(-x+y) \pm 0.0577(x+y+z)$ , the plus and minus signs being taken for the left and right pictures respectively.

### Discussion of Session V

In the absence of any known orientational statistics for triaxial objects in polymers, it was necessary to draw on data from metals in order to demonstrate a practical application of F C Frank's three-dimensional orientation maps.

The orientations of the individual grains in a polycrystalline metal are rarely, if ever, randomly distributed and, to display and investigate the nature of distributions of grain orientations, R M Longden and J Weinbren (1984) have used a scanning electron microscope to obtain electron back scattering patterns from individual grains in metallographically polished sections of both as-cast and annealed copper. In figures 1(a) and (b), and 2(a) and (b) respectively, their data are presented as stereo pairs of the R-map for each section. To observe these three-dimensional maps, the reader should photocopy the figures, position each stereo pair in a stereo viewer and adjust the relative position of the pair until the central markings  coincide.

F C Frank speculated on the R-map for pure cube-textured copper. There will be a Gaussian cluster of points at the origin. There will undoubtedly be some twinning, represented by small clusters on the triangular faces. (The triangular faces represent rotations about  $\langle 001 \rangle$  of  $60^\circ$ , the octagonal faces represent rotations about  $\langle 001 \rangle$  of  $45^\circ$ , and the biggest rotation about  $\langle 001 \rangle$ , represented by each of the 24 corners to the cell, is  $62.95^\circ$ ). As likely as not, the specimen will have been scratched during preparation, in which case a few large grains might have nucleated. These will be represented by points on the  $\langle 100 \rangle$ ,  $\langle 110 \rangle$  and  $\langle 111 \rangle$  spars spanning the origin to the octagonal faces, cell edges and triangular faces respectively.

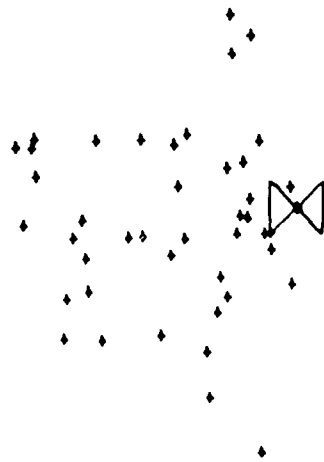


One convenient classification of polymers is into those which do and those which do not crystallise. The degree of crystallisation can be as high as 90% by volume and the creation of preferred crystal orientations, during the mechanical deformation of polyethylene for example, is well known. When sufficient polymer crystal preferred orientation data becomes available, that data could be displayed with advantage by using one of F C Frank's three-dimensional orientation maps.

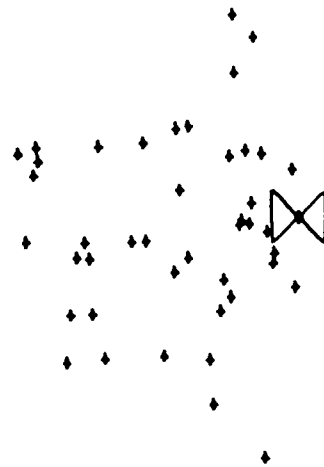
Another obvious polymer application for the maps is in the display or orientations of chopped reinforcement ribbon. The fabrication of components from sheet moulding compounds and from dough moulding compounds imparts substantial degrees of preferred orientation to the chopped strands. The generation of F C Frank's three-dimensional maps lends itself to computer methods so real-time display and control of chopped ribbon orientation is certainly feasible.

#### References

R M Longden and J Weinbren (1984) "Textures in Metals" Stage III report, H H Wills Physics Laboratory, University of Bristol



(a)



(b)

Figure 1. Rodrigues parameter determinations for as-cast copper, displayed as a stereo pair of the three-dimensional R-map viewed along y



(a)

(b)

Figure 2. Rodrigues parameter determinations for annealed copper, displayed as a stereo pair of the three-dimensional R-map viewed along y

Session VI: Electromagnetic wave propagation in composite materials

# THE PROPAGATION OF LIGHT THROUGH FIBRE REINFORCED COMPOSITES

J P Sargent and C Upstill

H H Wills Physics Laboratory,  
University of Bristol, Tyndall Avenue,  
Bristol, BS8 1TL, U.K.

## Abstract

*In situ* detection and measurement of sub-micron gaps between fibre and matrix material in low fibre content epoxy and polyester resin composites can be achieved by examination of the manner in which light is transmitted in a direction transverse to the fibre axis. We consider the optics of a matrix in which is embedded a fibre with an annular interfacial gap between fibre and matrix, and present calculations and experimental observations for both air and water filled gaps. Although carried out using model composites, the methods we have investigated can in principle be applied to any low fibre volume fraction composite. The experimental work reported has shown that the presence of absorbed water gives rise to a small ( $\sim 0.3\%$ ) permanent increase in refractive index of the matrix resin.

For gaps larger than a few wavelengths, we show how a simple geometrical optics ray tracing procedure may be used to describe the distribution of light. For small gaps, and for angles greater than the critical angle, a more useful approach is in terms of evanescent waves, which give rise to transmitted waves beyond the gap as a result of optical tunnelling. We present calculations of the flux transmitted across interfacial gaps for plane polarised light and compare these with experimental observations. Using the fact that a phase shift difference is introduced between the TM and TE evanescent waves which have optically tunneled through a small interfacial gap, we show that such gaps may be readily detected by observation of the bright contrast which they produce when viewed between crossed polars. In addition, we demonstrate how quantitative measurements of very small ( $\sim \text{nm}$ ) gap widths can be made from measurements of the phase difference between the TM and TE transmitted waves. Finally, we discuss the use of the exact theory for the scattering of electromagnetic radiation by coaxial dielectric cylinders.

## Introduction

A necessary prerequisite for a fibre reinforced composite to function in a structurally efficient manner is that load transfer from matrix to fibre should take place. In resin composites, it is known from measurements of mechanical properties that realisation of load transfer is progressively impaired during water uptake from humid in-service environments. Loss of load transfer amounts to loss of interfacial adhesion and/or loss of the mechanical contact that gives rise to interfacial friction. Physically, this implies the creation of gaps at the interface. Photomicrographs of glass-fibre composite specimens known to have sustained mechanical damage, or to have been subjected to weathering, frequently show fibres which exhibit a characteristic pattern of light and dark bands parallel to the fibre axis when viewed in transmitted light. In addition, close inspection

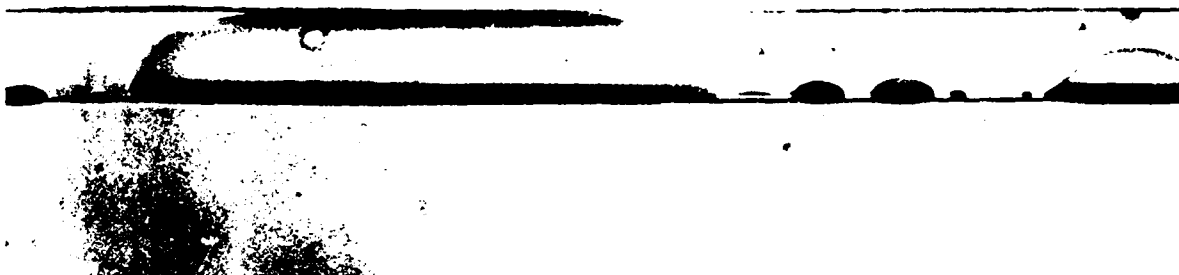


Figure 1. Transmission optical photomicrograph of a debonded glass fibre in an epoxy matrix, showing regions in which the interfacial gap contains both air (large dark areas) and water.

of individual fibres often reveals areas of interfacial contrast, which in some cases are lighter and in other cases darker than elsewhere. For example, Figure 1 is a transmission optical photomicrograph of an isolated fibre in an epoxy/glass-fibre composite which has been immersed for 24 hours in distilled water at  $95^{\circ}\text{C}$ . In general, some of this contrast is because of the development of a refractive index mismatch between the fibre and matrix material and some because of the creation of an interfacial gap.

#### Development of a refractive index mismatch

If there is intimate contact between fibre and resin such that there is no interfacial gap, and if there is no refractive index mismatch between fibre and resin, then the fibre will be invisible when viewed in transmitted light. In these circumstances the fibre will only be seen when viewed between crossed polars; residual stress birefringence in either material, caused by resin cure shrinkage and/or differential thermal contraction between fibre and matrix materials during cooling from the resin cure temperature to room temperature, shows up as regions of bright contrast. Figure 2 shows such a pattern of stress birefringence for an



Figure 2. Transmission optical photomicrograph of a glass fibre in an epoxy matrix viewed between crossed polars, before exposure to water.

epoxy/glass-fibre composite photographed under crossed polars with the microscope objective focussed on the plane of the fibre axis. The specimen was subsequently immersed in distilled water for 2.7 hours at 92°C and, with the microscope modified so that the specimen could be illuminated with parallel light from a laser, photomicrographs were taken with the objective lens focussed in the plane of the fibre axis (Figure 3a) and at a distance of 200 $\mu$  above the fibre axis (Figure 3b).

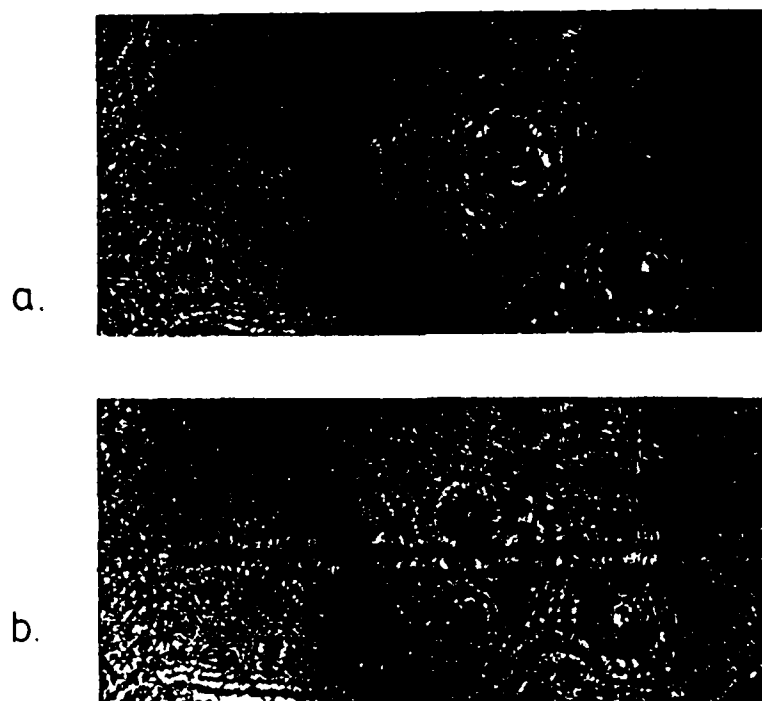


Figure 3. Transmission optical photomicrograph of the specimen shown in Figure 2 but viewed with laser light and after 2.7 hours immersion in distilled water at 92°C. (a) objective focussed on the plane of the fibre axis, (b) objective focussed 200  $\mu$  above the fibre axis.

Images similar to those recorded in Figure 3a and b can be generated simply by immersion of a glass fibre in immersion oils: in Figure 4a and b, we show images of a single S glass fibre covered with drops from two oils of differing refractive index, and focussed (a) in the plane of the fibre axis and (b) at a distance of 200 $\mu$  above the fibre axis. The refractive index of the oil differs from that of the fibre by +0.005 on the right hand side of the figure and by -0.005 on the left, a refractive index gradient existing in the oil mixture between these two regions. In the middle of the image the refractive index of the fibre and immersion oil exactly match and no fibre can be seen. Comparing Figure 3 with Figure 4, it is evident that in the epoxy/glass-fibre specimen shown in Figure 3 there has been a small increase in refractive index of the resin as a result of water uptake, and that this causes the fibre to behave as a very weak diverging



1

10

•

10



AD-A153 284

PROCEEDINGS OF THE WORKSHOP ON NDE OF POLYMERS HELD AT  
VIMEIRO PORTUGAL ON 4-5 SEPTEMBER 1984(U) BRISTOL UNIV  
(ENGLAND) H H WILLS PHYSICS LAB 05 SEP 84

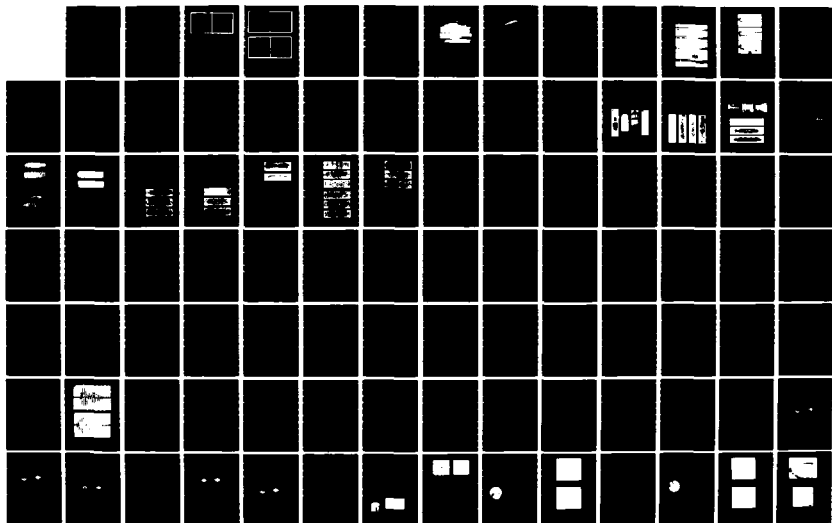
3/4

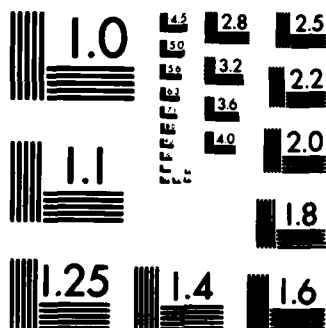
UNCLASSIFIED

DAJA45-84-M-0182

F/G 11/9

NL





MICROCOPY RESOLUTION TEST CHART  
NATIONAL BUREAU OF STANDARDS 1963-A

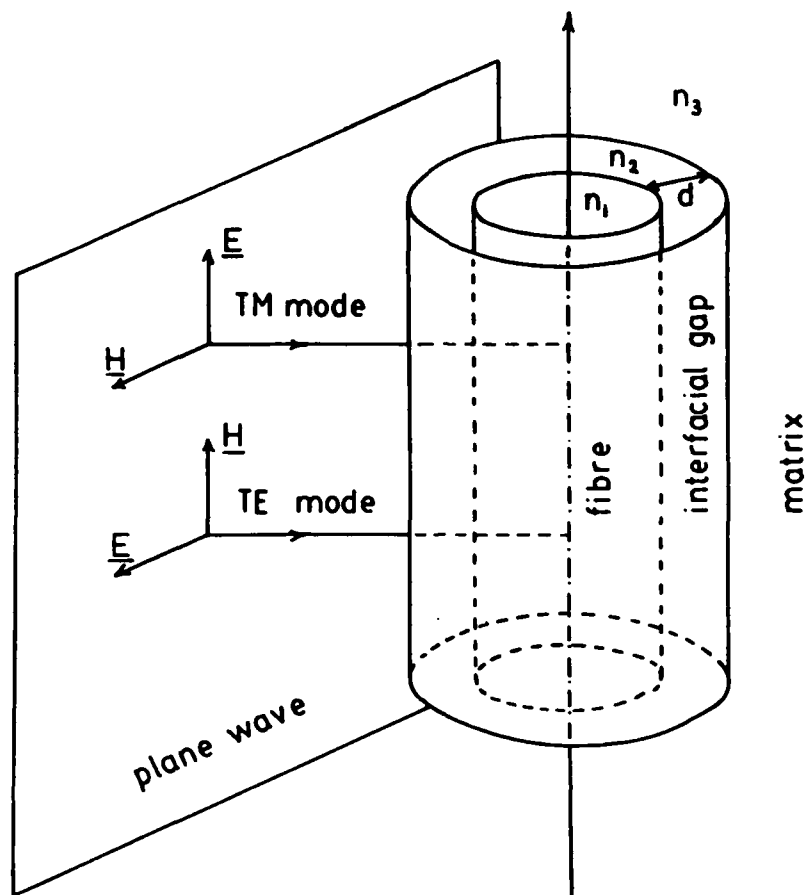


Figure 5. Optical geometry for a composite specimen comprising a glass fibre (refractive index  $n_1$ ) surrounded by a concentric annular interfacial gap ( $n_2$ ) contained within a resin matrix ( $n_3$ ).

2-dimensional surfaces, which we observe in sections, e.g. as lines on a photograph or in the focal plane of a microscope. If they occur, such caustics dominate the microscope image.



Figure 6. In geometrical optics, a family of rays envelope a focal surface or *caustic* (bold line). Note that the caustic is "one-sided".

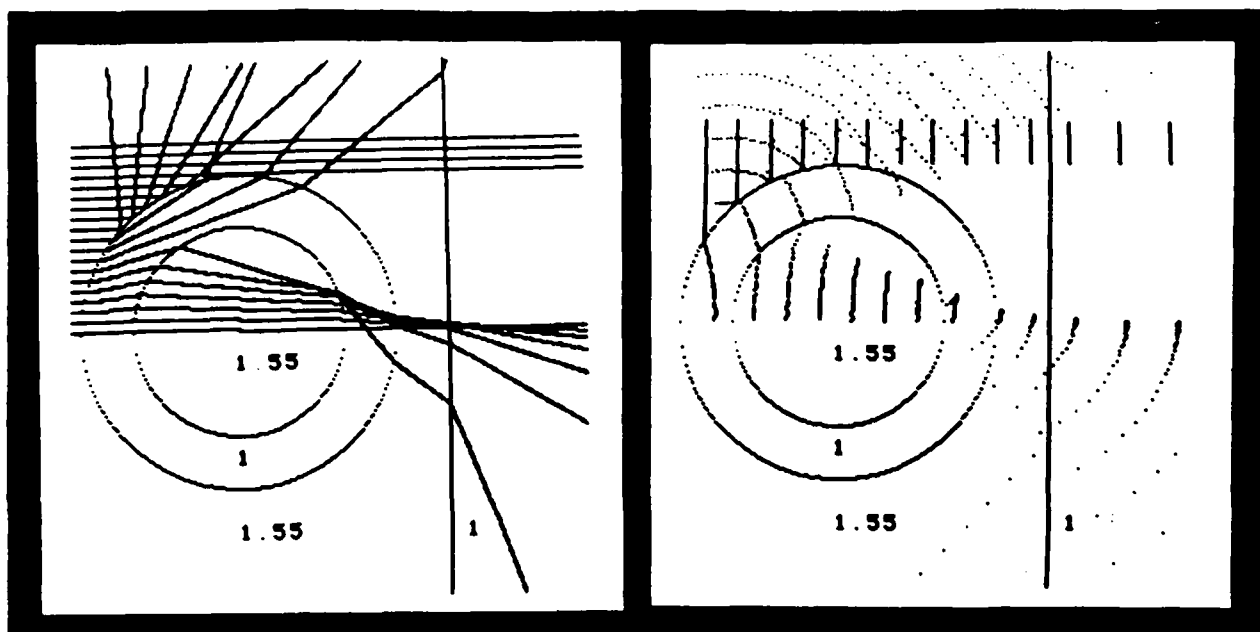


Figure 7a. Ray diagram for plane parallel light incident upon a glass fibre embedded in resin with an air gap at the interface. Fibre diameter is  $D = 10\mu$ , Interfacial gap  $d = D/2$ .  
 b. As (a) but showing wavefronts at 4 wavelength intervals, for a free-space wavelength  $\lambda = 546\text{nm}$ .

Figure 7 is a geometrical optics ray diagram for a  $10\mu$  diameter glass-fibre embedded in resin and with an air filled gap at the interface; Figure 7(b) shows the corresponding wavefront diagram. The caustics for this geometry are shown schematically in Figure 8. In a real composite the interfacial gap will, of course, be much smaller than that illustrated in Figure 7. The consequence of reducing the gap size is to reduce the thickness of the shadow as demonstrated in Figure 9(a) and (b). Figure 10 shows ray and wavefront diagrams computed for a composite in which a water solution has replaced the air in the interfacial gap. Note that in Figures 7 to 10 no allowance has been made for multiple reflections from any interface.

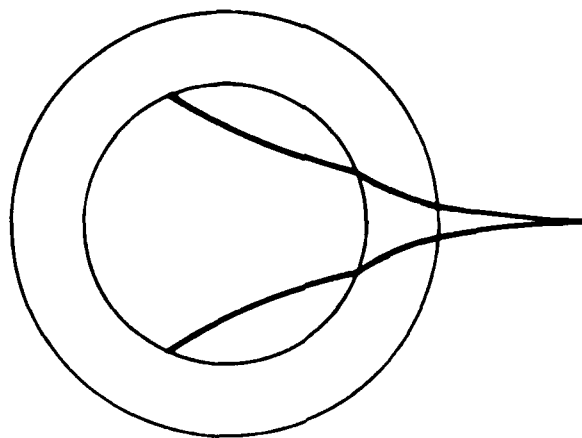


Figure 8. Caustics of ray family for Figure 7.

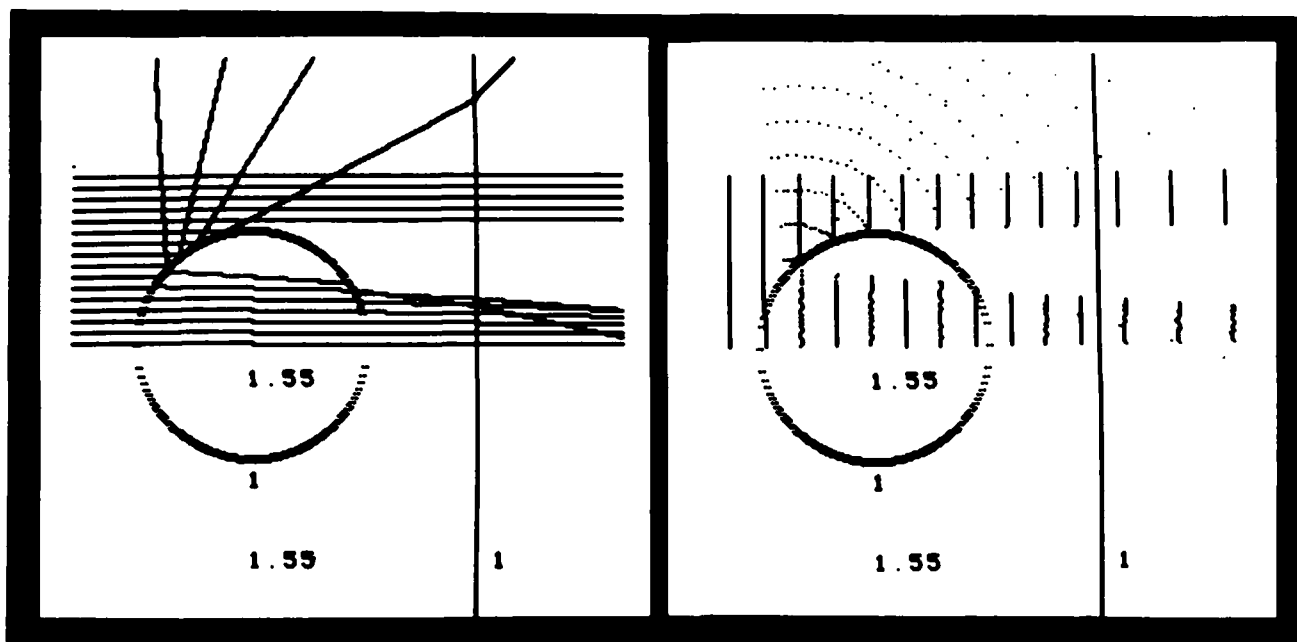


Figure 9. As Figure 7 but with an interfacial gap  $d \sim \lambda/2$ .

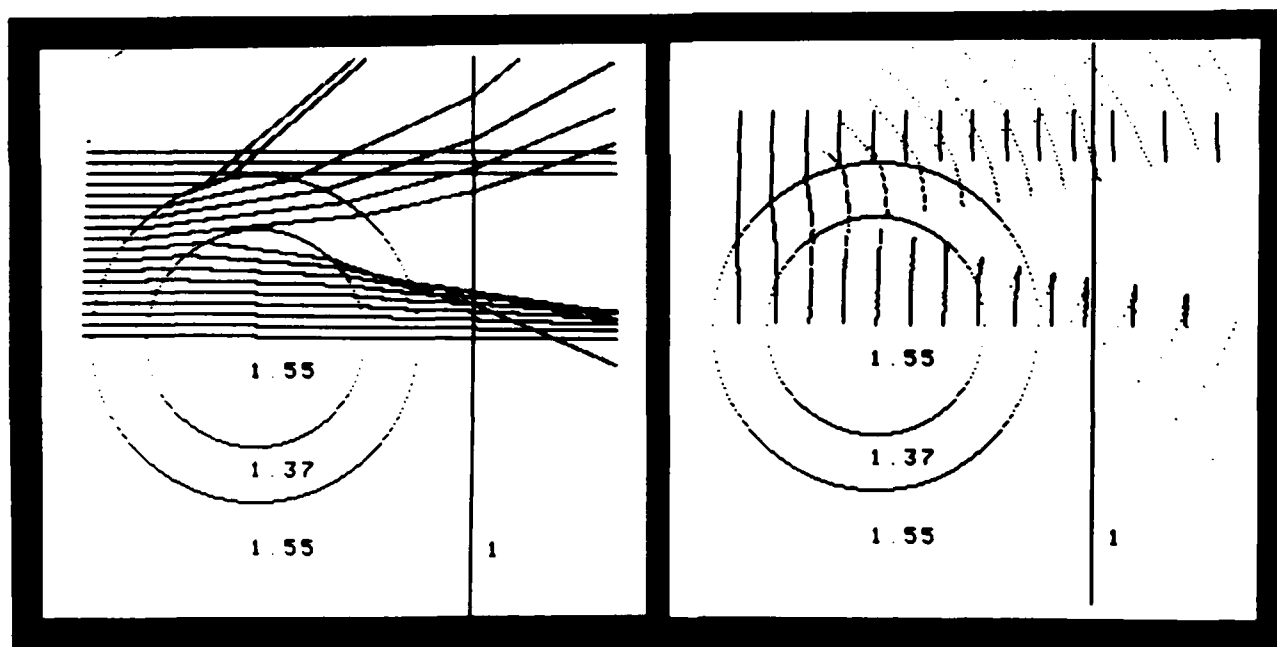


Figure 10. As Figure 7 but with a water solution filled gap at the interface. Fibre diameter  $D = 10\mu$ , interfacial gap  $d = D/2$ .

#### Evanescent wave optics of interfacial gaps

If the interfacial gap is small (less than  $\sim \lambda$ ), internal reflection is not total beyond the critical angle and a transmitted wave appears beyond the gap. Electric fields extend into the gap beyond the first interface; these fields, which decrease exponentially with increasing distance, give rise to evanescent waves propagating in a direction parallel to the surface. If another interface is sufficiently close (specifically the interface between air gap and fibre in our case), fields are excited beyond

that interface, and the net result is that some light is transmitted. This phenomenon is known as frustrated total internal reflection and is described by e.g. Feynman (1965), Hecht and Zajac (1974) and Kline (1970). Ignoring multiple reflections within the gap, Kline (1970) gives equations for the energy transmission coefficient  $T$  following frustrated total internal reflection of plane parallel waves incident upon a parallel sided interfacial gap, between matrix and fibre of the same refractive index  $n_1$ , for either TE or TM mode polarisation:

$$T_{TM} = 2\exp(-2d/\Delta)[1 - \cos(2\alpha_{TM})] \quad (1a)$$

$$T_{TE} = 2\exp(-2d/\Delta)[1 - \cos(2\alpha_{TE})] \quad (1b)$$

where  $d$  = gap width,  $\Delta = \lambda/(2\pi(n_1^2 \sin^2 \theta_1 - n_2^2)^{1/2})$ ,  
 $\theta_1$  = angle of incidence,  $\alpha_{TM} = 2\tan^{-1}[(n_1/n_2)^2 \lambda/(2\pi\Delta n_1 \cos \theta_1)]$  and  
 $\alpha_{TE} = 2\tan^{-1}[\lambda/(2\pi\Delta n_1 \cos \theta_1)]$ .

These equations are valid for  $d > \Delta$ ; note that  $\Delta$  is a function of  $\theta_1$ , and that for  $n_1 = 1.55$  and  $n_2 = 1$ ,  $\Delta = 0.13\lambda$  when  $\theta_1 = 90^\circ$ , and  $\Delta = 0.58\lambda$  when  $\theta_1 = 42^\circ$ . Note also that the expression Kline gives for  $\Delta$  is in error by a factor of  $\cos \theta_1$ , which we have corrected here.

If the interfacial gap is very small, then waves will be multiply reflected within the gap, with a contribution to the observed intensity distribution at each reflection. For plane waves incident upon a parallel sided gap, Kline (1970) indicates how the single-wave theory (equation 1 above) may be extended to include these multiply reflected waves. The energy transmission coefficients for either TM or TE mode propagation, allowing for multiple reflections, can be shown to be:

$$T_{TM} = (1 - \cos 2\alpha_{TM})/[\cosh(2d/\Delta) - \cos 2\alpha_{TM}] \quad (2a)$$

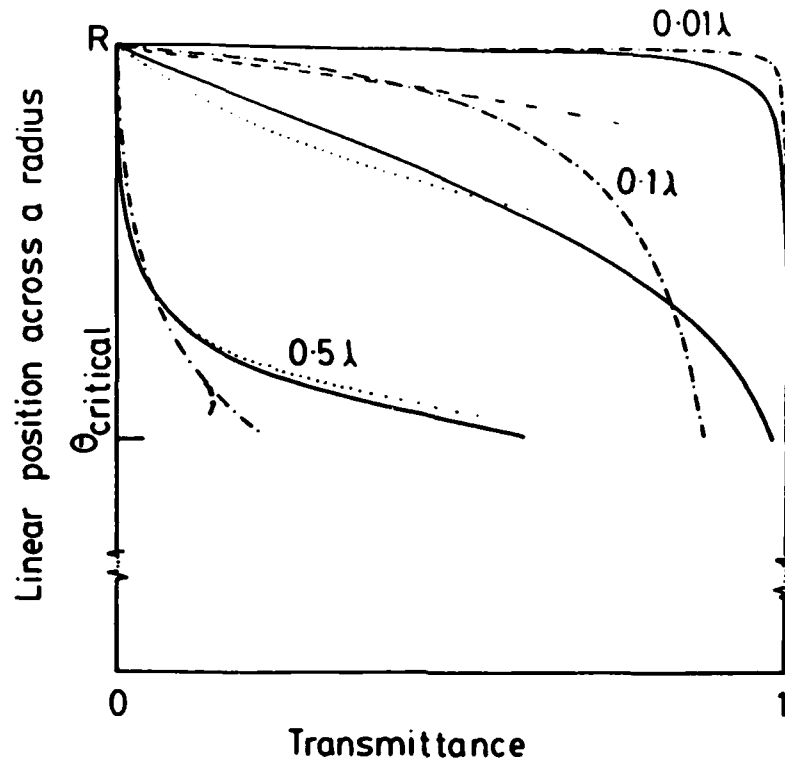
$$T_{TE} = (1 - \cos 2\alpha_{TE})/[\cosh(2d/\Delta) - \cos 2\alpha_{TE}] \quad (2b)$$

where the variables are as defined for equations 1a and 1b.

Weinstein (1947) and Carniglia and Mandel (1971) have independently derived expressions for the attenuation of the transmitted intensity as a function of gap width. It can be shown that their results are equivalent to our equations 2a and 2b above.

Figure 11 shows distributions of transmitted intensity along that fibre radius perpendicular to the direction of incident parallel light. The distributions were calculated using equations 2a and 2b, for interfacial gaps of  $0.5\lambda$ ,  $0.1\lambda$  and  $0.01\lambda$ , and for comparison we also show distributions calculated using equations 1a and 1b (i.e. ignoring multiple reflections) for gaps of  $0.5\lambda$  and  $0.1\lambda$ . In all these calculations, at each point at which the contribution to the transmitted intensity was evaluated, the gap between matrix and fibre has been approximated by a parallel-sided interface tangential to the true interface (the angle of incidence is different at each point).

Figures 12a and b show photomicrographs for an epoxy/glass-fibre specimen with an interfacial gap whose width increases along the length of the fibre. The fibre was viewed and oriented such that only (a) TM or (b) TE mode propagation was supported: the differences in attenuation between the two modes with increasing gap size are clearly seen.



#### Key

- TE mode, single wave
- ..... TM mode, " "
- TE mode, multiply reflected
- TM mode, " "

Figure 11. Distributions of transmitted intensity along that fibre radius perpendicular to the direction of incident parallel light.

#### Polarisation effects associated with interfacial gaps

When the fibre is viewed between crossed polars with the fibre axis inclined at an angle of  $45^\circ$  to the direction of the crossed polars, those regions which showed dark contrast (Figures 12a and b) now show up bright against a dark background: this effect is shown in Figure 12c. Because the fibre is inclined at an angle of  $45^\circ$ , both TE and TM propagation modes will be excited at the interfacial gap with equal intensity. Hence the observed transmitted light will be comprised of a superposition of the two modes, each of which will have suffered a phase change on traversing the interfacial gap, rendering the light no longer linearly polarised, but in general elliptically polarised. Equations giving the phase shifts  $\Phi_{TM}$  and  $\Phi_{TE}$  as a function of gap width  $d$  and angle of incidence  $\theta_i$  (above the critical angle) have been derived by Carniglia and Mandel (1971):

TM mode

a.

TE mode

b.

aligned 45°  
to X polars

c.

Figure 12. Photomicrographs of a debonded fibre showing: (a) its appearance when viewed with the optic axis of the polariser parallel to the fibre axis (TM mode), (b) its appearance when viewed with the optic axis of the polariser perpendicular to the fibre axis (TE mode), and (c) its appearance when viewed between crossed polars and oriented at 45° to their axes.

$$\tan \Phi_{TM} = [(\cos^2 \theta_i - n_1^2(n_1^2 \sin^2 \theta_i - 1))/2n_1 \cos \theta_i (n_1^2 \sin^2 \theta_i - 1)^{1/2}] \\ \times \tanh[Kd(n_1^2 \sin^2 \theta_i - 1)^{1/2}],$$

$$\tan \Phi_{TE} = [(n_1^2 \cos 2\theta_i + 1)/2n_1 \cos \theta_i (n_1^2 \sin^2 \theta_i - 1)^{1/2}] \\ \times \tanh[Kd(n_1^2 \sin^2 \theta_i - 1)^{1/2}] \quad (3)$$

for an air gap between matrix and fibre of refractive index  $n_1$ , with light of frequency  $K = 2\pi/\lambda$ .

Figure 13 shows the phase difference ( $\Phi_{TM} - \Phi_{TE}$ ) plotted as a function of angle of incidence for gap sizes (in wavelengths) in the range from (a) 0 to 1 and (b) 0 to 0.1. Notice from Figure 13 that the phase difference rapidly approaches a limiting value for gaps greater than about 0.2, or is double valued. Thus, for any measurement of retardation, a considered choice of angle of incidence should be made. It should also be borne in



mind that as the gap width increases, the attenuation increases at different rates for TE and TM waves. For this reason, introduction of equal and opposite retardation will not necessarily result in complete extinction of the transmitted light. Instead, a minimum of transmitted intensity may occur.

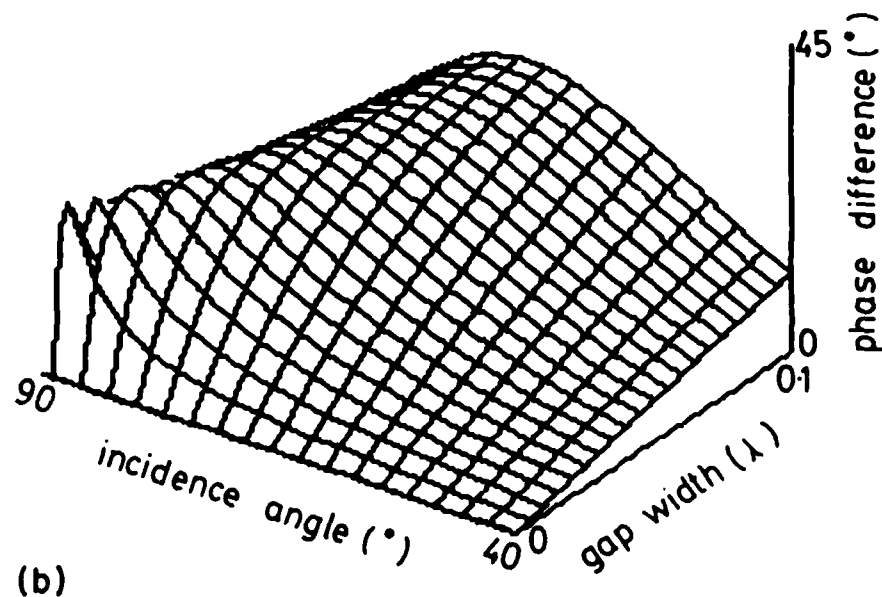
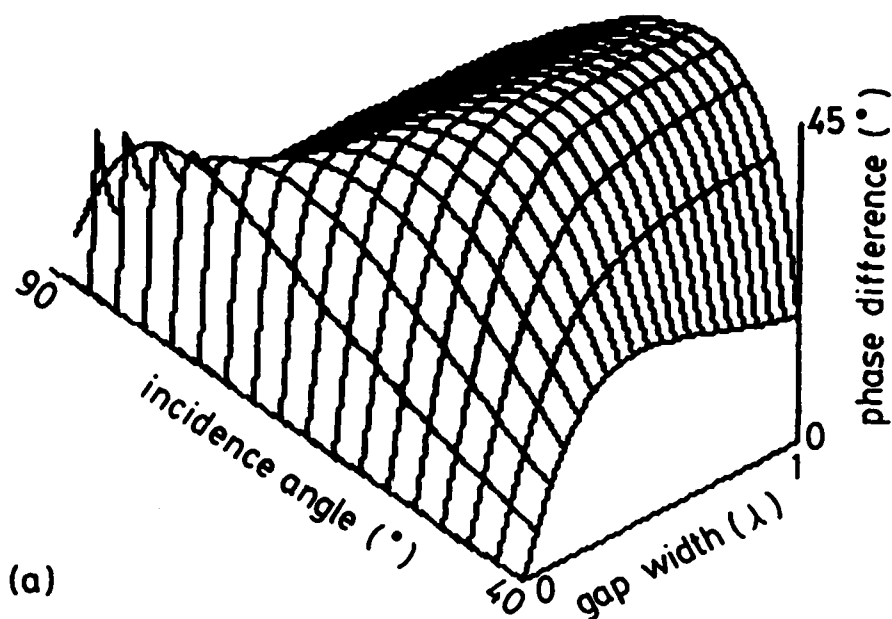


Figure 13a. Phase difference between TE and TM modes of the transmitted wave calculated using equation 3. Gap width increment is  $0.05\lambda$ , incidence angle increment is  $2.86^\circ$ .  
 b. As (a), but for gap widths between 0 and  $0.1\lambda$ , with width increments of  $0.005\lambda$ .

For a given fibre orientation with respect to the axes of the polariser and analyser, the phase change introduced by the debonded region is in an opposite sense to that introduced at fully bonded interfaces. This can be demonstrated in a fibre containing a small amount of stress birefringence by introducing a gradually increasing known retardation into the optical path; in the bonded region the brightness and width of the area of transmitted light gradually increases (i.e. that due to stress birefringence alone), whilst at the same time the brightness and width of the region of light transmitted in the debonded region (i.e. that due primarily to the phase difference existing between the TE and TM waves) decreases.

Adjacent to the bright region in Figure 12c there exists a dark band. This is a contour of zero phase difference, corresponding to those locations where the phase difference introduced by the stress birefringence is equal and opposite to that introduced by the interfacial gap. This condition is only valid as long as the principal stress axes lie in the same directions as the TE and TM mode directions, which is frequently the case, since the principal stress directions arising from stress birefringence are usually axial, radial and circumferential with respect to the fibre. Recall that stress birefringence arises as a result of differential shrinkage during resin curing and during cooling from the resin cure temperature. For fibres which are oriented with their axes perpendicular to the direction of light propagation, the hoop stress can be neglected. It is important to be aware that the observed retardation is a result of phase changes introduced in the complete optical path. Phase changes can arise from additional affects including refraction from the optical components and transmission through stress birefringent regions within the resin. However these are usually small effects.

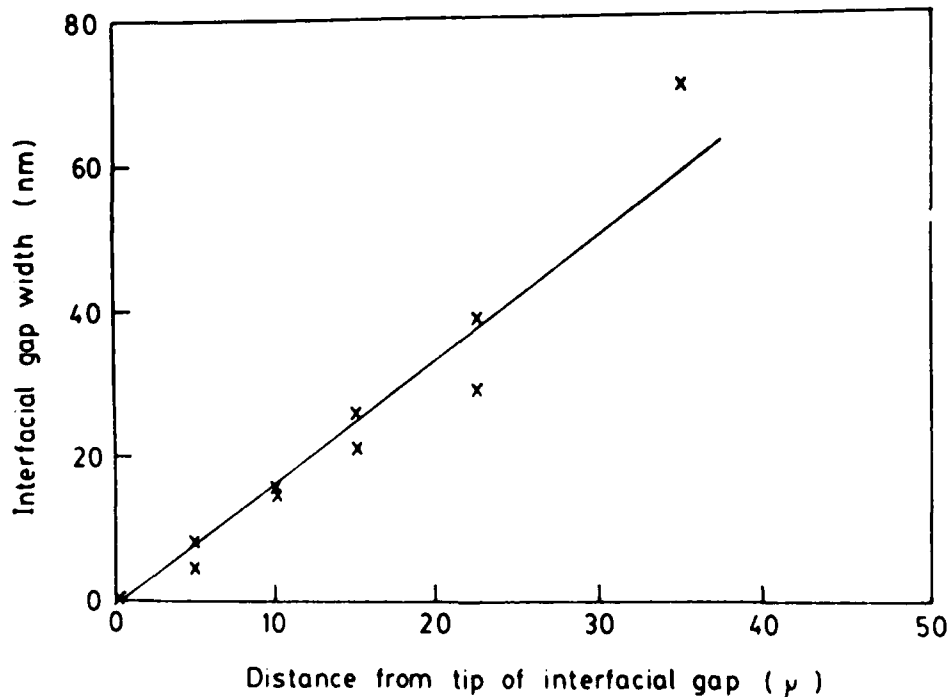


Figure 14. Interfacial gap width as a function of distance from the interface crack tip for the fibre shown in Figure 12.

The fibre in Figure 12 showed a very small amount of stress birefringence and exhibited a retardation gradient across its diameter, i.e. a retardation proportional to the thickness of fibre traversed by the light. This can be seen in the region of bonding, by observation of the dark edges and light central region. Selection of a point at an angle of incidence of approximately  $60^\circ$  yielded a stress birefringence measurement of approximately 2 nm. Measurement in an adjacent region, on the dark contour line where the phase difference introduced by the gap is equal and opposite to that introduced by the stress birefringence, in conjunction with measurements from the surface shown in Figure 13, gives a gap width estimate of 3 nm.

Thus the phase shift may be used either indirectly, by noting the positions of the zero phase change dark contour and by making measurements of the stress birefringence in adjacent regions, or by making direct measurements of the retardation introduced by the interfacial gap and taking due account of the background phase shift. Direct measurements of phase difference have been performed upon the fibre shown in Figure 12 for an angle of incidence of  $60^\circ$ . The interfacial gap size estimated by measuring phase differences is plotted in Figure 14 as a function of distance from the interface crack tip. Figure 15 shows a sequence of photomicrographs for an epoxy/glass-fibre specimen oriented with the fibre axis at an angle of  $45^\circ$  to crossed polars, in which an oil immersion objective (x100) was focused at gradually decreasing distances from the fibre axis. Figure 15 (a) is a schematic diagram showing the debonded region. An important feature of the images in Figure 15 is the generation of interference effects (indicated by an arrow) adjacent to the debonded region. Similar effects were observed with an epoxy/carbon-fibre specimen (Figure 16).

So far, we have assumed that the interfacial gap between matrix and fibre can be treated as a series of parallel-sided interfaces upon which parallel light is incident from one direction. In reality, there will be contributions from evanescent waves which have propagated around the interface from regions remote from the point of interest. Such contributions will in general be from regions having a different angle of incidence and therefore different apparent gap width. Neither geometrical optics ray tracing nor the evanescent wave treatment above can explain intensity distributions such as those shown in Figures 15 and 16 and we need to invoke exact theories for scattering by coaxial dielectric cylinders.

### Scattering Theory

The theory of scattering of electromagnetic waves normally incident upon an infinitely long circular cylinder of arbitrary radius and arbitrary (uniform) refractive index was developed by Rayleigh as long ago as 1881. This predates by some years the better-known solution of the case of scattering by spheres, now usually known as Mie theory (Mie, 1908), although there are earlier independent solutions in the literature. Similarly, the solution to the cylinder problem has been rederived and discussed many times (for references, see van de Hulst (1957) and Kerker, (1969)). Mireles (1966) has shown that for each cylinder radius, there is a unique angular scattering pattern corresponding to each refractive index.

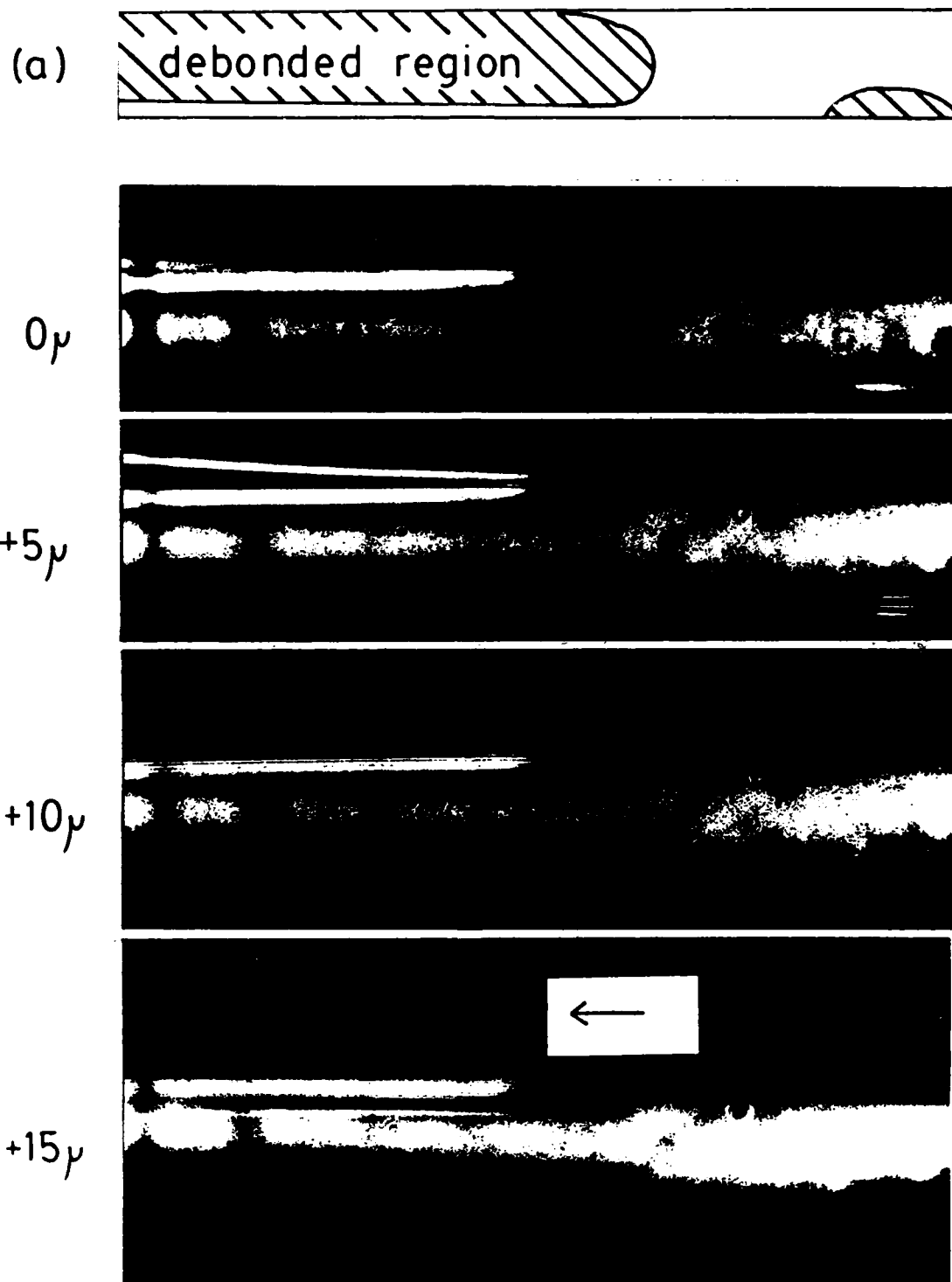
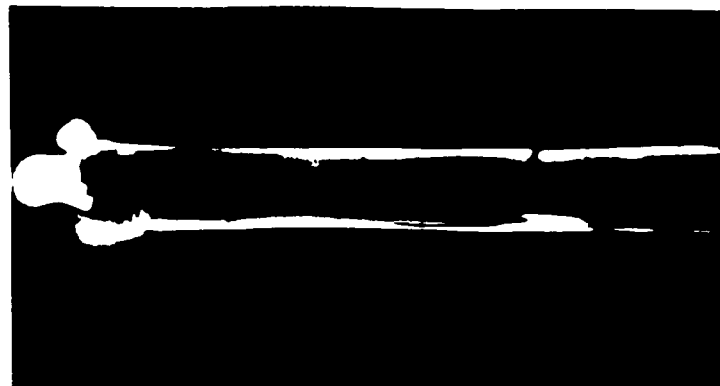
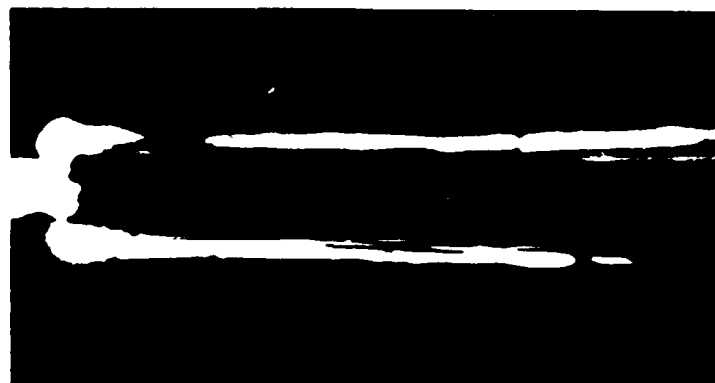


Figure 15. Interference effects (indicated by an arrow) for a debonded glass fibre in an epoxy matrix.

+0 $\mu$



+5 $\mu$



+10 $\mu$

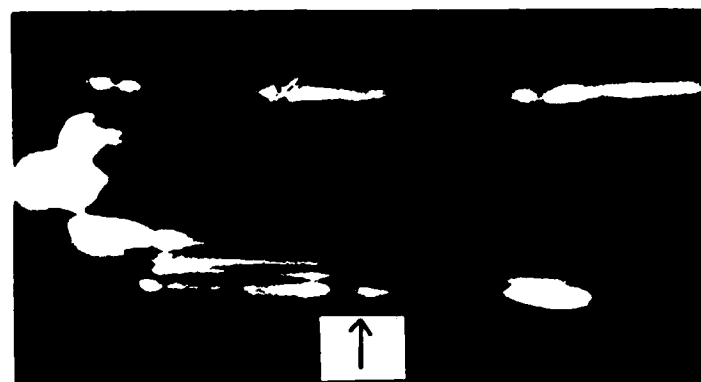


Figure 16. Interference effects (indicated by an arrow) for a debonded carbon fibre in an epoxy matrix.

Our main interest is in the extension of Rayleigh's theory to scattering by coaxial infinite circular cylinders at normal incidence, which has been derived independently by Thilo (1920), Adey (1955) and Kerker and Matijevic (1961). (Note that Farone and Querfeld (1966) further extended the theory to oblique incidence, but Sammadar (1970) has shown that there is no simple rigorous solution for oblique incidence, and that Farone and Querfeld's result is in error). We believe that this theory may usefully be applied to the problem of scattering by a fibre debonded from the matrix of a fibre-reinforced composite, i.e. surrounded by a coaxial region (interfacial gap) of different refractive index. Comparison with experiment should enable us to detect the formation of such gaps and monitor their widths.

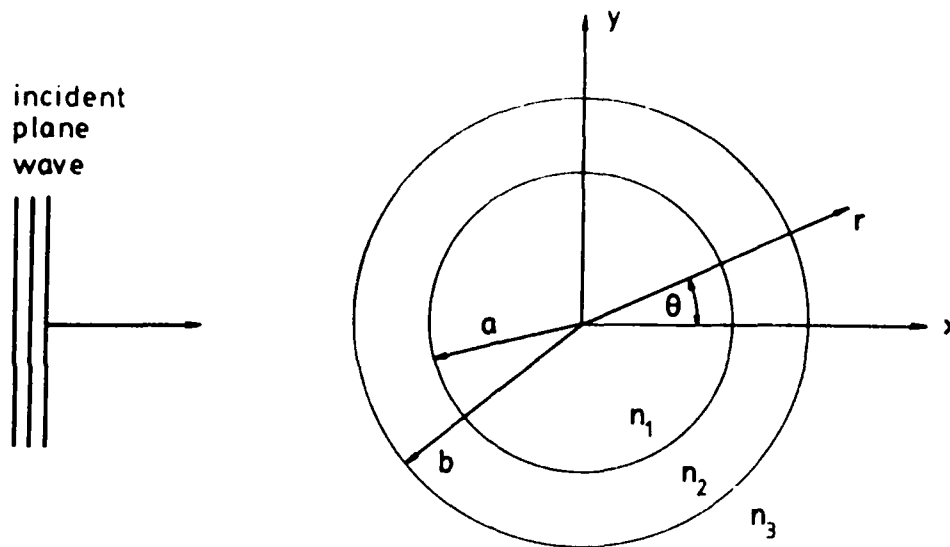


Figure 17. Coordinate system for scattering by coaxial cylinders.

Using the coordinate system shown in Figure 17, the radii of the inner and outer cylinders are given by  $a$  and  $b$  respectively; the coordinates  $r$  and  $\theta$  are defined by  $x = r\cos\theta$ ,  $y = r\sin\theta$ ; the incident beam travels in the  $x$ -direction and  $\theta$  is the angle between incident and scattered beams. For an incident plane wave of unit amplitude and frequency  $K = 2\pi/\lambda$ , with its electric vector parallel to the cylinder axis (TM mode), the fields at a point  $(r, \theta)$  are as follows.

In the fibre, region 1 ( $r < a$ ),

$$E_1 = E_1^{sc} = \sum_{m=-\infty}^{\infty} i^m D_m J_m(n_1 k r) \exp(im\theta) \quad (4a)$$

In the interfacial gap, region 2 ( $b > r > a$ ),

$$E_2 = E_2^{sc} = \sum_{m=-\infty}^{\infty} i^m [B_m H_m^{(2)}(n_2 k r) + C_m H_m^{(1)}(n_2 k r)] \exp(im\theta) \quad (4b)$$

and in the matrix, region 3 ( $r > b$ ),

$$E_3 = E_3^{in} + E_3^{sc}$$

$$\text{where } E_3^{in} = \sum_{m=-\infty}^{\infty} i^m J_m(n_3 K r) \exp(im\theta)$$

$$\text{and } E_3^{sc} = \sum_{m=-\infty}^{\infty} i^m A_m H_m^{(1)}(n_3 K r) \exp(im\theta) \quad (4c)$$

In these equations, superscripts in and sc represent incident and scattered fields;  $J_m$  is a Bessel function of the first kind and  $H_m^{(1)} = J_m + iY_m$ ,  $H_m^{(2)} = J_m - iY_m$  are Hankel functions,  $Y_m$  being the Neumann function. The unknown (complex) scattering amplitudes  $A_m$ ,  $B_m$ ,  $C_m$  and  $D_m$  are found in terms of Bessel and Hankel functions, from the boundary conditions of continuity of the electric and magnetic fields at the various interfaces: this involves considerable algebra (see e.g. Kerker and Matijevic, (1960)). For the case when the magnetic vector is parallel to the cylinder axis (TE mode), the field equations are as above, but in the determination of the scattering amplitudes the electric field  $E$  is replaced by the magnetic field  $H$ ,  $H$  by  $-E$ , and permeability  $\mu$  by permittivity  $\epsilon$  (which in practice means that matrix elements which were multiplied by refractive index no longer depend on refractive index, and vice-versa). From equations 4 (above), in principle we can calculate the intensity at any point. However, the magnitude of computation required is considerable, and a variety of approximations merit consideration.

Datta and Som (1975) give details of numerical methods for calculating the intensity at points within the inner cylinder; this scheme is applicable to our case, but the results they present are for cylinder diameters comparable with the wavelength of the incident radiation.

The far-field intensity reduces to

$$I(\theta) = |A_0 + 2 \sum_{m=1}^{\infty} A_m \cos m\theta|^2 \quad (5)$$

but this is still far from simple to compute, as we require the coefficients  $A_m$ . Both algebra and computation are simplified if the innermost cylinder is a conductor (Adey (1956)), but that is not appropriate to most fibre reinforced composites.

A more useful simplification is the 'thin sleeve' approximation, which is applicable if the interfacial gap is small compared with the fibre radius, i.e.  $b-a \ll a$ . Adey (1956) indicates how the expressions for the scattering amplitudes  $A_m$ ,  $B_m$ ,  $C_m$  and  $D_m$  may be simplified in this approximation, whilst Senior and Weil (1977) derive expressions for the fields outside hollow cylinders of infinitesimal thickness; they present calculations for infra-red scattering by thin-walled ice crystals with diameters comparable to the wavelength, but claim that the numerical procedures are economical for diameters up to a few wavelengths.

Far-field intensities have been computed by several workers for scattering by clad and graded-index optical fibres, (see e.g. Farone and Querfeld (1966), Marcuse and Presby (1975), Watkins (1974), and references therein), and comparisons with experiment have led to determinations of fibre diameter and cladding thickness to within 1% - better than obtainable by any other means, such as electron microscopy. Unfortunately, none of these calculations have involved combinations of wavelength, cylinder radii and refractive index appropriate to fibres in reinforced composites.

Marcuse and Presby (1975) have commented on some of the problems of numerical evaluation, and on the volume of computation required to find curves of scattered intensity which fit particular experimental

observations: the curves are extremely sensitive to changes of cylinder radius and refractive index. Thus it appears that full calculations of scattered intensity are likely to be impracticable as a general measuring tool, but could prove valuable to monitor variations of parameters for a given specimen.

In a study of unclad fibres of uniform refractive index, van der Meulen and Strackee (1979) found that, for scattering of visible light by fibres with diameters in the range 1 to 10  $\mu$ , the number of minima (fringes) of forward scattered intensity in the angular range 0 to 90° was proportional to a size parameter  $2\pi a/\lambda$  (where  $a$  = fibre radius) and insensitive to refractive index. From calculated curves of upper and lower limits on the number of minima, as a function of size parameter, they were able to estimate fibre diameters to within 10%, from experimental measurements at only one wavelength. We conjecture that an analogous scheme for studying scattering by coaxial cylinders would be well worth investigating, with a view to applying it to the measurement of interfacial gaps around fibres in fibre reinforced composites.

#### Acknowledgements

One of us (JPS) gratefully acknowledges financial support from the US Army, Grant No (DAJA45-83-C-0030).

#### References

- Adey A W, (1956) Can. J. Phys., 34, 510.  
Carniglia C K and Mandel L, (1971) J. Opt. Soc. Am., 61, 1043.  
Datta A K and Som S C, (1975) Appl. Opt., 14, 1516.  
Farone W A and Querfeld C W, (1966) J. Opt. Soc. Am., 56, 476.  
Feynman R P, Leighton R B and Sands M, (1964) "The Feynman lectures on Physics", Vol. II, chap. 33, Addison Wesley, Reading, Mass.  
Hecht E and Zajac A, (1974) "Optics", chap. 4, Addison Wesley, Reading, Mass.  
Kerker M, (1969) "The Scattering of Light and Other Electromagnetic Radiation", chap. 6, Academic, New York.  
Kerker M and Matijevic E, (1961) J. Opt. Soc. Am., 51, 506.  
Klein M V, (1970) "Optics", chap. 11, Wiley, New York.  
Marcuse D and Presby H M, (1975) J. Opt. Soc. Am., 65, 367.  
Mie G, (1908) Ann. Physik, 25, 377.  
Mireles R, (1966) J. Math. Phys. (Camb., USA), 45, 127.  
Rayleigh Lord, (J W Strutt), (1881) Phil. Mag., 12, 81.  
Sammadar S N, (1970) Nuovo Cimento, B66, 33.  
Senior T B A and Weil H, (1977) Appl. Opt., 16, 2979.  
Thilo G, (1920) Ann. Physik, 62, 531.  
van de Hulst H C, (1957) "Light Scattering by Small Particles", chap. 15, Wiley, New York.  
van der Meulen A and Strackee L, (1979) Appl. Opt., 18, 3751.  
Watkins L S, (1974) J. Opt. Soc. Am., 64, 767.  
Weinstein W, (1947) J. Opt. Soc. Am., 37, 576.



# MICROWAVE PROPAGATION IN CARBON FIBRE REINFORCED COMPOSITE MATERIAL

A.D. Carr

Marconi Research Centre, Great Baddow, Chelmsford, Essex

## ABSTRACT

The detection of water, absorbed by carbon fibre composite material, is attempted by two methods using microwave radiation. The attenuation of 50% fibre volume sheet material has been measured as 60 dB cm<sup>-1</sup> at 9.6 GHz. Accelerated moisture absorption by immersion in boiling water over a 25 hour period, produced a detectable change in attenuation; of the order of 0.4 dB for 2 mm thick samples. Measurement of the permittivity of the composite sheet proved to be impossible owing to its high effective conductivity. An estimate of the order of 10 ( $\Omega$ m)<sup>-1</sup> has been made for the conductivity of the dry material.

## INTRODUCTION

The application of non-destructive evaluation methods to the detection of flaws, for example cracks, delaminations, voids or water presence in composite materials is certainly more complex when compared to traditional materials such as metals. The relatively wide variation encountered in the properties of nominally identical composite samples, produces comparable variations in the data obtained from applied N.D.E. methods and makes evaluation of test results difficult. Examples of techniques which have been applied with some success include ultrasonic scanning and x-radiography. The use of microwave radiation to probe the microstructure of structural materials has apparently not received a great deal of attention. Clearly its use would be limited to non-metals. However even in this restricted field the author has found only one report of an application in the N.D.E. context. This involved the detection of voids and cracks in ceramic material by measurement of the radiation scattered by defects.

Microwave radiation is employed industrially to monitor water levels in a wide range of products; for example paper, soap, cement and foodstuffs. The physical phenomena generally exploited in all these applications is that water strongly absorbs radiation in the centimetre wavelength region of the spectrum. Variations in the power transmitted through the product can be measured and used to effect on line changes in the manufacturing process. Moisture absorption during production and in service lifetime is a problem also associated with composite material components. Diffusion of water into the resin matrix may have several effects, some of which are reversible and others which are not. Swelling and plasticisation of the resin are examples of effects which it may be possible to reverse by drying. Irreversible damage, however, can be caused by the accumulation of water at fibre/resin interfaces. It has been shown (Ashbee 1969) that dissolution in absorbed water of soluble material found on the fibre surfaces, specifically alkali metal oxides, leads to the formation of pressure pockets in the resin by the process of osmosis. Stresses set up in the resin as a result, lead to the irreversible breakage of bonds at the

fibre/resin interface and hence to a reduction in load transfer ability between the two. The presence of these cracks and the photoelastic contrast produced by the stresses have both been observed experimentally.

A method of non-destructively determining the degree of water absorption in a composite material would therefore appear to be desirable, particularly, for example, in the aircraft industry where considerable long-term exposure to moisture is encountered. The aim of this study was to investigate the application of microwave techniques to the problem of water detection in a unidirectional carbon fibre reinforced composite.

#### EXPERIMENTAL AND DISCUSSION OF RESULTS

After consideration of the methods used to measure moisture content in the industrial materials mentioned earlier and also of the waveguide equipment available it was decided to attempt the measurement of two different quantities, namely attenuation and dielectric permittivity of the carbon composite. The sheet material used throughout the experimental work was manufactured from Fothergill and Harvey Code 69 epoxy resin and Courtaulds "EXAS" fibre in a unidirectional, 2 mm thick lay up. The fibre volume was nominally 50% with a 2.5% void content.

Measurement of the transmission of microwaves through a sample was carried out on the waveguide apparatus shown diagrammatically in Fig. 1. A Gunn oscillator device acted as the radiation source and provided an output power of 8 mW at 9.6 GHz. The device was protected against interference from reflected power by a short isolator section. The 4.3 cm square composite coupons were clamped between two open ended waveguide horns with the fibre direction parallel to the polarisation.

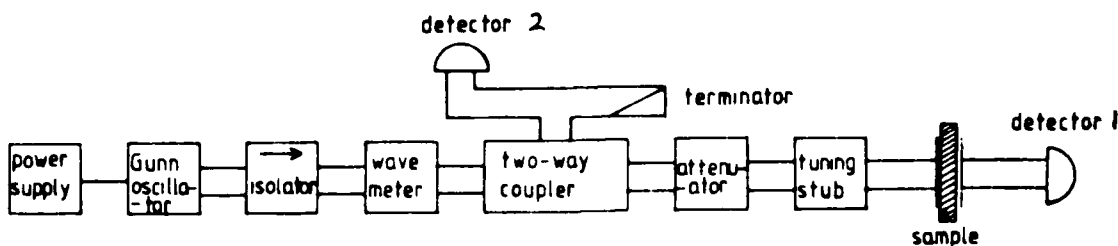


Figure 1. Apparatus used for sample attenuation measurement

The attenuation measurement was carried out by firstly noting the transmitted signal at detector 1 with the sample in place, and then increasing the calibrated attenuator with the sample removed, until the transmitted power fell to its previous value. The two termination conditions i.e. sample in place or absent, will both present large and different impedance mismatches to the open ended waveguide and so different power reflections will occur. This variation would

appear as part of the sample attenuation by its effect on the transmitted signal. To overcome this problem and ensure that equal power levels were reflected under the two different termination conditions, a two arm tuning stub device was placed in line on the generator side of the sample. By adjustment of shorting plates in the E and H plane arms, matching of the load to the waveguide could be achieved. Detector 2, mounted on a 10 dB coupler was used to measure the reflected power during matching. Since the transmission of the composite was found, as expected, to be sensitive to fibre orientation relative to the polarisation direction, reference marks were made on all samples to ensure repeatable positioning between successive measurements.

Accelerated moisture absorption into the composite material was achieved by immersing coupons in boiling water for periods of one or two hours. During immersion the samples were freely suspended by a small plastic clip thus ensuring that water uptake was not inhibited in any region. At the end of each immersion period the sample surfaces were thoroughly dried of excess water and allowed to cool to room temperature before being clamped in position. Matching was then performed until the reflected power at detector 2 fell to zero. With the sample removed the line was rematched and the calibrated attenuator wound in until the transmitted power fell to its previous value. The procedure was repeated a minimum of five times to estimate the errors associated with the measurement.

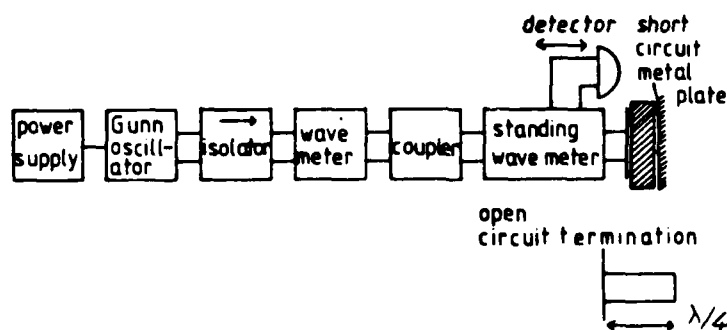


Figure 2. Apparatus for permittivity measurement.

Evaluation of the complex permittivity of the composite material was also attempted and the waveguide apparatus for this measurement is shown in Fig. 2. The method (Von Hippel, 1962) involves measurements on the standing wave set up when a plane dielectric material is placed across the guide. It can be shown that, if the sample is backed by a short circuit metal plate, the impedance viewed from the front face is given by:

$$Z_s = Z_0 \frac{[V - j \tan(2\pi x_0 / \lambda)]}{[1 - jV \tan(2\pi x_0 / \lambda)]} = Z_0 A_s \quad (1)$$

where  $V$  is the inverse of the voltage standing wave ratio,  $x_0$ , the distance of the first standing wave minimum from the sample,  $\lambda$  is the

guide wavelength and  $Z_0$  is the waveguide characteristic impedance. A similar expression is valid if a quarter wave shorted section of waveguide is placed behind the sample, forming an open circuit termination, with the new measured values of  $x_0$  and  $V$  substituted in equation 1 to give a second complex value  $A_0$ . For a non-magnetic material the permittivity is given by:

$$\epsilon^* = \epsilon_0 \frac{[(1/\lambda_c)^2 + (1/\lambda)^2 - 1/A_0 A_s]}{(1/\lambda_c)^2 + (1/\lambda)^2} \quad (2)$$

where  $\lambda_c$  is the cut off wavelength of the fundamental mode. Test measurements conducted on good, low loss dielectric materials such as paraffin wax and polypropylene showed close agreement with accepted values. However, the accuracy of the method when applied to the carbon fibre composite was found to be insufficient to determine the permittivity and any variations due to water absorption. The major source of experimental error ( $\pm 0.5$  mm) was in determining the distances  $x_0$  of the minima from the sample face and it is thought that the minima must lie within the error distance. A subsequent evaluation of  $x_0$  from other data described later showed that the first minimum was very close to the sample as a result of the high effective conductivity of the carbon fibre.

The voltage standing wave ratios (V.S.W.R.) were determined to an accuracy of  $\pm 0.03$  for the short circuit termination condition. A plot of values obtained during the first hour of immersion is shown in Fig. 3. Both ratios increase with time indicating a rise in reflectivity of the composite with water uptake. An order of magnitude estimation of the effective conductivity can be made from this data if a simplified model is invoked. The waveguide is assumed to be

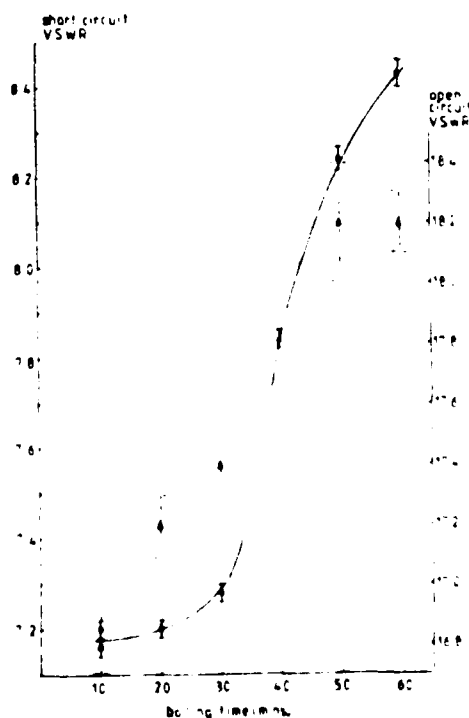


Figure 3

Short (o) and open circuit (Δ) voltage standing wave ratio plotted against boiling time.

lossless and the sample is treated as being completely enclosed inside the guide and terminated by a matched load. This second condition is approximated fairly well in the experimental situation since the sample attenuation was large and a wave, reflected by the back face, will be substantially attenuated after traversing a double thickness and will have little effect on the standing wave pattern.

The wave impedance of a material is given generally by  $Z = \sqrt{\mu^*/\epsilon^*}$  where  $\mu^*$  and  $\epsilon^*$  are the complex permeability and permittivity respectively. For non-magnetic materials  $\mu^* = \mu_0$ , the value of free space and  $\epsilon^*$  is given by

$$\epsilon^* = \epsilon\epsilon_0 - j\sigma/\omega \quad (3)$$

$\epsilon$  is the relative permittivity,  $\sigma$  the effective conductivity and  $\omega$  is the angular frequency. Expressing  $Z$  in modulus/argument form we get

$$Z = \sqrt{\mu_0/\epsilon\epsilon_0} (1 + \sigma^2/(\epsilon\epsilon_0)^2 \omega^2)^{-1/4} e^{1/2 j \tan^{-1}(\sigma/\epsilon\epsilon_0 \omega)} \quad (4)$$

The V.S.W.R. of an impedance  $Z$  loaded onto a waveguide of characteristic impedance  $Z_0$  is given by

$$V' = |Z_0|/|Z| \quad \text{for } Z < Z_0 \quad (5)$$

and from the graphical data this ratio is  $\sim 10$ . Equating the values of  $|Z|$  in (4) and (5) and substituting  $\epsilon = 3$  as the dielectric constant of the resin and  $Z_0 = 500\Omega$ , a value of  $30 (\Omega m)^{-1}$  is calculated for  $\sigma$ .

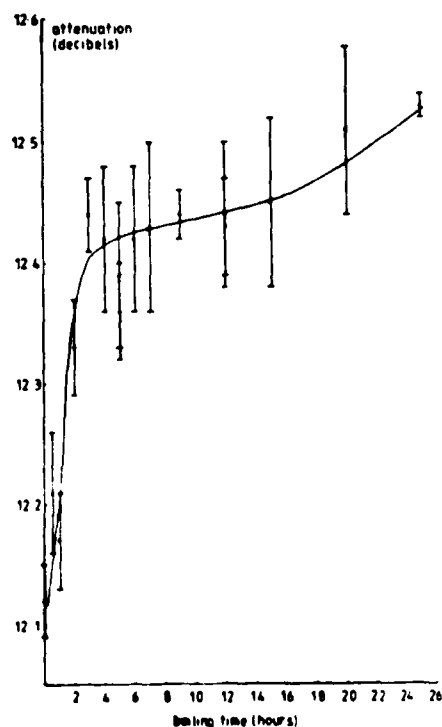


Figure 4

Attenuation variation with boiling time for carbon fibre reinforced composite

A second estimate of sample conductivity can be obtained from the measured attenuation of the carbon fibre composite. Fig. 4 shows the

change in attenuation with boiling time for one particular example over a 25 hour period. An initial rapid rise from 12.12 dB to over 12.4 dB during the first 5 hours is followed by a much slower rise to 12.5 dB after the full immersion time. The initial rise corresponded to an uptake of 15 mg of water determined by weighing the sample. The characteristic length for the attenuation of the E field is the skin depth  $\delta$ . This is related to the material conductivity  $\sigma = (2/\mu_0 \sigma \omega)^{1/2}$  and both the electric and magnetic field vectors are reduced by  $1/e$  in traversing the skin depth. The power attenuation P, in decibels over a distance z is therefore given by

$$P = 10 \log_{10} e^{-2z/\delta} \quad (6)$$

Substitution into equation (6) of the measured loss of 12 dB for a sample thickness of 2 mm results in a conductivity of  $12 (\Omega\text{m})^{-1}$  i.e. of the same order as was estimated from the V.S.W.R. data.

The conductivity values can be used to estimate the distance  $x_0$  of the first standing wave minimum from the sample face. Taking the composite to be at  $z = 0$  with the z axis parallel to the direction of wave propagation, the standing wave pattern is formed by the addition of the reflected and incident wave according to

$$V(z) = V_{\text{inc}} e^{-jkz} + V_{\text{refl}} e^{jkz} \quad (7)$$

The  $e^{j\omega t}$  time factor is assumed. The voltage reflection coefficient at z is defined as

$$\Gamma(z) = \frac{V_{\text{refl}}}{V_{\text{inc}}} e^{2jkz} = \Gamma(0) e^{2jkz} \quad (8)$$

and  $\Gamma(0)$ , the reflection coefficient at  $z = 0$  is related to the mismatch between the waveguide impedance  $Z_0$  and the impedance of the composite according to:

$$\Gamma(0) = |\Gamma| e^{j\Phi} = [Z_L - Z_0] / [Z_L + Z_0] \quad (9)$$

After substitution of eqns (9) and (8) into (7) and taking the modulus of both sides:

$$|V(z)| = |V_{\text{inc}}| \sqrt{1 + |\Gamma|^2 + 2|\Gamma| \cos\Phi} \quad (10)$$

where  $\Phi = \varphi + 2kz$ .

The first minimum in V will occur when  $\Phi = \pi$ .  $\Gamma(0)$  can be found from equation (9), by using equation (4) with  $\sigma = 30 (\Omega\text{m})^{-1}$  and its complex value is  $\Gamma(0) = 0.87 e^{j3.0}$ . Using  $\varphi = 3.0$  and  $k = 2\pi/\lambda_g$  where  $\lambda_g$ , the guide wavelength is 4 cm at  $10^{10}$  GHz, then  $x_0$  is found to be 0.04 cm from the sample face. Clearly this is well within the estimated position measurement error of 0.05 cm and so is impossible to measure with the present apparatus. It would also seem doubtful whether the accuracy of the standing wave meter method could be improved sufficiently to attain the resolution required for the detection of absorbed water.

The plot of sample attenuation of radiation with boiling time showed a distinct change in gradient after 5 hours with a much slower rise rate occurring after this time. Examination of sample cross sections under an optical microscope showed the fibre density to be on average lower in a surface region of a few tens of microns thickness, compared with the interior density. Without being able to estimate quantitatively the diffusion rates in regions of different fibre density it would appear that water absorption would occur more rapidly into the surface region than the more densely packed interior. Water diffusion takes place to any appreciable extent in the resin only. Therefore regions with a greater fibre content would present a more convoluted path around the fibres and so impede the progress of diffusing water to a greater extent. A fall in absorption rate would therefore be expected when the interior region is encountered, and this is observed in the experimentally measured fall off in attenuation after 5 hours immersion time.

#### CONCLUSION

The detection of water absorption by carbon fibre composite material has been shown to be feasible by measurement of the attenuation of microwave radiation. The insertion loss at 9.6 GHz is of the order of  $60 \text{ dB cm}^{-1}$  for radiation polarised perpendicular to the fibre direction. After a 25 hour immersion period in boiling water a change of 0.4 dB as a result of water uptake was found for the 2 mm thick composite sample. The appearance of an initial high absorption rate followed by a much slower rate is attributed to a greater fibre density existing in the interior of the sheet compared with the surface region. Estimates of the effective conductivity of the composite put the value at the order of a few tens of ohms/m. This relatively high conductivity is responsible for the failure of the permittivity measurement method to detect any changes as a result of water absorption.

Application of the transmission method as a non-destructive testing technique appears to be possible though the specific experimental set up and interpretation of results would depend very much on the individual situation. The relatively large measurement error of the insertion loss indicates the sensitivity of the method to misalignment of the fibre direction with the polarisation and is also partly due to the fact that the inherent attenuation of the composite is somewhat greater than the change produced by absorbed water. An improvement to the sensitivity of the method to water uptake could be made by employing a bridge technique to measure the difference in attenuation between the material under test and a known standard of similar value.

#### REFERENCES

- Ashbee, K.H.G., Wyatt, R.C. (1969) Proc. Roy. Soc. A312, 557-564.  
Von Hippel, A.R. (1962), "Dielectrics and Waves", Wiley, London.

#### ACKNOWLEDGEMENTS

This work was carried out while I was studying for a M.Sc. degree at Bristol University. I should like to acknowledge the assistance given by my supervisors Drs K.H.G. Ashbee and C. Gill.

POTENTIAL OF HOLOGRAPHIC INTERFEROMETRY  
FOR NON DESTRUCTIVE TESTING OF POLYMER COMPOSITES

W.J. Beranek  
TNO-IBBC

Abstract

A survey is given of tests, which have been carried out to study defects in polymeric tubes, using holographic interferometry. Possibilities are discussed to use these techniques in real-time in-process.

1. Introduction

In holographic interferometry a hologram is made of an object in the unloaded and in the loaded position. The two virtual images will come to interference and as a result a fringe pattern is formed. These fringes are contourlines for the change in optical path-length. If the holographic set-up is properly chosen, the fringe pattern can also be regarded as contourlines for a displacement component.

If the tested object has some defect which influences the physical behaviour under load, the interference pattern will also undergo some changes. In some cases these changes will be typically for the kind of defect, but in other cases no conclusions can be drawn.

The paper describes the results of a series of tests on polymer tubes, (homogeneous, glass-fiber and carbon-fiber) in which a number of tubes had some natural or artificial defects.

2. Holographic interferometry

Basically the tests have to be carried out on an optical table, unless a pulse laser is used. The applied loads generally may be very small. The object should be mate reflecting, so most of the time the objects are painted white.

There is a number of holographic techniques which can be used for testing objects of various shape. For the testing of the tubes the following techniques have been used:

- a. Double exposure and real-time holography, using one beam of illumination.
- b. Double exposure and real-time holography, using two beams of illumination (holographic moiré).
- c. Time average holography (vibrating object)

When one beam of illumination is used, the displacement component in the direction of the bisector of the angle between the direction of illumination and the direction of observation is obtained. The interference patterns are generally clear as long as the texture of the object does not change under load, see Fig. 1a. The quality of double-exposure holograms is generally somewhat better than that of real-time holograms. But in the first case just one kind of loading can be investigated, whereas in the second case the kind of loading as well as the magnitude of the load can be changed.

When two beams of illumination are used, the technique is called holographic-moiré. Now the out-of-plane component of the displacement and one in-plane component of the displacement can be obtained in the same set-up at one and the same loading step. For each direction of illumination a carrier of parallel equidistant fringes is applied and the interference of the two (mismatched) basic interference patterns will show a moiré pattern. This moiré pattern in turn can be regarded as a contourline map for the wanted displacement component. Generally the in-plane component is recorded, as the out-of-plane component can also be obtained by method a.



As the obtained interference pattern is a second-order pattern, the results are seldom as clear as in case a., but fringe contrast can be enlarged optically (afterwards) or electronically (during real-time holography), see Fig. 1b. The set-up is somewhat more complicated as in case a., but the application of a mirror to form the second beam of illumination keeps things relatively simple. The application of the carrier fringes however, always requires a rotation of the hologram (or the object) between the unloaded and the loaded position of the object.

In the case of time-average holography, one beam of illumination is applied and the exposure of the hologram takes a few seconds whilst the object is vibrating. Nevertheless clear interference patterns are obtained for the investigated vibration mode of the object, see Fig. 1c. In this way each vibration mode of the object requires a separate hologram. But if a rough idea of the various vibration modes of the object is sufficient, another technique can be applied. A real time hologram is made of the object in the unloaded position and carrier fringes are applied by rotating the beam of illumination. During vibration locally the carrier fringes are wiped out and all vibration modes can be recorded in real time, see Fig. 1d.

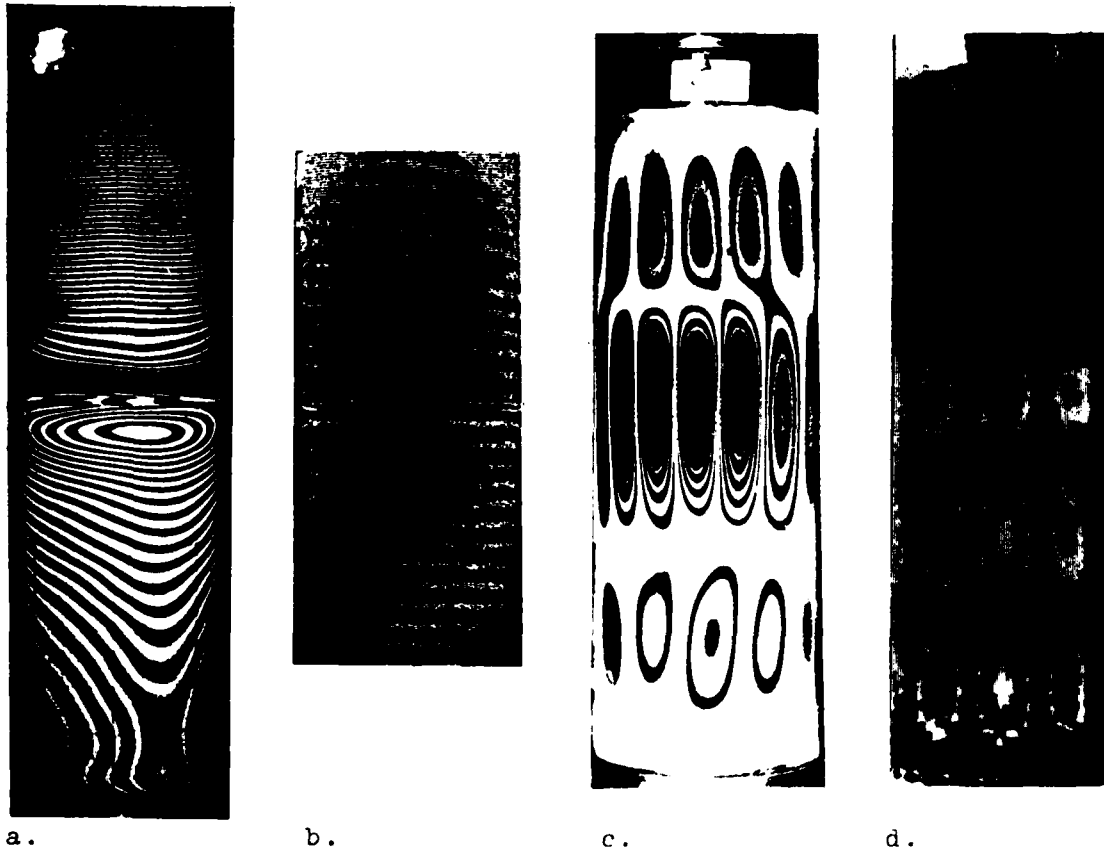


Fig. 1 Holographic interference patterns.  
a. one beam of illumination; axial tension  
b. holographic moiré; axial tension  
c. time average; vibration  
d. vibration in real time

### 3. Detection of defects in homogeneous tubes

First of all one has to find out for which loading case a certain defect will give a noticeable change in the interference pattern. As an example the interference patterns are given for the connection of two tubes which are not perfectly in line, see Fig. 2. The effect of torsion proves to be negligible, internal pressure and a temperature change show similar patterns in which the influence of the connection is vaguely visible. Axial tension however, shows striking changes of the pattern in the vicinity of the connection.

The second step is to find out if the change of the interference pattern will also have some influence on the strength or the good behaviour of the object during lifetime. So from Fig. 2d it follows that the two tubes under tension will show bending disturbances in the vicinity of the connection and the magnitude of the bending stresses can easily be determined.

About the tensile strength of the connection under pure tension however, no information is available. So the strains in the axial direction have been determined with the help of holographic-moiré, see Fig. 1b. But also this pattern will hardly give any information about the strength of the connection; obviously plane sections remain more or less plane under tension independently of the strength of the connection.

As a matter of fact, in all tests where the tensile strength of such connections or similar ones was investigated, no adequate information from the tests was obtained. It seems that under such low loads (as is required in non-destructive testing) good and bad connections show a similar behaviour, and differences in behaviour may only be expected at much higher loads.

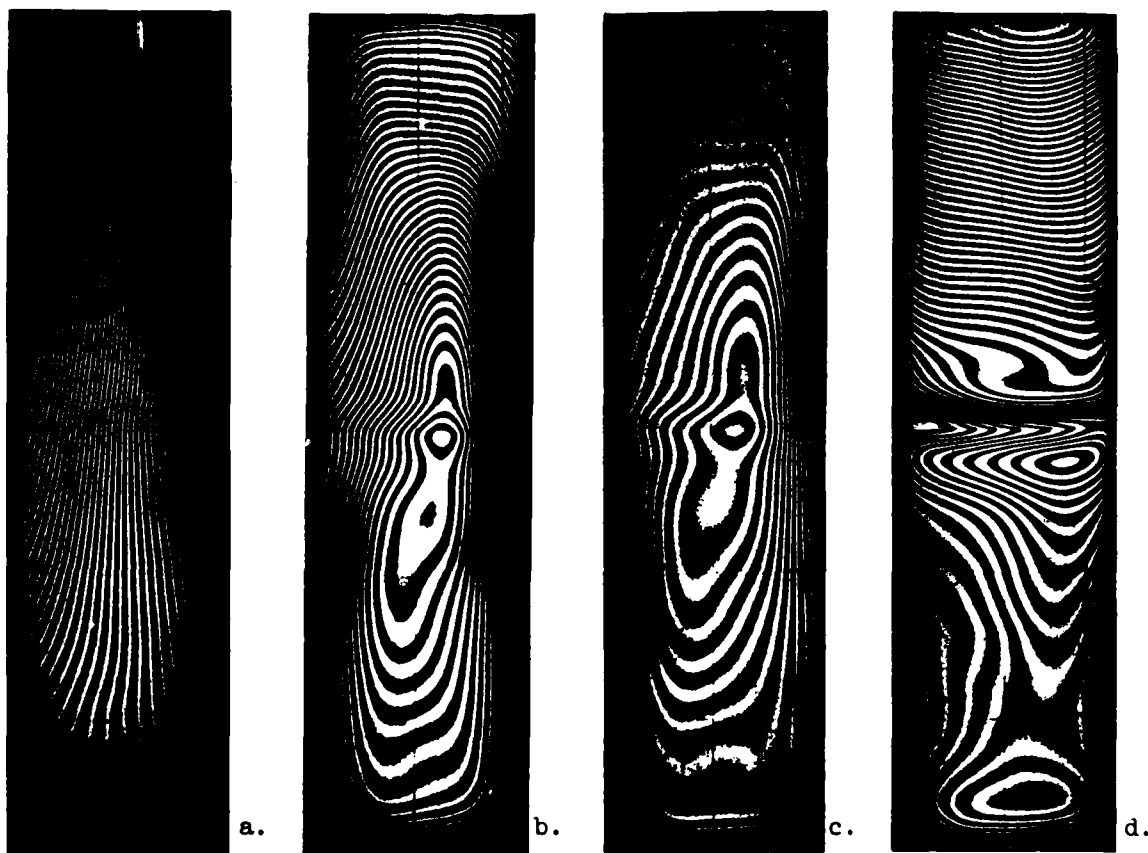
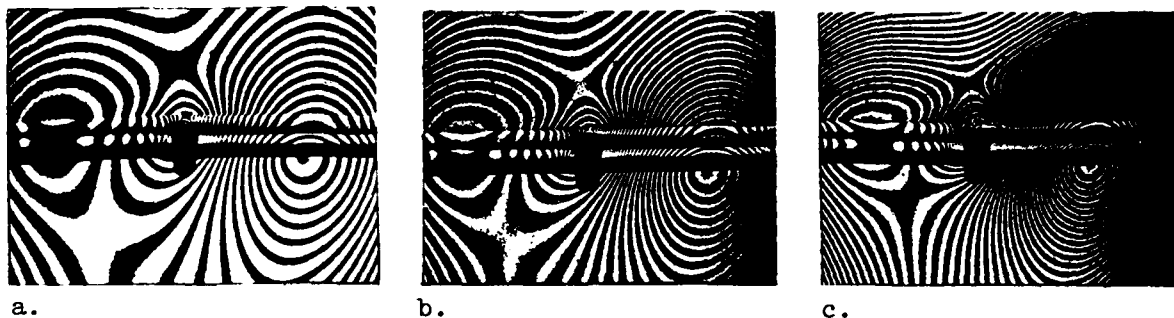


Fig. 2 Connection of two homogeneous tubes; interference patterns for the out of plane displacements.  
a. torsion; b. internal pressure; c. temperature change; d. axial tension

Usually the strength of the connection is determined with the help of a destructive test: the pin indentation test. Results may be expected after a few months. It was tried to obtain information at short notice by making a series of holograms after the pin had been driven into the hole which is made in the connection. Fig. 3 shows some results, obviously the material is strongly creeping, but no indication was found about the strength of the connection, depending of the shape and variation in shape as function of time, of the interference pattern.

#### 4. Check of the qualities of glass-fiber tubes

Holographic tests have been carried out to detect aberrations in the winding pattern and to check the theoretically determined stiffnesses in axial and tangential direction. In Fig. 4 the results are shown for three tubes under internal pressure, two of the tubes having a deviating winding pattern. The out-of-plane displacements show marked differences.



a. b. c.  
Fig. 3 Out of plane displacements for a pin indentation test.  
First exposure 75 s after application of the pin, second exposure after:  
a. 30 s; b. 60 s; c. 120 s

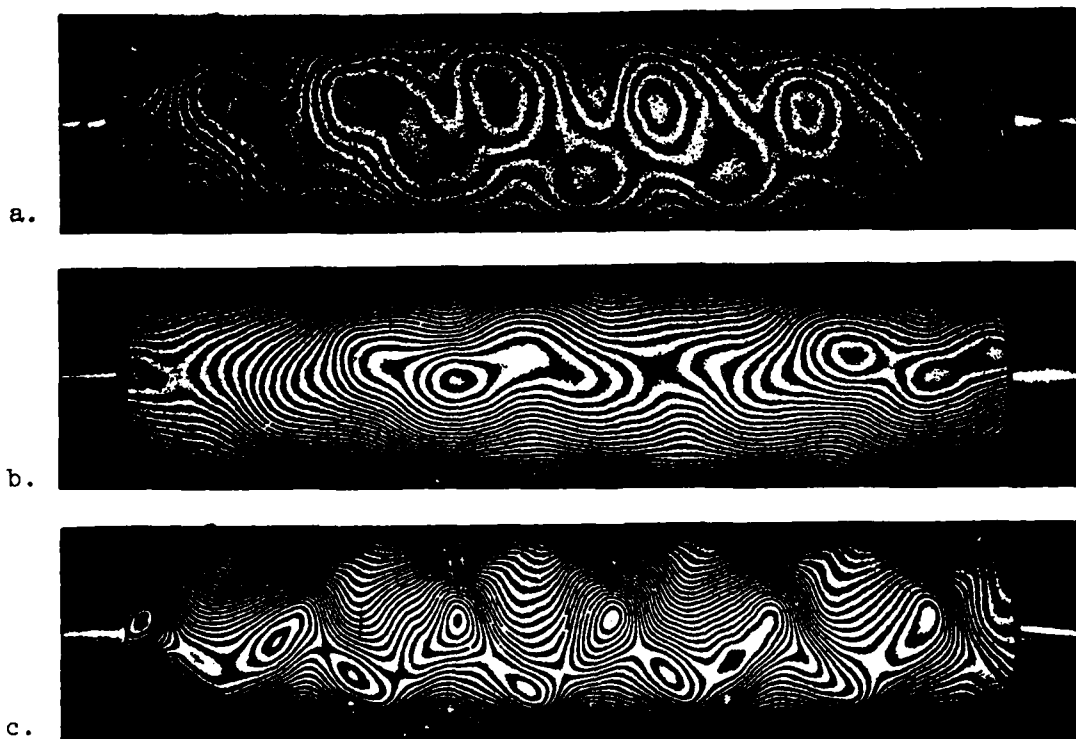


Fig. 4 Out of plane displacements for three glass fiber tubes with different winding patterns.

The interference patterns of Fig. 4 have also been provided with carrier fringes. Optical differentiation will then show contourlines for the slopes in axial or tangential direction, see Fig. 5.

For the determination of the axial and tangential stiffness the tubes have been submitted to internal pressure in radial and axial direction, and the in-plane and out-of-plane displacements have been determined with the aid of holographic-moiré. The results for the three tubes are shown in the Figs. 6, 7 and 8. The strain distribution in axial direction is shown as the average strain between each two successive contourlines for the displacement in axial direction. Especially tube No 3 in Fig. 8 shows marked differences in axial strain. But if the influence of the out-of-plane bending deformation is taken into account, it shows that the axial strain (in the middle of the wall thickness) is practically constant. That means that the variations in axial strain is only due to bending and can be deducted from out of plane displacements alone, which can be determined with method a.

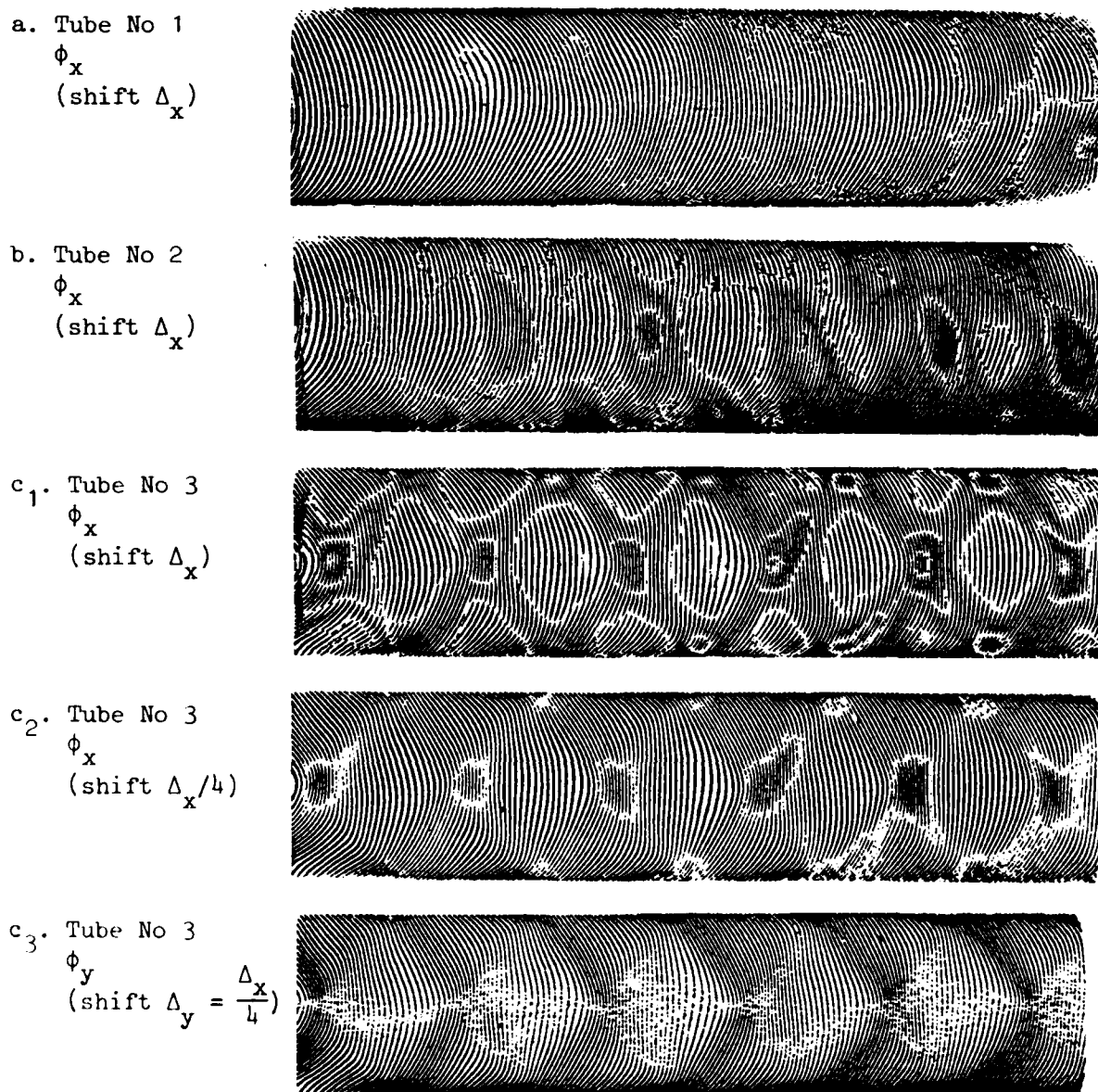


Fig. 5 Determination of the slopes of three glass-fiber tubes by optical differentiation (shifting two equal photographs towards each other)

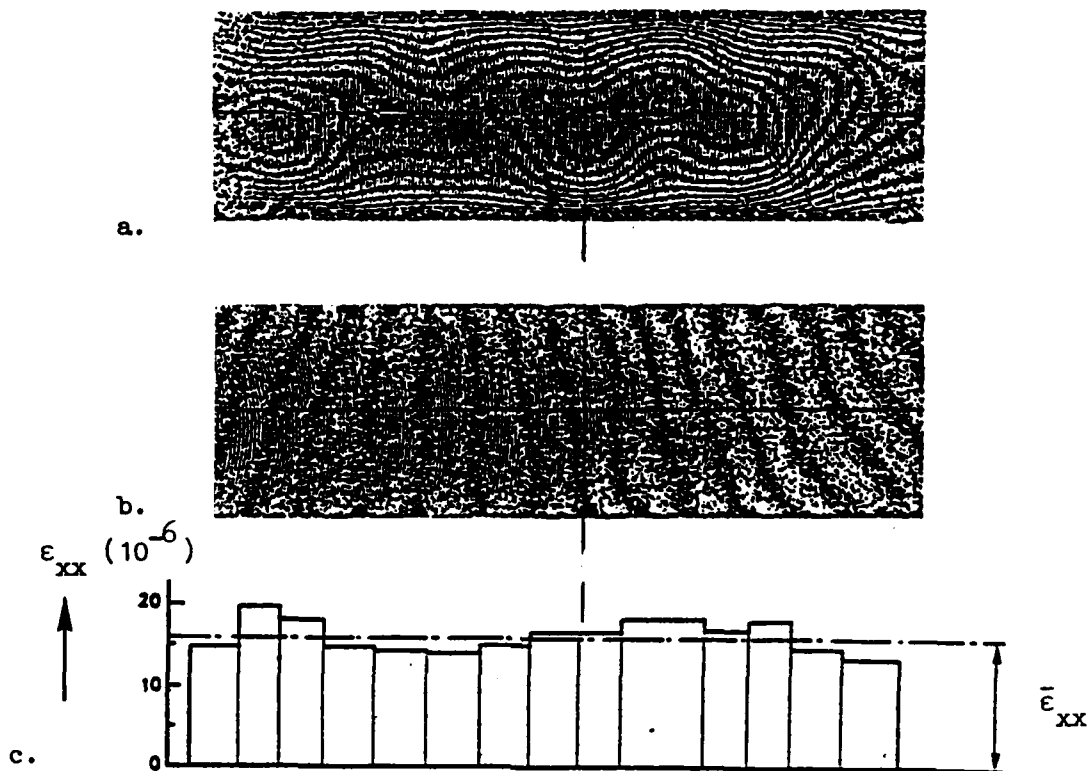


Fig. 6 Holographic-moiré for glass-fiber tube No 1  
 a. out-of-plane displacements; b. in-plane displacements in axial direction  
 c. average strain between successive contourlines and average strain over the full length of the tube.

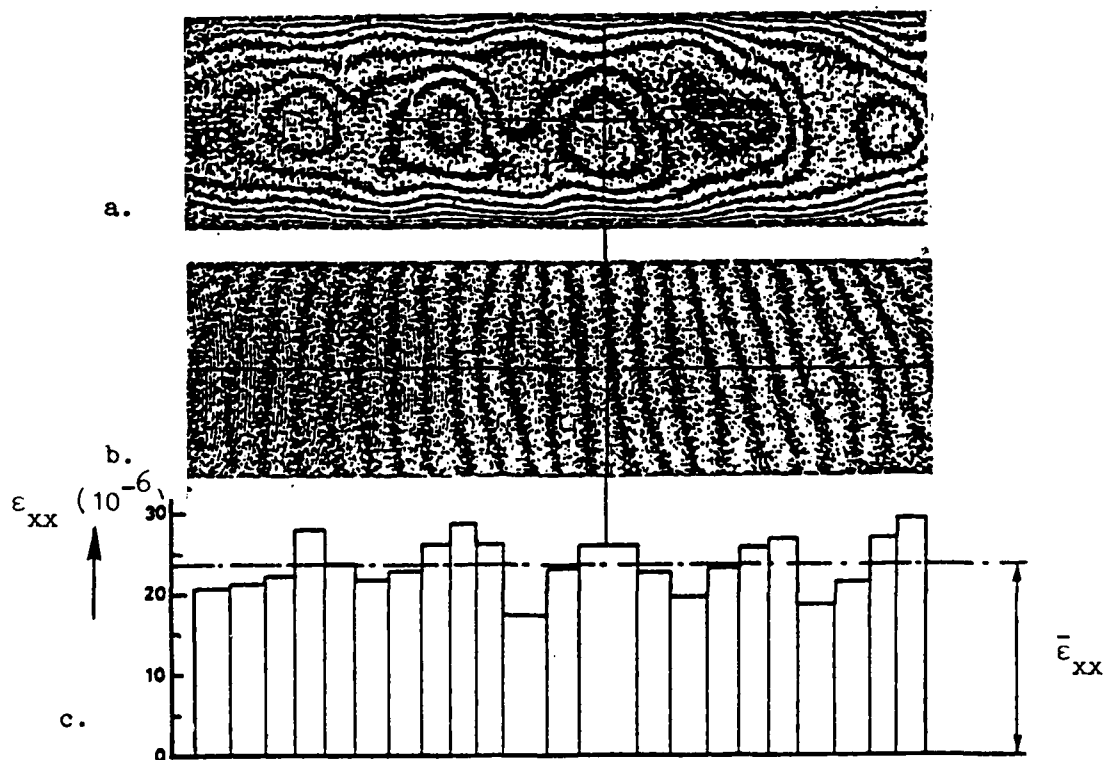


Fig. 7 Holographic-moiré for glass-fiber tube No 2  
 a. b. c. as in Fig. 6

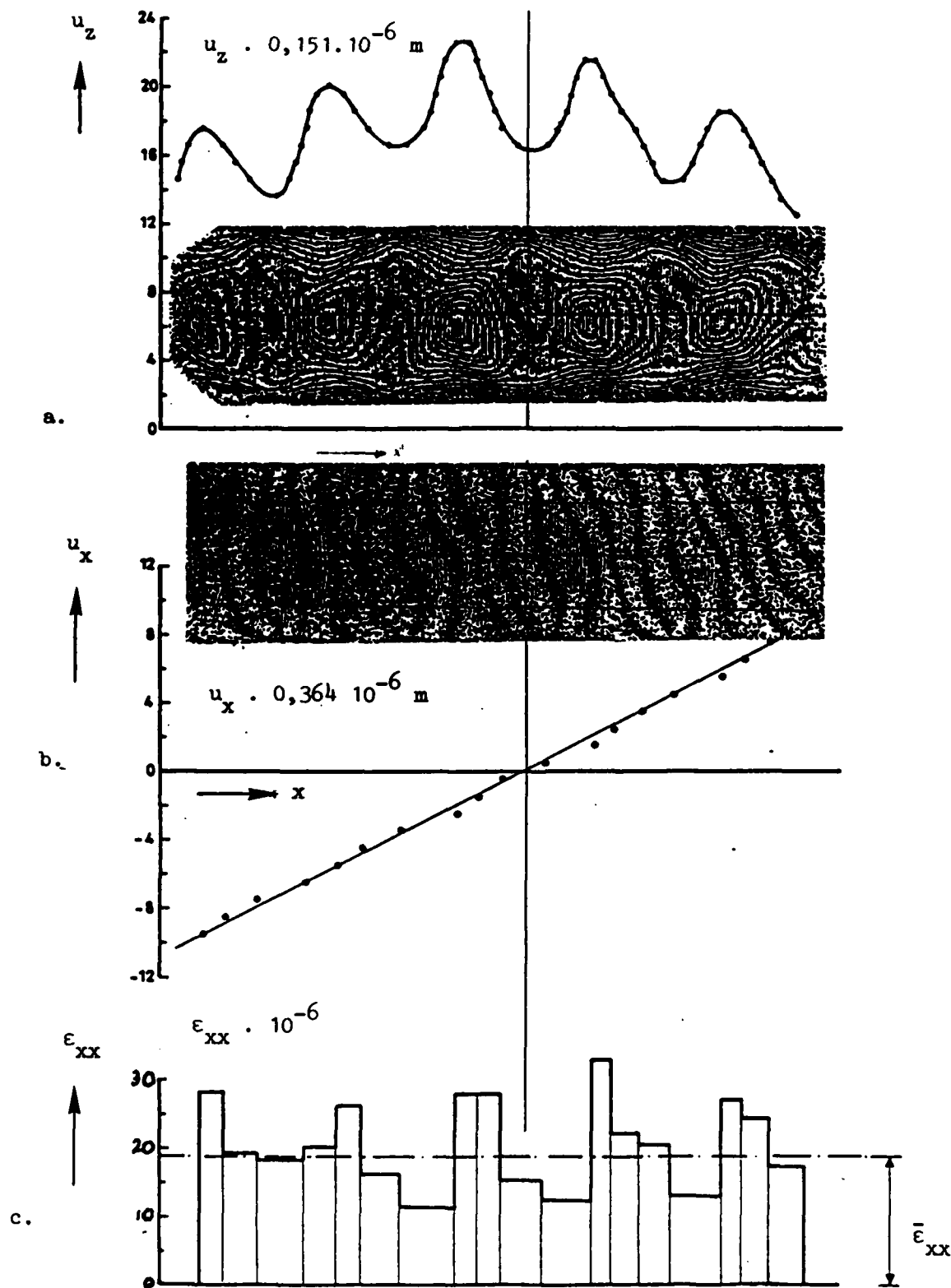


Fig. 8 Holographic-moiré for glass-fiber tube No 3  
a. out-of-plane displacements; b. in-plane displacements in x-direction  
(= axial direction); c. average strain  $\epsilon_{xx}$  between successive contour-  
lines and average strain over the full length of the tube.

##### 5. Detection of defects of carbon fiber tubes

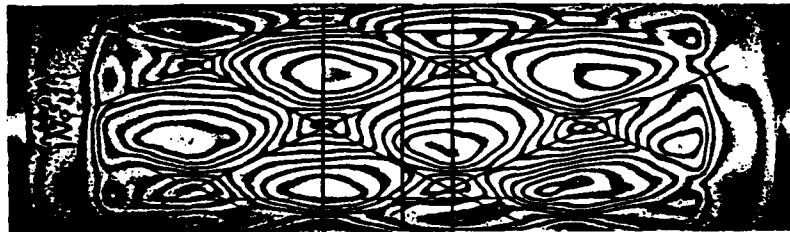
A series of carbon fiber tubes with artificial defects was tested to detect the defects. It became evident that one beam of illumination (case a.) and loading with internal pressure (radial only) and sometimes a temperature change ( $1^{\circ}\text{C}$ ) were sufficient to detect most defects. It proved to be very helpful however to apply three different load levels:

- A. low preload  $p_0$ , low load increment  $\Delta p = p_0$
- B. relatively high preload  $30 p_0$ , low load increment  $\Delta p = p_0$
- C. relatively high preload  $30 p_0$ , relatively high load increment  $\Delta p = 3 p_0$

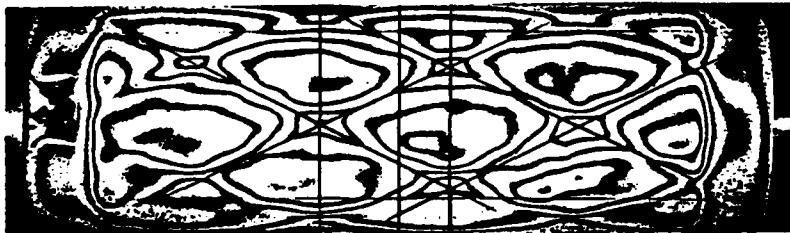
If certain defects were hardly visible at one load level, another load level might improve things considerably, as will be seen in various figures. For 5 tubes the interference patterns are shown at the load levels A., B., C.

Tube No 1 is without artificially applied defects. For the three load levels the shape of the interference pattern remains essentially the same, see Fig. 9. In the photographs lines have been drawn which form a system of diamond shaped areas. Along these lines the out of plane displacements are relative minima. The angle of the diamond shaped areas corresponds to the  $25^{\circ}$  winding angle. The load increment for load level A. and B. is the same; due to the much higher preload for level B, the out of plane displacements for level B are about half those for level A. For load level B. and C. the preload is the same, now the out-of-plane displacements are practically proportional to the load increment.

a. load level A



b. load level B



c. Load level C

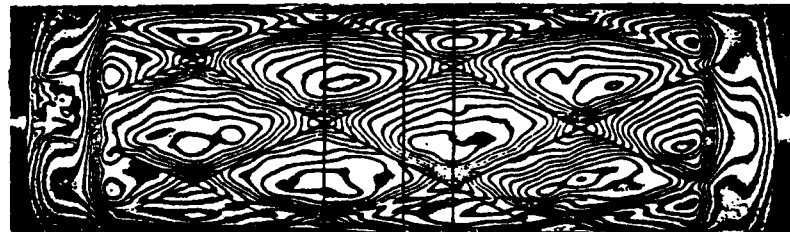


Fig. 9 Carbon-fiber Tube No 1, internal pressure

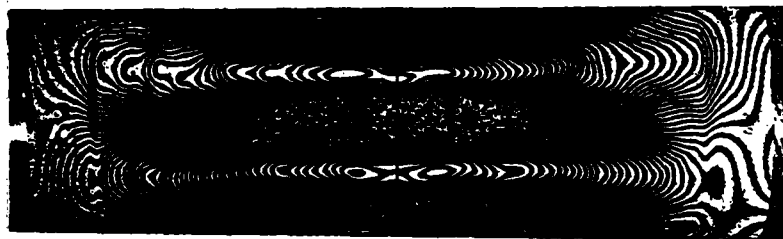
Tube No 2 has a second layer with a winding angle of  $35^\circ$  instead of  $25^\circ$ . At the left end of the tube there are loose fibres in the outer  $90^\circ$  layer, at the right end of the tube there are loose fibres in the inner  $90^\circ$  layer. Furthermore a teflon foil has been added between the first and the second layer, to simulate a delamination.

Although the loading is exactly the same as for tube No 1, the out-of-plane displacements for tube No 2 are totally different from those for tube No 1, see Fig. 10. The displacements at load level A are mainly due to an initially unroundness of the tube and there are no diamond shaped areas perceptible. At load level B a high preload is applied; the effect of the unroundness has disappeared but the diamond shaped areas are still not visible. The effect of the loose fibres in the outer  $90^\circ$  layer is now clearly visible (left side), but the loose fibres in the inner  $90^\circ$  layer (right side) can hardly be recognised. At load level C the diamond shaped areas are now vaguely visible. The loose fibres are less markedly visible, due to the much denser interference pattern.

The artificial delamination is absolutely not visible. In an effort to visualize this defect, the tube is also submitted to infrared radiation and to a three point bending test, see Fig. 11. But in none of the photographs a trace of delamination is visible. The bonding of the layers must have been sufficient to withstand the applied loads.

On the other hand the interference pattern due to the temperature change does show loose fibres in the outer as well as in the inner layer.

a. load level A



b. load level B



c. load level C

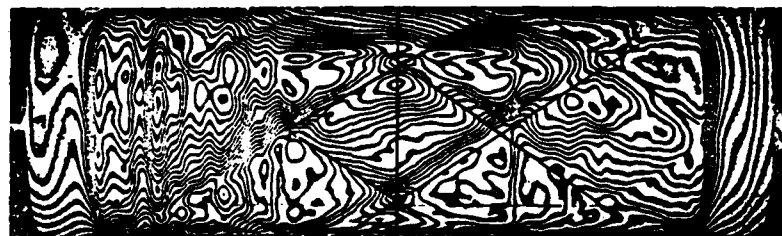


Fig. 10 Carbon-fiber tube No 2; internal pressure



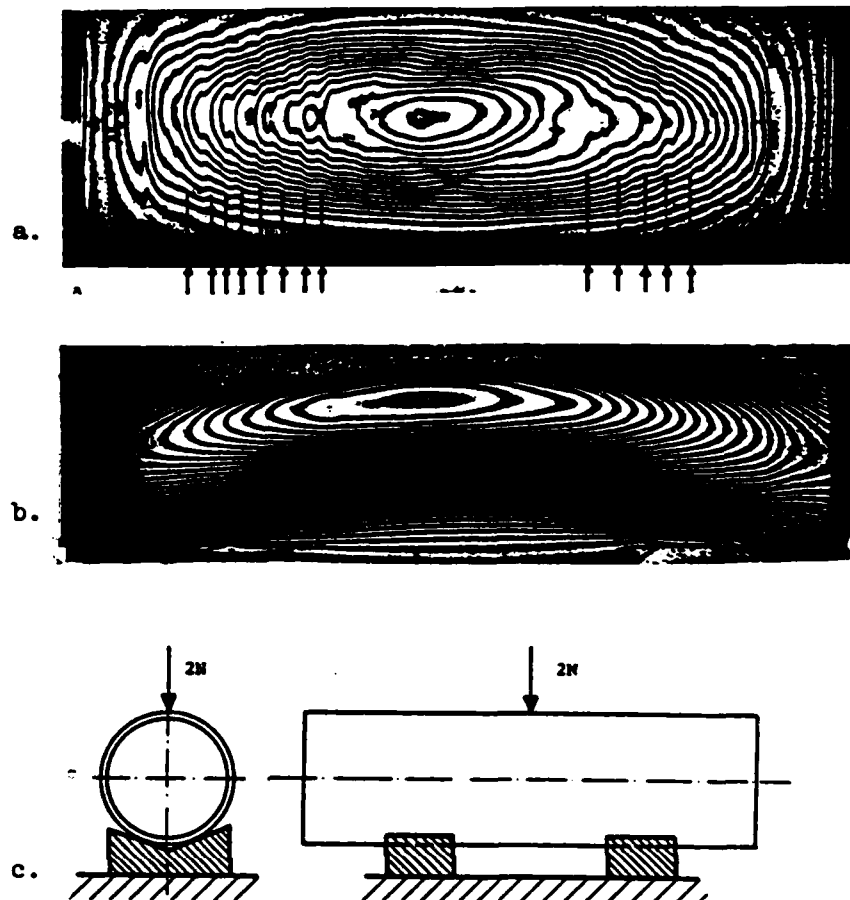


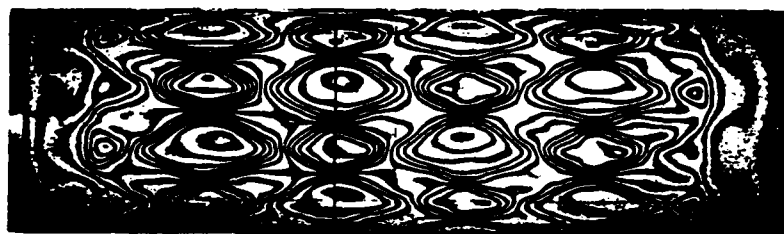
Fig. 11 Carbon-fiber tube No 2

- a. temperature change by infra-red radiation
- b. interference pattern due to a three point bending test
- c. set-up for the three point bending test

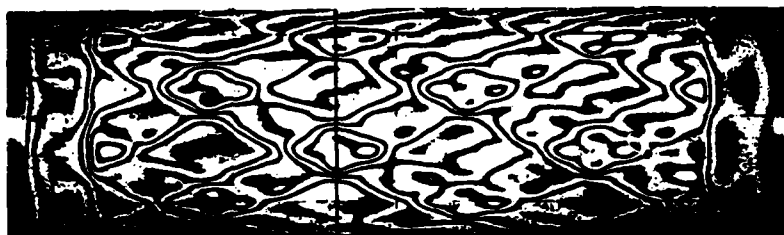
In tube No 3, after pre-hardening of the first  $90^\circ$  layer only half of the tube has been sanded. The helical winding in the  $25^\circ$  layer has been omitted. At all three load levels the shape of the interference pattern remains essentially the same, see Fig. 12. The diamond shaped areas are well visible at load level A and C, just as in Fig. 9. But at load level C it is also visible that the diamond shaped areas are sub-divided into four smaller areas of unequal magnitude, due to the absence of the helical winding in the  $25^\circ$  layer.

Tube No 4 is provided with an aluminium layer at the inside of the tube. It was a damaged tube with cracks at the central part. Due to the aluminium layer there are no diamond shaped areas visible, see Fig. 13. The concentration of the interference fringes gives at all three load levels an indication of defects. A high preload is essential however to clearly distinguish between the defects. The small more or less circular interference patterns indicate the presence of small cracks. Furthermore local bends can be seen in more or less straight interference fringes (cross-section I and II). In section I-I the out of plane displacements are slightly increased towards the surrounding and in section II-II they are slightly decreased. This indicates that in section I-I a winding is missing and that in section II-II an extra winding has been applied.

a. load level A



b. load level B

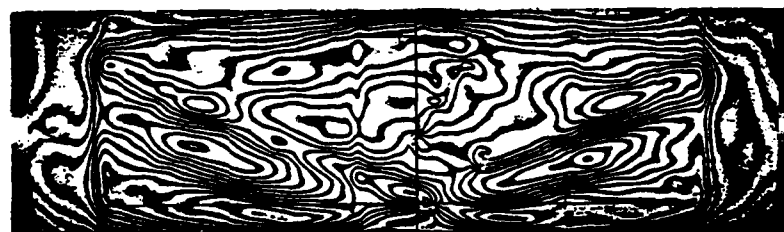


c. load level C



Fig. 12 Carbon-fiber tube No 3, internal pressure

a. load level A



b. load level B

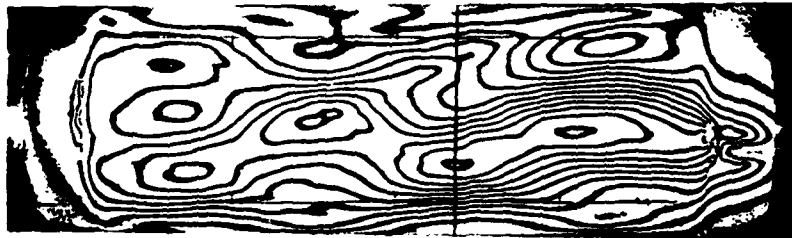


c. load level C



Fig. 13 Carbon-fiber tube No 4, internal pressure

a. load level A



b. load level B



c. load level C

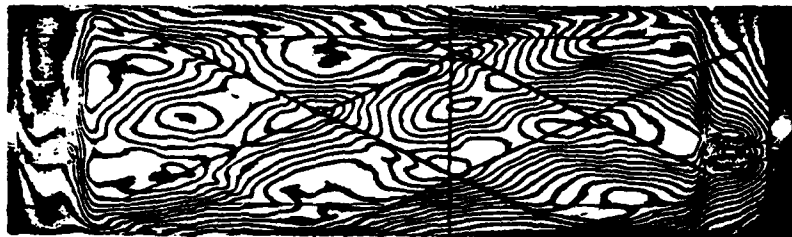


Fig. 14 Carbon fiber tube No 5, internal pressure

Tube No 5 is almost identical with tube No 1, but supplied with an aluminium layer at the inside. Furthermore the outer  $90^\circ$  is unimpregnated. The diamond shaped winding pattern is only slightly visible at load level C, see Fig. 14. For all load levels the concentration of the interference fringes at both ends of the tube indicate damaged zones which occurred during previous tests.

All tubes have also been investigated by holographic-moiré, which has not given any further information. Also the vibration modes at the various natural frequencies have been determined in real time. Depending of the winding pattern there are differences in the various natural frequencies, but the vibration modes themselves did not provide information about defects.

6. Possibilities to use holographic interferometry for non destructive testing and evaluation in real time and in process

A certain kind of defects in polymer products is easily detected just by simple out-of-plane holography. As the product has to be loaded in some way, a test set-up has to be made and the optical table can be incorporated in this set-up. The kind of set-up will of course depend on the kind of product to be investigated and its sensibility for appropriate loads. Load increments are always small and especially heating by radiation is easily applied.

Real time holography is practically always possible with polymer products. Evaluation can be carried out by comparing the obtained interference pattern with a reference pattern. If the actual pattern and the reference pattern are both provided with carrier fringes, the patterns can be superimposed and the difference of the two patterns will be seen as a moiré pattern. The patterns can also be stored on video tape and evaluated elsewhere.

Making a single or double exposure hologram in the traditional way, will take 5 to 10 minutes. The application of commercially available photo-thermo-plastic material and equipment will reduce this time to a few seconds. The dimensions of such holograms are limited, however, and it seems that the traditional way of making holograms is somewhat more fool-proof.

For a uniform quality of the interference pattern a mate reflecting surface is required. So in laboratory circumstances the model is mostly painted or sprayed white. The paint has to be dry however, before the hologram is made. But also medium bright or even black surfaces will give good interference patterns, as long as the surface is mate reflecting. The time of exposure obviously will have to be increased. The quality of the hologram and of the interference pattern will decrease however, the more the object has a strongly directed reflection, like a (poor) mirror. Recording the interference pattern with a video camera can give quite reasonable results if the diaphragm is adjusted in a proper way.

Industrial applications of holographic interferometry are the testing of inflated tires (time average for the determination of the vibrational mode structure or out-of-plane double exposure in conjunction with a small change of inflation pressure to show defects). In aircraft industry disbond of honeycomb structures is tested by double exposure out-of-plane holography, applying radiation to obtain temperature changes (aircraft wings, solar panels).

References:

- R.K. Erf, 'Holographic nondestructive testing' Academic Press, New York, London  
W.J. Beranek and A.J.A. Bruinsma, 'A geometrical approach to holographic interferometry' Experimental Mechanics, Sept. 1980.

## Discussion of Session VI

A number of practical examples were suggested for application to NDE of the elegant experiment by Sargent and Upstill. Since the only piece of equipment required is a good polarising microscope, it could certainly be used as an on-line method to check whether or not molecular size interfacial gaps are present in, say, the low fibre volume fraction flash that is produced during compression moulding of fibre reinforced plastic laminates. Much interest was also generated by the idea that the experiment offers a direct method for assessing the effectiveness of fibre surface coatings including coupling agents. Owing to the low fibre volume fraction demanded by the theory in its present form, this would best be done on token samples.

Since the work by Sargent and Upstill must be applicable generally to electromagnetic radiations, speculations were made about the detailed nature of propagation through composites of infra-red and radio waves, i.e. of waves with wavelengths very much larger than a fibre diameter.

A D Carr's presentation on microwave propagation prompted interesting comments in respect of possible application of sheets of uniaxial carbon fibre reinforced plastic as polarisers for a microwave polaroscope.

During discussion of the role of holography in NDE, attention was drawn to the mechanical stability demanded of the optical systems. "Holography belongs to the technology of opticians and not to the technology of engineers". Mr Beranek remarked that the holographic techniques described by him are not suitable for use in a factory environment. Professor Jansson strongly disagreed and offered the following comments.

Traditional holographic interferometry is known to have extremely high resolution (better than  $0.3 \mu\text{m}$ ) and high accuracy, but the technique suffers from being tedious and is sensitive to vibrations and other environmental disturbances.

Today however, new techniques make it possible to use holography directly, on the factory floor and by unskilled employees. Furthermore, there is no need

for high power lasers, thus reducing both the capital outlay and the seriousness of accidents.

The determination of the sign of the deformation has been difficult until recently, but can now be carried out by sandwich holography.

A number of inventions for the use of holography in industrial applications has been made by Abramson (1981) and co-workers. Thus, studies of the deformation and vibration of large machines, whole live human beings, metal and plastic products, injection moulds in use as well as the microscopic vibrations in the eardrum of a listening grasshopper have been reported by several authors, e.g. Abramson (1981), Dirtoft et al (1984).

The possibility of repositioning the sample in the equipment after different kinds of treatments, further extends the range of applications (Dirtoft et al, 1984).

The swelling of complete upper dentures (made from PMMA), due to water absorption, has been studied directly in the aqueous system. Continuous measurements were carried out and the dimensional changes could be followed over several weeks. By repositioning the denture, it was also possible to study its deformation after being used by a person for a lengthy period of time. (Dirtoft et al, 1984)

Holography has also been successfully used to measure the post shrinkage and the warping of injection moulded plastic products by using a recently developed apparatus placed close to the injection moulding machine in the fabrication hall. (Dirtoft and Jansson, 1984)

In conclusion it is clear that, due to the new simplified techniques, holographic interferometry has become a valuable tool for routine non-destructive testing and quality control.

## References

N Abramson, "The Making and Evaluation of Holograms" Academic Press, 1981

I Dirtoft, J-F Jansson and N Abramson, "Dimensional changes in Plastic Products measured by Hologram Interferometry" to be submitted to Applied Optics, 1984

I Dirtoft, B Terselius and N Abramson, "Holography - a new method to follow dimensional changes during sorption in upper complete dentures", to be submitted to J of Biomed Mat Res, 1984

I Dirtoft, B Terselius and N Abramson, "Swelling measured by holography and other methods in upper complete dentures in water" to be submitted to J Dent Res, 1984

I Dirtoft, "Holographic Measurement of Deformation in Complete Upper Dentures - Clinical Application" Springer Biomedical Science 31, 100-104, 1982

Session VII: Fracture mechanics as a method for quality control



## uPVC - THE STATE OF THE ART

Dr R Lyall

Bartol Ltd, Pollard Moor Works, Padiham, Burnley, Lancs BB12 7JR

### Abstract

uPVC pressure pipe has been used extensively for the last 25 years. Although experience has been generally very satisfactory, there have been a few premature failures, a fact which has concerned both suppliers and water companies.

Recent co-operative work by the uPVC process industry, material suppliers and university research teams has lead to the development of better methods of quantifying the quality of a uPVC pressure pipe.

Since most failures are initiated by the propagation of cracks, the concept and test methods of fracture mechanics have been applied. It has been found that materials which are 'identical' when compared under historical methods can now be quantitatively graded.

The new test methods have been included in a British Standard for pressure pipe and will ensure that all pressure pipe is manufactured to a uniformly high standard.

### 1. Introduction

For over 20 years uPVC pipe has been used for pressure and non-pressure applications within the water industry. It is currently estimated that some 40% of all new water distribution pipes installed are manufactured from uPVC and this high level of usage reflects the general satisfaction with the performance of the product.

However, there has been a number of premature failures which has caused concern both to the users and suppliers within the water industry. It has been disturbing that the pipes which have failed in service are nearly always satisfactory as judged by conventional standards. These are based on simple mechanical tests measuring burst strengths and times to failure under constant stress.

Over the last five years there has been a programme of work aimed at understanding the reasons for failures and developing test methods which are applicable in a manufacturing situation and which will distinguish between the pipes that may fail from those which will perform to their design performance. The work has been a collaborative effort, co-ordinated by the Polymer Engineering directorate and conducted by the main uPVC pressure pipe extrusion companies and university researchers, but mainly the group headed by G P Marshall at Manchester Polytechnic.

This paper summarises the results of the work and describes the new test methods which are now being used within factory bases and which allow a more quantitative approach to the manufacturing of uPVC pipe of defined qualities.

## 2. Historical Standards & Design Philosophy

National and international standards define the minimum requirements for uPVC pressure pipe. All main national standards base their design criteria around simple mechanical tests measuring burst pressures and times to failure. PVC, as with other thermoplastics, exhibits time dependent properties. (British Standard BS3505)

The conventional method for determining the design stress is to determine the failure characteristics by pressure testing relatively short samples of pipe over relatively short time scales (approximately 10000 hours at 20°C). The resultant hoop strength is plotted against time to failure on a double logarithmic scale and, by convention, extrapolated to obtain a failure stress at 50 years.

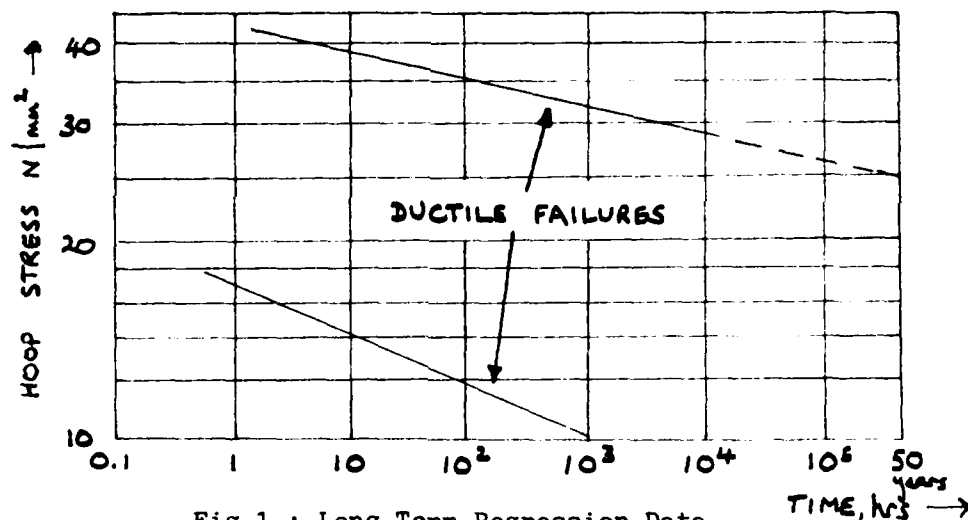


Fig.1 : Long Term Regression Data

The 50 year design stress is obtained by applying a safety factor to the failure stress. This factor varies between 2.0 and 2.5, for different countries reflecting the results of their specific experiences. This safety factor is intended to cover the unpredictable conditions that can influence the service life of the pipe and not to cope with any irregularities in the quality of the pipe.

At ambient temperatures, the failure characteristics of uPVC pipe produced in the laboratory are consistent and repeatable. The failure mode in the laboratory is always accompanied by a significant amount of swelling and deformation. This type of failure mode is never seen in the field. Service failures show no gross deformation of the pipe (eg. 'brittle' as opposed to 'ductile' failures) and by their nature are not predictable.

The extrapolation technique has been the subject of discussion for an appreciable period. With many plastic materials, it is possible to generate brittle pipe failures by pressure testing at elevated temperatures. At these temperatures (60°C is used for PVC) the mode of failure resembles the service failures more closely. In some countries there is a general acceptance that the absence of brittle failure at 60°C can be used as a criteria that the regression line based on ductile failures at 20°C may be extrapolated linearly to 50 years. Considerable progress has been made in this area, although it seems debatable whether the application of elevated temperatures raises more questions than those answered. (Benjamin, P (1980))

### 3. Failure Mechanisms in Service

The unpredictable nature of the failures that occur shows that the failure mechanism is not directly related to the bulk properties on which current design stresses are based. From the examination of failed pipe, it is now believed that the failure process can be generally described.

The failures originate at flaws or structural defects within the pipe. No material can be perfectly homogenous and the defects or foreign particles within the structure act as stress concentrations in a similar way to surface scratches developed during handling and installation.

In the field, the loading conditions differ significantly to those in the laboratory pressure tests. In addition to tensile hoop stresses generated by the internal pressure, secondary loads can develop due to insufficient pipe support. In particular, bending over point loads in poor bedding conditions can cause stresses which are high and localised. Most failures initiate from the lower surface of the pipe and it is believed that these localised stresses, usually associated with identifiable point loads, are the prime cause of crack initiation.

Because thermoplastics are time dependent materials, the initial defect does not instantaneously start to grow. There is an incubation period where creep deformation causes an increase in the crack opening displacement (COD) to a critical level. (Marshall. G P (1982)) (Williams, J G (1978)). Following the incubation period, the crack extends in size and there is a period of slow growth when the crack extends across the section. The initiation and growth of the crack is resisted by the toughness of the material.

Complete failure of a pipe can occur in two ways. Point loading tends to produce a crack of disproportionate length in the axial direction, due to the compressive stresses immediately above the load which suppresses crack growth through the pipe wall.

If the crack can progress through the pipe wall, then leakage may occur which reduces the stresses which may arrest the crack. Alternatively, unstable failure will occur before the crack has traversed the section. The crack will develop axially to the size whereby it becomes unstable to cause a catastrophic failure.

#### 4. Revised Design Philosophy

From the above discussion which suggests that service failure is generally caused by delayed cracking, three factors govern the pipe performance:

- i) the toughness of the material
- ii) the defects - size, distribution
- iii) the applied stress condition - the combined effect of internal pressure and external loads.

The initial work has been to determine new test methods which would allow the toughness of the PVC pipe to be measured simply and accurately.

The toughness of the pipe material depends upon the molecular chain length, commonly termed K-value, and the processing history. For materials suitable to be processed and to satisfy the internal pressure carrying characteristics needed, the K-value has relatively little effect upon the properties of the final product. However, the extrusion history is critical in defining the properties of the finished product.

PVC is thermally unstable and cannot be processed without addition of a stabiliser/lubricant system. The additive system has to be in balance with the process conditions/extruder/die for adequate properties to be achieved in the finished product. The process of fusing the polymer particles into a homogenous matrix is termed gelation. Several indirect methods (optical/chemical/rheological, Benjamin, P (1980)) exist to estimate the degree of fusion achieved. Historically, the degree of fusion has been used as a guide to the quality and hence toughness of the material. However, each of the methods suffers from the same weaknesses; each method is indirect, formulation dependent and not absolute.

#### 5. Test Methods

Fracture mechanics testing methods have been developed in recent years to predict the behaviour of polymers in engineering applications. With PVC, the points to prove were:

- i) whether a measurement of toughness could be made.
- ii) whether toughness distinguished between pipes which were known to be of different qualities.
- iii) whether toughness could be measured simply and absolutely from pipe samples in a factory environment.

## 5.1 Initial Tests

'Unnotched' testing of uPVC does not simulate the brittle failure mode seen in service. There is a need to resort to the use of pre-notched samples. The influence of crack depth on failure stress can be characterised by devising a value of fracture toughness  $K_c$  given by:

$$K_c = \sigma_f Y \sqrt{\pi a}$$

where  $\sigma_f$  is the brittle failure stress, 'a' is the crack depth and 'Y' is a geometrical factor dependent on test configuration. (Rooke, D P and Cartwright D J (1976)).

A range of different sample geometries for estimating the failure toughness values of uPVC is shown below. (Marshall, G P (1982)). One of the difficulties is ensuring that failure occurs at stresses significantly below either gross or net section yielding across the ligament area ahead of the notch. (Marshall, G P (1983)). ASTM recommend that values of  $K_c$  are valid if fracture stress  $\sigma_f$  is less than  $0.85 \sigma_y$ .

The initial tests were conducted in simple tension, with sets of pipe which showed markedly different levels of gelation. Poorly gelled pipe failed at stresses well below net section yield for flaws greater than the critical flaw size ( $a_0$ ) and a toughness value can be determined. ( $K_c = 2.75 \text{ MN/m}^{3/2}$ ). A value for the well gelled pipe cannot be determined, with the pipe showing a characteristic which can be confused with the yield line above.

The measurement of toughness in bending is more suitable for higher toughness matrices. Because collapse in bending only occurs when a plastic hinge is developed across the section, the effective yield stress is enhanced to  $1.5 \sigma_y$ , ( $\sigma_y$  is the stress at first yield). Hence brittle failures are more likely to occur for small critical flaw sizes before net section collapse. Three-point bending samples were used to evaluate  $K_c$  values - especially for large diameter pipes which allow flat samples to be machined from longitudinal pipe sections.

$K_c$  was evaluated over a range of pipe qualities and very large differences were observed; typically over the range from 2.0 to  $4.0 \text{ MN/m}^{3/2}$  when measured over a period of a few seconds.

Fracture toughness values are sensitive to strain rate and time, as with other material properties of thermoplastics.  $K_c$  was measured over a time scale of up to several thousand hours and differences in toughness observed between the poorly and well gelled pipe in the instantaneous tests are maintained. (Marshall, G P (1982) (1983))

Flexural loading has many attractions for evaluation of large diameter pipes, but is not simple to use for assessment of smaller diameters, since curvature effects can be significant. Different geometries were tested before a split notched ring was chosen.

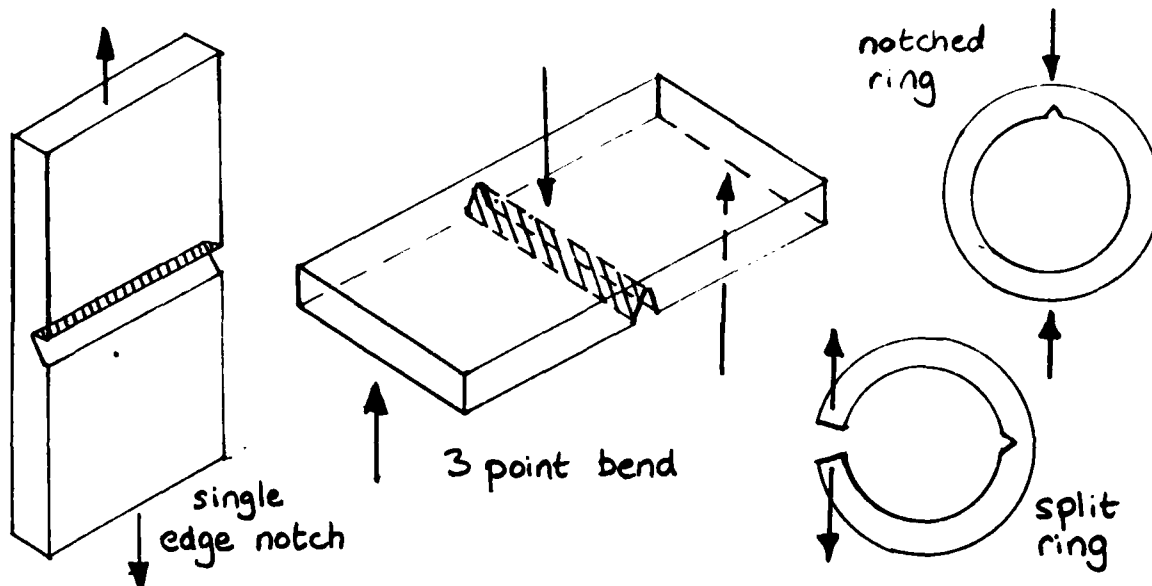


Fig.2 : Different Designs of Test Samples

The rings were tested to failure at a constant deflection rate, the failure occurring in a brittle manner. Reproducibility of results was excellent and there was again good resolution between the high and low toughness pipes.

## 5.2 Effects of Test Parameters

Thus a test had been developed which satisfied the criteria of quantifying the quality of the pipe, while at the same time being simple to use in a manufacturing environment.

However, on further testing over a range of pipe samples (diameters from 75mm to 600mm, wall thicknesses of 4mm to 30mm) there was doubt as to whether the K-values being developed were true material properties. Although the results were self-consistent within one geometry range of pipe (110-150mm), the values were not self-consistent when viewed across the whole range and when compared with the historical qualitative assessments of gelation. In particular, K-values obtained for large diameter, thick walled pipes were generally appreciably higher than those obtained from small diameter, thin wall pipes. When viewed by historical methods, it was expected that the toughness of the thin wall matrices would be at least as great as that from the thicker walled samples.

### 5.2.1 Dynamic Testing

Simple observation of the notch in a ring tested to failure at a fixed deflection rate shows that the peak load is greater than the load required for the initiation of the growth of the notch. The difference between initiation and peak loads is likely to vary with the toughness level of the pipe. With low toughness uPVC, there is substantial slow crack extension prior to 'brittle' failure. This will give invalid levels of  $K_c$  as the slow growth varies with the critical crack depth. With high toughness uPVC, the crack initiates at much higher stresses

when the plastic zone is large and this limits the extent of slow crack growth. Thus, with uPVC, the peak load data gives a more valid level of  $K_c$ . Typically, there is a difference of up to a factor of 2 between the  $K$ -values determined from initiation and peak loads. (Marshall, G P (1983)).

This problem can be resolved by using a fixed load, assuming initial flaw lengths and measuring the time to failure at a given  $K$ -value.

### 5.2.2 Geometry Effects

This apparent lack of correlation across all geometries prompted the question of further geometry and testing effects and, indeed, this has proved to be the case.

#### (a) Influence of Notch Sharpness

Simple stress concentration theory gives the stress  $\sigma_c$  at a notch 'a' and tip radius 'r' as

$$\sigma_c = \sigma \left( 1 + 2\sqrt{\frac{a}{r}} \right)$$

Tests were conducted over a range of tip radii, and  $K_c$  was plotted against ' $r$ '. For tip radii ( $r < 0.025\text{mm}$ ), the conventional independence of 'strength data' was illustrated while for blunter cracks, the effect of decreasing stress concentration was observed.

The systematic difference between the high and low toughness pipes over the whole range of notch radii indicates that differences in gelation do cause real toughness changes. (Marshall, G P (1982)).

#### (b) Sample Size Effects

The Effect of Thickness was measured in samples up to 40mm thick. Using the initiation values and thickness up to 15mm, there is little effect on the measured  $K$ -value.

The Effect of Width was found to be critical. There is a large effect (approximately 50% variation) with width in the range 3 - 15mm. (Marshall, G P (1983)). This is the range in which most pressure pipes fail.

These results generally agree with earlier findings of Chan and Williams (1981) on MDPE. As in the case of MDPE, the results can be fitted by a solution to the post yield theory of Bilby (1963).

This fit to the post yield theory has been checked on several other samples of uPVC and experimentally appears to be valid. The effect of width, especially in the range of 3 - 15mm appears to explain the previous lack of consistency of fracture toughness values across the full product range.

## 6. Conclusion

With the corrections to allow for the effect of test parameters, the split ring test now meets the criteria that were originally set.

The uPVC pipe industry has been provided with a quantitative, simple tool to help monitor, control and develop production quality. This is the first major new technique to be introduced for several years and is likely to be followed by the development of other techniques.

In the uPVC process industry there is a need for improvement of techniques in two general areas: these are techniques for product and process development and for process and quality control in the subsequent manufacturing activity.

The application of fracture mechanics measurements is a good step forward. However, there is scope for improvement in terms:

- a) detection/measurement of any impurities/defects.  
The current method is a simple impact test. Improvements are being attempted by both mechanical tests with better resolution and by non-destructive (ie x-ray) methods.
- b) convenient techniques to resolve any variations within materials and processing.  
At the moment the uPVC processing industry relies on a combination of relatively simple tests on incoming material and attention to the consistency and reliability of processing.

This combination has lead to the development of relatively efficient manufacturing processes, producing good quality product. Better on line techniques for detection of 'out of tolerance' product properties will allow further improvements in both processing efficiency and product quality to be made.

## 7. References

- |                                |  |
|--------------------------------|--|
| Benjamin, P                    | Plastics and Rubber: Material and Applications,<br>Nov 1980          |
| Marshall, G P                  | Plastics and Rubber Processing and Applications<br>Vol.2, No.4, 1982 |
| Williams, J G                  | Adv. Polym. Science, 1978 p.27                                       |
| Rooke, D P &<br>Cartwright D T | Stress Intensity Factors, HMSO, London, 1976                         |



Marshall G P

Plastics and Rubber Processing  
Vol.3, No.3, 1983

Chan M K V and  
Williams J G

Polym. Eng. Science 21(15) (1981) p.1019

Bilby et al

Proc. Royal Society, London A, 272 (1963), p.304

# THE FATIGUE DAMAGE MECHANICS OF FIBROUS LAMINATES

A Poursartip, M F Ashby and P W R Beaumont

University of Cambridge  
Department of Engineering  
Trumpington Street, Cambridge CE2 1PZ

## ABSTRACT

A damage model is proposed based on the idea that physical damage changes the moduli of the composite. By nondestructively monitoring these moduli during fatigue, damage growth can be determined. A critical or "terminal" damage is then defined, so that the moduli allow the residual life to be calculated. Empirical laws are derived for damage growth as a function of the stress range, mean stress and the terminal damage. These laws can be used to predict the shape of the S-N curve, and lives and damage growth rates under variable amplitude loading, with reasonable accuracy.

## INTRODUCTION

During fatigue of a fibrous composite, damage accumulates within it. The damage may have several components: fibre breakage, matrix cracking, delamination, axial splitting, decohesion between matrix and fibre, and so forth. The damage can be monitored non-destructively by measuring one of the properties of the composite: the moduli, for instance, or the electrical conductivity, or light scattering, or the X-ray absorption, or ultrasonic attenuation, or the damping coefficient.

### The Damage Model

Let fatigue damage be measured by the variable  $D$ . At the start of life  $D$  is zero unless damage  $D_i$  has been introduced during fabrication, or by earlier history. Cyclic loading causes damage to increase from  $D_i$  to  $D_f$  at which failure occurs.

Let the damage growth rate depend on cyclic stress range  $\Delta\sigma$ , the load ratio  $R$ , and on the current value of  $D$ . Then, at constant temperature and frequency,

$$dD/dN = f(\Delta\sigma, R, D) \quad (1)$$

This can be integrated to give the lifetime,  $N_f$ :

$$N_f = \int_{D_i}^{D_f} \frac{dD}{f(\Delta\sigma, R, D)} \quad (2)$$

The difficulty is that we do not know the function  $f$ . But modulus can be measured to monitor damage. If a relation exists between axial modulus  $E$  and the damage  $D$ :

$$E = E_0 g(D) \quad (3)$$

where  $E_0$  is the undamaged modulus, then

$$\frac{1}{E_0} \frac{dE}{dD} = g'(D) \quad (4)$$

where  $g'$  means the derivative of  $g$  with respect to  $D$ . Using the chain rule for differentiation and substituting into eqn. (1), we find:

$$\frac{1}{E_0} \frac{dE}{dN} = g' \left( g^{-1} \left( \frac{E}{E_0} \right) \right) f(\Delta\sigma, R, g^{-1} \left( \frac{E}{E_0} \right)) \quad (5)$$

where  $g^{-1}$  is the inverse of  $g$ :

$$D = g^{-1} \left( \frac{E}{E_0} \right) \quad (6)$$

This equation suggests two alternative approaches to studying damage in composites. First, a damage-accumulation function,  $f(\Delta\sigma, R, D)$ , can be guessed or inferred from a model, inserted into eqn. (5), and the result compared with experiment. Alternatively, data can be gathered for  $E/E_0$  as a function of  $N$  and, knowing  $g(D)$ ,  $f(\Delta\sigma, R, D)$  can be determined experimentally, using:

$$f(\Delta\sigma, R, D) = \frac{1}{g'(g^{-1}(\frac{E}{E_0}))} \frac{1}{E_0} \frac{dE}{dN} \quad (7)$$

To do so, the right hand side of the equation is evaluated for a range of values of  $\Delta\sigma$  at constant  $E/E_0$  and constant  $R$ , for a range of  $R$  at constant  $\Delta\sigma$  and  $E/E_0$ , and for a range of  $E/E_0$  at constant  $\Delta\sigma$  and  $R$ . The function  $f$  is then determined from a plot of the results.

#### General Fatigue Behaviour of a Quasi-Isotropic Carbon Fibre Laminate

In tension-tension fatigue matrix cracking and delamination occur. The first appearance of damage is of matrix cracks in the  $90^\circ$  plies, followed by matrix cracking in the  $45^\circ$  plies, and edge cracks (small delaminations) at the  $45^\circ/90^\circ$  and  $90^\circ/-45^\circ$  ply interfaces. The edge cracks at the  $90^\circ/-45^\circ$  interfaces become dominant and grow in from the edge as a large, single,

or occasionally two or three large, delaminations. The longer the fatigue life, the more delamination growth takes place before failure. If the fatigue life is sufficiently long, the  $0^\circ$  plies become extensively damaged, essentially in the form of fibre breakage and longitudinal splitting.

#### Damage Caused by Delamination

The theoretical axial modulus of a balanced, symmetric laminate is (Jones, 1975)

$$E_o = \frac{1}{X_{11} t} \quad (8)$$

where  $X_{11}$  is the first element of the inverse extensional stiffness matrix ( $A_{ij}^{-1}$ ) and  $t$  is the laminate thickness. Then, if we assume that one or more interfaces delaminate completely, splitting the laminates into two or more separate sublaminates, all of them subjected to the same longitudinal extension (but no longer the same transverse strain), the new stiffness is  $E^*$ :

$$E^* = \sum_{i=1}^m \frac{E_i t_i}{t} \quad (9)$$

where  $E^*$  is the new stiffness of a laminate where one or more plies have completely delaminated,  $m$  is the number of sublaminates formed,  $E_i$  is the laminate stiffness of the  $i$ th sublaminate, and  $t_i$  is the thickness of the  $i$ th sublaminate.

The stiffness  $E$  of a partially delaminated specimen can be calculated using a linear rule of mixtures (O'Brien, 1982):

$$E = E_o + (E^* - E_o) \frac{A}{A_o} \quad (10)$$

where  $A$  is the delaminated area,  $A_o$  is the total interfacial area, and  $E^*$  is given by eqn. (9).

Figure 1 shows that  $E^*$  (corresponding to total delamination of the relevant interfaces) is  $\approx 0.65 E_0$ . There is an empirical linear relationship between stiffness and delamination size. In the delaminated strips at the edges of the specimen, cracking of the off-axis plies is so complete that their contribution to the laminate stiffness can be totally ignored. In the undelaminated areas, however, we must assign undamaged moduli to the off-axis plies.

We now define our damage  $D$  as the normalised area  $A/A_0$  eqn. (10), within which only the  $0^\circ$  plies are undamaged. Thus the function  $g(D)$  in eqn. (3) can be expressed as:

$$g(D) = 1 - 0.35 D \quad (11)$$

for our CFC laminate (see Figure 1). Then:

$$D = 2.857 (1 - E/E_0) \quad (12)$$

and from eqn. (7):

$$f(\Delta\sigma, R, D) = -2.857 \left( \frac{1}{E_0} \frac{dE}{dN} \right) \quad (13)$$

#### The Damage Rate as a Function of the Stress Amplitude

The stiffness reduction rate for all specimens was calculated by fitting a least-squares regression line to the appropriate section of stiffness reduction-cycle curves. The damage rate  $dD/dN$  was then calculated using the derivative with respect to  $N$ , of eqn. (12):

$$\frac{dD}{dN} = -2.857 \left( \frac{1}{E_0} \frac{dE}{dN} \right) \quad (14)$$

Figure 2 shows the damage rate  $dD/dN$  as a function of stress range  $\Delta\sigma$ . All the data are for a load ratio  $R = 0.1$ . Each point represents a different test. Both axes are logarithmic.

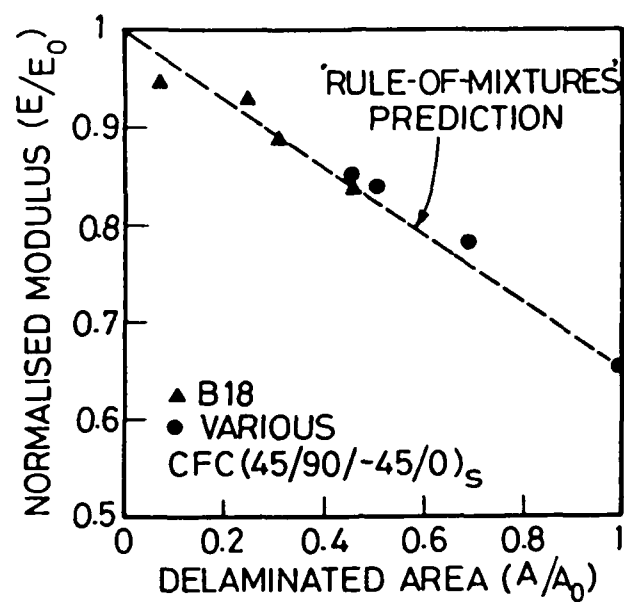


Figure 1

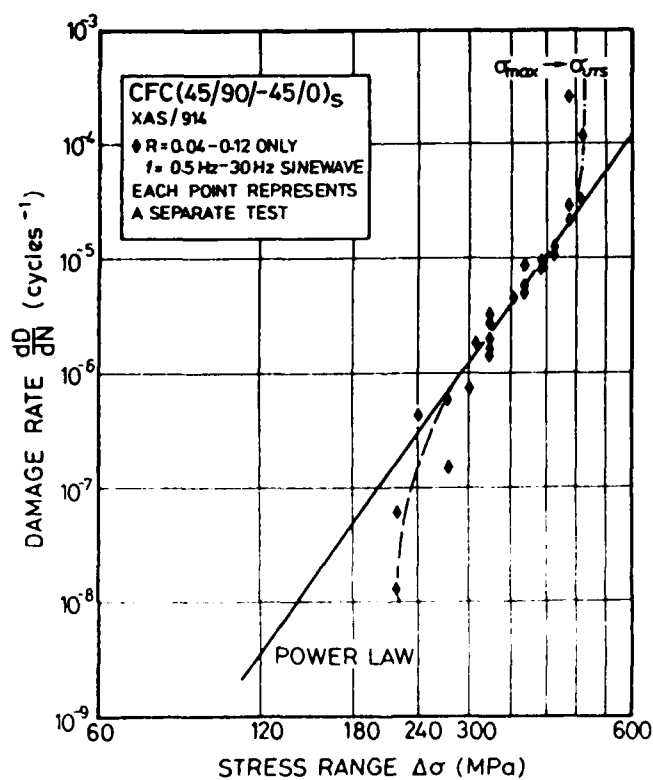


Figure 2

There are three regimes of behaviour:

- (1) Below a threshold stress of about 250 MPa, no damage forms.
- (2) A power-law relation between  $dD/dN$  and  $\Delta\sigma$  over most of the stress range.
- (3) At stresses approaching the ultimate tensile strength of the material, we observe essentially static failure.

A least-squares regression line fitted to the data points between  $\Delta\sigma = 240$  MPa and 480 MPa,  $R = 0.1$ , gives the following empirical equation:

$$\frac{dD}{dN} = 9.189 \times 10^{-5} \left( \frac{\Delta\sigma}{\sigma_{UTS}} \right)^{6.393} \quad (15)$$

with a coefficient of correlation of 0.964. The mean ultimate tensile strength,  $\bar{\sigma}_{UTS} = 586$  MPa.

Equation (15) is shown in Figures 2 and 3 as a solid line.

#### The Damage Rate as a Function of the Mean Stress

Figure 3 is another log-log plot of damage rate  $dD/dN$  as a function of stress range  $\Delta\sigma$ . However, all test results, at different load ratios  $R$ , are shown. The numbers next to each point indicate the value of  $R$  at which the test was conducted (when  $R = 0.1$  this is omitted). Inspection of this plot shows a mean stress effect. For example, when  $\Delta\sigma = 220$  MPa, increasing the mean stress from  $R = 0.1$  to  $R = 0.53$  accelerates the growth rate by at least a factor of 4. Similarly, tests runs at  $\Delta\sigma = 160$  MPa with  $R = 0.6$  show growth rates comparable to those one would expect if there were no threshold behaviour, and the power-law relation obeyed.

The data are replotted in Figure 4 as the damage rate  $dD/dN$  as a function of the mean stress. Each set of points represents a different stress range. For a given stress range, there is a limited range of mean stresses that can be applied, without going into compression, or exceeding the UTS of the



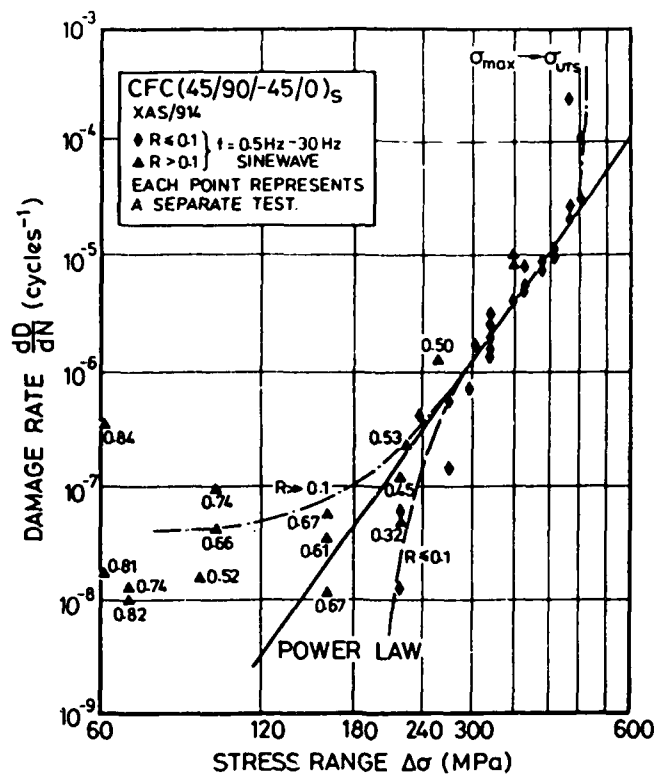


Figure 3

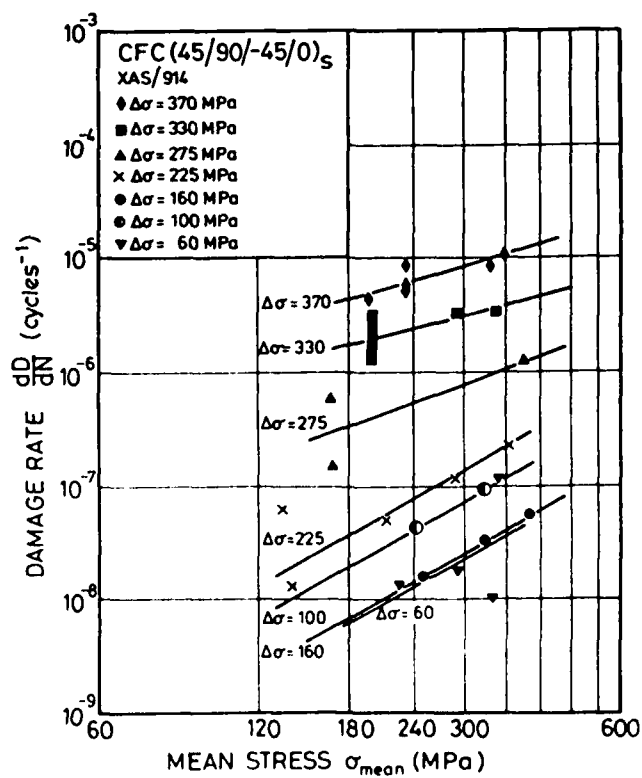


Figure 4

laminate. The mean stress effect seems larger at low stress ranges. However, the effect of the mean stress on the damage rate, is much smaller than that of the stress range.

Least-squares regression lines were fitted to the data for  $\Delta\sigma = 225, 160, 100, 60$  MPa in turn. The slopes were 2.88, 2.74, 2.60, 2.61, respectively. Taking the average slope, we have:

$$\frac{dD}{dN} \propto (\sigma_m)^{2.71} \quad (16)$$

#### The Terminal Damage

Figure 5 is a plot of normalised stiffness  $E/E_0$  versus cycles; all the curves for tests with the same maximum stress  $\sigma_{\max} = 517$  MPa; but with different stress ranges. Though the damage rates and lives vary considerably, the amount of stiffness reduction at failure is reasonably constant. This suggests that the failure criterion is determined by the maximum stress.

Figure 6 shows the variation of stiffness reduction at failure with maximum stress applied. The horizontal axis is subdivided into two parts. For  $(1 - E/E_0) < 0.35$ , the only damage present is  $D_1$ , the damage due to delamination. Above  $(1 - E/E_0) = 0.35$  any extra stiffness reduction is due to fibre breakage and splitting of the  $0^\circ$  plies.

The scatter is large, but there is a linear relation between maximum stress and damage at failure. Plotted on Figure 6 are lines of constant elastic strain to failure. Talreja (1982), O'Brien (1982) and earlier theories such as the maximum strain criterion (Jones, 1975) have postulated that the critical failure parameter is the applied strain.

In a load-controlled fatigue test, as  $E$  decreases due to cycling, the maximum strain  $\epsilon$  increases. When  $\epsilon = \epsilon_c$  failure occurs.

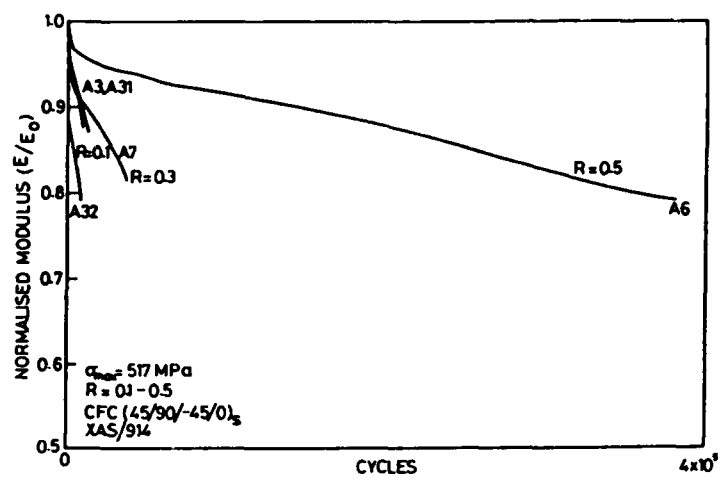


Figure 5

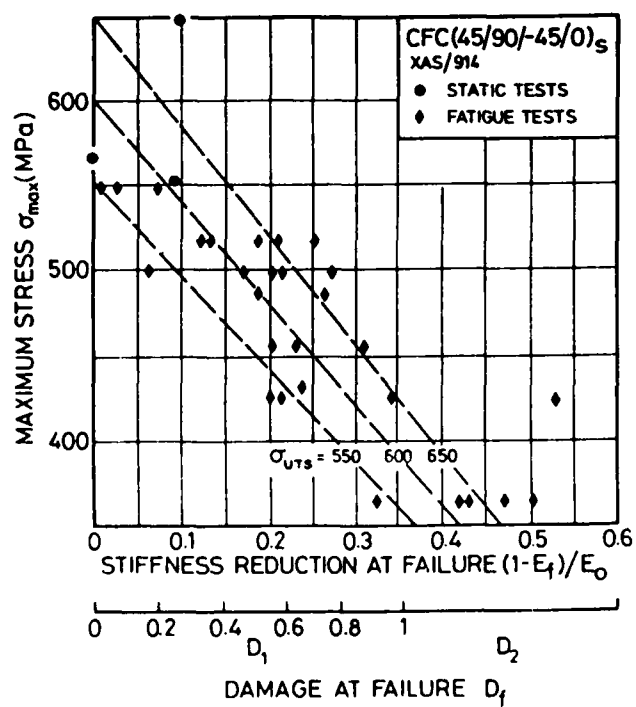


Figure 6

Under static loading, assuming no stiffness reduction,

$$\epsilon_c = \frac{\sigma_{UTS}}{E_o} \quad (17)$$

After cycling at some maximum stress  $\sigma_{max}$ , the strain is:

$$\epsilon = \frac{\sigma_{max}}{E} \quad (18)$$

where E is the reduced modulus due to damage.

Rearranging eqns. (17) and (18), and using eqn. (12), we have, at failure,

$$D_f = 2.857(1 - E_f/E_o) = 2.857 (1 - \sigma_{max}/\sigma_{UTS}) \quad (19)$$

The lines plotted for  $\sigma_{UTS} = 550, 600, 650$  MPa respectively. The data is reasonably well explained by this hypothesis.

#### General Equation of Behaviour in Tension, and Prediction of the S-N Curve

In the range  $\Delta\sigma = 240$  MPa to  $\Delta\sigma = 480$  MPa we have:

$$\frac{dD}{dN} = 9.189 \times 10^{-5} \left( \frac{\Delta\sigma}{\sigma_{UTS}} \right)^{6.393} \quad (15)$$

for  $R = 0.1$ , where the mean ultimate tensile strength,  $\bar{\sigma}_{UTS} = 586$  MPa.

The effect of mean stress is such that, at low stress amplitudes,

$$\left( \frac{dD}{dN} \right)_{R>0.1} = \left( \frac{dD}{dN} \right)_{R=0.1} \times \left( \frac{\sigma_m (R > 0.1)}{\sigma_m (R = 0.1)} \right)^{2.71} \quad (20)$$

The amount of damage at failure,  $D_f$ , is determined by the maximum applied stress:

$$D_f = 2.857 \left(1 - \frac{\sigma_{\max}}{\sigma_{\text{UTS}}}\right) \quad (19)$$

Recalling eqn. (2), and substituting for  $f(\Delta\sigma, R, D)$  from eqn. (15), then:

$$N_f = \int_{D_i}^{D_f} 1.088 \times 10^4 \left(\frac{\Delta\sigma}{\sigma_{\text{UTS}}}\right)^{-6.393} dD \quad (21)$$

At the start of the test  $D_i = 0$ .  $D_f$  is determined by eqn. (20); as the damage rate calculated from eqn. (14) is valid only for  $R = 0.1$ , we substitute in for  $\sigma_{\max}$  in terms of  $\Delta\sigma$ ,

$$\sigma_{\max} = \frac{\Delta\sigma}{1 - R} = 1.11 \Delta\sigma \quad (22)$$

Equation (21) then reduces to:

$$N_f = 3.108 \times 10^4 \left(\frac{\Delta\sigma}{\sigma_{\text{UTS}}}\right)^{-6.393} \left(1 - \frac{1.11 \Delta\sigma}{\sigma_{\text{UTS}}}\right) \quad (23)$$

and if  $R \neq 0.1$ :

$$N_f = 3.108 \times 10^4 \left(\frac{\Delta\sigma}{\sigma_{\text{UTS}}}\right)^{-6.393} \left(\frac{\sigma_m (R = 0.1)}{\sigma_m (R > 0.1)}\right)^{2.71} \left(1 - \frac{\sigma_{\max}}{\sigma_{\text{UTS}}}\right) \quad (24)$$

This will underestimate the life at high stress ranges, as the mean stress exponent of (2.71) was calculated using low stress amplitude data.

Figure 7 is the S-N curve for the laminate ( $R = 0.1$ ). The life predicted from eqn. (23) is also plotted for  $\sigma_{\text{UTS}} = 550, 600, 650$  MPa respectively. The effect of changing  $\sigma_{\text{UTS}}$  by 100 MPa is very small at the low stress, high cycle end of the range. However, the high stress, low cycle region is very sensitive to a change in the assumed tensile strength.

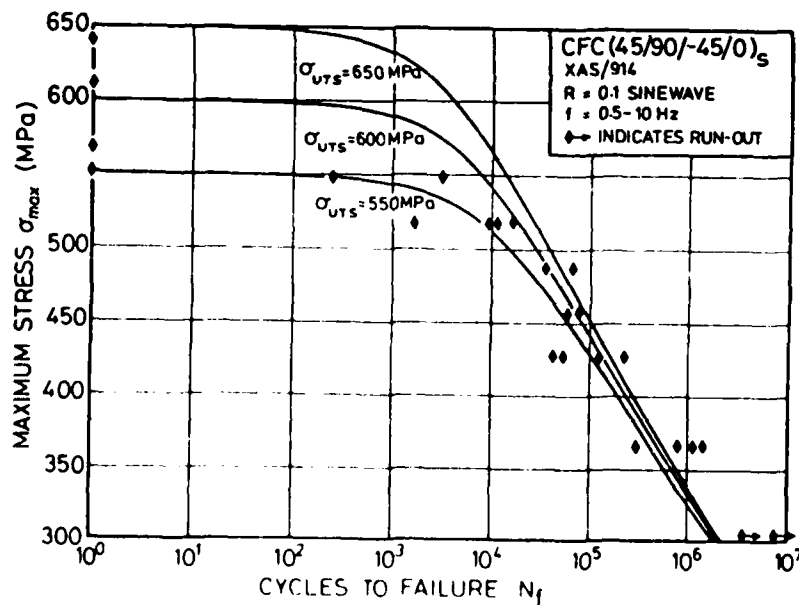
Agreement between observed and predicted lives to failure is good, though this agreement merely verifies that there is no inconsistency in our treatment so far. However, we could predict the S-N curve for other R-ratios, given than  $R > 0$ .

#### ACKNOWLEDGEMENTS

The authors would like to thank Paul Smith and Paul Steif for many interesting discussions during the course of this work. This work was financially supported in part by the Science and Engineering Research Council and the US Army European Research Office.

#### REFERENCES

- Jones, R M (1975) 'Mechanics of Composite Materials', Scripta (McGraw-Hill), Washington, DC
- O'Brien, T K (1982) Proc. 1982 Joint SESA-JSME Conf. Exp. Mech., Hawaii, p. 236
- Talreja, R (1982) Proc. 3rd Risø Int. Symp. Metall. and Mater. Sci., (Risø Press), p. 137



## Discussion of Section VII

Dr Lyall was asked whether fracture mechanics testing is practised during manufacturing runs. The answer given is "yes" in the case of PVC pressure pipe manufacture.

Dr Beaumont's presentation stimulated discussion on the origin of the fatigue damage ultimately responsible for the failure of fibre reinforced plastics. This discussion included comments on the physics of adhesion between reinforcing fibres and plastics. It appears likely that the adhesion between, say, fibreglass and epoxy resin lies in the "no man's land" between physisorption and chemisorption. It was pointed out that, even for the simplest of systems, such as the adsorption of argon gas atoms on freshly cleaved graphite crystals, rigorous theoretical models have still not been satisfactorily developed.

Session VIII: Vibrations, elastic waves and ultrasonics



VARIABLE FREQUENCY ULTRASOUND DETECTION OF PHYSICAL CHANGES  
IN GELS AND SOLIDS

Norman Barraclough

Instituto Eduardo Torroja, Consejo Superior de Investigaciones Cientificas  
Avda de la Paz s/n, Chamartin, Madrid 33, Spain

Summary

Variable frequency ultrasound waves have been passed through fresh cement paste specimens. At 5-minute intervals a continuous scan over a range of 30 to 60 kcl (kHz) of ultrasound frequency has been applied to the specimen and the energy transmitted by the specimen has been recorded graphically. In about five hours the paste evolves from a near gel to a solid. The data permit a three-dimensional study to be made of the setting process: as a function of time (X); rate of energy transmission (Y); and ultrasound frequency (Z). It is observed that as a general trend Y increases with X for all values of Z. But for certain values of X and Z there are inflections of Y which indicate energy absorption by the paste for narrow ranges of time and ultrasound frequency. For approximately the same values of X but other values of Z the value of Y may not show an inflection, suggesting that the paste structure at a given time during its physical evolution resonates for certain frequencies of the ultrasound. It is suggested that this technique may be more generally useful for monitoring structural evolution of materials, including polymers.

Introduction

Many materials start as gels or near gels and, as a consequence of chemical and/or physical change, they subsequently become recognisable as solids. Such physical and/or chemical transformation can be followed by passing through the material ultrasound (elastic) waves and recording the amount of ultrasonic energy the material transmits per unit time as its elastic properties evolve. This permits the determination of energy/time relationships which purport to

correspond with specific changes and discontinuities in the evolving properties of the material.

There is a further and more useful property. If the ultrasound waves applied to the material cover a certain range of wavelengths, all of which are applied at each time interval for which a record is taken, it is possible to discover if the energy/time relation is also dependent on the ultrasound frequency. This in turn can lead to correlations between ultrasound frequency and specific variations in the energy/time diagram and hence to identification of stages in the evolution of the material that are more sensitive to specific ultrasound frequencies. In the study of polymerisation, especially when this proceeds at relatively slow rates, it is likely that individual physical and chemical processes can be closely monitored by passing a range of ultrasound frequencies through the material at suitable intervals and noting changes in the energy/time relation for different frequencies.

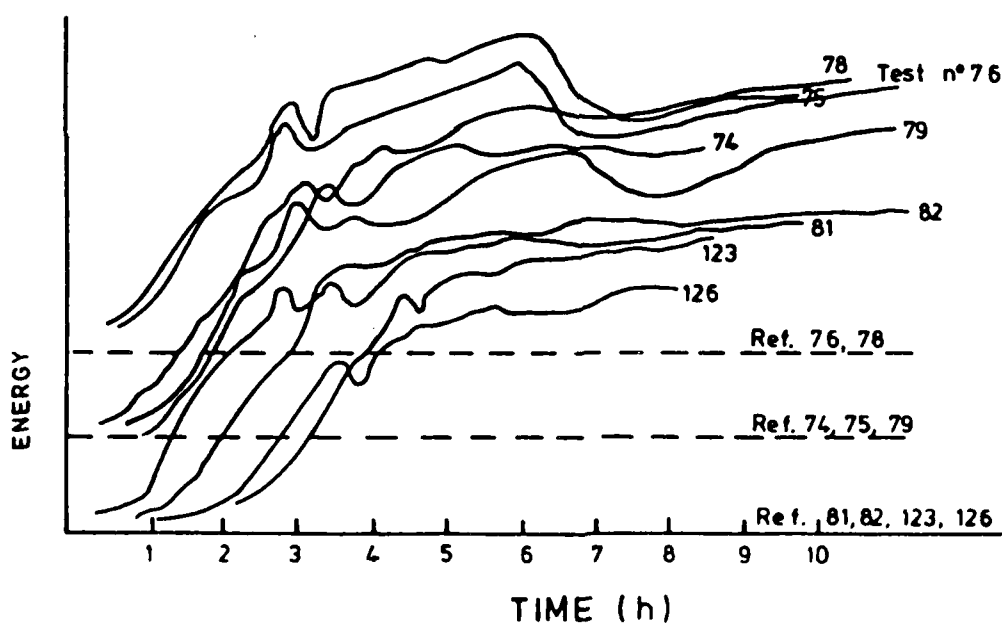


Figure 1

In tests carried out during the setting of cement paste, utilising both constant and variable frequency ultrasound, experimental results show inflections in the energy/time diagram (see Fig. 1) which suggest resonance for transmission by certain structures of the setting paste. That these inflections are attributable to resonance is supported by changing the

frequency of the ultrasound and noting that the inflections are usually displaced to another point of the real-time axis (see Figs. 2 and 3). Also, these inflections cannot be attributed to temporary decreases in the elastic properties of the evolving material, since simultaneous records of the ultrasound velocity through the specimen show a uniformly increasing velocity with time (see Fig. 4).

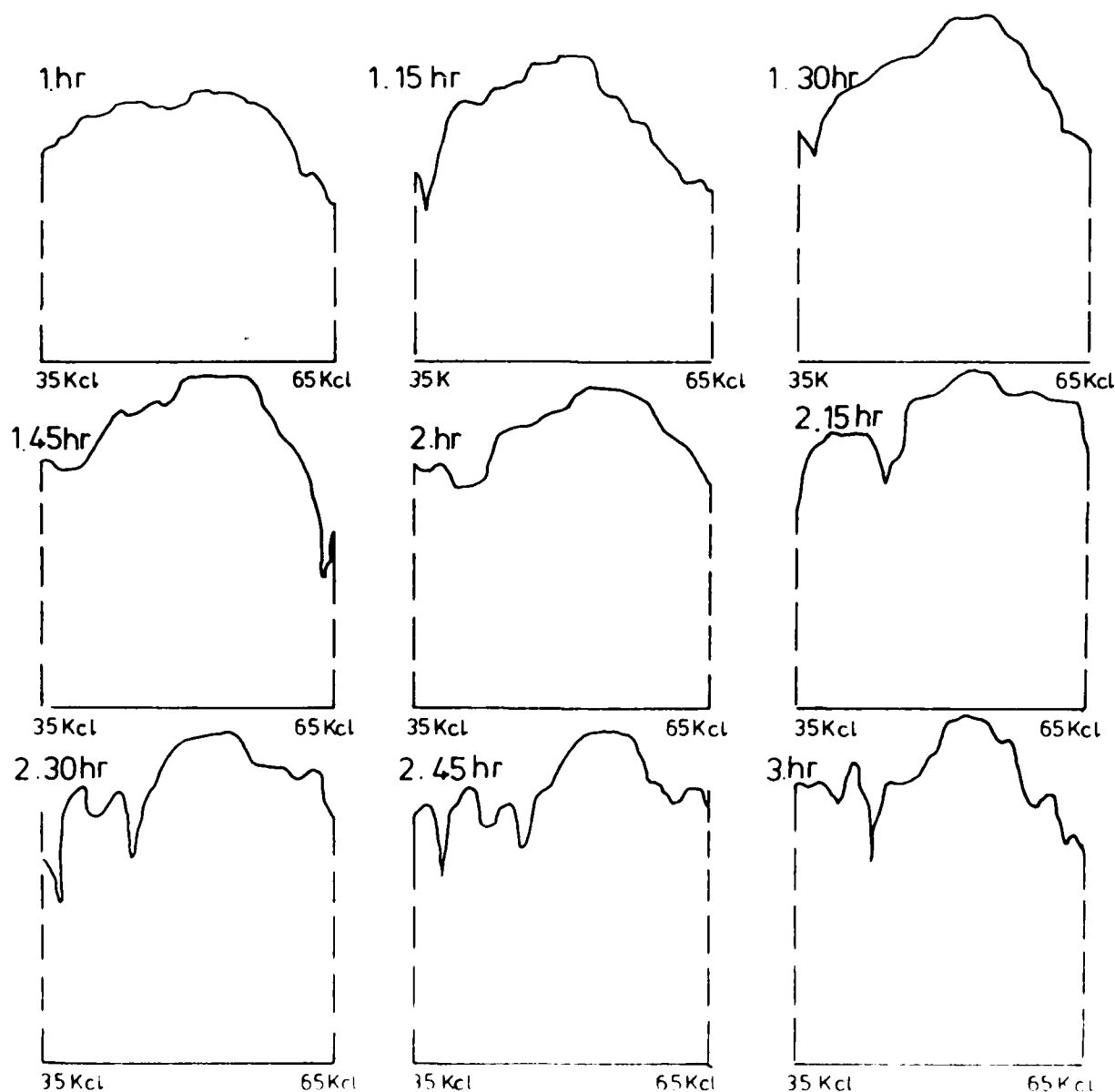


Figure 2

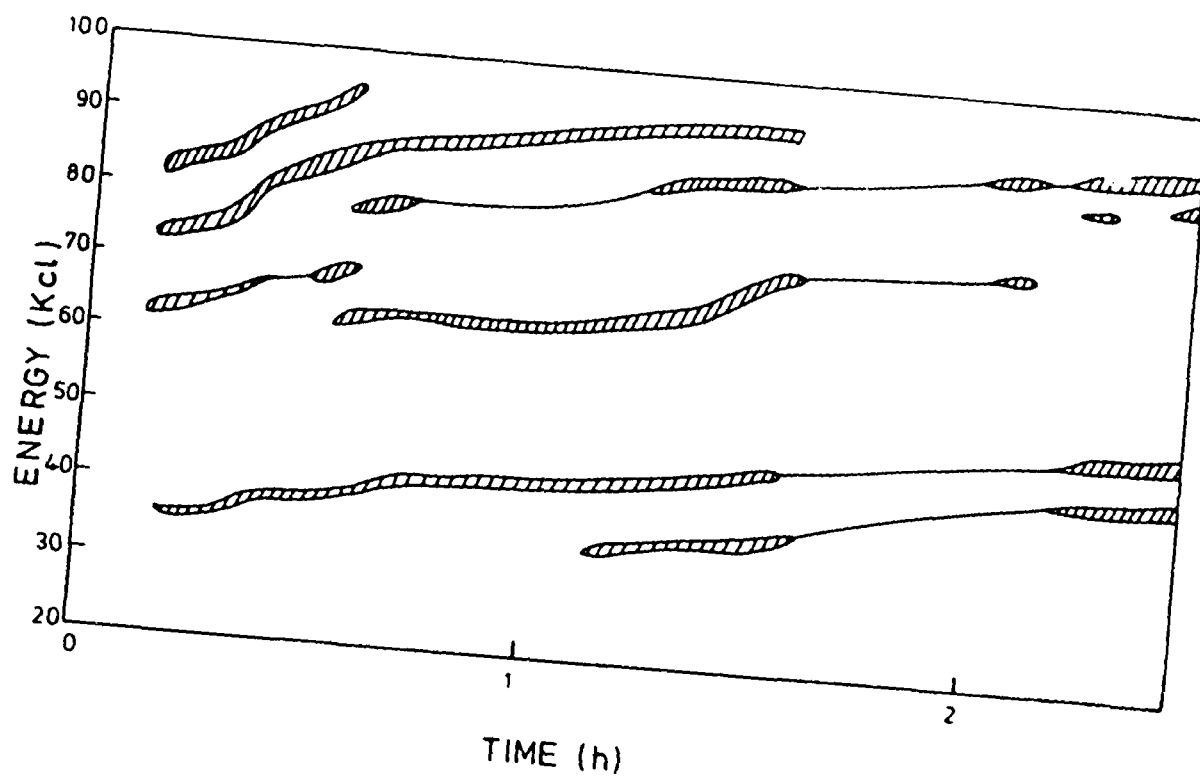


Figure 3

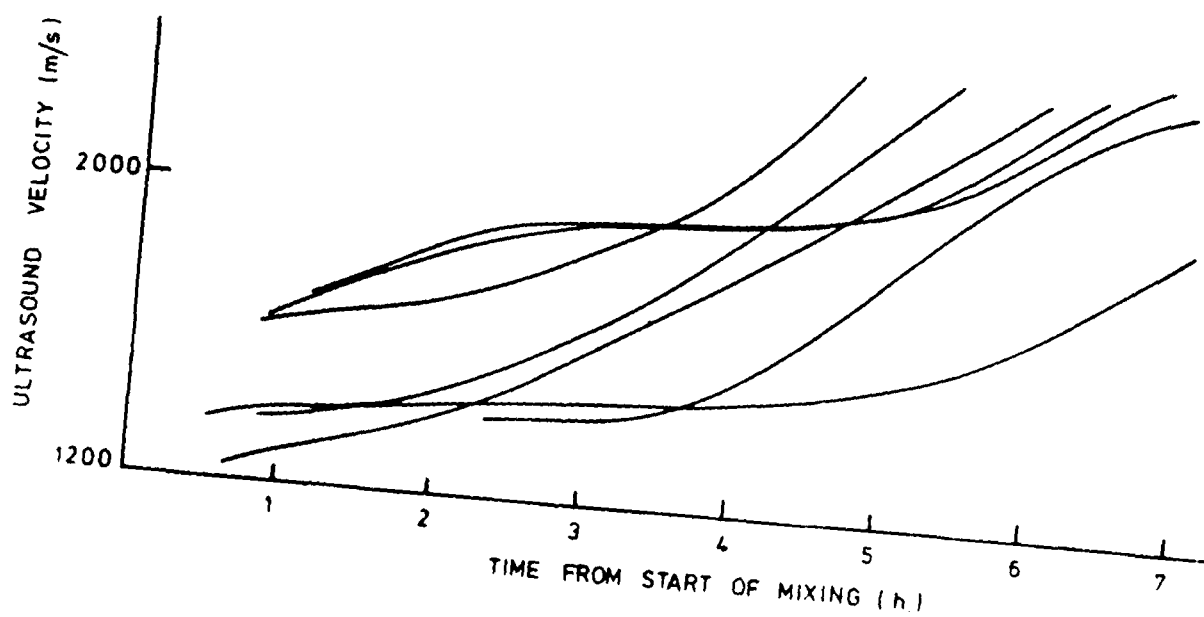


Figure 4

## Ultrasound energy transmission in evolving materials

The transmission of ultrasound waves by a material relates to its elastic properties and hence to its microstructural discontinuities and organisation. If the microstructure is complex and without clear-cut interfaces between its various phases, only statistically sampled results about its general physical properties may be deduced from its transmission of ultrasound. The amount of energy passing through a material undergoing fairly rapid physical and chemical changes is mainly a consequence of changes in elastic properties. However, if the relationship between real-time and energy shows clear inflections such as are evident in Fig. 1, the like of which cannot be attributed to uniformly progressive phenomena such as progressive curing (polymers) or progressive hardening (cement) but indicate events that occur within narrow time intervals of the whole, then these inflections presumably reveal additional facts about the evolution of the material. Thus, the energy/time diagram is a useful source of data for the structural analysis of an evolving material. This technique becomes much more powerful if constant frequency ultrasound is substituted by a variable frequency source of ultrasound so that a given range of frequencies of ultrasound energy can be applied at regular time intervals. In the present investigation it has been found that the specific inflections in the energy/time diagram are dependent on both the real-time and the frequency of the applied ultrasound (see Figs. 2 and 3).

The material chosen for the investigation reported here is cement paste during its initial setting process. Cement paste is a complex material consisting of powdered clinker (containing mainly tricalcium silicate, bicalcium silicate, tricalcium aluminate and tetracalcium ferrite aluminate) and water, which combine chemically to form, in the course of a few hours, a solid material that continues to harden during many weeks. The hardness asymptotically approaches a maximum value at very long time. Physically, the cement paste changes from an initial quasi-colloid substance during the initial minutes after mixing to a more or less rigid solid after about an hour and the subsequent progressive hardening is believed to correspond to increase in the proportion of crystallized material.

### Experimental details

Cylindrical specimens weighing about 300 gm and measuring 3.5 cm in diameter and about 8 cm in height were cast from fresh cement paste, in which the proportion cement/water was slightly varied from one batch of tests to the next. Each specimen was placed in a plastic cylinder open at both ends. Specimens thus encapsulated were placed vertically with flat ends between two ultrasound transducers, one emitting and the other receiving the radiation. Acoustic contact with the emitter was made through a grease layer (Fig. 5).

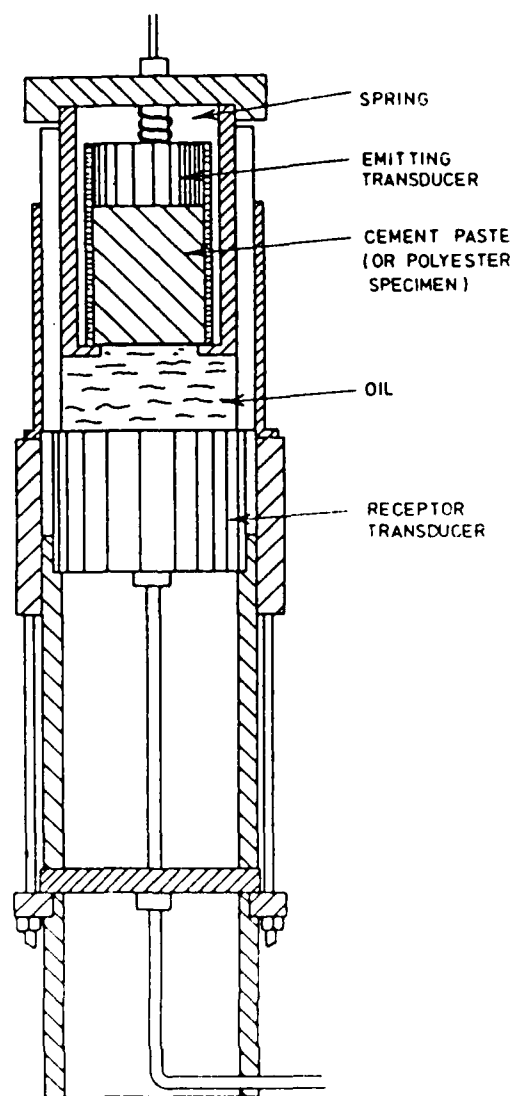


Figure 5

Ultrasound energy recording was started about ten minutes after the cement and water were first mixed. Initially the specimens were soft and malleable and lacked all obvious signs of rigidity and elasticity. The signal reaching the receiving transducer was amplified and recorded on tape. The amplified signal (decibels) was used as a measure of energy. The signal was also displayed shown as trains of impulses on the oscilloscope (Fig. 6). Fig. 1 shows the energy/time relationship recorded as the specimen sets to a solid. Fig. 6a shows the ultrasound wave train received at a stage of inflection of the energy/time diagram, and Fig. 6b shows the wave train received at a later stage in the setting of a specimen at which time the diagram energy/time reveals no inflection.

The results of tests using constant frequency ultrasound show that the transmitted energy increases with time. Taking the smooth envelope of the data as an approximation for the overall behaviour, the relation between the energy and time we find is:

$$\log E = t^{1/n} + K \quad (1)$$

where  $E$  is the energy transmitted in unit time,  $t$  is the time from the start of the cement setting process and  $n$  and  $K$  are constants.  $n$  lies between 2 and 3. It should be noted that this expression seeks only to roughly describe the  $E/T$  relationship. It does not include any inflections, some of which give rise to deep minima.

Inflections are sharper and more frequent during the earlier part of the test. In the later stages of setting they are more extensive along the time axis and less extensive along the energy axis.

Inflections are thought to be indicative of chemical changes in the paste, such as large scale readjustments in the molecular structure. As already pointed out, they cannot be attributed to sudden changes in elastic properties of the material because such changes would produce changes in ultrasound velocity. Velocity/time data reveal no inflections and, in most cases, the velocity increases continuously with increasing time. The probable explanation of the  $E/T$  inflections is that they are due to energy absorption

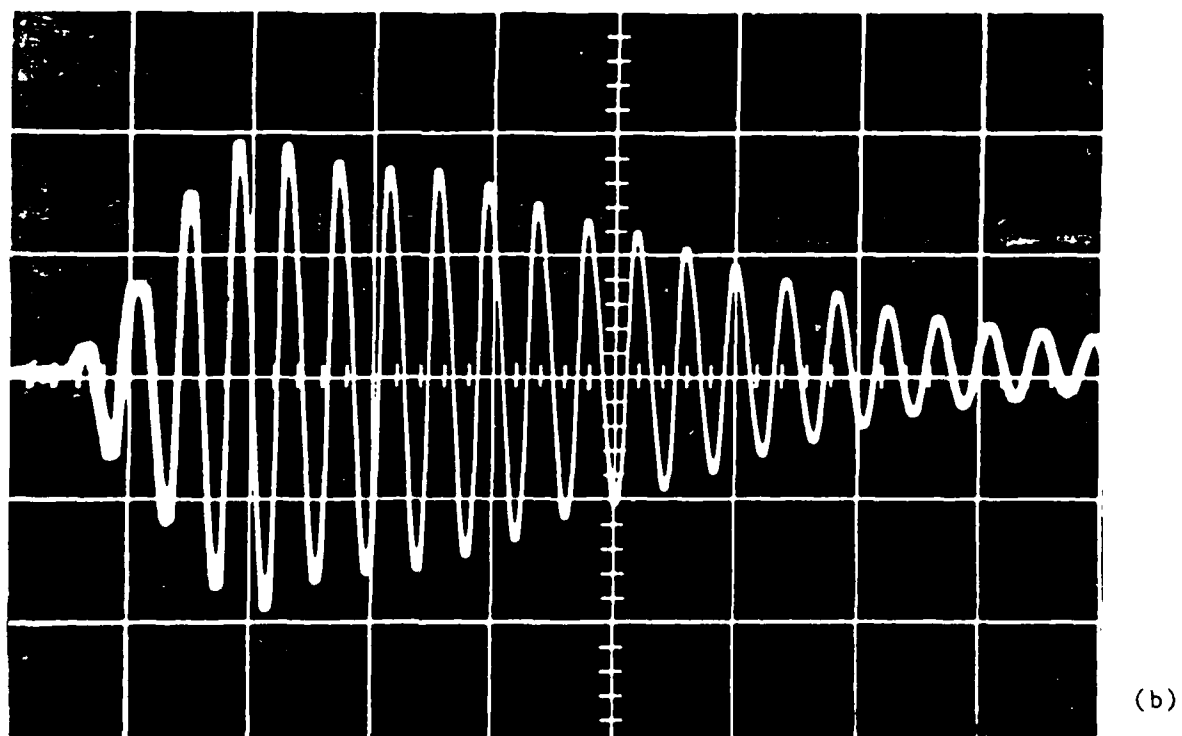
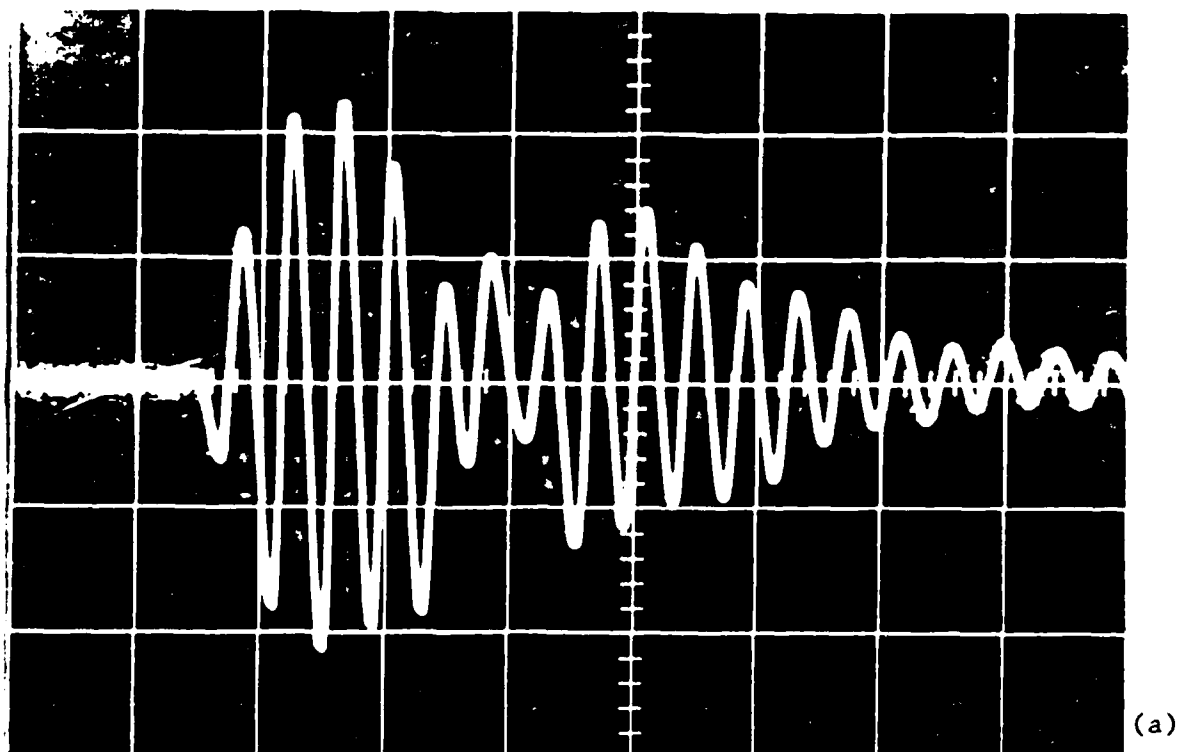


Figure 6. Trains of impulses (a) at the bottom of an inflection, and (b) at a stage of no inflection



associated with resonance. There are chemical phases in the paste which, when transmitting elastic waves of certain ultrasound frequencies, are stimulated to resonate. If these resonating masses vibrate within less hardened paste that separates the more rigid structural masses from each other, it is likely that energy is absorbed in the form of heat generated by internal friction.

#### Experiments with variable frequency ultrasound

To achieve variable ultrasound frequency the emitting transducer was connected to an electronic frequency modulator so as to cause the quartz element to vibrate at frequencies other than its own natural frequency. This arrangement proved quite successful and the intensity of the waves emitted by the transducer was almost constant over a range of about 30 kcl (kHz) centred on its natural frequency (which in this case was about 45 kcl). Consequently it was possible to apply to the cement specimens frequencies in the range 30 kcl (kHz) to 60 kcl (kHz). Since the full range of frequencies cannot be applied simultaneously, the procedure adopted was to make scans over the range of frequencies at frequent intervals, say every 10 minutes. An automatic device was set up whereby the range of frequencies was covered in about 2 minutes, and an energy/frequency diagram was obtained for each successive scan. A sequence of such scans, taken at 15-minute intervals, is shown in Fig. 2. The results were then transferred to a three-dimensional diagram.

Separate two-dimensional diagrams, obtained at consecutive time intervals, show that the precise location of an inflection, referred to the time axis, corresponds to a certain frequency in the frequency axis. However, at a different frequency, the "same" inflection may appear at a different time on the time axis; hence, by altering the frequency, the inflection at a given time on the time axis can be made to disappear. Fig. 3 shows the approximate continuity of inflections in the frequency/time plane. Most such inflections tend to appear at higher frequencies as time elapses. This suggests that the inflections in the amount of energy transmitted by the paste are due to energy absorption caused by the resonance of specific microstructures in the setting paste under the action of specific ultrasound frequencies, and as the cement paste structure evolves, so the resonating structures also change in such a way as to become resonant to higher frequencies. When the cement paste has

set quite hard such resonating inflections disappear. This observation is attributed to the fact that the material develops into a more uniformly structured mass, i.e. into a mass with more uniform elastic properties.

#### Monitoring the curing of a polymer (polyester)

A cylindrical specimen of a polyester resin was prepared and allowed to cure at room temperature over a period of about five hours. During this time a variable frequency scan was taken of the material at selected intervals. The sequence of energy/frequency diagrams shows a fairly uniform repetition of shape, the main difference being in the increase of energy transmitted at all frequencies as the curing proceeds. The results further demonstrate that the material has a complex resonating capacity in terms of frequencies, although this seems to remain fairly constant throughout the cure process; see Fig. 7.

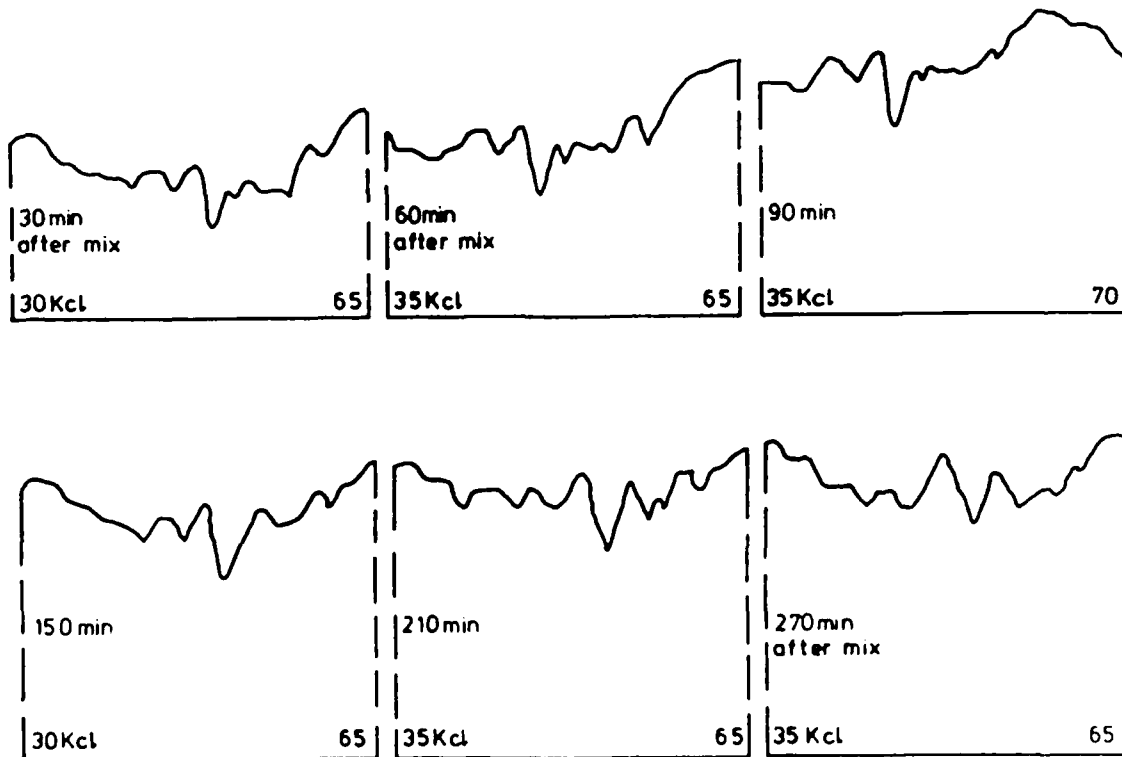


Figure 7

## Conclusions

The propagation of ultrasound, and in particular the nature of propagation of variable frequency ultrasound, has the following useful features when studying rapidly evolving microstructures.

1. A real-time record of the energy transmitted by the material during the course of its transformation gives information about the elastic properties during the process of change. Detailed analysis of the relationship between the rate of energy transmitted and the real-time can be related to individual phenomena. For instance, observation of an exponential relationship between energy transmitted and time may indicate that the sources of change (e.g. the origins of curing, of setting, or of solidification) are increasing at any time  $t$  in direct proportion to the density of such sources. It is postulated that this could be so in a crystallization process which develops uniformly from every region of material already crystallized. In expression (1), an exponent  $n = 2/3$  is compatible with the mass of the crystallized material growing uniformly from all its surface. On the other hand, if the crystallized matter consists mainly of linear threads, which mainly grow along their lengths, an exponent of about  $1/3$  is expected. Combinations of both morphologies would lead to exponents  $\sim 1/2$ .
2. Variable frequency ultrasound offers the possibility of obtaining information about the nature of separately vibrating masses that may develop in an evolving material in the course of its physico-chemical transformation. By subjecting the material to a periodic scan covering a range of frequencies it is possible to detect at what real-time values and for what frequencies there are resonances between the material - or parts of it - and the applied variable frequency ultrasound transducer. If at a time  $t_1$  a resonance is discovered for a frequency  $f_1$  and at a subsequent time  $t_2$  the displaced resonance appears at a frequency  $f_2$ , it is possible to estimate the rate of development (change in size, in stiffness, etc) of the possible vibrating masses which resonate first at frequency  $f_1$  and later at frequency  $f_2$ . In general, by constructing a three-dimensional map

defined by the real-time axis, the rate of energy transmission of the material, and the ultrasound frequency, it is possible to follow the inflections due to particular resonances, as these inflections become displaced along the time-frequency surface; see Fig. 3.

## ULTRASOUND REFLECTION TOMOGRAPHY OF CRACKS IN POLYESTER RESIN

M. Moshfeghi and P. D. Hanstead

University of Bristol

H. H. Wills Physics Laboratory, Bristol BS8 1TL, England

### Abstract

A new technique has been developed for carrying out real-time ultrasound reflection tomography using cylindrically diverging beams with highly damped broadband probes. The carrier information of the pulse is dispensed with and only the peak of the rectified rf pulse and its corresponding time of arrival are used for the reconstruction. A simple deconvolution filter has been used to remove the blurring caused by simple backprojection. Computer simulations are presented illustrating the deconvolution accuracy. Experimental images show resolution of wavelength order. Images of real defects in polyester resin samples are obtained by using compression waves.

### Introduction

Ultrasonic tomographic imaging is a powerful diagnostic tool in Non-Destructive Testing (NDT) and medical imaging. In NDT applications, defect location and sizing information are obtained from the image. Medical imaging provides early diagnosis of diseased tissue by painless non-invasive methods. Transducers used in pulse-echo mode are still the most widely used arrangement in NDT and medical imaging. The parameter reconstructed is the reflectivity distribution through the object. The most widely used technique, B-scan, produces poor lateral resolution compared with range resolution. One way to overcome this is to do compound B-scanning with some deconvolution processing to remove blurring<sup>1</sup>, but this requires long scanning times and large amounts of data to be processed.

A new broadband pulse-echo technique for reconstructing a cross-sectional picture of acoustic reflectivity has been reported<sup>2,3</sup> which achieves high resolution in both range and lateral directions. A broadband diverging wavefront acoustic pulse is emitted from an omnidirectional transducer into a 2D reflecting medium and the resultant backscattered echoes are recorded as a function of time at the receiver. It is assumed that the speed of sound is constant over the region of interest and that the amplitude of the wave backscattered from any scatterer is independent of the direction of the impinging wave. Under these assumptions, when the same transducer is used as the receiver, the rf backscattered echoes represent line integrals of the acoustic reflectivity over concentric arcs centered at the transducer position as shown in Fig. 1. When a different transducer is used as the receiver, the line integrals are along ellipses whose foci are the transmitter/receiver positions. The ellipse represents the locus of points of equal transmitter-receiver pair round trip time. By translating the transducer(s) over a suitable aperture the image can be reconstructed. Apertures frequently used are circular and line apertures.

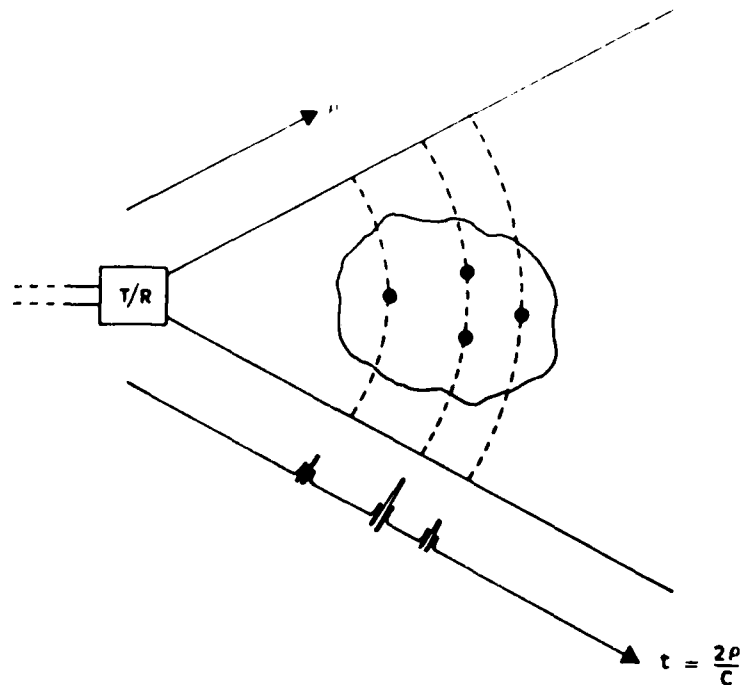


Fig. 1. The same transducer used as a transmitter and receiver. The echo sequence forms a projection representing line integrals of the acoustic reflectivity over concentric arcs centered at the transducer position.

Both of the above assumptions break down in real materials, in particular the second one in NDT applications, where defects are often strong specular reflectors and only visible to a limited portion of the aperture. Thus the concept of the point spread function (PSF) as the single point resolution of the imaging system is not totally valid, but it is still a good indicator and useful in testing the maximum theoretical resolution of the reconstruction algorithm. In the analysis to follow, time delays along extremum paths (between the point reflectors and the probe) are used for image reconstruction rather than diffraction theory. These ray paths are however, often the same or nearly the same as the characteristic solution lines to the wave equation, which includes diffraction effects. Thus, although some energy travels along diffraction paths, a large proportion travels along the extremum ray paths as assumed here.

The data recording for a circular aperture, using a single probe, is shown in Fig. 2. The reflectivity of the object in the plane of the transducer motion is  $f(r, \theta)$ , where the origin of the polar coordinate system is the center of rotation for the probe, along a radius  $R$ . Let the resultant echo data recorded at the same transducer as a function of time be  $g_\phi(t)$ , where  $t = 2\rho/c$  and  $\rho(\phi, r, \theta)$  is the distance from the probe at  $(R, \phi)$  to the object point reflector at  $(r_0, \theta_0)$ . It is to be assumed that the receiver gain corrects for attenuation. The simple backprojection of the signals  $g_\phi(t)$  for every angle  $\phi$  round the object without prior filtering gives rise to an image  $Z(r, \theta)$ , where :

$$Z(r, \theta) = \int_0^{2\pi} g_\phi(t) d\phi \quad (1)$$

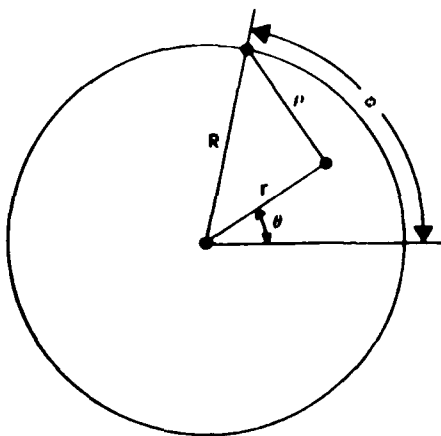


Fig. 2. The data recording geometry for a circular aperture. The probe is at  $(R, \phi)$  and a point reflector is at  $(r_0, \theta_0)$ .

Thus, to reconstruct the image, the amplitude of the A-scan evaluated at time  $2\rho/c$  is smeared back over an arc of radius  $\rho$  in image space. This is repeated for each point in each of the A-scans at different transducer positions and the contribution from them superposed to form the image.

The line-integral interpretation of the recorded echo data leads to the intuitive idea that the echo data generated by the transducer can be regarded as 1D projections of the 2D object  $f(r, \theta)$ . In comparison with X-ray tomography projections of an unknown density function, these acoustic projections of the reflectivity function  $f(r, \theta)$  seem distorted because the wavefronts are diverging and the integration paths are curved. However if the object is small compared with  $R$ , the paths that intersect the object are nearly straight. This approximation is quite analogous to the paraxial approximation in optics. Another fundamental difference between ultrasound reflection tomography and X-ray tomography is that in the former, if the beam covers the object, one transducer position gathers reflectivity information from all the object. But in X-ray tomography the source-detector pair has to be moved over an aperture for an equivalent amount of information about absorptivity.

In the classical convolution/backprojection, the projections are along straight lines. Simple backprojection of projections of a point object results in an image with a star shape blurring. The superposition of a continuous set of lines around the point is equivalent to the rotation over a circumference of  $2\pi$ . Thus, intuitively, the PSF for a point object is  $1/r$ . Mathematically, the Fourier coefficients of the simple backprojected image are equal to the exact Fourier coefficients divided by the frequency vector. Analysis has shown that a superior reconstruction can be achieved by first convolving each projection with a filter function, and then backprojecting the modified projections<sup>4,5</sup>. This is called convolution backprojection. The filter functions are derived by Fourier inverting the frequency vector (reciprocal space radius) and usually have strong central maxima with symmetric heavily damped bipolar sidelobes. The filtering operation then effectively weights the projections with the frequency vector and results in a correct image.

Returning to the simple backprojection along circles for the ultrasound case, it has been shown<sup>2</sup> that if very wideband pulses are used then eqn. (1) becomes :

$$Z(r,\theta) = [ (1/r) * f(r,\theta) ] + \epsilon(r,\theta) \quad (2)$$

Where \* denotes convolution. The first term in eqn (2) is the usual  $1/r$  blurring for simple backprojection along straight lines. The second term is an error term which is a resultant of the curvature of the circles. For the point reflector at  $(r_0, \theta_0)$  we have :

$$\epsilon(r_0, \theta_0) = 0 \quad \text{and} \quad \lim_{R \rightarrow \infty} \epsilon(r, \theta) = 0 \quad (3)$$

Thus at the point reflector the error term is zero but it increases as the distance from the point reflector is increased because the curvature of the circles makes the line integrals depart from straight lines. Also in the limit of  $R \rightarrow \infty$  the integral paths tend to straight lines and the error term vanishes.

There are two different approaches to removing the blurring. Iterative techniques similar to those for X-rays could be modified for curved rays and employed. These methods, however, result in long processing times. Alternatively, analytical methods could be employed which would not take into account the error term above but could be done in much shorter processing times. Here the projections are first convolved with a deblurring kernel and then backprojected. This makes the impulse response of a point reflector look like the kernel in data space and achieves diffraction limited resolution. The deblurring kernel used for our images is the empirical two term simple filter of Fig. 3.

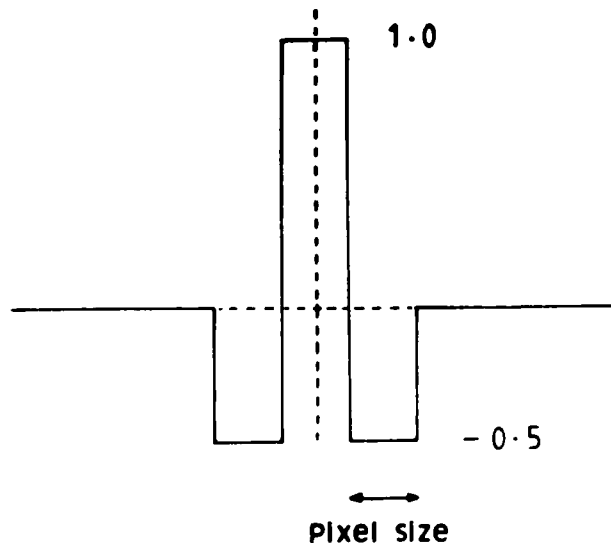


Fig. 3. The simple filter used for deconvolution.



One method to avoid the need for the convolution is to transmit a pulse which takes the shape of the deblurring kernels. This way, the projections need not be modified and can be backprojected as they are. In practice, however, it is difficult to control the shape of the transmitted pulse and pulse shape does change in travelling through the object.

#### Data reduction

The real-time system to be developed is shown in block diagram form in Fig. 4. The object is first scanned and data gathered. The data is then processed and the image displayed. The main problem in attaining a real-time system is reducing the processing times. Other researchers working towards similar systems have come to the conclusion that real-time systems are not feasible without the use of array processors<sup>7</sup>. Our approach is to reduce the amount of data to be processed by discarding redundant information and aim towards a cheap microprocessor-based setup.

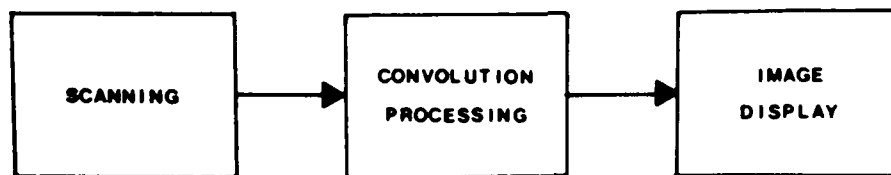


Fig. 4. A Block diagram of the imaging process.

The data reduction method used by us is well suited for short pulses and can be used where the image field is uncluttered, as is the case for most NDT problems. In narrowband systems, spatial information about the object is conveyed on phase measurements of long pulses. In wideband pulse-echo techniques, however, information is conveyed on the basis of echo-delay measurements of short pulses. Under such circumstances, the function of the phase information of the short pulses is to suppress sidelobes after backprojecting the projections. The same function, however, could be realized by a much simpler method which would not require backprojecting the full shape of the waveform and would result in much faster processing times.

Consider the three echoes in Fig. 5(a). The peak of the pulses can be used as an accurate indicator of their arrival. For each of the pulses the entire pulse is replaced by a rectangular pulse that spans one data sample centered about the rectified pulse peak, and takes on the amplitude of the peak as in Fig. 5(b) (for our setup, rectification is done in software). The uncertainty depends on how fast the waveforms are sampled but these average out because of their random nature. One could alternatively replace the peak by more than one data sample, or reconstruct the image on a coarser pixel size. This artificial pulse sharpening process is equivalent to digital filtering of the echoes by an ideal spiking filter<sup>8</sup>, but does not consume the computation time of the former and has been used by other authors<sup>9</sup>. If the resulting pseudo-delta functions are backprojected, the 1/r blurring will result. The simple filter of Fig. 3. is used to remove the blurring. The result of convolving the kernel with the pseudo delta functions is the kernel itself, scaled according to the amplitude of the delta functions

as shown in Fig. 5(c). Thus, the impulse response of point scatterers has been made to look like the deblurring kernel in a controlled manner. The negative sidelobes of the kernel perform the same deblurring and sidelobe suppression function that the phase of the original rf waveform did. For a point reflector the mainlobe of the kernel would give a positive contribution to the intensity at that point for all the projections. On the other hand, for points near and around the point reflector the negative sidelobes of the kernel will counterbalance the positive contributions from other projections and thus remove some of the blurring.

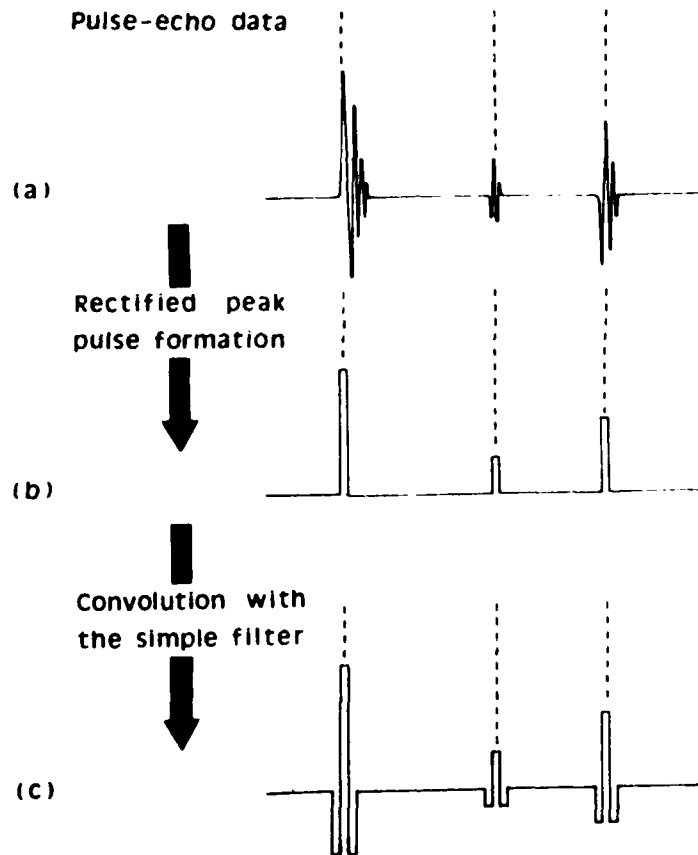


Fig. 5. The data reduction process. (a) The original pulse-echo data. (b) Replacing the pulses with pseudo-delta functions centered at the position of the peak of the pulses with magnitudes of the modulus of the pulses. (c) The modified projections obtained by convolving (b) with the simple filter.

Another method to reduce the processing time has been the choice of the weighting functions used for correlating the ray interaction with the pixels. In X-ray tomography, various weighting factors are used like the area of intersection between the pixel and the ray, or the distance from the center of the pixel to the center of the ray. These choices are, however, lengthy to implement on a computer. Our choice of the weighting function has

been a simple one of 1 or 0, where 1 is assigned to the pixel with its center closest to the ray center and 0 to the rest. This reduces computation time considerably but is less accurate. The improvement one gets by using more complicated weighting functions, however, is very slight and in our opinion is not worth the additional computation cost. If the picture is reconstructed on a coarser pixel size than the sampled data then the need for these weighting functions disappears anyway.

### Line aperture

The data recording process for a straight line aperture is shown in Fig. 6. Cartesian coordinates better suit this geometry. Consider a point reflector  $(x_0, y_0)$  in the  $x$ - $y$  object plane. As the probe is moved along the  $x$  axis, its output generates a hyperbola in the  $x$ - $\rho$  plane (data space) given by :

$$\rho = [ y_0^2 + (x_0 - x)^2 ]^{1/2} \quad (4)$$

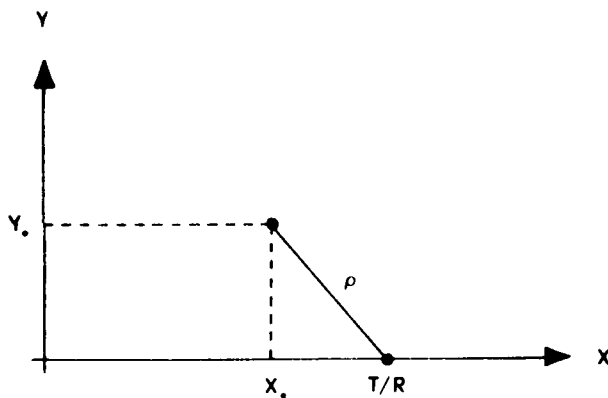


Fig. 6. The data recording geometry for a line aperture. The probe is moved along the  $x$ -axis and there is a point reflector at  $(x_0, y_0)$ .

Much work has been done by other authors <sup>10,11,12</sup> to use hyperbolic delay-summing so that the A-scan signals at different transducer positions arrive in phase with one another. The scattering amplitude at each pixel is reconstructed by integration along the hyperbolic curve unique to that pixel. This technique has been named Synthetic Aperture Focusing Technique (SAFT). Although one would expect the process of delay-summing to be equivalent to convolution backprojection, it has been shown that the latter method is capable of a better PSF for wideband pulses <sup>6</sup>.

Computer simulations have been written to generate echo data by reflecting a given pulse from isolated point targets. These data are then used to reconstruct an image of the targets. The sampling rate simulated is 11.84 MHz which in water corresponds to a spatial sampling of 1/16th of a mm. The transmitted waveform is assumed to be a positive rectangular pulse of 85ns duration. This is an easy choice as it represents one data sample with the above sampling rate.

The first simulation attempted was for a point target at  $X_0=64\text{mm}, Y_0=64\text{mm}$ , with one transducer transmitting and receiving so that backprojections were along circles. A 128mm aperture from  $X=1\text{mm}$  to  $X=128\text{mm}$

was simulated on the  $Y=0$  axis, along which the transducer was moved in 1mm steps so that 128 circles were backprojected. Fig. 7(a). is a 32 by 32 pixels isometric plot of the resultant simple backprojected image, where pixel size is 1mm and the vertical axis is the normalized reconstructed reflectivity. For an ideal image one would like just a delta function at the reflector position but the blurring is clearly evident, as are the missing zones in it due to the finite aperture. Fig. 7(b). shows a cross section plot along  $Y=64\text{mm}$ , which is the line AB in Fig. 7(a). A plot of  $|1/x|$  centered at the reflector position is superimposed for comparison with theory. Clearly, due to the curvature of the circles and the error term in Eqn. (2), the blurring is less than that for straight lines. If the projections are convolved with the simple filter of Fig. 3 before backprojection, the resultant backprojection becomes that of Fig. 7(c). The cross section plot along  $Y=64\text{mm}$ , which is line CD on the diagram, is shown in Fig 7(d). The blurring has largely been removed.

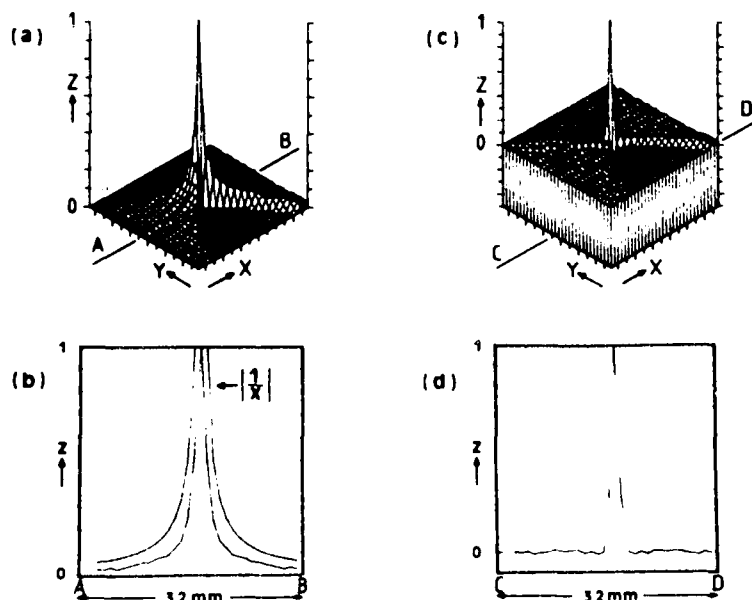


Fig. 7. Computer simulations for a linear aperture with backprojection along circles. (a) The simple backprojection image. (b) Cross section plot of (a) along AB with  $|1/x|$  superimposed. (c) Image obtained by convolution backprojection using the simple filter. (d) Cross section plot of (c) along CD.

An array with 128 elements from  $X=1\text{mm}$  to  $X=128\text{mm}$ , with element spacing of 1mm, was simulated. Data for the same point reflector as before was generated but this time each element was used as a transmitter and all others (including the transmitter) receiving at the same time. This process was repeated for all the elements. The process of simple backprojection of the data along ellipses results in the isometric plot of Fig. 8(a) with the corresponding cross section plot of Fig. 8(b). The first thing to note is that the blurring is much worse than that for circles. Secondly, the blurring is much closer to the  $|1/x|$  blurring than the blurring for

circular backprojection. This is because the degree of curvature for ellipses near the point reflector is less than that for circles. The convolved image with the simple filter is shown in Fig. 8(c) with the cross section plot of Fig. 8(d). Although the blurring is decreased, the PSF is much worse than that of Fig. 7(d). This is in agreement with Norton<sup>6</sup> who found similar degradation in the PSF of backprojection along ellipses as compared to circles for a circular aperture.

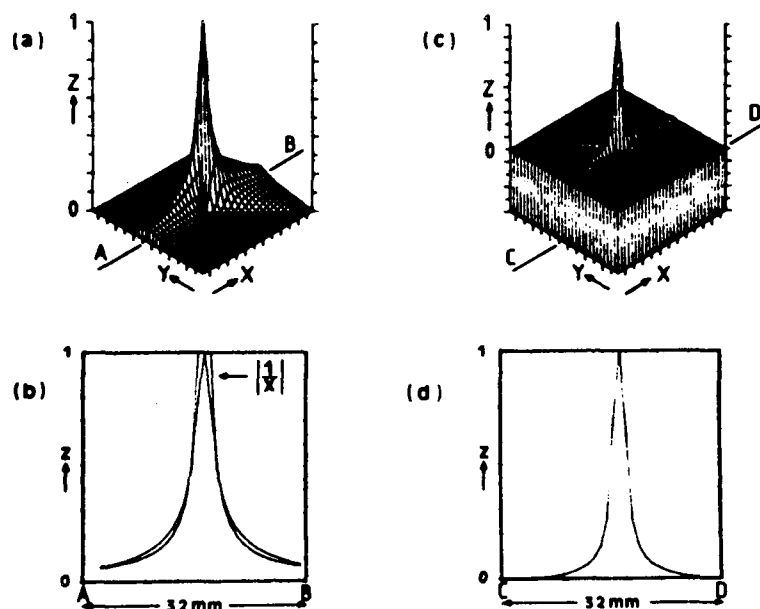


Fig. 8. Computer simulations for a linear aperture with backprojection along ellipses. (a) The simple backprojection image. (b) Cross section plot of (a) along AB with  $|1/x|$  superimposed. (c) Image obtained by convolution backprojection using the simple filter. (d) Cross section plot of (c) along CD.

With the straight line aperture of Fig. 6, an infinite aperture would correspond to  $x=-\infty$  to  $x=+\infty$ . This would give wavelength-limited resolution. In practice, however, the finite angular width of the beam, the loss of energy towards the edges of the beam, and the impracticality of moving the probe over an infinite line limit the data gathering to a finite aperture. This causes the resolution to become aperture dependent and the PSF to become spatially variant as was the case for Figs. 7 and 8. Points further away from the probe see a smaller aperture and show worse lateral resolution. The computer simulations above were repeated for points further away from the probe and it was clear that the transverse resolution worsens the further away the reflector is from the probes. Experimental images of test objects in water show transverse resolutions (for a finite aperture) that are about an order of magnitude worse than the resolution in the longitudinal direction.

### Circular aperture

There are many practical situations like scanning the human breast, cylindrical rods, pipes, etc., where there is circular symmetry and a full 360 degree scan is possible. This means that all the rays within the plane of the circle will be intercepted by the probe, making the technique sensitive to all spatial frequency components generated by the object and giving diffraction-limited resolution. Therefore circular apertures were used for the experiments. The same probe was used to act as both the transmitter and receiver. This way the backprojections would be along circles rather than ellipses, as desired for the optimum PSF. Referring back to Fig. 2. the point response of the reflector at  $(r_o, \theta_o)$  is no longer hyperbolic but takes a cosine form and is given by :

$$\rho = [ R^2 + r_o^2 - 2Rr_o \cos(\phi - \theta_o) ]^{1/2} \quad (5)$$

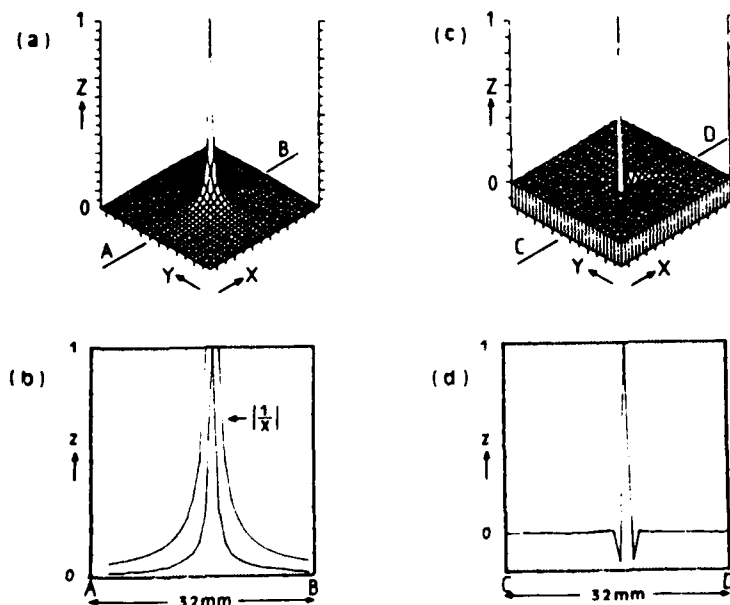


Fig. 10. Computer simulations for a circular aperture with circular backprojecting. (a) The simple backprojected image. (b) Cross section plot of (a) along AB with  $|1/x|$  superimposed. (c) Convolution backprojection image using the simple filter. (d) Cross section plot of (c) along CD.

The computer simulations were adapted for the circular aperture and backprojection along circles. The same waveform, sampling rate and pixel size were used but now  $R=64\text{mm}$  and the target is at the center of rotation. The center of rotation is equivalent to the cartesian co-ordinate  $X=64\text{mm}, Y=64\text{mm}$  and the line  $\phi=0$  is equivalent to  $Y=64\text{mm}$ . The aperture was sampled at 360 transducer locations in 1 degree intervals of  $\phi$ . The simple backprojected isometric image is shown in Fig. 10(a). Unlike the simulations

before, the PSF for a full circular aperture is circularly symmetric and spatially invariant. Thus the cross section radial plots are more representative of the blurring. That of Fig. 10(a) is shown in Fig. 10(b) together with  $|1/x|$ . Again the blurring is less than those for straight lines. The convolution of the projections with the simple filter before backprojection produced Fig. 10(c), with the cross section plot of Fig. 10(d). The PSF has a main lobe with negative sidelobes each side of it. The negative sidelobes represent points where the negative sidelobes of the simple filter have overcorrected the blurring around the reflector.

The same simulations of Fig. 10. were repeated but different filters used. When the three term Shepp-Logan filter <sup>4</sup> of Fig. 11(a) is used as the deconvolution kernel the cross section plot of the resultant image becomes that of Fig. 10(b). Similarly the three term Linear Superposition with Compensation filter <sup>5</sup>(LSC) of Fig. 11(c). gives the cross section plot of Fig. 11(d). Comparing these with Fig. 10(d) shows that for the simple choice of the weighting functions used the simple filter is better than the other two filters if negative scores are not displayed in the final image. Simulations for points off center proved that the resolution was spatially invariant.

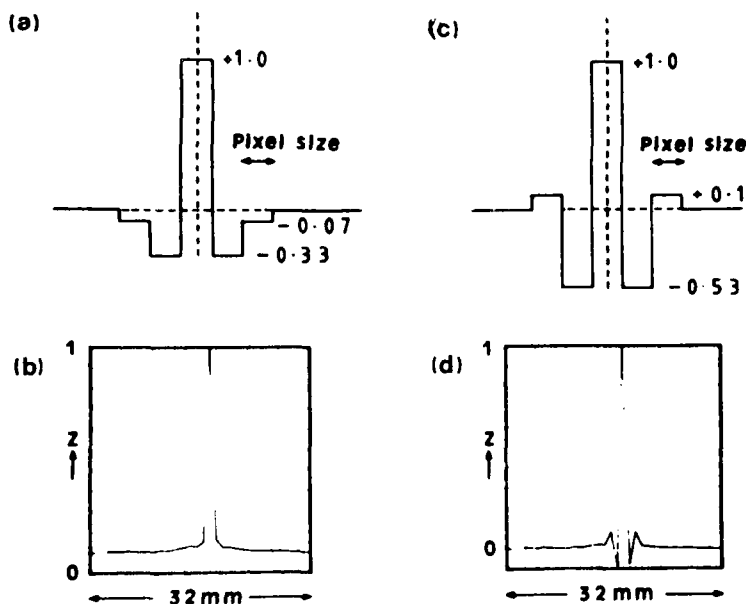


Fig. 11. Computer simulations for different filter functions. (a) The three term Shepp-Logan filter. (b) Cross section plot of the convolution backprojection image using the filter of (a). (c) The three term LSC filter. (d) Cross section plot of the convolution backprojection image using the filter of (c).

#### Dynamic range

The dynamic range of an imaging system needs to be as large as possible in order to distinguish between reflectors of different reflectivity. The

same geometry as Fig. 10 was simulated but with two point reflectors in the object space. In addition to the reflector in the center of rotation, which had a reflectivity of unity, another reflector of reflectivity 0.1 was simulated 2mm (corresponding to 2 pixels) off center. The resulting simple backprojected image of Fig. 12(a) and its cross section plot, Fig. 12(b), show that the weaker reflector is totally submerged under the blurring of the stronger reflector. After convolution with the simple filter, however, the two are resolved as shown in Fig. 12(c) and 12(d). This example represents an increase in the dynamic range of 20 dB.

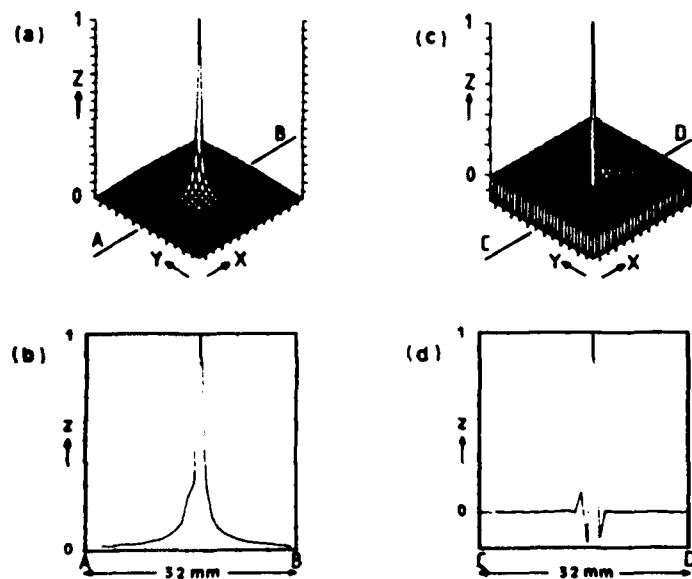


Fig. 12. Computer simulations for dynamic range. Two point reflectors of reflectivity 1 and 0.1 in object space, 2mm apart. (a) The simple backprojected image. (b) cross section plot of (a) along AB. (c) convolution backprojection image using the simple filter. (d) Cross section plot of (c) along CD.

#### Finite angle of view

Supposing that the dimension of the object to be reconstructed is  $n$  pixels then the number of pixel values to be determined is about  $\pi n^2/4$ . As the echo data would also be sampled at a spatial frequency corresponding to the pixel size then each transducer position would give  $n$  data samples of pulse-echo data. Therefore the minimum number of transducer positions,  $D$ , needed to determine the pixel values is :

$$D = \pi n/4 \quad (6)$$

These positions should be equally spaced from  $\phi=0$  to  $\phi=2\pi$ . If the above number of positions are synthesized on a smaller aperture the image-forming capacity of the resulting data will clearly be reduced.



There are some imaging situations where the scanning is limited to a restricted angular range because of an obstacle being in the way. If the beam does not cover the object fully even for a full 360 degree scan some reflectors will be seen by only a limited portion of the aperture. In addition there is the problem of specular reflectors in ultrasonics, where even if the above two limitations do not occur the reflector might still be visible only at a few points on the aperture. This restriction of limited angle in object space manifests itself into a limited angular range of frequency components in the frequency space of the object.

The same geometry of Fig. 10. was simulated but this time the aperture was limited to 60 degrees,  $\phi = -30$  to  $\phi = 30$ , and was sampled at one degree intervals. The respective plots are shown in Fig. 13 (a)-(d). The PSF is generally degraded with a broader mainlobe. Also evident are the conical ridges, usually associated with a restricted angle of view, radiating away from the mainlobe. These effects were also evident with the simulations of Fig. 7 and Fig. 8, as finite apertures were synthesized. For angles less than 60 degrees the blurring of the simple backprojection images became worse than the  $|1/X|$ .

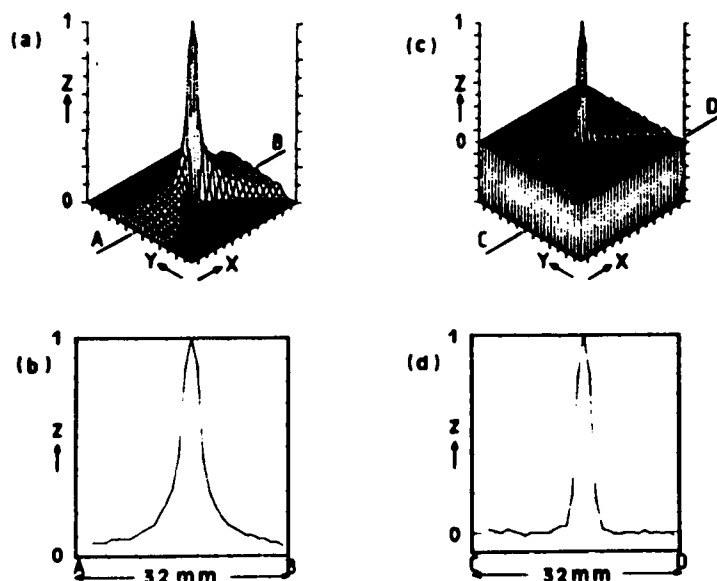


Fig. 13. Computer simulation for a limited angle scanning of 60 degrees. (a) The simple backprojection image. (b) Cross section plot of (a) along AB. (c) Convolution backprojected image using the simple filter. (d) Cross section plot of (d) along CD.

### Attenuation

Media in which ultrasonic waves propagate are lossy and the amplitude of the waves decrease with distance. If the absorptivity of the medium is constant then the absorption is exponential. With a cylindrically diverging

wave the attenuation due to geometric beam spreading is also  $1/\rho^{1/2}$ , where  $\rho$  is the distance from the center of curvature. Thus ignoring loss by backscattering and mode conversion, for a specular reflector distance  $\rho$  from the probe the amplitude  $A$  of the returned echo is :

$$A = A_0 \times 1/(2\rho)^{1/2} \times e^{-2\rho\sigma} \quad (7)$$

Where  $A_0$  is the original transmitted wave amplitude and  $\sigma$  is the absorption coefficient.  $2\rho$  appears in the equation because of the go and return path. For point scatterers the beam diverges spherically after incidence on the scatterer and causes an attenuation of  $1/\rho$  for the return path to the probe. thus eqn. (7) becomes :

$$A = A_0 \times 1/(\rho)^{3/2} \times e^{-2\rho\sigma} \quad (8)$$

If one knows the type of reflector that is being imaged the corresponding correction can be made either in software or by altering the gain of the receiver. If both types of reflectors are present in the image field an average correction can be done which would under-correct for point scatterers and overcorrect for specular reflectors. For the images in this paper no attenuation correction has been done and this seems to be tolerable for most NDT application but for medical applications little detail in the interior of images is seen without attenuation correction, specially where absorption is high and large organs are imaged.

This technique is inherently a near field imaging technique because of the  $1/\rho^{1/2}$  sound pressure decrease of the cylindrical beam. With long pulse probes there are large scale pressure fluctuations in the near field and these would have to be included in the attenuation correction. Short pulse probes, however, have much reduced fluctuations and produce better range resolution. As the latter are to be used for this technique these small pressure fluctuations produce minimum degradation in images even though they are not corrected for.

#### Experimental images in water

One of the questions being addressed has been to determine how few the number of levels the amplitude of the waveforms is quantised to needs to become before the images become inadequate. All the images presented in this paper have been produced with at most 8 levels (3 bits) of amplitude information and the images are more than adequate. The images have been reconstructed on a 128 pixels square grid. The sampling rate of the waveforms was 11.84 MHz. It was found that 90 to 120 transducer positions gave acceptable results and more transducer positions did not significantly improve the image. This agrees well with Eqn. (6). The images are displayed on an 8 level grey scale and stored on disk. A dot matrix printer has also been used to generate a coarse grey scale for printouts of the images. The simple filter has been used for deconvolution for all the experimental images. Negative values are displayed as black. If the images were to be rectified, then where the negative sidelobes of the simple filter have overcorrected the blurring would be displayed as image points, and false information would be conveyed.

For carrying out resolution tests water bath imaging was performed. There are different ways of obtaining a cylindrically diverging beam. One could use a transducer long in one direction and narrow in the other, as compared to a wavelength. This could be done by inserting a mask with a thin slot immediately in front of the probe, where the mask material has good absorption such as foam plastic adhesive strips. Alternatively one could use a transducer with cylindrical focus, where the beam diverges after the focus point.

The approach finally taken was to use an ordinary parallel beam unfocused probe and place an acoustic diverging cylindrical lens in front of it 13. The lens was made from perspex as it has reproducible properties. In this way by using lenses of different radius of curvature the same probe can be used to generate different beamwidth angles. The lens was 40mm long, 12mm wide, with a radius of 6.25mm. The probe used was a wideband highly damped Panametrics Videoscan immersion transducer of 0.5 inch crystal diameter with center frequency of 5 MHz. When used with this probe the beamwidth was 40 degrees at the 6 dB points. The scanning arrangement was to place the object on a turntable, with the transducer fixed in position for mechanical ease.

A resolution specimen, Fig. 14(a), consisting of two chromel-alumel wires of 0.17mm diameter with center to center spacing of 0.4mm was scanned with one of the wires being on the center of rotation. The diameters of the wires are just over half a wavelength at the center frequency, thus representing good point-scatterers, and the center to center spacing is just over a wavelength (for 5 MHz  $\lambda=0.3\text{mm}$  in water). The aperture was sampled at 90 positions at 4 degree intervals and the amplitude of the waveforms quantized to two levels only. The delay times corresponding to the peak of the received pulses are displayed against transducer angle in Fig. 14(b). The wire on center ( $r=0$ ) generates a straight line in data space but the wire off center gives rise to the cosine-like point responses of Eqn. (5). The gaps in the data are caused by shadowing and interference.

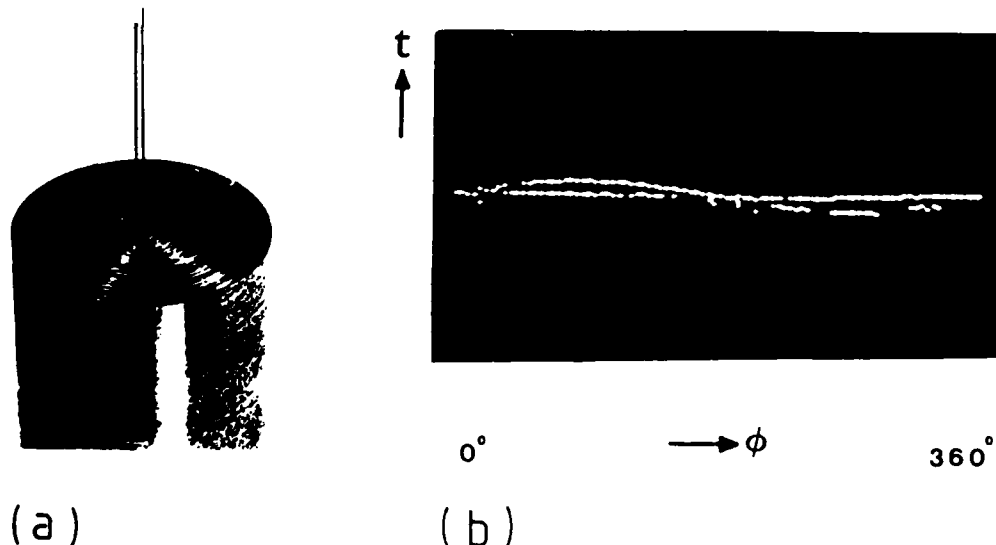
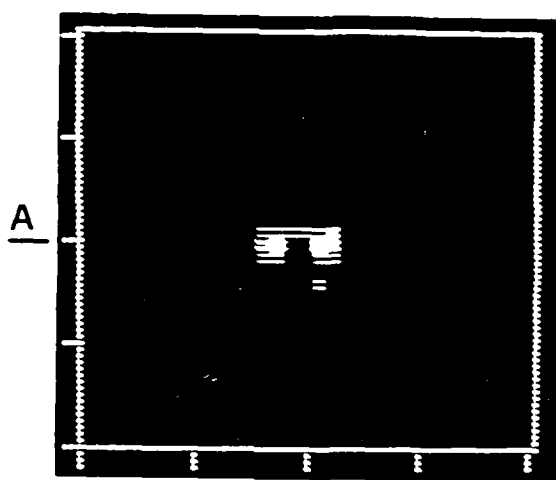
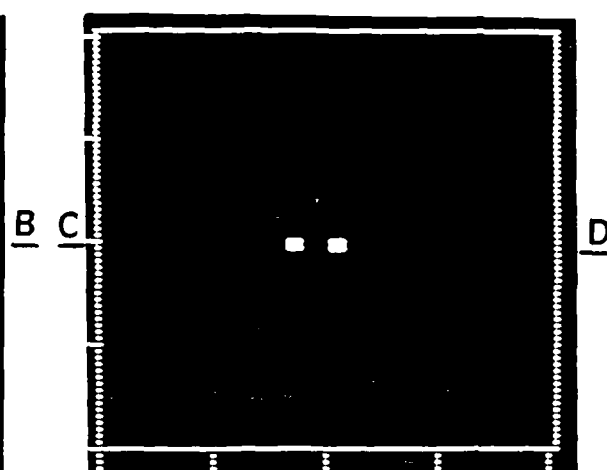


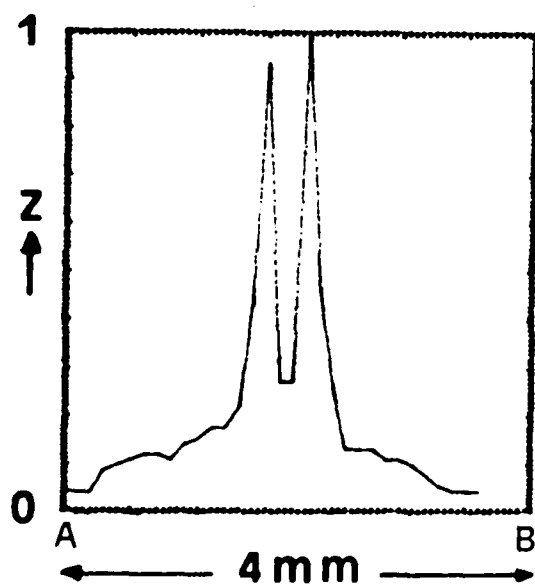
Fig. 14. (a) Two chromel-alumel wires with center to center spacing of 0.4mm. (b) The peak delay time of the pulses against transducer angle.



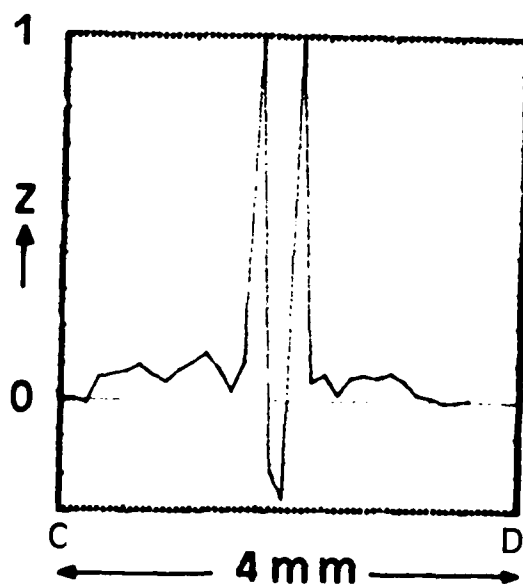
(a)



(c)



(b)



(d)

Fig. 15. (a) The simple backprojection image. The image is a 32x32 pixel picture with pixel size 1/8mm. (b) Cross section plot of (a) along AB. (c) The convolution backprojection image. (d) Cross section plot of (c) along CD.

The simple backprojection processing of the data leads to the image of Fig. 15(a). This is a 32x32 pixel image, with a pixel size of 1/8mm. Fig. 15(b) is a cross section plot along AB. The two wires are somewhat blurred. The convolution processed image is shown in Fig. 15(c), and its cross section plot along CD is shown in Fig. 15(d). The two wires are clearly resolved, despite the gaps in the data.

Fig. 16. shows a test object made of brass rods of 1mm diameter (  $3\lambda$  in water ) which form the letter "A". A full 360 degree aperture was synthesized by 120 transducer positions at 3 degree intervals. Amplitude of the waveforms was quantized to only 8 levels. Fig. 17(a) shows the 128x128 simple backprojection image with pixel size 1/4mm. The convolved image, Fig. 17(b) , shows better contrast. Not only has the outline of the letter "A" been resolved but the circular nature of the rods with correct sizing of their diameters is also apparent. The gaps in the boundary of some of the rods are a result of the shadowing by other rods. A pixel size of 1/8mm showed even better resolution but not all the rods would be seen on the maximum picture size of 128x128.

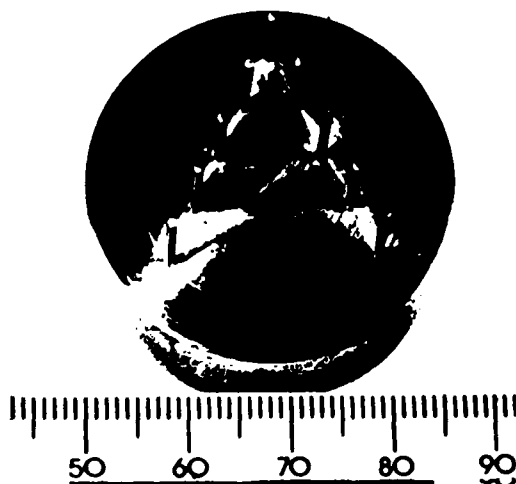
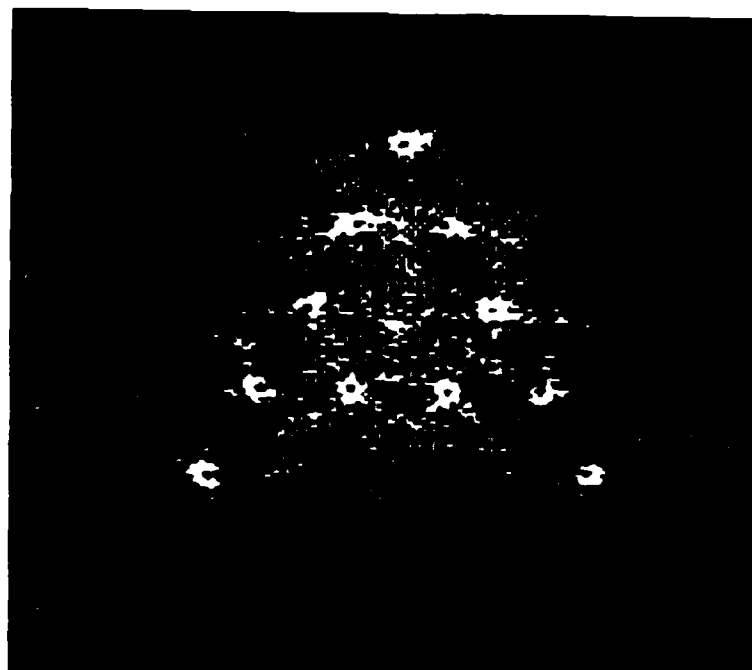


Fig. 16. Test object made of 1mm diameter brass rods to form the letter "A".

#### Imaging of defects in rods

Testing circular rods was done by employing a narrow parallel beam wideband transducer, coupled to the specimen by water. For the coupling the immersion technique was used but the same effect could be produced by water jet coupling where the former is inconvenient. This has the advantage of uniform and non-abrasive coupling with ease for automated testing. If there is a large velocity mismatch between water and the specimen (as is the case for most metals like aluminum and steel) the curved surface acts like a diverging lens as desired, and the parallel beam diverges inside the

(a)



(b)

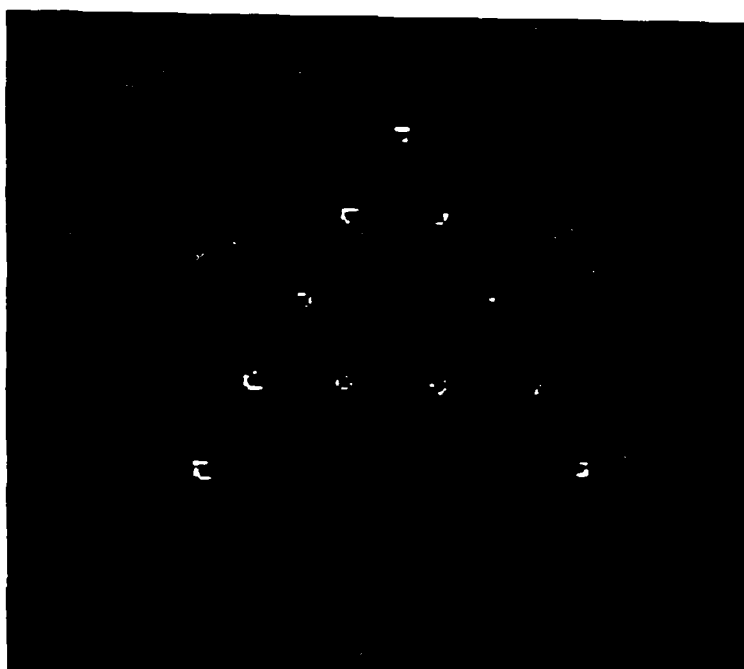


Fig. 17. (a) The simple backprojection image of the letter "A". The image is a 128x128 pixel picture with pixel size 1/4mm. (b) The convolved image.

specimen as shown in Fig. 18. In the paraxial approximation the diverging wavefronts can be approximated by circles. The center of such circles is no longer the transducer position but is offset from the specimen surface by a distance  $f$ , given by <sup>14</sup>:

$$f = \frac{r}{(v/c - 1)} \quad (9)$$

Where  $r$  is the radius of the specimen,  $v$  is the velocity in the specimen and  $c$  the velocity in water.

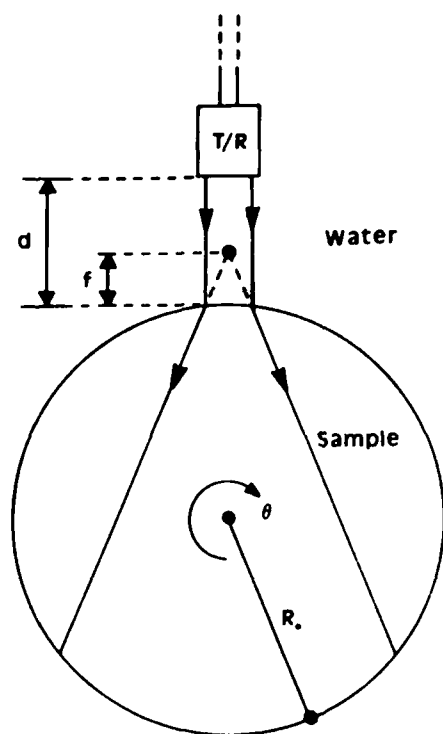


Fig. 18. Water immersion testing setup for rod samples. The curved surface of the sample acts as a diverging lens and produces a diverging wavefront.

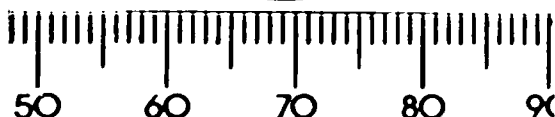
If the parallel beam of the transducer is incident on the boundary of the specimen at right angles or nearly so then the mode inside the specimen is compression waves with little or no shear waves present. The stand-off distance,  $d$ , between the probe and the front surface of the specimen should be large enough such that interfering multiple echoes between them arrive after the back wall echo.

This geometry was used to image three cylindrical holes of diameters 3mm, 2mm and 1mm in an aluminium block of radius 14mm. The holes were

centered on a radius of 6mm and equally spaced in angle ; Fig. 19 shows the sample. Again the aperture was sampled at 120 angles at 3 degree intervals and amplitude quantized to 8 levels. Fig. 20(a) shows the 128x128 simple backprojected image reconstructed on pixel size 1/2mm, and the convolved image is shown in Fig. 20(b). An interfering echo gave rise to an artifact streak in the image. The 3mm and 2mm holes are imaged as holes with the correct diameter to one pixel accuracy. The 1mm hole, however, is less than a wavelength ( for 5MHz  $\lambda=1.3\text{mm}$  in aluminium ) and is imaged as a point reflector. Because the velocity of compression waves in aluminium is about four times that in water the sampling rate of 11.84 MHz corresponds to a spatial sampling of just under 1/4mm. Note that even though the front and back wall echoes of the sample were much larger than the hole echoes, because the holes are seen by a bigger portion of the aperture than points on the outside boundary, the holes appear much brighter. This is not a problem in this case as the walls are just markers. If, however, the image field has both specular and point reflectors then the specular reflector, even though it might be a stronger reflector, would appear weaker.



Fig. 19. An aluminium test sample with three holes of 3, 2 and 1mm diameter.



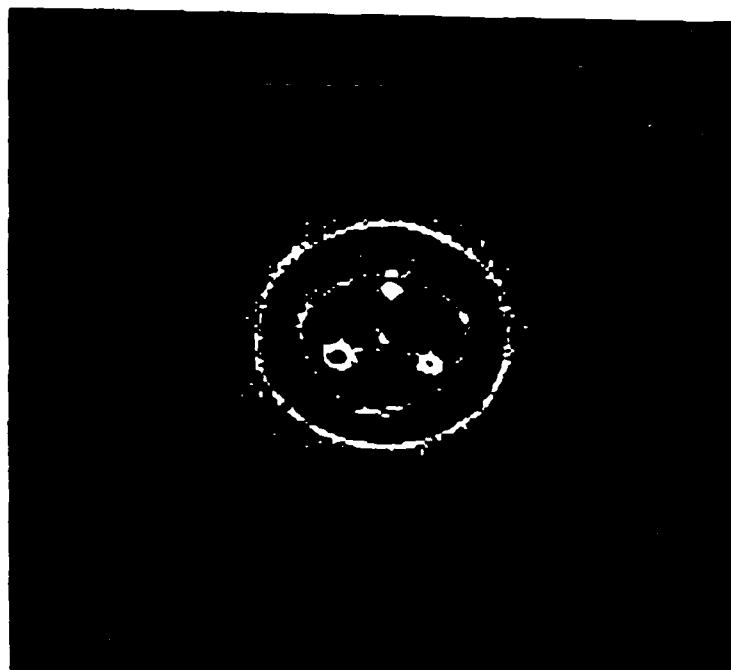
#### Images of defects and cracks in polyester resin

Fig. 21(a) is a side view of a general purpose cylindrical polyester resin sample of diameter 0.77cm and length 0.9cm. It has a line-type void defect running parallel to its axis. Fig. 21(b) is the end view optical image of (a) obtained by looking down along A. As before 120 projections were obtained with 8 level amplitude quantization, and the simple backprojected image is shown in Fig. 22(a), with a pixel size of 1/8mm. The blurring for this image has the missing cones shape PSF of limited angle scanning. The velocity mismatch between the resin and water is not as great as that for aluminium and water. Indeed, the velocity in the resin ( $\approx 2530$  m/s) is somewhat under twice that in water. Under such conditions the beam divergence is not great enough to cover all the sample. Therefore, even for the full aperture synthesized here, the defect is only seen by a finite portion of the aperture. The convolved image is shown in Fig. 22(b) and shows much better defect location information.

The polymer sample shown in Fig. 23(a) is a side view of a .77cm diameter by 7cm long rod of general purpose polyester resin which had been



(a)



(b)

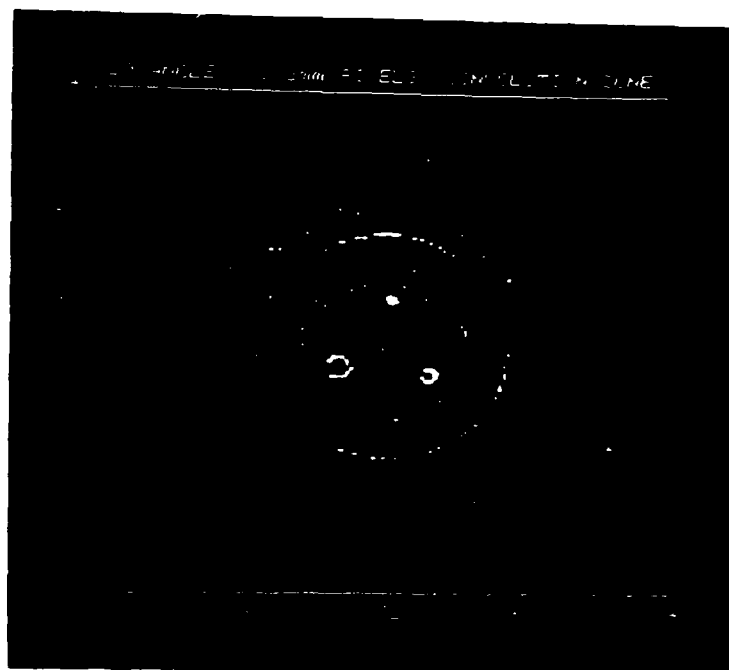
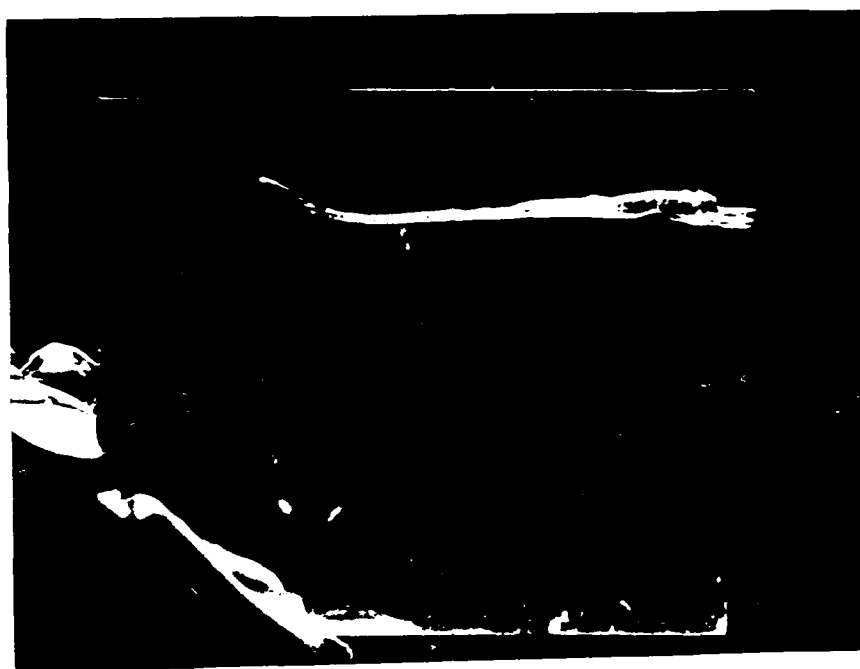
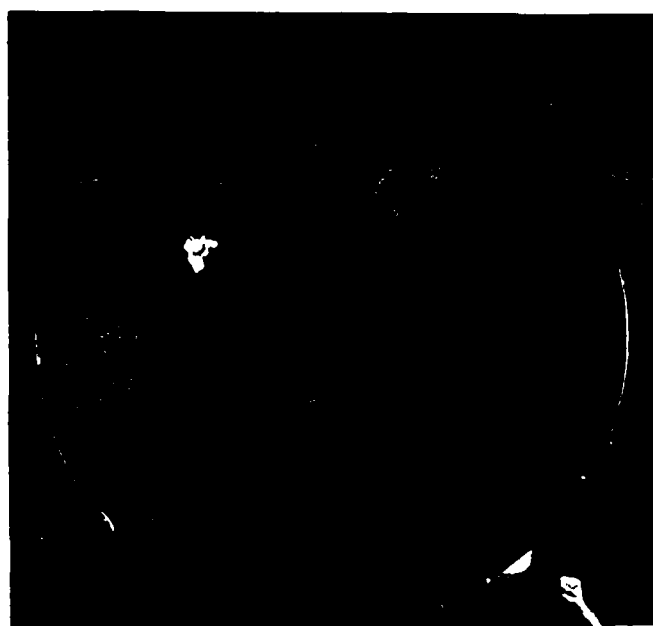


Fig. 20. (a) The simple backprojection image of the aluminium sample. The image is a 128x128 pixel grid with pixel size 1/2mm. (b) The convolved image.



← A

(a)



(b)

Fig. 21. (a) Side view of a general purpose polyester resin with a line-type void defect running almost parallel to its axis. (b) cross sectional view obtained from (a) by looking down along A.

AD-A153 204 PROCEEDINGS OF THE WORKSHOP ON NDE OF POLYMERS HELD AT  
VIMEIRO PORTUGAL ON 4-5 SEPTEMBER 1984(U) BRISTOL UNIV  
(ENGLAND) H H WILLS PHYSICS LAB 05 SEP 84  
UNCLASSIFIED DAJA45-84-M-0182 F/G 11/9

PROCEEDINGS OF THE WORKSHOP ON NDE OF POLYMERS HELD AT  
VIMEIRO PORTUGAL ON 4-5 SEPTEMBER 1984(U) BRISTOL UNIV  
(ENGLAND) H H WILLS PHYSICS LAB 05 SEP 84  
DAJA45-84-M-0182 F/G 11/9

4/4

DAJA45-84-M-0182

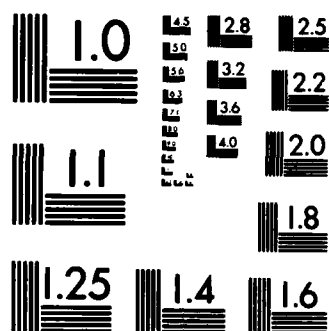
F/G 11/9

NL

END

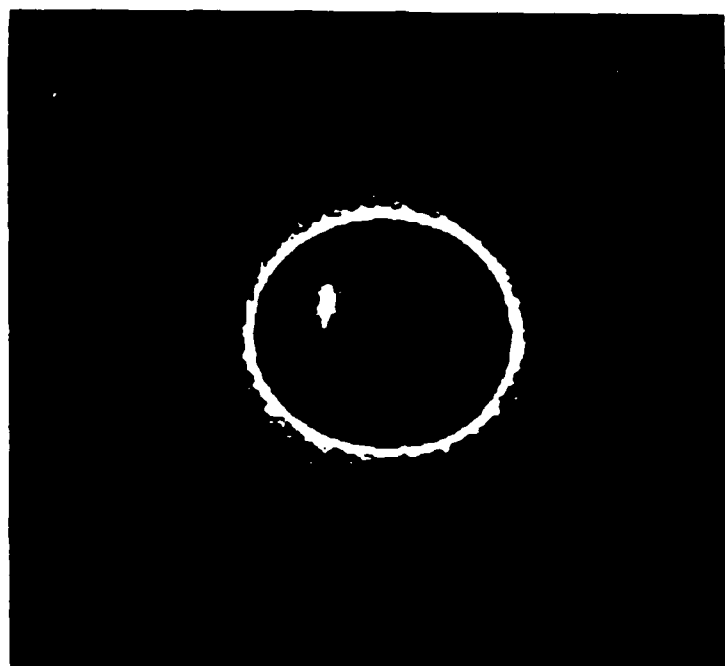
FILMED

DTIC



MICROCOPY RESOLUTION TEST CHART  
NATIONAL BUREAU OF STANDARDS-1963-A

(a)



(b)

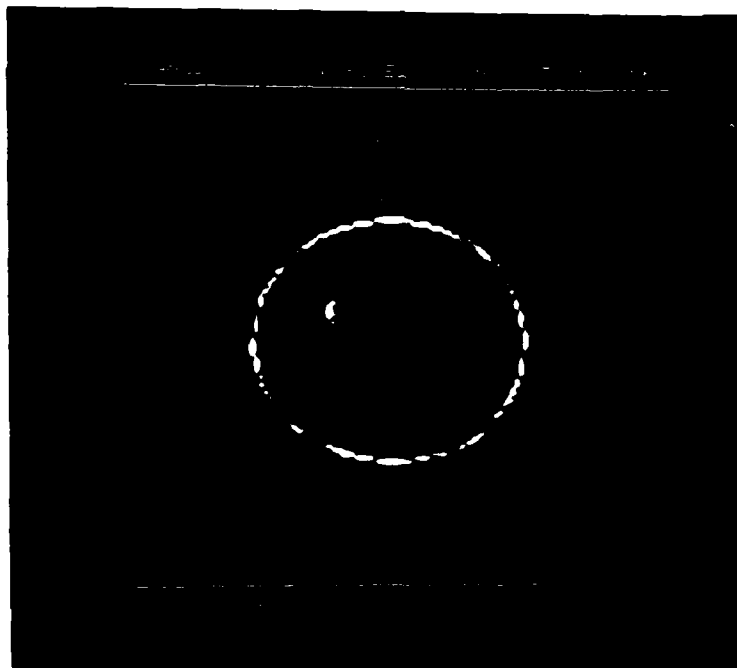


Fig. 22. (a) The simple backprojection of the resin sample with a void in it. The image is a 128x128 pixel picture grid with pixel size 1/8mm. The blurring has missing cones because of the finite angular beam. (b) The convolved image.

cast seven years ago with a single  $10\mu\text{m}$  diameter E-glass fiber along the axis. Fig. 23(b) is an end on view optical image of (a) obtained by looking down along A. The stress field created in such a model composite by the differential contraction that occurs between the fiber and matrix material during cooling from the Curie temperature to room temperature is well documented<sup>15,16</sup>. Under the action of this stress field, a crack oriented more or less parallel to the axis of the rod had propagated, from the fiber interface, during the passage of some seven years.

This sample was scanned with the aperture being sampled at 120 positions in 3 degree intervals and amplitude being quantized to 8 levels. The simple backprojected image is shown in Fig. 24(a), where pixel size is  $1/8\text{mm}$ . Here despite the combination of the finite beamwidth and the specular nature of the crack, the crack has been imaged. The double reflections from the crack register themselves as a spurious image on the top part of the image. The other double echoes on the opposite side of the crack fall outside the resin and are not seen because all echoes after the back wall echo are gated off. These problems when imaging specular reflectors are limitations of all ultrasonic techniques. A trained operator, however, would expect and recognize these spurious images because they occur at regular intervals in image space. The convolved image is shown in Fig. 24(b) and shows less blurring.

It must be mentioned that polyester is a highly absorptive material. For these two samples the back wall echo was about 10 dB below the front wall echo and because of the small dimensions of the samples most of this can be attributed to absorption and not beam spreading. It would therefore be difficult to penetrate samples much larger than the ones shown here. Even so, there are many situations where NDT testing of small resin samples could find good use.

#### Future developments

All the images in this paper have been obtained using compression waves. It is hoped to extend the technique to shear wave imaging so that the two image modes could complement each other and reveal more information about the object. All the images here were processed off-line using a high level language. Once having found the best way to process the data, the processing could then be written in a low level language for real-time operation. It is expected that the data reduction technique outlined here would result in processing times an order of magnitude shorter than other techniques which employ backprojection of the full waveform.

The pressure field of the diverging beam falls off at the edges. There will therefore be points in the aperture where the echoes from a point reflector are weaker because of this. If no correction is made for this those aperture points do not contribute much to the reconstruction. This can be corrected for if an angular weighting factor is incorporated in the backprojection which takes the form of the inverse of the beam profile. Preliminary results have shown that although this correction does improve the PSF in the immediate vicinity of the point reflectors, it does spread background noise throughout the rest of the image. This needs to be investigated further.

A →



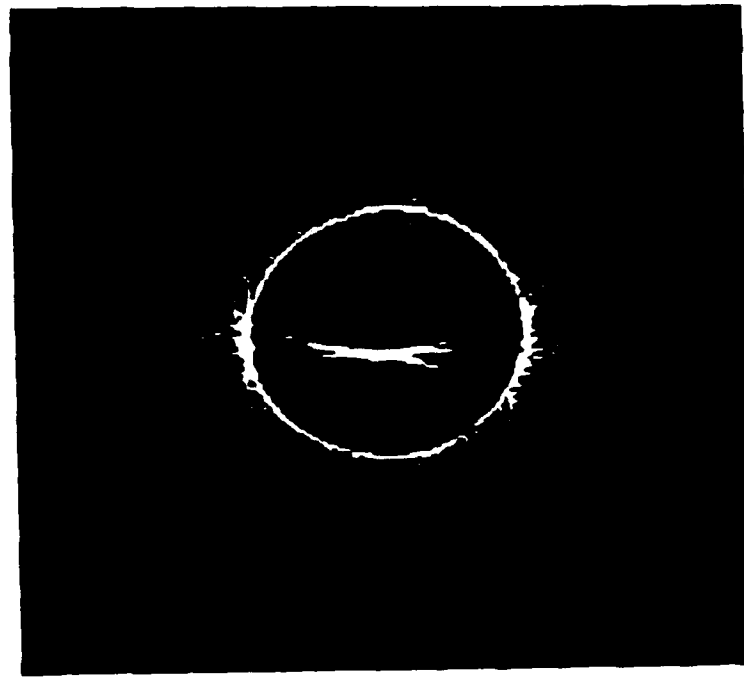
(a)



(b)

Fig. 23. (a) Side view of the general purpose polyester resin sample with a crack almost transverse to its axis. (b) cross section view obtained by looking down A.

(a)



(b)

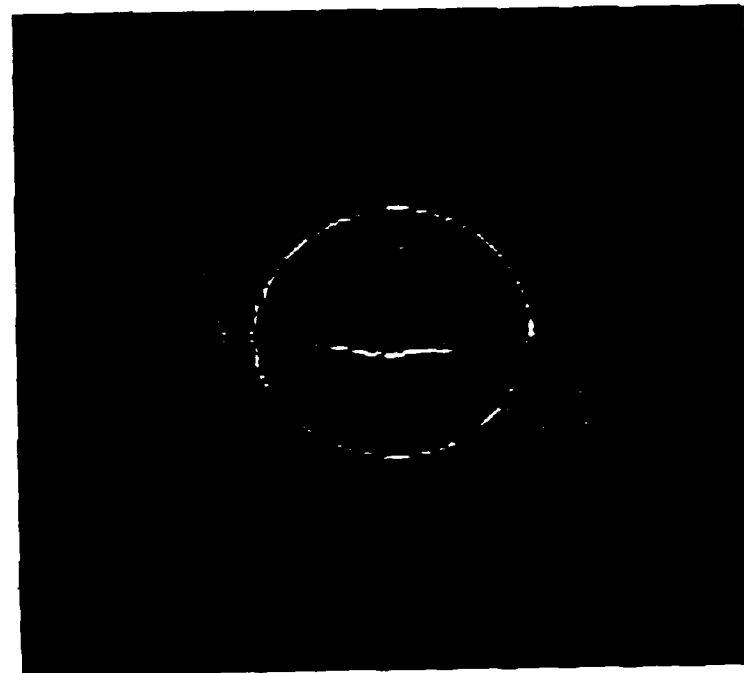


Fig. 24. (a) The simple backprojection image of the resin sample with a crack in it. The picture is a 128x128 pixel grid with pixel size 1/8mm. The multiple reflection between the front surface and the crack have given rise to a spurious image.(b) The convolved image.



## Conclusion

A wideband imaging technique has been described which uses only the time of arrival of the echo data and the peak amplitude of the pulses, and ignores the carrier information of the pulses for image reconstruction. These steps reduce the computation task considerably to pave the way for a cheap portable real-time system. Images of resolution targets have shown diffraction-limited resolution for a full circular aperture. Quantizing the amplitude to only eight levels has shown acceptable images of real defects in polyester resin samples. A simple deblurring kernel has been tested with both computer simulations and real data to remove the blurring caused by simple backprojection.

## Acknowledgment

This work has been supported by the Royal Society's Paul Instrument fund, Messrs Wells-Krautkramer, and a Bristol University scholarship. The authors are grateful to H. Young for preparing the test samples and scanning jig. Discussions with J. P. Sargent, L. Wallis, F. Duck and S. J. Norton are appreciated. The resin samples were supplied by K. H. Ashbee.

## References

1. D. Hiller, and H. Ermert, Tomographic reconstruction of B-scan images. in: Acoustical Imaging, Vol 10 (ed.: Alais and Metherell), pp 347-364, Plenum Press, New York, 1980.
2. S. J. Norton and M. Linzer, Ultrasonic Reflectivity Tomography: Reconstruction with circular transducer arrays. Ultrasonic Imaging 1, pp 154-184, 1979.
3. P. D. Hanstead, Simplified digital synthesis of ultrasonic images. Proc. R. Soc. Lond. A 374, pp 491-502 (1981).
4. L. A. Shepp and B. F. Logan, The Fourier reconstruction of a head section, IEEE Trans Nucl Sci, Vol. NS-21(3), pp 21-43, June 1974.
5. Z. H. Cho, I. Ahn, C. Tsai, Computer algorithms and detector electronics for the transmission X-ray tomography, IEEE Nucl. Sci. NS-21, No. 1 (1974), pp 218-227.
6. S. J. Norton, Reconstruction of a reflectivity field from line integrals over circular paths, J. Acoust. Soc. Am. 67(3), pp 853-863, Mar. 1980.
7. S. Ganapathy, W. S. Wu and B. Schmolt, Analysis and design considerations for a real-time system for non-destructive evaluation in the nuclear industry, Ultrasonics, November 1982.
8. S. Trietel and E. Robinson, The design of High-Resolution Digital Filters, IEEE Transactions on Geoscience Electronics, Vol. GE-4, pp 25-38, 1966.
9. K. Liang, B. T. Khuri-Yakub, and G. S. Kino, Reflection tomography at 50 and 300 MHz, IEEE Ultrasonic symposium, pp 925-929, 1981.

10. S. A. Johnson, et al, High spatial resolution measurement techniques for characterization of static and moving tissues, Ultrasonic Tissue Characterization II, M.Linzer ed., National Bureau of Standards, Spec. Publ. 525 (U.S. Government Printing Office, Washington, D.C., 1979).
11. P. D. Corl, G. S. Kino, A Real-Time Synthetic-Aperture Imaging System, in: Acoustical Imaging, Vol 9 (ed. Metherell), pp 341-355, Plenum Press, New York, 1980.
12. J. R. Fredrick, et al, Improved Ultrasonic Nondestructive Testing of Pressure Vessels, Nuclear Regulatory Commission Report NUREG/CR-0909 (Sep. 1979).
13. P. D. Hanstead, A new method for ultrasonic inspection, C.E.G.B. Technical Disclosure, no 291, 1978.
14. J. Krautkrämer, H. Krautkrämer, Ultrasonic Testing of Materials, Third revised edition, pp 54, Springer-Verlag, 1983.
15. H. Poritsky, Analysis of thermal stresses in sealed cylinders and the effect of viscous flow during anneal, Physics, Vol 5, December 1934.
16. G. D. Redston, J. E. Stanworth, Glass to metal seals, J. Soc. Glass Technol, Vol 29, pp 48-76, 1945.

### Discussion of Session VIII

Mr Barraclough invited hypotheses other than the one he postulated for time-dependent absorption of different ultrasound frequencies within his material. P D Hanstead (Bristol University) suggested that resonance of the sample might explain the observations since the cell length was of the right order to give resonance modes at the frequencies observed. This explanation would be consistent with the monotonically increasing velocity with time which Mr Barraclough had reported, while the pulse length shown in his illustration was sufficiently long to last for several traverses of the sample, thus permitting constructive or destructive interference.

Dr R E Green Jr complimented Moshfeghi and Hanstead on their development and application of algorithms used in their low-cost (\$4,000) method for digital synthesis of high resolution ultrasonic images. There was some discussion of the limitations of ultrasonic techniques for polymer NDE, the most important of which limitations are due to intrinsic attenuation.

There was some discussion of the possibility of analysis of modes of vibration and/or of the transmission of elastic waves in order to detect fabrication defects in polymers. The physical basis for this is that voids and cracks have significant effects on the elastic moduli of solids. The general problem of the effects of ellipsoidal inclusions (including voids) on elastic moduli was treated in a lecture course by J D Eshelby in the 1950's at the University of Birmingham.

Taking as first example the case of a spherical void in a solid with Poisson's ratio  $\sigma = 1/3$ , the constants  $\alpha$  and  $\beta$  in Section 5 on page 389 of Eshelby's (1957) paper "The determination of the elastic field of an ellipsoidal inclusion, and related problems" are  $2/3$  and  $7/15$  respectively. Hence, on page 390, as  $\kappa_1 \rightarrow 0$   $A \rightarrow 3$  and as  $\mu_1 \rightarrow 0$   $B \rightarrow 2$ , and  $\kappa_{eff} = \kappa(1 - 3v)$ ,  $\mu_{eff} = \mu(1 - 2v)$  where  $v$  is the volume fraction of voids. The analysis for the limiting case of identical randomly oriented "penny-shaped" cracks was published by Bristow (1960) and the relevant equations, equations (8) in Bristow's paper with one misprint corrected, are

$$\frac{\Delta E}{E} = - \frac{16(1 - \sigma^2)(10 - 3\sigma)}{45(2 - \sigma)} a^3 n$$

$$\frac{\Delta \mu}{\mu} = - \frac{32(1 - \sigma)(5 - \sigma)}{45(2 - \sigma)} a^3 n$$

$$\frac{\Delta \kappa}{\kappa} = - \frac{16(1 - \sigma^2)}{9(1 - 2\sigma)} a^3 n$$

$n$  is the number of cracks per unit volume,  $a$  is the crack radius.

As far as was known by those attending the workshop, no attempts have been made to relate the effects of voids and cracks on elastic moduli to the propagation of sound waves in polymers. However, it was noted with interest that attempts have been made to relate the effects of cracks on elastic moduli to the changes in seismic wave velocities that are observed prior to earthquakes. Earthquakes generate seismic waves and these are of the following two kinds: P waves (primary waves) which are longitudinal, compressive waves travelling with velocity  $v_p$  and S waves (secondary waves) which are transverse, shear waves travelling with velocity  $v_s$ .

$$v_p = \sqrt{\frac{\lambda + 2\mu}{\rho}}, \quad v_s = \sqrt{\frac{\mu}{\rho}}$$

so

$$\left(\frac{v_p}{v_s}\right)^2 = \frac{\lambda + 2\mu}{\mu} = \frac{\kappa}{\mu} + \frac{4}{3} \quad \text{since} \quad \lambda = \kappa - \frac{2\mu}{3}$$

$$= \frac{2(1 + \sigma)}{3(1 - 2\sigma)} + \frac{4}{3} = \frac{2(1 - \sigma)}{(1 - 2\sigma)}$$

That is, the ratio  $v_p/v_s$  depends only on Poisson's ratio. Scholz et al (1973) note that the velocity ratio falls from 1.75 to as low as 1.52 well before an earthquake and then recovers to a higher value immediately preceding the earthquake. The duration of the abnormally low velocity ratio appears to be related to the magnitude of the subsequent earthquake.

Using the corrected equations from Bristow (1960),  $\Delta\mu/\mu \sim 1.45 a^3 n$  and  $\Delta\kappa/\kappa \sim 3.33 a^3 n$  if  $\sigma = 1/4$ .

Substituting  $\frac{v_P}{v_S} = \frac{3}{2}$  in  $\left(\frac{v_P}{v_S}\right)^2 = \frac{\kappa - \Delta\kappa}{\mu - \Delta\mu} + \frac{4}{3}$

yields  $a^3 n \sim 1/5$ .

By virtue of drainage from nearby cracks and pores, the freshly created cracks will gradually become filled with water so  $\kappa$  should increase but  $\mu$  should remain virtually unchanged. Hence, the pumping of water into crustal cracks is expected to produce an increase in velocity ratio and presumably accounts for the observed recovery of  $v_P/v_S$ . To explain the apparent correlation between the time required for this recovery and the magnitude of the subsequent earthquake, Scholz et al (1973) point out that the magnitude of the dilatancy, and hence the magnitude of the water percolation required to fill the cracks, is determined by the magnitude and extent of the crustal strain energy density which subsequently is relieved by the earthquake.

The use of velocity ratio measurements to detect cracks in laboratory specimens is of considerable interest. However, in order to make sure that a P-wave and not a rod-wave is generated, it is necessary to stimulate a vibration with wavelength very much shorter than the specimen length. For a 1/10" cube of sintered diamond for example, this means a frequency of at least 50 MHz which is somewhat higher than the frequencies obtainable from most commercial transducers.

#### References

- J D Eshelby (1957) Proc Roy Soc A241, 376  
 J R Bristow (1960) Brit J Appl Phys 11, 81  
 H Scholz, L R Sykes and Y P Aggarwal (1973) Science 181 803

Session IX: Rubber elasticity and anisotropy under stress

# CHAIN ORIENTATION DETECTED WITH DEUTERIUM NMR IN UNIAXIALLY DEFORMED POLYMERIC NETWORK.

Bertrand DELOCHE

Laboratoire de Physique des Solides, (CNRS LA2) Université de Paris Sud,  
91405 Orsay (FRANCE)

## ABSTRACT

The orientational order generated in rubbers by uniaxial stress is probed with deuterium NMR. The experiments are done either on deuterated swelling agents as NMR probes or directly on labeled polymeric chain segments. In both cases the  $^2\text{H}$ -NMR spectra exhibit a residual quadrupolar interaction when the sample is under constraint and such a residual interaction yields the corresponding degree of orientational order. In both cases the induced order exhibits the explicit dependence on the extension ratio predicted by the kinetic description of rubber elasticity.

## 1 - INTRODUCTION

The rubber state exists in variety of flexible macromolecular chains (polyisoprenes, polybutadienes) which are held in a threedimensional array by chemical crosslinks (covalent bonds) and physical junctions (entanglements). This state is somewhat unique in that the constituent polymer chains are fluid but the bulk material does not flow and so retains its form.

The rubber may be deformed elastically by external forces eg simple tension; optical birefringence measurements show that the system becomes anisotropic. How does the macroscopic strain affect the chain behaviour? Such a question related to the deformation involved at the molecular level is relevant from a basic and applied perspective. This is the reason why it received increasing attention in the past few years. Indeed various microscopic techniques (neutron scattering, fluorescent polarization, infra-red spectroscopy) are currently being used to examine elastomeric chains under deformation. Among the techniques which are sensitive to orientational behaviour, deuterium NMR ( $^2\text{H}$ -NMR) has emerged as a powerful for probing local ordering in polymeric networks. Specifically we propose to describe here how to use this technique to study the orientational order generated in uniaxially deformed rubbers.

The methodology exploits the observation of residual quadrupolar interactions in the form of a resolved doublet structure in the  $^2\text{H}$ -NMR spectra when the system becomes anisotropic ie under constraint. The measurements are done either on deuterated swelling agents, as NMR probes, or directly on labeled polymeric chains; clearly these experiments allow the detection of an orientational anisotropy at the chain level and give access to the corresponding order parameter.

## 2 - BACKGROUND

### 2.1. Rubber Elasticity

The classic description of rubber elasticity is based on a single gaussian-chain model (1). Under the assumption of constant volume and affine molecular deformation such a theory leads to the following relationship between uniaxial stress  $\sigma$  and small strain (Hooke's regime) :

$$\sigma = E (\lambda^2 - \lambda^{-1}) \quad [1]$$

where  $E$  is Young's modulus and  $\lambda$  is the extension ratio ie the ratio of the deformed sample length to the original length.

The hypothesis of molecular affine deformation determines the orientational distribution of the chain end to end vectors  $R$  relative to the direction of the applied constraint. Then, from the orientational distribution of the chain segments relative to  $R$  one can obtain the second moment  $\langle P_2 \rangle$  of the segmental orientation function relative to the constraint axis ( $\hat{z}$ ). This yields in the framework of gaussian chains:

$$P_2(\cos\theta) \approx \frac{1}{5N} (\lambda^2 - \lambda^{-1}) + O\left(\frac{\lambda^4}{N^2}\right) \quad [2]$$

$P_2(\cos\theta)$  is the second Legendre polynomial and  $\theta$  is the angle between the direction of the applied force and the statistical segment under interest;  $N$  is the number of statistical segments per chain.  $\langle P_2(\cos\theta) \rangle$  and  $\sigma$  exhibit the same  $\lambda$ -dependence in the limit of low deformation ( $\lambda^2 \ll 1$ ).

## 2.2. Deuterium NMR

The general features of  $^2\text{H}$ -NMR in anisotropic fluid phases have been discussed in detail in reference 3. Briefly we recall that the  $^2\text{H}$ -NMR spectra of deuterium labeled anisotropic fluids are dominated by the interaction of the deuteron nuclear quadrupolar moment with the residual electric field gradient (efg) at the nucleus. So the Zeeman hamiltonian  $H_Z$  is perturbed by a quadrupolar hamiltonian  $H_Q$  ( $H_Z \gg H_Q$ ) which is orientation dependent relative to the direction of the steady magnetic field  $\vec{B}_0$ . A first order calculation (4) leads to the structure of levels indicated in figure 1. The conventional  $H^2$ -NMR line is split into a symmetrical quadrupolar

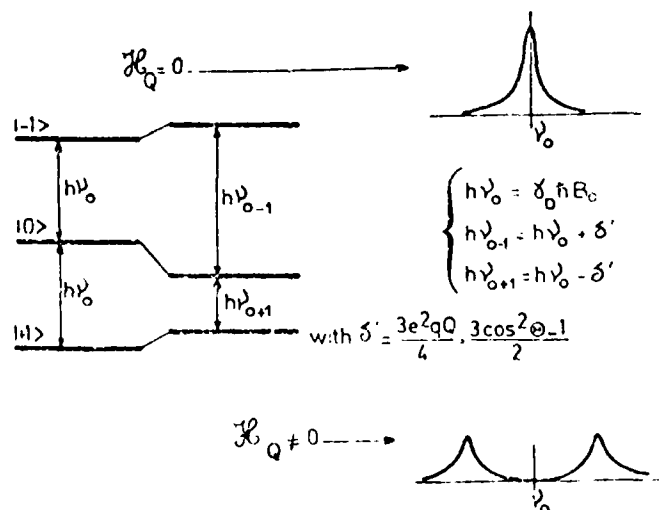


Figure 1: Structure of the levels of deuterons (nuclear spin  $I = 1$ ) in the absence or presence of quadrupolar interaction  $H_Q$ . NMR transitions frequencies and lineshapes under irradiation with radiofrequency field are also indicated.  $\nu_0$  is the deuteron Larmor frequency ( $\nu_0 = 6.53$  MHz for a field  $B_0 = 10$  KG.).

doublet when  $H_Q \neq 0$ . With an axial efg tensor, the doublet spacing is given



in frequency units by:

$$\Delta\nu = \frac{3}{2} \nu_q (P_2(\cos\theta)) \quad [3]$$

$\nu_q$  is the static quadrupolar coupling constant. The  $P_2$  term is the second Legendre polynomial;  $\theta$  is the angle between the C-D bond and the direction of the magnetic field  $\vec{B}_0$ . There is one such quadrupolar doublet for each chemical site and for each distinct orientation of the C-D bond relative to  $\vec{B}_0$ .

Motions of the C-D bond modulate  $\theta$  and a time average has to be taken when the C-D bond reorients with frequencies larger than that of the static interaction ( $\sim 200$  KHz); relation [3] then becomes:

$$\Delta\nu = \frac{3}{2} \nu_q \langle P_2(\cos \theta(t)) \rangle \quad [4]$$

So the quadrupolar splitting appears proportional to the orientational order parameter of the C-D bond with respect to  $\vec{B}_0$ . Because of such averagings, the  $^2\text{H}$ -NMR spectrum of an anisotropic fluid medium consists of doublets than can be discrete and well resolved.

In the case of uniaxial reorientations around a symmetry axis (ie. this one of the applied tension in our case) making the angles  $\Omega$  with  $\vec{B}_0$  and  $\theta$  with the C-D bond, the averaging over azimuthal angles leads to the following expression for the splitting:

$$\Delta\nu = \frac{3}{2} \nu_q \langle P_2(\cos\theta(t)) \rangle P_2(\cos\Omega) \quad [5]$$

Then the effective quadrupolar coupling constant is  $\nu_q \langle P_2(\cos\theta(t)) \rangle$  where the average can be defined as the orientational order parameter of the C-D bond relative to the symmetry axis under interest.

The current resolution available for observing  $\Delta\nu$  ( $\sim 1$  Hz) in conjunction with the inherently large value of the C-D quadrupolar constants ( $\nu_q \sim 200$  KHz) enables one to measure orientational order differing from the isotropic state by as little as a few parts in  $10^5$ .

### 3 - EXPERIMENTAL

#### 3.1. Deuterium NMR approach

From the experimental point of view, the  $^2\text{H}$ -NMR may be conveniently done either on deuterated swelling agents (5), used as NMR probes of the swollen polymeric matrix, or directly on labeled chains segment of the network (6-7).

All  $^2\text{H}$ -NMR spectra were obtained after signal averaging from FT NMR equipment operating with a conventional electromagnet (the magnetic field  $\vec{B}_0$  is perpendicular to the stretching direction,  $\Omega = 90^\circ$ ) or a superconducting magnet ( $\vec{B}_0$  is parallel to the stretching direction,  $\Omega = 0^\circ$ ).

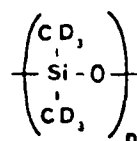
#### 3.2. Materials

Most experiments were performed on hexadeuteriobenzene dissolved in diene rubbers and on labelled chains of some silicone rubbers.

The set of diene rubbers are tetrafunctional polybutadiene (PB) networks; all these networks were prepared from peroxide cross-linking of a polybutadiene precursor (Diene 45 NF). The cross-linking reaction was always carried out in the dry state varying the curing agent concentration. Each

network is characterized by its mean molecular weight  $M_c$  derived from the corresponding values of the volume fraction of polymer  $\phi_e$  at swelling equilibrium, using cyclohexane as a good solvent.

The set of silicone rubbers are end-linked polydimethylsiloxane model networks, containing a known fraction (20%) of perdeuterated chains PDMS (D).



These networks were synthesized by reacting stoichiometric mixtures of labelled and unlabelled precursors chains with tetrafunctional cross-linkers(8); the end-linking reaction was carried out in toluene of 70% polymer concentration. The synthesis of perdeuterated precursors is described in reference (9). These networks are characterized by the molecular weight between cross-links  $M_n$  i.e. the molecular weight of the precursor ( $3.000 < M_n < 25000 \text{ g.mol.}^{-1}$ ). The molecular weight distribution is about 1.5, the same as for the precursor polymer.

### 3.3 Uniaxial stress

Tension was applied to samples the nominal dimensions of which were typically 40 mm x 6 mm x 1 mm as described in reference 5 so that the stretching direction is coincident with the axis of the NMR tube, i.e.

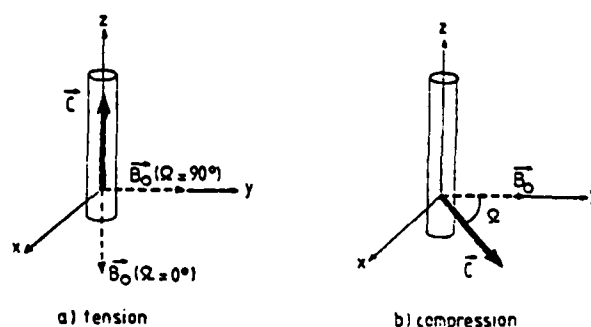


Figure 2: Orientation of the spectrometer magnetic field  $\vec{B}_0$  with respect to the applied uniaxial stress  $C$ : a)  $\vec{B}_0$  is perpendicular or parallel to the direction of the elongation b)  $\vec{B}_0$  is always along the  $y$  axis while the direction of the compression may be varied within the plane  $(x, y)$  by rotating the NMR tube around its vertical axis.

parallel or at right angles to the spectrometer magnetic field  $\vec{B}_0$ . The extension ratio  $\lambda = \frac{L}{L_0}$  was estimated from the stretched and unstretched lengths measured optically by monitoring the spacings ( $\sim 25 \text{ mm}$ ) between marks on the sample.  $L$  was determined to within  $\pm 0,2 \text{ mm}$ .

The compression was obtained by squeezing a small piece of the sample between two semi-cylindrical jaws. This assembly was introduced into the bottom of the NMR tube; in this way the angle  $\Omega$  between the compression direction relative to  $\vec{B}_0$  can be varied continuously, rotating the tube by hand around its vertical axis, as indicated on figure 1. The compression ratio ( $\lambda < 1$ ) was estimated from the thickness of the sample.

Deuterated probes ( $C_6D_6$ ) were dissolved in the elastomer by exposing dry (preweighed) samples to the vapor/liquid of the swelling agents. The volume fraction of polymer  $\phi$  was determined by weighing the samples before and after the NMR experiment.

#### 4 - RESULTS

##### 4.1. Solvent orientation

Figure 3 shows the change of the  $^2H$ -NMR spectrum of deuterobenzene in a PB network as the sample is uniaxially elongated. The spectrum changes from a single narrow line in the relaxed state ( $\lambda = 1$ ) to quadrupolar doublets. The observed residual interaction for  $\lambda > 1$  are indicative of anisotropic reorientational diffusion for  $C_6D_6$  constrained by the uniaxial field generated by the elongated network chains. The corresponding orientational order parameter  $\langle P_2 \rangle$  of the benzene  $C_6$  axis can be deduced from the relation 5 with  $\nu_Q = 190$  kHz and  $\Omega = 90^\circ$ : typically  $\langle P_2 \rangle = 2.5 \cdot 10^{-3}$  for a relative elongation of 30%.

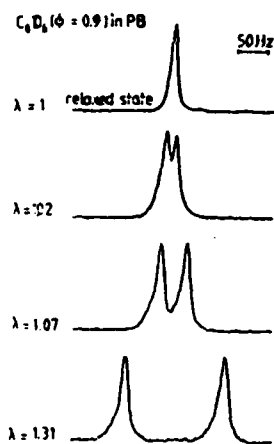


Figure 3: 13 MHz  $^2H$ -NMR spectra of  $C_6D_6$  in a uniaxially strained PB network (polymer volume fraction  $\phi = 0.9$ ). The mean molecular weight  $M_c$  between junctions is about  $10.000 \text{ g.mol}^{-1}$ .

As shown on figures 4 and 5, this strained induced orientation appears quite general, regardless of the nature of the polymer matrix and of the probe molecule. For instance the figure 5 shows that nearly spherical molecules (chloroform) as well as flexible short chains (n-heptane) are oriented within the deformed network.

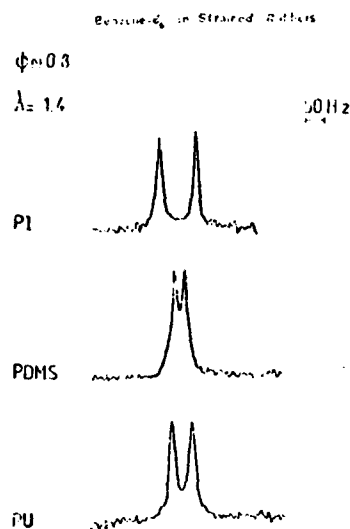


Figure 4: 13 MHz  $^2\text{H}$ -NMR spectra of  $\text{C}_6\text{D}_6$  in uniaxially strained polyisoprene (PI), polydimethylsiloxane (PDMS) and polyurethane (PU) networks (polymer volume fraction  $\phi = 0.8$ )

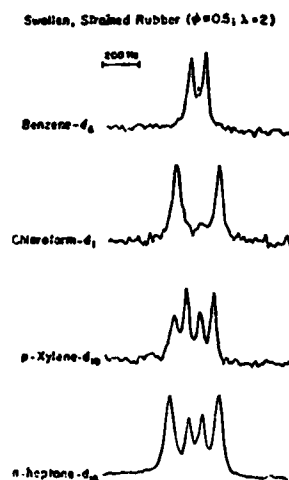


Figure 5:  $^2\text{H}$ -NMR spectra of various deuterated swelling agents in a polyisoprene network ( $M_c \sim 3500$ ). The latter two solvents have chemically inequivalent deuterons and so exhibit more than one quadrupolar doublet.

#### 4.2. Chain segment orientation

Figure 6 shows characteristic spectra of PDMS (D) as the sample is uniaxially compressed ( $\lambda < 1$ ) or elongated ( $\lambda > 1$ ) along a direction perpendicular to the steady magnetic field  $B$  ( $\Omega = 90^\circ$ ): here too quadrupolar doublets ( $\Delta\nu \neq 0$ ) are still observed for  $\lambda \neq 1$ . But in part due to a broader linewidth in the relaxed state ( $\delta\nu \sim 30$  HZ) the observed spectral resolution

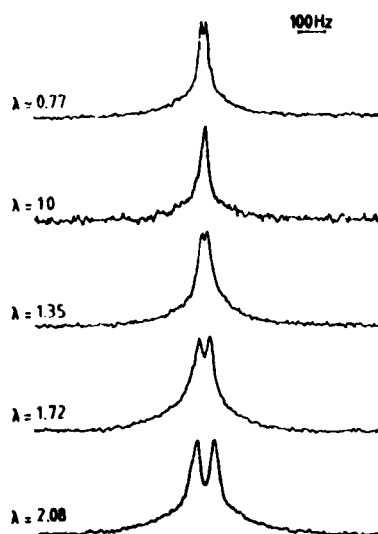


Figure 6: 13 MHz  $^2\text{H}$ -NMR spectra of perdeuterated chains of polydimethylsiloxane networks, PDMS(D), as the sample is uniaxially compressed ( $\lambda < 1$ ) or elongated ( $\lambda > 1$ ). The molecular weight  $M_n$  of polymer between cross-links is 25.000.

is lower than the experiments on dissolved probes. One primary source of this lack of resolution can be attributed to a superposition of  $\Delta\nu$  derived from a distribution of chain length between junctions (7, 10); segments of short chains exhibit higher orientational order than those in longer chains for a given  $\lambda$ .

The complete angular variation  $\Delta\nu(\Omega)$  reported in figure 7 shows that it reproduces exactly the  $|P_2(\cos\Omega)|$  as in as in relation [5]. So clearly the polymer chain (or portions of them) which give rise to the doublet may be visualized as a uniaxial fluid of segments exhibiting anisotropic reorientational diffusion with respect to the direction of the applied constraint. For instance we may consider that the chain segments diffuse in such a way that they cannot be oriented in any other direction than along the axis of stress for times longer than a few  $10^{-5}$  sec.

At this level, let us noticed that the same kind of  $^2\text{H}$ -NMR experiments on labeled chains has been recently achieved on polybutadiene networks (see reference 7).

#### 4.3. Solvent versus segment orientation

What is the relationship between the order parameter  $\langle P_2 \rangle$  as measured on the solvent probes and on the chain segments? The answer to this question required a comparison of the following complementary systems(11) : PDMS(D) swollen with  $\text{C}_6\text{H}_6$  and PDMS swollen with  $\text{C}_6\text{D}_6$ . Identical tetrafunctional end-

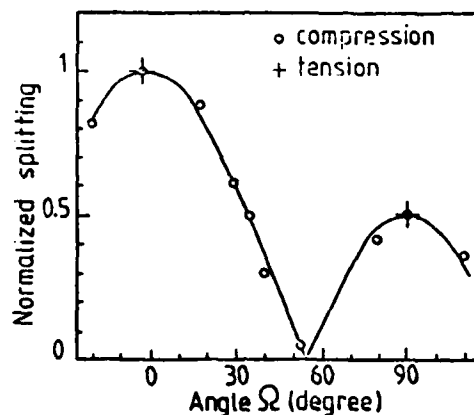


Figure 7: Variation of the normalized splittings of the PDMS(D) as a function of the angle between the uniaxial constraint and the steady magnetic field. The continuous line is the function  $|P_2(\cos\Omega)|$ .

linked PDMS networks ( $M_n = 25,000$ ) were used at the same degree of swelling  $\phi = 0.92$ . Figure 8 illustrates the variation of the quadrupolar splittings

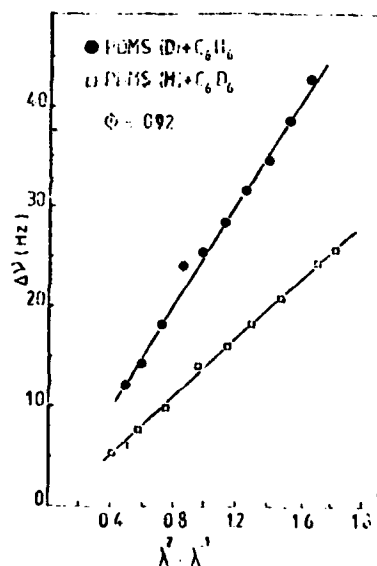


Figure 8: Plot of the quadrupolar splittings  $\Delta\nu$  versus  $\lambda^2 - \lambda^{-1}$  for both networks in the limit of small deformations ( $\lambda < 2$ ). The observed values of  $\Delta\nu$  are reversible with the extension ratio  $\lambda$ .

with the elongation. It appears that in both cases the data fit well with a  $\lambda^2 - \lambda^{-1}$  law (as previously observed on polyisoprene (5) and polybutadiene (12) networks). This strain dependence, related to the isovolume character of the orientation process under simple extension, is in agreement with the relation [2], in the low deformation limit. So the striking feature

of the observed averaging effect is that the splitting  $\Delta\nu(\lambda)$  (and thus the corresponding order parameter  $\langle P_2 \rangle$ ) measured via the swelling agents remains proportional to the one measured directly on the polymer chain segments. Moreover, the respective  $\langle P_2 \rangle$  have a similar magnitude for a given elongation  $\lambda$ . Specifically, according to the relation [5] where  $\Omega = 90^\circ$ ,  $\nu_0 = 176$  KHZ for PDMS(D) and  $\nu_0 = 190$  KHZ for  $C_6D_6$ , and by taking into account the extra averaging effect due to the free rotation of the  $CD_3$  around the Si- $CD_3$  bond, we find for  $\lambda = 2$  that the order parameter of the symmetry axis of the methyl group is equal to  $8.10^{-4}$  while this one of the symmetry axis of the benzene is equal to  $3.10^{-4}$ ; so they differ by less than one order of magnitude. This result indicates that, for such a degree of swelling, the solvent molecules are faithful probes of the polymeric environment.

## 5 - CONCLUDING REMARKS

This work on strained elastomer networks demonstrates that the  $^2H$ -NMR is a powerful non-destructive technique for probing polymeric chain ordering. In particular the order of magnitude agreement between the solvent and segment orientational order and the fact that the investigation via the solvent-probe leads to the same strain dependence as the direct study of the polymeric backbone does indicate that reorientational diffusion of swelling agents is strongly coupled to the segment ordering of the polymer. This suggests that deuterated solvents may be confidently used to test orientational phenomena in strained rubbers. Moreover the use of labeled probe obviates the need to label network chains and so facilitates the examination of the effect of cross-linking density on orientational order (12).

On the other hand the phenomena of solvent orientation certainly involves solvent-segment (and segment-segment) short range orientational correlation within the elongated network. Such correlations may affect the optico-elastic properties of swollen networks as emphasized in reference 5.

## 6 - REFERENCES

- (1) Treloar L.R.G. (1975) . The Physics of Rubber Elasticity, Clarendon Press, Oxford.
- (2) Roe R.J. and Krigbaum W.R. (1964) J. Appl. Phys. 35, 2215
- (3) Charvolin J. and Deloche B. (1979), The Molecular Physics of Liquid Crystals, Academic Press, London 15, 343.
- (4) Abragam A. (1961) The Principles of Nuclear Magnetism, Oxford University Press 7, 219.
- (5) Deloche B and Samulski E.T. (1981) Macromolecules 14, 575.
- (6) Deloche B., Herz J. and Beltzung M. (1982) . J. de Physique Lett 43, 763.
- (7) Gronski W., Stadler R. and Jacobi M. (1984) Macromolecules 17, 741.
- (8) Herz J., Belkebir A and Rempp P. (1973), Eur. Polym. J. 9, 1165.
- (9) Beltzung M., Picot C., Rempp P. and Herz J. (1982) Macromolecules 15, 1594
- (10) Samulski E.T. (1984), to be published in Polymer.
- (11) Toriumi H., Deloche B., Herz J and Samulski E.T., submitted to Macromolecules.
- (12) Dubault A., Deloche B. and Herz J. (1984) to be published in Polymer.

## Bi-dimensional compression testing

K H G Ashbee and F C Frank

University of Bristol  
H H Wills Physics Laboratory  
Tyndall Avenue  
Bristol BS8 1TL, England

### Abstract

A bi-dimensional compression testing apparatus is described whereby a plurality of interfitting anvils, of substantially gee-shaped configuration, is advanced simultaneously but independently in such a way as to impose two-dimensional compressive strain. The method can be applied to specimens of any polygonal cross-section that have fixed angles. Designs are presented for triangular, rectangular and hexagonal cross-sections. Working models have been built for the rectangular version, one of which is capable of imposing infinite bi-dimensional compressive strain.

### Introduction

Most applications of elastomers exploit their capacity to undergo large reversible deformation. However, the nature of this large reversible deformation is rarely investigated as a method for nondestructive evaluation. One reason for this is that, whereas most applications of elastomers involve the imposition of biaxial deformation, satisfactory experimental methods exist



only for uniaxial deformation. The invention described here concerns the development of a method for bi-dimensional deformation, to infinite compressive strain if required.

#### Designs for bi-dimensional compressive testing rigs

For a fixed angled polygon of  $N$  sides, there are  $(N - 2)$  degrees of freedom and these can be taken as the lengths of  $(N - 2)$  successive sides. Thus, an arbitrary triangle with fixed angles has one degree of freedom because, if one edge length is stipulated, the other two are determined. An arbitrary quadrilateral of fixed angles has two degrees of freedom. In the special case of a rectangle, the two degrees of freedom are its length and width, either of which can be varied independently of the other. A pentagon of fixed angles has three degrees of freedom, a hexagon four, an octagon six, and so on. Bi-dimensional compression of a fixed angled polygon of  $N$  sides requires  $N$  gee-shaped elements. Figures 1, 2 and 3 illustrate the preferred geometries of gee-shaped elements by means of which bi-dimensional compression can be applied to bar stock of triangular, rectangular and hexagonal cross-sections respectively. For each cross-section there exists an alternative shape and configuration for the gee pieces which, although acceptable in geometry, is less convenient in respect of presentation of flats normal to the desired motions.

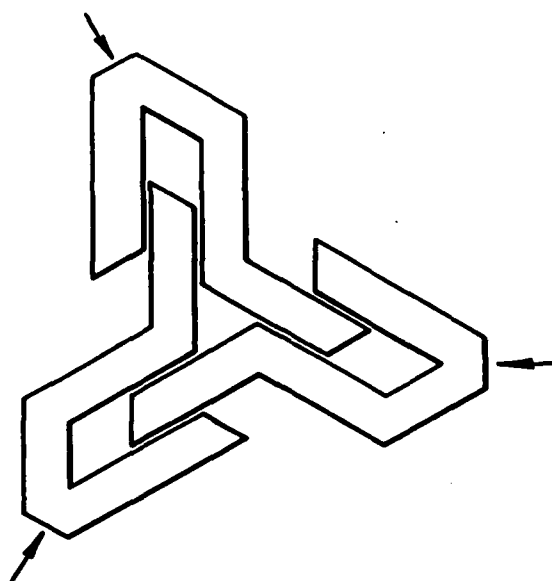


Figure 1. Three-gee design for bi-dimensional compression

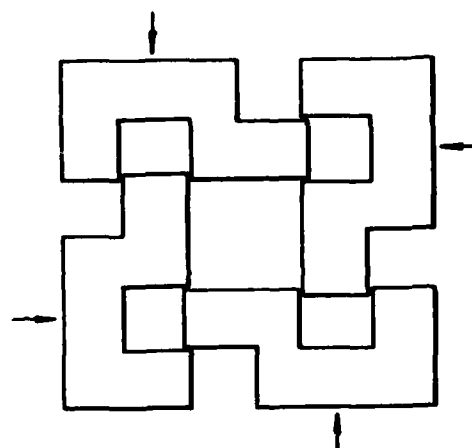


Figure 2. Four-gee design for bi-dimensional compression. This design readily permits two independent strains to be imposed in the plane of the gees

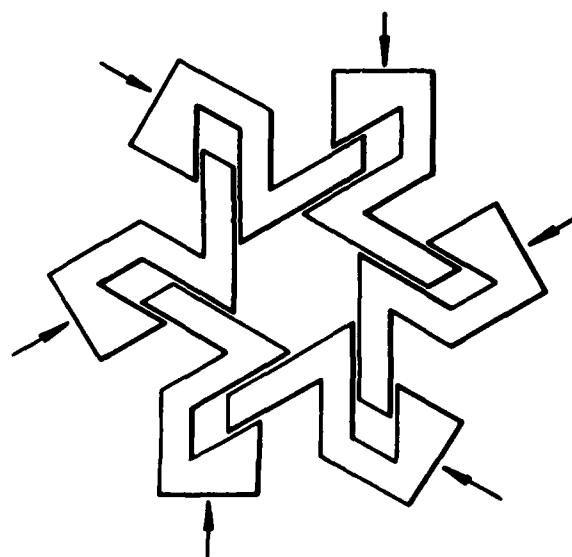
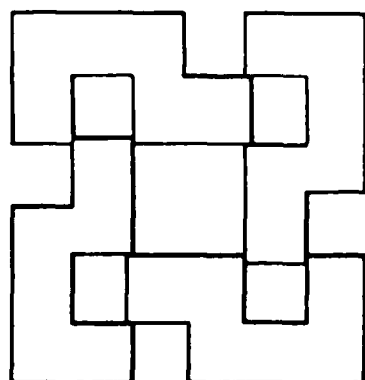


Figure 3. Six-gee design for bi-dimensional compression

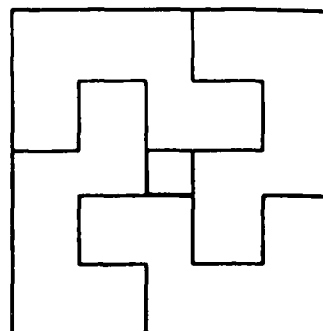
With each design, identical displacement of the gees towards the centre creates uniform compressive strain in the plane of the gees, i.e. creates uniaxial tensile strain normal to the plane of the gees. The four-gee design is particularly interesting since independent displacement of the two pairs of opposed gees creates a state of triaxial strain in the specimen, viz the two independent strains imposed in the plane of the gees and the strain normal to that plane that is determined by the condition of (near) incompressibility during deformation of the specimen.

#### Working bi-dimensional compression rigs

Finite strain rectangular cross-section and infinite strain rectangular cross-section forms of the invention have been built. In the former, the four working components are identical square cornered gee-shaped elements. Figure 4 shows the four elements (a) in the fully open, and (b) in the fully closed configuration. These elements are housed within a square frame which carries four identical lead-screw/cross-head assemblies so that they can be advanced in pairs in such a way as to achieve two independent displacements parallel to each of two perpendicular directions. If identical displacement rates are required, this is conveniently secured by using the scroll from a self-centring four-jaw chuck. In the apparatus demonstrated at the workshop, Figure 5(a) and (b), each lead screw is rotated by hand via a wheel and worm. By counting the number of turns of the worm, the advance of any cross-head can be measured. By introducing a load measuring cell between a cross-head and the pair of gee-shaped elements that it moves, the load generated by that movement may be determined.

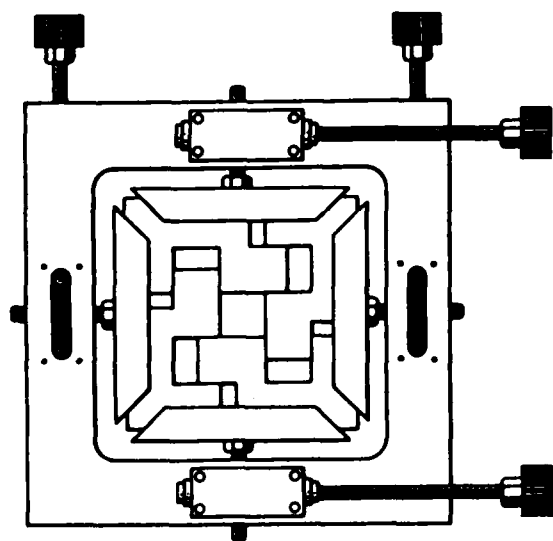


(a) gees fully open

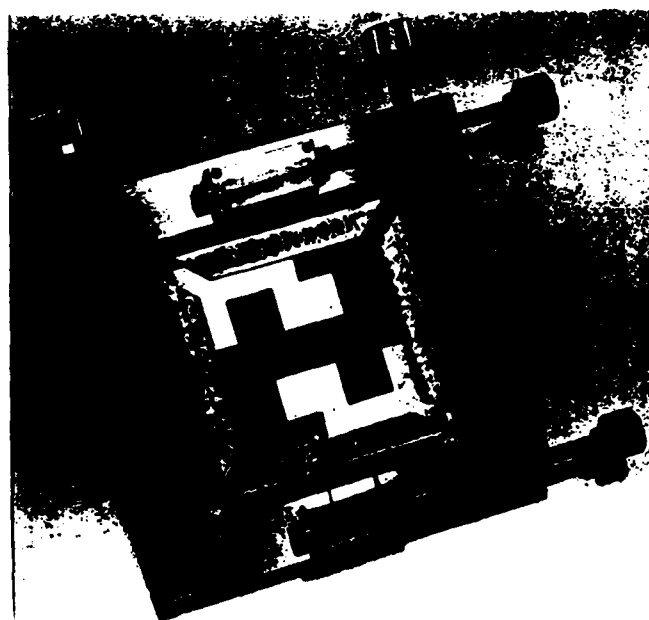


(b) gees fully closed

Figure 4. Plan view of the four-gee finite strain design



(a)



(b)

Figure 5. (a) Plan view and (b) photograph of the finite strain four-gee bi-dimensional compression apparatus

In the infinite strain rectangular form of the apparatus, Figures 6 and 7, the working components are four identical gee-shaped elements with non-anvil faces so oriented that the elements completely intermesh when the assembly is fully compressed. Thus, the anvil surfaces define a four-sided prism, not

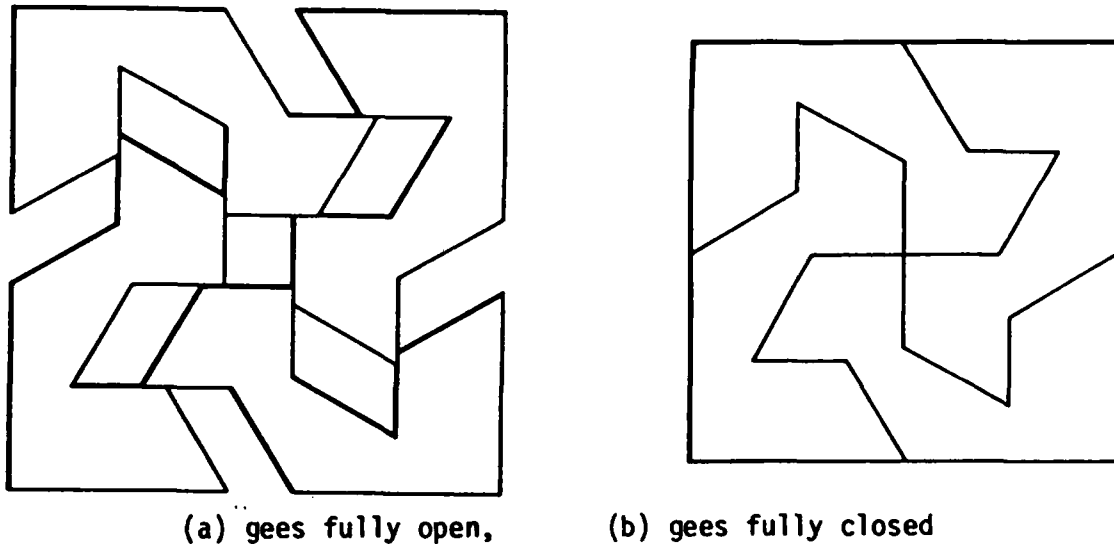


Figure 6. Plan view of the four-gee infinite strain design

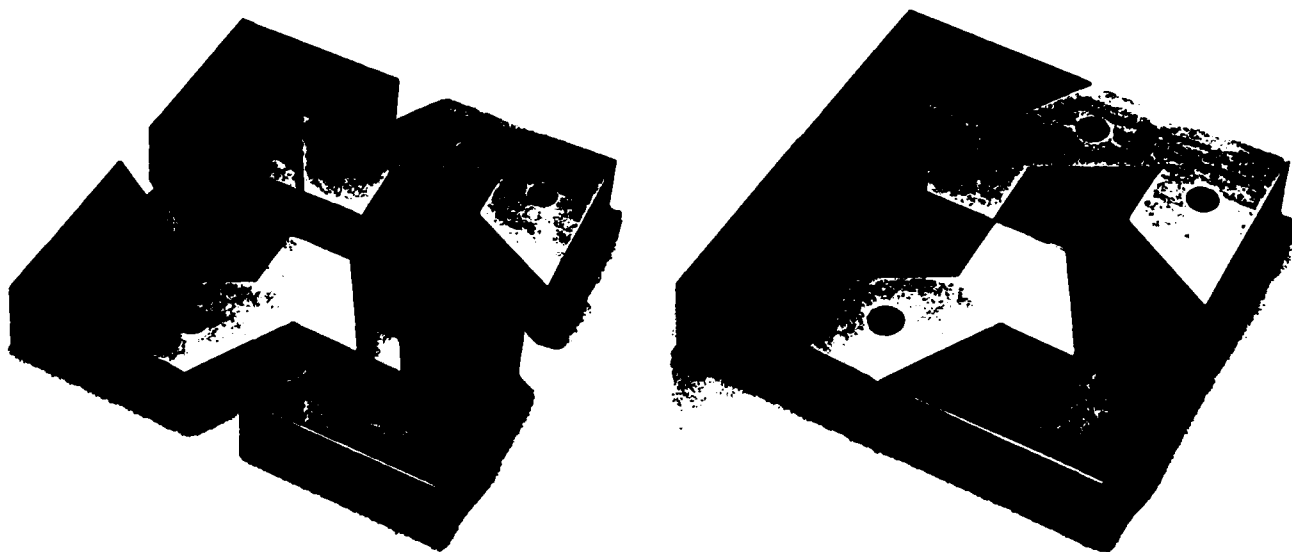


Figure 7. The four-gee infinite strain bi-dimensional compression rig.

This rig fits inside the frame of the lead-screw/cross-head assembly shown in Figure 5

necessarily square, with all dimensions down to zero. In principle, this embodiment may be used to impose any bi-dimensional shape change. In practice, near infinite strain deformations are conceivable only with an incompressible fluid as test-piece. With a rubber-like material as test-piece, there exists some value of tensile strain at which the corresponding stress becomes negative. Thus, for deformations involving compression along x and extension along y, at some value of  $\lambda_y$  the test-piece will separate from the y-platens. That is, there are limits on the strain that can be applied in practice. However if, at the point of y-platen separation, plugs are rammed into the open ends ( z faces ) of the confined cell until the specimen again makes contact with the y-platens, further extension along y becomes possible. Thus, by forcing in plugs in the z directions, it should be possible to achieve enormous extension in the y direction. Of course, the changes in dimensions of the confined cell necessitate changes in size of the z-plugs although, by using a soft metal shim for z-plugs, it may be possible to avoid this and so continuously carry on with the deformation.

The ideas described here are protected by UK patent application 84/14028 dated 1 June, 1984.

## Discussion of Session IX

Professor Sir Charles Frank asked Dr Deloche whether he would care to speculate on what kind of  $^2\text{H}$ -NMR spectra might be expected in elastomers subjected to bi-dimensional deformation. Deloche was not able to hazard a guess but expressed a strong interest in carrying out the experiment. He pointed out that the apparatus would need to be non-conducting whereupon Dr Ashbee produced a four-gee finite strain bi-dimensional compression rig that had been fabricated from machinable mica glass-ceramic with nylon bolts as lead-screws.

Dr Ashbee showed another application of the bi-dimensional compression invention, namely the manufacture of super-high fibre volume fraction composites. One manufacturing defect always present in uniaxial compression moulded fibre reinforced materials is matrix-rich regions, i.e. regions that contain few or even no fibres. Examples (after Kelly, 1972) can be seen in the micrograph reproduced in Figure 1. Using bi-dimensional compression moulding, uniaxial fibre reinforced plastics having remarkably uniform fibre distributions, and fibre contents as high as 90% for glass and carbon fibres and higher than 95% for kevlar fibres, have been manufactured.

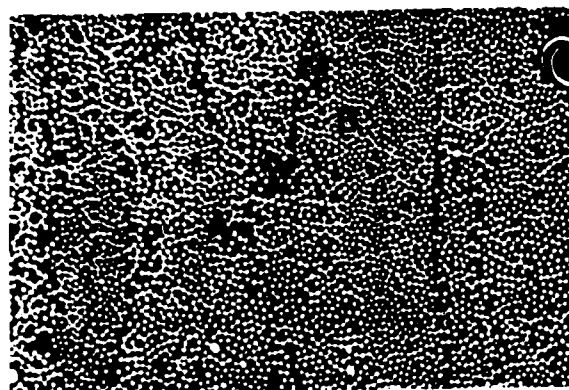


Fig.1 A cross-section of a fibrous composite composed of carbon fibres in an epoxy resin. *A* denotes a place where the fibres effectively surround the matrix, and *B* a region where the fibres are approximately most closely packed

## Reference

A Kelly, Microstructural Parameters of an Aligned Fibrous Composite, in "The Properties of Fibre Composites" proceedings of a conference held at National Physical Laboratory, Nov 4 1971, IPC Science & Technology Press Ltd (1972) p5

Session X: Closing remarks



There exists in polymer technology very little by way of in-process non-destructive evaluation. This is because, unlike metals, polymers are not readily characterised by clear-cut microstructural variations that can be identified and attributed to defects, or to deficiencies in fabrication method, or to incorrect heat treatment.

In components fabricated from polymers, including polymers in the rubbery state, there exists a class of microstructural defects which have their origins in processing. These defects include inhomogeneous mixing, inclusion of foreign bodies, segregation, incomplete cure, inhomogeneous cure, molecular orientation, macroscopic anisotropy and residual stress. This workshop addressed the feasibility of new exploitation of physical techniques to secure, for use as a processing tool, the real-time detection of such defects. "To keep our feet on the ground" formal contributions by practising technologists were also scheduled. Other observers from industry were invited and all were encouraged to interject "state of the art" comments whenever appropriate.

In as far as it addressed specific materials, the workshop was directed towards the fabrication of thermosets, thermoplastics, elastomers and resin based composite materials. For each kind of material, the meeting was timely and welcome. For example, the high cost of replacing rubber items, from tyres to intricate components in electro-mechanical devices, is currently receiving increased attention and made emphasis at the workshop on the nature of mechanical weakness in rubber and its detection by non-destructive means especially appropriate. No less desirable, in view of recent recognition of the cost benefits available if non-specified raw materials could be used to fabricate structures and components from composite materials, was the need for an appraisal of advanced techniques for on-line changing of processing of fibre reinforced plastics.

There have been many recent advances in experimental techniques for probing polymer structures, some of which are being developed commercially especially for medical diagnostic purposes. X-ray and ultrasonic tomography are examples. When producing the workshop programme it was decided to play-down

**END**

**FILMED**

**5-85**

**DTIC**